GLOBAL NON-DYNAMIC REFINEMENT OF RADIAL ORBIT ERROR FOR ALTIMETRIC EARTH SATELLITES

RORY DUNCAN GRAY

Doctor of Philosophy

ASTON UNIVERSITY

July 1993

ASTON UNIVERSITY

GLOBAL NON-DYNAMIC REFINEMENT OF RADIAL ORBIT ERROR FOR ALTIMETRIC EARTH SATELLITES

RORY DUNCAN GRAY

Doctor of Philosophy

July 1993

THESIS SUMMARY

The accuracy of altimetrically derived oceanographic and geophysical information is limited by the precision of the radial component of the satellite ephemeris. A non-dynamic technique is proposed as a method of reducing the global radial orbit error of altimetric satellites. This involves the recovery of each coefficient of an analytically derived radial error correction through a refinement of crossover difference residuals. The crossover data is supplemented by absolute height measurements to permit the retrieval of otherwise unobservable geographically correlated and linearly combined parameters. The feasibility of the radial reduction procedure is established upon application to the three day repeat orbit of SEASAT.

The concept of arc aggregates is devised as a means of extending the method to incorporate longer durations, such as the 35 day repeat period of ERS-1. A continuous orbit is effectively created by including the radial misclosure between consecutive long arcs as an infallible observation. The arc aggregate procedure is validated using a combination of three successive SEASAT ephemerides. A complete simulation of the 501 revolution per 35 day repeat orbit of ERS-1 is derived and the recovery of the global radial orbit error over the full repeat period is successfully accomplished.

The radial reduction is dependent upon the geographical locations of the supplementary direct height data. Investigations into the respective influences of various sites proposed for the tracking of ERS-1 by ground-based transponders are carried out. The potential effectiveness on the radial orbital accuracy of locating future tracking sites in regions of high latitudinal magnitude is demonstrated.

KEYWORDS AND PHRASES

- Crossover
- Arc Aggregate
- SEASAT and ERS-1
- Repeat Orbit
- Transponder

Acknowledgements

I would like to thank Aston University for its financial assistance. I would also like to express my gratitude to Dr Philip Moore whose unwavering support and exceptional patience throughout the duration of the research has proved invaluable.

CONTENTS

List of Tables

List of Figures

CHAPTER 1

INTRODUCTION

During the past two decades altimetric satellites have enabled great strides to be made in the detailed monitoring of the ocean surfaces of the Earth. Since 1973, when Skylab became the first satellite to include an altimeter in its payload, GEOS-3 (1975), SEASAT (1978), GEOSAT (1985) and presently ERS-1 (1991) and TOPEX/POSEIDON (1992) have all been successful in providing high quality altimetric data. Follow-on missions of the latter three are now being planned.

Current altimeter observations are generally accurate to the order of 10cm. However, precise positioning of the sea surface is limited, primarily by inaccuracies in the radial component of the computed orbit of the spacecraft. The principal effects occur as a result of mismodelling of the gravitational field of the Earth, although significant non-gravitational sources, due to air drag, solar radiation pressure and initial position errors also contribute. The main objective of the research carried out is to investigate the possibility of a global reduction of the ephemeris error in the radial direction, to a level comparable with that of the instrumental measurement.

A non-dynamic analytical radial correction to dynamic long arc ephemerides is deduced for a satellite travelling in a low eccentric, frozen, repeat orbit, from consideration of both the gravitational and non-gravitational contributions. A radial data set is geometrically obtained from ascending and descending ground-track intersection points of a long arc orbit. This has the advantage of eliminating from the direct altimeter data both the relatively large geoidal errors and any time invariant biases. A procedure is proposed whereby each coefficient of the radial correction expression is recovered through a refinement of the crossover residuals. The crossover data is supplemented by absolute height measurements to permit the

retrieval of the otherwise unobservable geographically correlated and linearly combined parameters.

The feasibility of the method is initially established upon application to the three day repeat orbit of the NASA satellite SEASAT (1978-64A), operational during three months of 1978. In anticipation of the thirty five day repeat orbit of the European Remote Sensing satellite, ERS-1, the concept of arc aggregates is devised. The inclusion of the radial orbital misclosure as an infallible observation enables successive ephemerides to be effectively amalgamated into a single continuous orbit. Several non-gravitational radial correction terms are unique to individual arcs of an aggregate, whereas other purely periodic gravitational constituents are common to each. The arc-dependent and arc-independent parameters are identified and the aggregate extension carried out using consecutive SEASAT long arcs.

A complete simulation of the 501 revolution per 35 days repeat orbit of ERS-1 has been constructed, using the creation of a clone of the GEM-T1 gravity field model. The aggregate technique is applied and the recovery of the global radial orbit error over the full length of the repeat period is accomplished.

The reduction of the radial orbit error is dependent upon the geographical locations of the supplementary direct height data. Various proposals for ground-based transponder sites from which tracking of ERS-1 might be achieved are examined. Using laser ranging data from an early ERS-1 three day repeat orbit, the respective effectiveness of each position on the error reduction procedure is investigated and optimum locations are considered.

Strong evidence of the possible improvement in the accuracy of altimetrically derived oceanographic and geophysical information is produced. Future employment of the procedures and recommendations proposed throughout the thesis should provide considerable assistance in achieving that goal.

CHAPTER 2

ALTIMETRY

§ 2.1 The Altimeter

The development of the altimeter in the early 1970's greatly enhanced the ability to study and monitor variations in the ocean surfaces of our planet. An altimeter is an electronic measuring device carried on board a satellite which is used to calculate the distance between the electronic centre of the instrument and the instantaneous sea surface directly beneath. The altimetric concept involves a microwave radar pulse emitted by the nadir-pointing altimeter, the spread of the pulse forming a "footprint", typically a few kilometres in diameter, on the surface below, as shown in Figure (2.1).

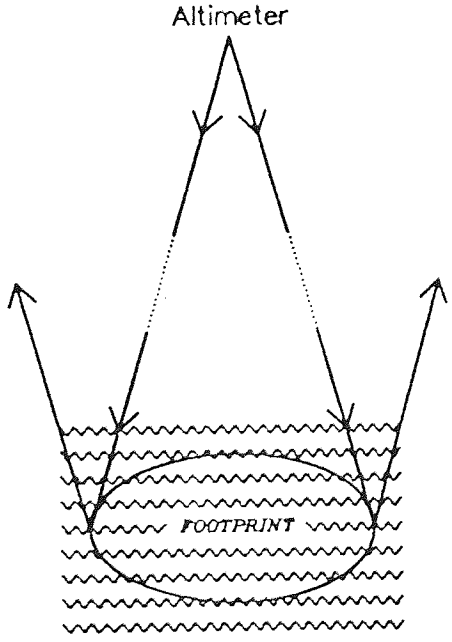

Figure (2.1)
The altimetric principle

The pulse is reflected by the surface in a manner dependent upon the surface characteristics and some of the reflected signal is received back by the altimeter. The time taken from transmission to reception is recorded together with the returned waveform. The distance from the satellite to the sea surface is then derived by the on-board software. By including an altimeter in the payload of artificial satellites, geodesists can measure the mean sea level and its variability due to ocean currents and tides. The inaugural altimetric mission was Skylab, launched in 1973, which acted as proof of the concept. This was followed by GEOS-3 (1975) and then by SEASAT, which in 1978 became the first state-of-the-art satellite totally dedicated to ocean observation. Subsequently altimeters have been carried by GEOSAT (1985), ERS-1 (1991) and most recently TOPEX/POSEIDON (1992), with ERS-2, GEOSAT and TOPEX/POSEIDON follow-ons planned.

§ 2.2 Reference Ellipsoid and Geoid

In order for an altimetric observation to become useful in an absolute sense, the measurement is formed with respect to a convenient reference surface. This is taken to be an ellipsoid centred at the centre of the Earth, having semi-major axis ≈ 6378 km in the Earth's equatorial plane, semi-minor axis ≈ 6357 km along the Earth's polar axis, equivalent to a flattening of 1/298.26. This reference surface closely approximates the actual shape of the Earth. The geoid is then defined to be that equipotential surface perpendicular to the overall force due to the gravitational and rotational accelerations as measured at the surface of the Earth. The height of the geoid, N, coincides with that at which the mean sea surface would lie if the sea was of uniform density, had no currents or tides and was unaffected by winds and atmospheric pressure.

§ 2.3 Altimetric Height Corrections

Having obtained a raw altimeter height measurement, h_{raw}, corrections must be made in order to derive the final observed height, h_{alt}. Various atmospheric conditions affect the radar pulse as it travels through the air between the satellite and the sea surface. Air pressure and humidity at different levels of the atmosphere create refraction effects which alter the speed of the signal. These meteorological conditions are measured by other instruments such as on-board microwave radiometers for the wet tropospheric correction and surface meteorological stations for atmospheric pressure, from which corrections are determined. Corrections required are the barometric correction, h_{bar}, ionospheric correction, h_{ion}, and the wet and dry tropospheric corrections, h_{wtrop} and h_{dtrop}, respectively.

During the first few weeks of the lifetime of a satellite its altimeter undergoes calibration tests which invariably discover timing or measurement biases. These are modelled and removed from any observations taken later by applying an instrumental correction, h_{inst}, to the raw measurement.

Corrections due to solid Earth and ocean tides, h_{set} and h_{ot}, respectively, are calculated from existing models to account for dynamic variations of the sea surface height during the time of travel of the altimetric pulse. Finally a term, h_{ssb}, is derived to take account of the presence of sea surface roughness, known as sea-state bias.

All these corrections are applied to the raw altimeter height to yield the final altimetric height observation as

$$h_{alt} = h_{raw} + h_{bar} + h_{ion} + h_{wtrop} + h_{dtrop} + h_{inst} + h_{ssb} + h_{set} + h_{ot} .$$

The accuracy of the instrument, i.e. that of h_{raw}, is generally at the few centimetre level for current altimeters such as that on ERS-1, but the corrected measurement,

h_{alt}, is dependent on the accuracy of the corrections. An r.m.s. value of 10cm for h_{alt} is typically quoted.

§ 2.4 Altimetric Applications

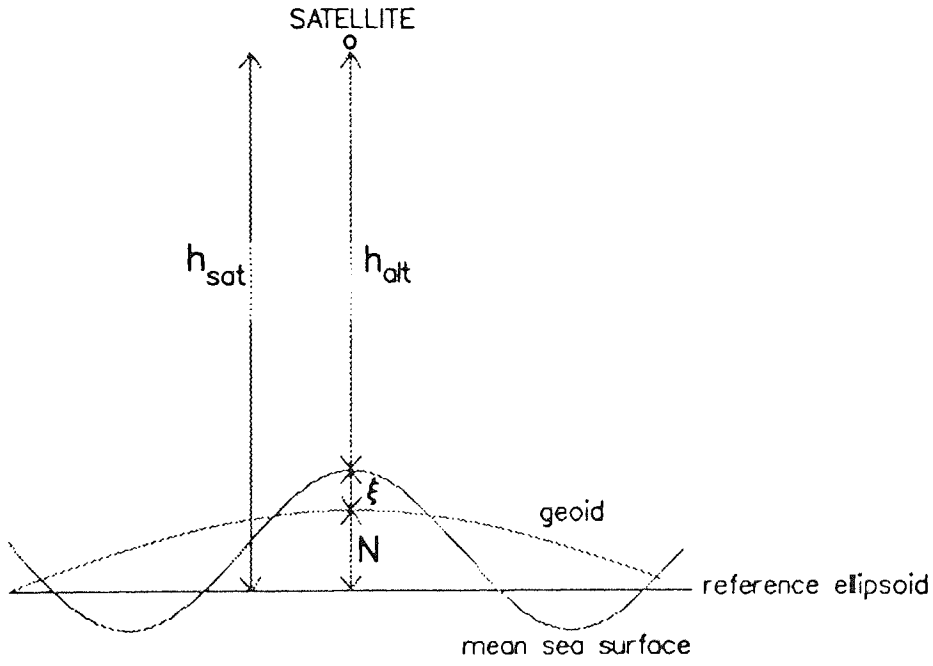

Figure (2.2)
Altimetric height observation

h_{alt} = corrected altimeter observation
ξ = sea surface topography height
h_{sat} = computed satellite orbital position
N = geoid height

The difference in height between the geoid and the actual sea surface (due to the phenomena mentioned in section §2.2) is known as the sea surface topography. Consider Figure (2.2). Let us assume a precise altimetric measurement (to within 10cm or less) and an equally accurate knowledge of the position of the satellite with respect to the reference ellipsoid. Under these conditions altimetric satellites can

provide important information about the sea surface topography given that the geoid is well known (or conversely about the geoid if the sea surface topography is well known), since, from Figure (2.2),

$$h_{sat} \approx h_{alt} + N + \xi + \nu \,, \qquad -(2.1)$$

where ν are random errors.

Although the altimeter measurement, h_{alt}, has been corrected for instrumental, atmospheric and surface wave height errors, by far the largest uncertainties in satellite altimetry are the orbital and geoid errors, i.e. errors in h_{sat} and N of equation (2.1). The latter are due to a lack of knowledge of the Earth's mass distribution. Orbital errors result from errors in the long wavelength gravity field model used to compute the satellite ephemeris, although they are compounded by other forces, especially atmospheric drag and direct and Earth-reflected solar radiation pressure (see chapter 3).

In general, given the state-of-the-art in precise orbit determination, it is safe to assume that for past and present altimetric satellites, the maximum along-track orbit error rarely exceeds 30m, whilst the maximum cross-track error rarely exceeds 3m. Over tens of metres along-track and cross-track, the radial component of altimetric orbits varies by a negligible amount, due to their near-circularity, and so non-radial orbit errors produce insignificant contributions to the error in h_{sat}. Thus, although the actual altimeter measurement is assumed normal to the reference ellipsoid, the radial component is the main contributor to altimetric orbit error, and indeed to altimetric error altogether, excluding the geoid. As the altimeter measurement error has components due to the geoid and orbit which are geographically correlated, differencing two radial height observations above the same point on the Earth will produce a result exclusive of such geographically related errors. Such differences can be obtained at crossover points (see chapter 4). The cancellation of the geoid height correction to altimeter measurement differences at crossovers is fundamental to

producing a precise data set, but the loss of the geographically correlated radial error of gravitational origin is a serious deficiency in the data type.

The following chapters describe in detail a method for using altimetric data in the form of crossover difference residuals to reduce the global radial orbit error. The method is then applied to actual measurements taken from the NASA satellite SEASAT (1978-64A), operational during three months of 1978, and to a simulation of ERS-1, launched in July, 1991. Both orbits were/are repeat orbits to allow variations of the sea surface to be observed over an extended period of time. Their low eccentricity allows minimum altitude variation, thus reducing along-track and cross-track orbit errors and the relatively high inclination gains good global coverage.

CHAPTER 3

RADIAL ORBIT ERRORS

A detailed theory of the radial orbit error of an artificial Earth satellite travelling in a frozen, repeat orbit of low eccentricity is now developed. The final fundamental expression ascertained is that from which the coefficients are recovered in the radial orbit error reduction procedures applied to SEASAT and ERS-1 in the following chapters.

§ 3.1 Keplerian Orbital Elements

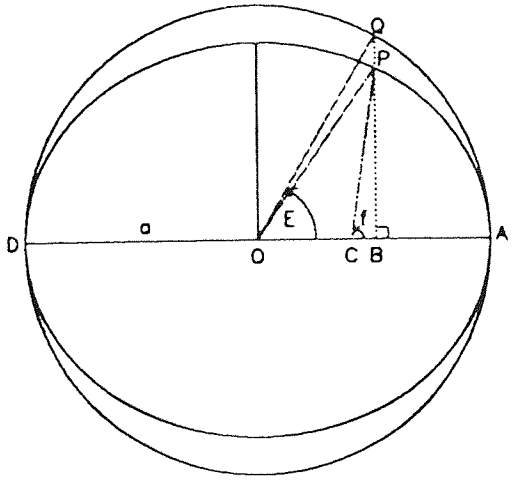

Figure (3.1)
The orbital ellipse

Consider a satellite at point P in Figure (3.1), in an elliptical orbit around the Earth, whose centre is at the focus of the ellipse, C. DA is the diameter of a circle of radius a with centre at O, the centre of the ellipse. This is the auxiliary circle. A is the point on the ellipse nearest to C and for artificial Earth satellites is called perigee. B is

the point on OA such that $\hat{PBA} = 90^o$. BP produced meets the auxiliary circle at Q, and this defines the eccentric angle, or eccentric anomaly, E, as the angle $\hat{QOA}$. The ratio $\frac{OC}{OA}$ (< 1) is the eccentricity, e, where OC = ae and CA = a (1 - e), a being the semi-major axis. P is the general point (a cosE , a $\sqrt{1 - e^2}$ sinE) and f is the true anomaly.

Figure (3.2) shows the projection of the orbital ellipse onto a unit sphere centred at the geocentre and inclined at an angle I to the equatorial plane of the Earth. γ is the point at which the ecliptic, the projection of the orbit of the Sun around the sphere, intersects the equatorial plane. γ is called the vernal equinox which precesses around the unit sphere with a period of approximately 26,000 years. Orbits are often derived with respect to the position of the vernal equinox at 0000hrs on 1st January, 2000. This is known as the J2000 reference frame, in which the x-axis is taken to be the line from the geocentre to γ, the y-axis is 90^o east of the x-axis in the equatorial plane and the z-axis is perpendicular to the other two axes, along the line from the geocentre to the north pole.

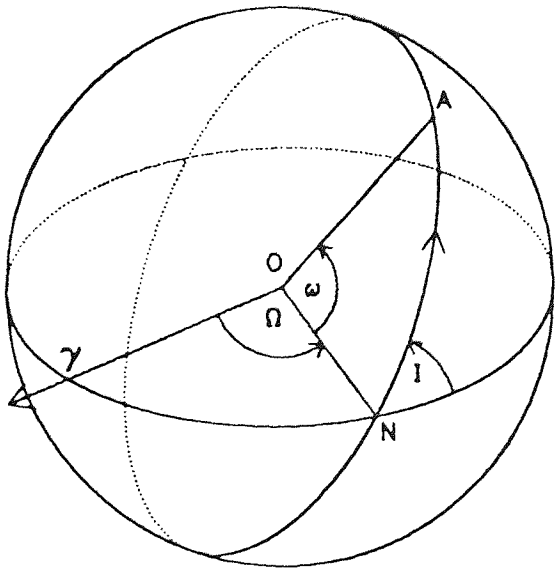

Figure (3.2)
Projection of the orbital ellipse onto the unit sphere

The northwards passage of the satellite intersects the equatorial plane of the Earth at N, the ascending node, where $\Omega = \gamma\hat{O}N$ is the right ascension of the ascending node. The angle between N and perigee subtended at O, $N\hat{O}A$, is the argument of perigee, ω.

a, e, I, Ω and ω are five of the six Keplerian elements which can be used to define the motion of the satellite in its elliptic orbit at any particular time, t. a and e define the size and shape of the ellipse, I and Ω the orientation of the orbital plane in space and ω specifies the orientation of the ellipse in the orbital plane. The sixth element is the mean anomaly, M. M defines the location of the satellite in the ellipse, that is the point P in Figure (3.1).

Suppose the satellite completes one revolution in time τ. Then the mean motion, n, is defined as $n = \frac{2\pi}{\tau}$ and the mean anomaly as

$$M = n\,(t - t_p), \qquad -(3.1)$$

where t_p is the time at which the satellite is at perigee, A.

M would be the angular distance travelled by the satellite since passing perigee as viewed from the centre of the Earth, if the satellite travelled at constant angular velocity. As the satellite moves in an ellipse, the angular velocity will not be constant in reality but is averaged out over one complete revolution to be equal to n. Since all altimetric satellites have a very low eccentricity = $O(10^{-2})$, these orbits are nearly circular. Hence P,Q and O,C of Figure (3.1) approximately coincide, $f \approx E$ and from Kepler's equation [Roy,1982]

$$M = E - e\sin E \quad , \qquad -(3.2)$$

$$M \approx E.$$

Keplerian elements are frequently used instead of Cartesian co-ordinates when describing satellite motion analytically as they give greater insight into the orbital

variations. Furthermore, with the exception of M, which increases by 2π radians in the time taken for one satellite revolution ($\approx$ 100 minutes for a satellite of 800km altitude), the Keplerian elements change slowly during the satellite motion, except near decay.

§ 3.2 Lagrange Planetary Equations

The Lagrange Planetary Equations are six differential equations which describe the variation of the Keplerian elements with time in terms of the other elements, namely [Kaula,1966];

$$\frac{da}{dt} = \frac{2}{na}\frac{\partial R}{\partial M}$$

$$\frac{de}{dt} = \frac{1 - e^2}{na^2 e}\frac{\partial R}{\partial M} - \frac{\sqrt{1 - e^2}}{na^2 e}\frac{\partial R}{\partial \omega}$$

$$\left.\begin{aligned}
\frac{d\omega}{dt} &= \frac{-\cos I}{na^2\sqrt{1 - e^2}\sin I}\frac{\partial R}{\partial I} + \frac{\sqrt{1 - e^2}}{na^2 e}\frac{\partial R}{\partial e} \\
\frac{dI}{dt} &= \frac{\cos I}{na^2\sqrt{1 - e^2}\sin I}\frac{\partial R}{\partial \omega} - \frac{1}{na^2\sqrt{1 - e^2}\sin I}\frac{\partial R}{\partial \Omega}
\end{aligned}\right\} \text{-(3.3)}$$

$$\frac{d\Omega}{dt} = \frac{1}{na^2\sqrt{1 - e^2}\sin I}\frac{\partial R}{\partial I}$$

$$\frac{dM}{dt} = n - \frac{1 - e^2}{na^2 e}\frac{\partial R}{\partial e} - \frac{2}{na}\frac{\partial R}{\partial a}$$

a, e, I, ω, Ω, M are the Keplerian elements at time t and R is the disturbing function that gives rise to the force that distorts the orbit away from the ellipse described in section §3.1.

For example, the gravitational force of the Earth acting on a satellite at a given time may be written as the gradient of the geopotential, U, where

$$U = \frac{\mu}{r} + R_{DIST} ,$$

R_{DIST} being that part of the geopotential due to the asphericity of the Earth's mass distribution ($R_{DIST} = 0 \Rightarrow U = \frac{\mu}{r} \Rightarrow$ Perfectly elliptical orbit) and μ defined by

$$\mu = n^2 a^3. \qquad -(3.4)$$

If no disturbing forces acted on the satellite and it moved only under the influence of a perfectly spherical Earth, then all the elements would remain constant except for the mean anomaly which would vary according to the equation

$$\frac{dM}{dt} = n. \qquad -(3.5)$$

§ 3.3 Mean Elements

The Keplerian elements discussed so far have been instantaneous at a given time, t, and are called osculating elements. Such elements describe the perfect ellipse a satellite would perform if it were subject to no perturbing effects apart from the central force term of the gravity field. For example, Ω is the angular position with respect to the vernal equinox at which the satellite would cross the equatorial plane of the Earth if no perturbatory forces acted on it from time t to the time of the crossing. Equations (3.3) describe the rates of change of these osculating elements and hence to determine the perturbations in each element, each equation must be integrated

analytically or numerically using the appropriate disturbing function. The equations are difficult to solve in this form and so a simplification is made.

If the elements are averaged over many revolutions of the spacecraft, then the mean elements $\bar{a}$, $\bar{e}$, $\bar{I}$, $\bar{\omega}$, $\bar{\Omega}$ and $\bar{M}$ result. Over the time length of an ephemeris, $\bar{a}$, $\bar{e}$ and $\bar{I}$ remain almost constant, whereas $\bar{\omega}$, $\bar{\Omega}$ and $\bar{M}$ vary approximately linearly in time, at least for e bounded away from zero under the effect of the dominant oblateness term [King-Hele,1987].

The mean elements are the instantaneous elements with their short-periodic components removed. For example, $\bar{\omega} = \omega - \delta\omega$, where $\delta\omega$ is the short-periodic perturbation in ω at time t. Denoting ξ to be any of the six elements,

$$\bar{\xi} = \begin{cases} \dot{\bar{\xi}} (t - t_0) + \xi_0 & \text{for} \quad \xi = \omega, \Omega \text{ or } M \\ \xi_0 & \text{for} \quad \xi = a, e \text{ or } I \end{cases} ,$$

where t_0 is the initial epoch of the orbit and ξ_0 the value of ξ at time t_0.

Figure (3.3) shows the variations in the osculating elements during the six day SEASAT orbit, from MJD43764 to MJD43770. The changes typify those for altimetric orbits, with $\bar{a}$, $\bar{e}$ and $\bar{I}$ remaining approximately constant, whereas $\bar{\Omega}$ and $\bar{M}$ vary linearly with time. $\bar{\omega}$ remains steady around 90°, since SEASAT performed a frozen orbit, as described in the next section. As a first approximation, the mean elements are used to replace the osculating elements in the Lagrange Planetary Equations, in which $\bar{a}$, $\bar{e}$ and $\bar{I}$ are held fixed on the right hand side with $\bar{\omega}$, $\bar{\Omega}$ and $\bar{M}$ assumed to have secular variations, even though for small e, the variation of $\bar{\omega}$, for example, can be non-linear [Cook,1966].

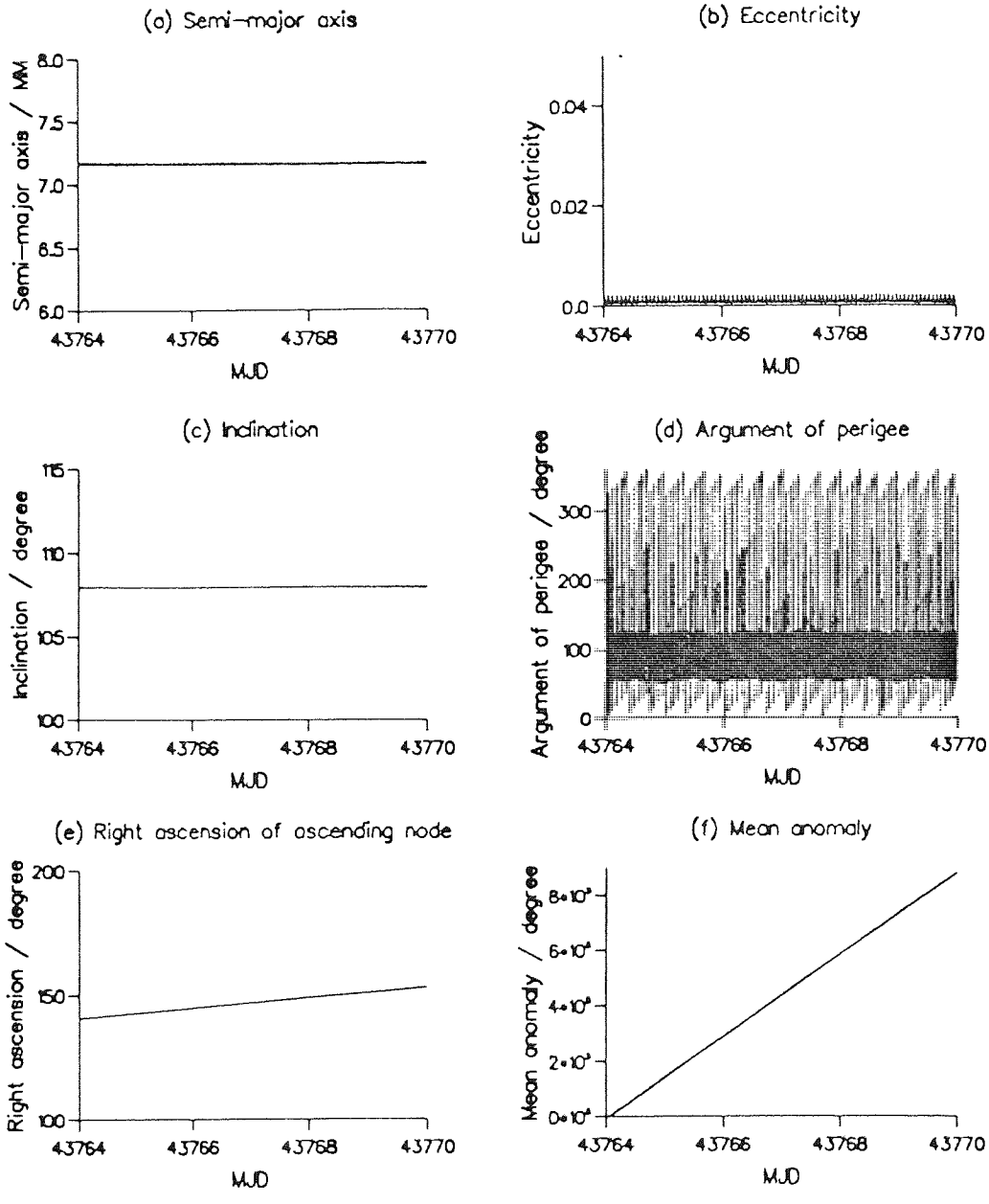

Figure (3.3)
Osculating element variations during SEASAT 6-day orbit, MJD43764 to MJD43770

§ 3.4 Frozen, Repeat Orbits

For an altimetric satellite to monitor dynamic variations of the oceans, it usually performs a repeat orbit, which results when the ground-track repeats after a fixed time interval, known as the repeat period, τ_p. In addition it is required that the

radial distances are as repeatable as possible. The argument of perigee, in particular, must have the same value after time τ_p, as shown schematically in Figure (3.4). Thus after time τ_p, ω must be equal to ω_o, its value at initial time t_o [Colombo,1984]. Hence for a repeat orbit,

$$\dot{\omega} = \frac{2\pi i}{\tau_p} \quad , \qquad \text{-(3.6)}$$

where i is an integer.

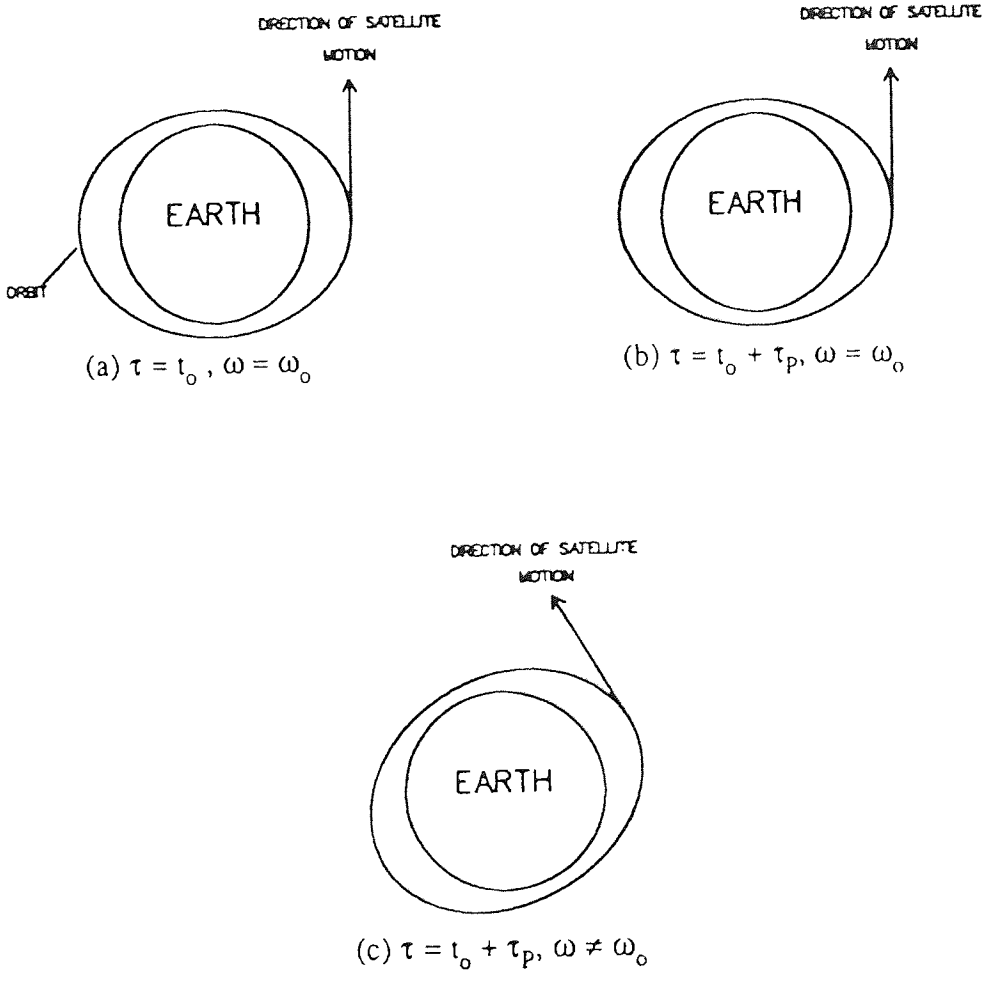

Figure (3.4)
To illustrate that, for a frozen orbit, argument of perigee must remain fixed after each repeat period

The main variation in ω is due to the second order zonal harmonic coefficient of the gravity field, C_{20}, namely [Kaula,1966];

$$\dot{\omega} \approx \frac{3nC_{20}}{4}\left(\frac{R_E}{a}\right)^2\left(\frac{1 - 5\cos^2 I}{(1 - e^2)^2}\right) \qquad -(3.7)$$

The value of C_{20} is of the order of 10^{-3}. Since a typical repeat period is of several days, then, for $i \neq 0$, equation (3.7) can only satisfy equation (3.6) for $e \approx 1$, which is impossible for low, altimetric orbits. Thus for an altimetric satellite to be in its repeat orbit requires $i = 0$, that is $\dot{\omega} = 0$, from equation (3.6).

One way to ensure ω is constant is to set $1 - 5\cos^2 I = 0$, from equation (3.7). In this case $\cos^2 I = \frac{1}{5} \Rightarrow I \approx 63.4^o$ or 116.6^o. These values for the inclination are known as the critical inclinations. One example of such a repeat orbit is that of TOPEX/POSEIDON, which has its inclination set at approximately 66^o, chosen such that $\dot{\omega}$ is small. However, inclinations near the critical inclinations give an incomplete global coverage and are away from the Sun-synchronous orbit required by multi-instrument satellites such as ERS-1. For ERS-1, the synthetic aperture radar community requires both constant shadowing for imagery and a Sun-synchronous orbit to provide the power needed by the instruments on board.

Another possibility for $\dot{\omega} \approx 0$ exists for low eccentric orbits. As $e \rightarrow 0$ the orbit is nearly circular and hence the precise location of perigee is ill-defined. In this case the non-singular elements $e\cos\omega$ and $e\sin\omega$ must be used to replace e and ω. If $\omega = 90^o$ and e is prescribed a specific value, the combined effect of the zonal harmonic coefficients is such that e and ω are invariant [Cook,1966], so that by "freezing" ω at 90^o a frozen, repeat orbit results. This is the case for both SEASAT and ERS-1.

§ 3.5 Perturbations to Satellite Orbits

Orbits for altimetric satellites at altitudes near 800km, such as ERS-1 and SEASAT, are usually generated for a duration of about six or seven days, during which time various disturbing forces act on the satellite. These cause corresponding disturbances, or perturbations, to build up over this period. The asphericity of the mass distribution of the Earth, the atmosphere, solar radiation pressure and gravitational attraction from other planets all combine to alter the trajectory of the orbit away from a perfect ellipse. Each of these effects is modelled when computing a satellite ephemeris from the tracking data (see chapter 5). However, due to uncertainties the perturbing forces cannot be modelled exactly and errors occur in the computed orbit. It is the radial component of this orbit error that is considered here. As will be revealed, the main contributions come from the mismodelling of the gravity field of the Earth. The geopotential is expressed as the sum of a series with each term dependent on a different geopotential coefficient. Errors in these coefficients then lead to radial orbit errors of gravitational origin.

As well as the gravitational orbit errors there are several non-gravitational constituents. Drag forces due to the atmosphere act on a satellite as it travels through the air. Errors in the atmospheric density model are absorbed by solving for daily drag coefficients. Failure to absorb all aerodynamic mismodelling within these solved for parameters leads to a corresponding radial orbit error due to drag. Similarly errors in the force models for solar radiation pressure create additional non-gravitational radial orbit error.

The gravitational and non-gravitational errors are summed to achieve an overall error due to both sources. In general, any orbital errors Δa, Δe and ΔM in a,e and M will produce a corresponding error Δr in the radial distance. From Figure (3.1), the geocentric distance, r, of a satellite from the centre of the Earth is given by

$$r^2 = CB^2 + BP^2$$

$$= (a \cos E - ae)^2 + \left(a \sqrt{1-e^2} \sin E\right)^2 .$$

Hence

$$r = a(1 - e \cos E) . \qquad -(3.8)$$

Thus small changes Δa, Δe and ΔE produce a change Δr in r where

$$\Delta r = \Delta a (1 - e \cos E) + a (-\Delta e \cos E + e \Delta E \sin E). \qquad -(3.9)$$

From equation (3.2),

$$\cos M = \cos(E - e \sin E) ,$$

i.e.

$$\cos M = \cos E \cos(e \sin E) + \sin E \sin(e \sin E)$$

$\Rightarrow$

$$\cos E = \cos M ,$$

to zero order in e. Similarly,

$$\sin E \approx \sin M.$$

Also, by equation (3.2),

$$\Delta E = \Delta M + \Delta e \sin E + e \Delta E \cos E.$$

Substituting these results into equation (3.9) leads to

$$\Delta r = \Delta a - a \Delta e \cos M + ae \Delta M \sin M + O(e).$$

So for altimetric satellites with e small,

$$\Delta r \approx \Delta a - a \Delta e \cos M + ae \Delta M \sin M . \qquad -(3.10)$$

The term in ΔM is retained although it contains a factor of the eccentricity, e, because the error ΔM is generally of order e^{-1}.

§ 3.6 Gravitational Radial Orbit Error

Mismodelling of the gravitational field of the Earth is, in general, the cause of the dominant error in the computation of a satellite ephemeris for orbits of altitude 800km or more. The gravity field is represented by the set of gravitational coefficients $C_{\ell m}$, $S_{\ell m}$. The geopotential can be represented in terms of the geocentric distance, r, the geocentric latitude, ϕ, and the geocentric longitude, λ, as [Kaula,1966];

$$U = \mu \sum_{\ell=0}^{\infty} \sum_{m=0}^{\ell} \frac{R_E^{\ell}}{r^{\ell+1}} P_{\ell m}(\sin\phi) \left[C_{\ell m} \cos(m\lambda) + S_{\ell m} \sin(m\lambda) \right] ,$$

where $P_{\ell m}$ is the associated Legendre function of degree ℓ and order m, and R_E is the mean equatorial radius of the Earth. U is the solution in spherical co-ordinates of Laplace's equation for a point external to the Earth.

The geopotential expansion, U, can be transformed using the method of Kaula into an expression in terms of the Keplerian elements as

$$U = \sum_{\ell=0}^{\infty} \sum_{m=0}^{\ell} U_{\ell m} \quad ,$$

where

$$\left.\begin{aligned} U_{\ell m} &= \frac{\mu R_E^{\ell}}{a^{\ell+1}} \sum_{p=0}^{\ell} F_{\ell m p}(I) \sum_{q=-\infty}^{\infty} G_{\ell p q}(e)\, S(\Psi_{\ell m p q}) \\ \text{with} \quad S(\Psi_{\ell m p q}) &= \begin{bmatrix} C_{\ell m} \\ -S_{\ell m} \end{bmatrix}_{\ell-m \text{ odd}}^{\ell-m \text{ even}} \cos\Psi_{\ell m p q} + \begin{bmatrix} S_{\ell m} \\ C_{\ell m} \end{bmatrix}_{\ell-m \text{ odd}}^{\ell-m \text{ even}} \sin\Psi_{\ell m p q} \\ \text{and} \quad \Psi_{\ell m p q} &= (\ell - 2p + q)(\omega + M) - q\omega + m(\Omega - \theta_g). \end{aligned}\right\} \text{-(3.11)}$$

$F_{\ell mp}(I)$ are inclination functions which rotate the potential from the equatorial to the orbital plane, $G_{\ell pq}(e)$ eccentricity functions to transform from true to mean anomaly, θ_g the Greenwich Mean Sidereal angle, i.e. the angle measured positive eastwards from the vernal equinox to the Greenwich Meridian in the equatorial plane.

Any errors $\Delta C_{\ell m}$, $\Delta S_{\ell m}$ in the coefficients $C_{\ell m}$, $S_{\ell m}$ will produce a corresponding error, ΔU, in the geopotential which can be approximated by

$$\Delta U = \sum_{\ell=2}^{\ell max} \sum_{m=0}^{\ell} \Delta U_{\ell m} \quad ,$$

where $\Delta U_{\ell m}$ is given by expression (3.11) with $\Delta C_{\ell m}$, $\Delta S_{\ell m}$ replacing $C_{\ell m}$, $S_{\ell m}$ and ℓmax is the maximum degree of the gravity field being used. Substitution of ΔU for R in equations (3.3) then yields the rates of change of the Keplerian elements due to errors in the gravity field model. Integration using the mean orbital ellipse described earlier will give the relevant gravitational perturbations in the elements. The final radial error $\Delta r^{(grav)}(t)$ due to gravitational field errors is then found by substituting for Δa, Δe and ΔM into equation (3.10).

The gravitational perturbations are derived by direct substitution of ΔU into the Lagrange Planetary Equations (3.3). For the semi-major axis,

$$\frac{da}{dt} = \frac{2}{na} \frac{\partial(\Delta U)}{\partial M}$$

$$= \frac{2}{na} \sum_{\ell=2}^{\ell max} \sum_{m=0}^{\ell} \frac{\mu R_E^{\ell}}{a^{\ell+1}} \sum_{p=0}^{\ell} F_{\ell mp}(I) \sum_{q=-\infty}^{\infty} G_{\ell pq}(e)$$

$$x \frac{\partial}{\partial M} \left\{ \begin{pmatrix} \Delta C_{\ell m} \\ -\Delta S_{\ell m} \end{pmatrix}_{\ell\text{-m odd}}^{\ell\text{-m even}} \cos\Psi_{\ell mpq} + \begin{pmatrix} \Delta S_{\ell m} \\ \Delta C_{\ell m} \end{pmatrix}_{\ell\text{-m odd}}^{\ell\text{-m even}} \sin\Psi_{\ell mpq} \right\}$$

Hence,

$$\frac{da}{dt} = \frac{2}{na} \sum_{\ell=2}^{\ell max} \sum_{m=0}^{\ell} \sum_{p=0}^{\ell} \sum_{q=-\infty}^{\infty} \left\{ \frac{\mu R_E^{\ell}}{a^{\ell+1}} F_{\ell mp}(I)\, G_{\ell pq}(e)\, (\ell - 2p+q) \right.$$

$$\left. \times \left[\begin{pmatrix} -\Delta C_{\ell m} \\ \Delta S_{\ell m} \end{pmatrix}_{\ell-m\ odd}^{\ell-m\ even} \sin\Psi_{\ell mpq} + \begin{pmatrix} \Delta S_{\ell m} \\ \Delta C_{\ell m} \end{pmatrix}_{\ell-m\ odd}^{\ell-m\ even} \cos\Psi_{\ell mpq} \right] \right\}$$

-(3.12)

For the eccentricity,

$$\frac{de}{dt} = \frac{1 - e^2}{na^2 e} \frac{\partial}{\partial M} \left\{ \sum_{\ell=2}^{\ell max} \sum_{m=0}^{\ell} \frac{\mu R_E^{\ell}}{a^{\ell+1}} \sum_{p=0}^{\ell} F_{\ell mp}(I) \sum_{q=-\infty}^{\infty} G_{\ell pq}(e) \right.$$

$$\left. \times \left[\begin{pmatrix} \Delta C_{\ell m} \\ -\Delta S_{\ell m} \end{pmatrix}_{\ell-m\ odd}^{\ell-m\ even} \cos\Psi_{\ell mpq} + \begin{pmatrix} \Delta S_{\ell m} \\ \Delta C_{\ell m} \end{pmatrix}_{\ell-m\ odd}^{\ell-m\ even} \sin\Psi_{\ell mpq} \right] \right\}$$

$$- \frac{\sqrt{1 - e^2}}{na^2 e} \frac{\partial}{\partial \omega} \left\{ \sum_{\ell=2}^{\ell max} \sum_{m=0}^{\ell} \frac{\mu R_E^{\ell}}{a^{\ell+1}} \sum_{p=0}^{\ell} F_{\ell mp}(I) \sum_{q=-\infty}^{\infty} G_{\ell pq}(e) \right.$$

$$\left. \times \left[\begin{pmatrix} \Delta C_{\ell m} \\ -\Delta S_{\ell m} \end{pmatrix}_{\ell-m\ odd}^{\ell-m\ even} \cos\Psi_{\ell mpq} + \begin{pmatrix} \Delta S_{\ell m} \\ \Delta C_{\ell m} \end{pmatrix}_{\ell-m\ odd}^{\ell-m\ even} \sin\Psi_{\ell mpq} \right] \right\}$$

$$= \sum_{\ell=2}^{\ell max} \sum_{m=0}^{\ell} \sum_{p=0}^{\ell} \sum_{q=-\infty}^{\infty} \frac{\mu R_E^{\ell}}{a^{\ell+1}} F_{\ell mp}(I)\, G_{\ell pq}(e) \frac{\sqrt{1 - e^2}}{na^2 e}$$

$$\times \left\{ \sqrt{1 - e^2}\, (\ell - 2p + q) \left[\begin{pmatrix} -\Delta C_{\ell m} \\ \Delta S_{\ell m} \end{pmatrix}_{\ell-m\ odd}^{\ell-m\ even} \sin\Psi_{\ell mpq} + \begin{pmatrix} \Delta S_{\ell m} \\ \Delta C_{\ell m} \end{pmatrix}_{\ell-m\ odd}^{\ell-m\ even} \cos\Psi_{\ell mpq} \right] \right.$$

$$- \quad (\ell - 2p) \left[\begin{pmatrix} -\Delta C_{\ell m} \\ \Delta S_{\ell m} \end{pmatrix}_{\ell\text{-m odd}}^{\ell\text{-m even}} \sin\Psi_{\ell mpq} + \begin{pmatrix} \Delta S_{\ell m} \\ \Delta C_{\ell m} \end{pmatrix}_{\ell\text{-m odd}}^{\ell\text{-m even}} \cos\Psi_{\ell mpq} \right] \Bigg\}.$$

Hence,

$$\frac{de}{dt} = \sum_{\ell=2}^{\ell max} \sum_{m=0}^{\ell} \sum_{p=0}^{\ell} \sum_{q=-\infty}^{\infty} \frac{\mu R_E^{\ell}}{a^{\ell+1}} \frac{F_{\ell mp}(I)\, G_{\ell pq}(e)\, q}{na^2 e}$$

$$\times \left[\begin{pmatrix} -\Delta C_{\ell m} \\ \Delta S_{\ell m} \end{pmatrix}_{\ell\text{-m odd}}^{\ell\text{-m even}} \sin\Psi_{\ell mpq} + \begin{pmatrix} \Delta S_{\ell m} \\ \Delta C_{\ell m} \end{pmatrix}_{\ell\text{-m odd}}^{\ell\text{-m even}} \cos\Psi_{\ell mpq} \right] + O(e).$$

-(3.13)

For the mean anomaly,

$$\frac{dM}{dt} = -\frac{1 - e^2}{na^2 e} \frac{\partial}{\partial e} \Bigg\{ \sum_{\ell=2}^{\ell max} \sum_{m=0}^{\ell} \frac{\mu R_E^{\ell}}{a^{\ell+1}} \sum_{p=0}^{\ell} F_{lmp}(I) \sum_{q=-\infty}^{\infty} G_{\ell pq}(e)$$

$$\times \left[\begin{pmatrix} \Delta C_{\ell m} \\ -\Delta S_{\ell m} \end{pmatrix}_{\ell\text{-m odd}}^{\ell\text{-m even}} \cos\Psi_{\ell mpq} + \begin{pmatrix} \Delta S_{\ell m} \\ \Delta C_{\ell m} \end{pmatrix}_{\ell\text{-m odd}}^{\ell\text{-m even}} \sin\Psi_{\ell mpq} \right] \Bigg\}$$

$$- \frac{2}{na} \frac{\partial}{\partial a} \Bigg\{ \sum_{\ell=2}^{\ell max} \sum_{m=0}^{\ell} \frac{\mu R_E^{\ell}}{a^{\ell+1}} \sum_{p=0}^{\ell} F_{\ell mp}(I) \sum_{q=-\infty}^{\infty} G_{\ell pq}(e)$$

$$\times \left[\begin{pmatrix} \Delta C_{\ell m} \\ -\Delta S_{\ell m} \end{pmatrix}_{\ell\text{-m odd}}^{\ell\text{-m even}} \cos\Psi_{\ell mpq} + \begin{pmatrix} \Delta S_{\ell m} \\ \Delta C_{\ell m} \end{pmatrix}_{\ell\text{-m odd}}^{\ell\text{-m even}} \sin\Psi_{\ell mpq} \right] \Bigg\}.$$

Hence,

$$\frac{dM}{dt} = \sum_{\ell=2}^{\ell_{max}} \sum_{m=0}^{\ell} \sum_{p=0}^{\ell} \sum_{q=-\infty}^{\infty} \frac{\mu R_E^{\ell}}{a^{\ell+1}} \frac{F_{\ell mp}(I)}{na^2}$$

$$\left\{ -\frac{1}{e}\frac{\partial G_{\ell pq}(e)}{\partial e}\left[\begin{pmatrix}\Delta C_{\ell m}\\ -\Delta S_{\ell m}\end{pmatrix}_{\ell\text{-m odd}}^{\ell\text{-m even}} \cos\Psi_{\ell mpq} + \begin{pmatrix}\Delta S_{\ell m}\\ \Delta C_{\ell m}\end{pmatrix}_{\ell\text{-m odd}}^{\ell\text{-m even}} \sin\Psi_{\ell mpq}\right]\right.$$

$$\left. + 2(\ell+1)\, G_{\ell pq}(e)\left[\begin{pmatrix}\Delta C_{\ell m}\\ -\Delta S_{\ell m}\end{pmatrix}_{\ell\text{-m odd}}^{\ell\text{-m even}} \cos\Psi_{\ell mpq} + \begin{pmatrix}\Delta S_{\ell m}\\ \Delta C_{\ell m}\end{pmatrix}_{\ell\text{-m odd}}^{\ell\text{-m even}} \sin\Psi_{\ell mpq}\right]\right\} + O(e).$$

-(3.14)

Equation (3.14) is the direct rate of change of the mean anomaly due to the errors $\Delta C_{\ell m}$, $\Delta S_{\ell m}$. However, an additional interaction term also occurs. From equation (3.4), the rate of change of a, given by equation (3.12), will perturb n and hence cause an additional disturbance to $\dot{M}$. Since $n = \left(\frac{\mu}{a^3}\right)^{\frac{1}{2}}$, the variation in n is given by

$$\Delta n = -\frac{3}{2}\sqrt{\frac{\mu}{a^5}}\,\Delta a,$$

i.e.

$$\Delta n = -\frac{3}{2}\frac{n}{a}\Delta a.$$

Hence the corresponding change in $\dot{M}$ is

$$\Delta\dot{M} = -\frac{3}{2}\frac{n}{a}\Delta a.$$

Integrating gives

$$\Delta M = \int -\frac{3}{2}\frac{n}{a}\Delta a\, dt \ . \qquad \text{-(3.15)}$$

Any perturbation Δa, including that caused by gravity field coefficient errors $\Delta C_{\ell m}$, $\Delta S_{\ell m}$, can be substituted into equation (3.15) to provide a corresponding interaction term ΔM_{int}.

Equations (3.12), (3.13) and (3.14) can be integrated under the assumptions of linear variations in the angular arguments, using the approximation

$$\Delta\xi = \int \dot{\xi} dt \approx \int \frac{\dot{\xi}}{\dot{\Psi}_{\ell mpq}} d\Psi_{\ell mpq} , \qquad -(3.16)$$

where $\dot{\Psi}_{\ell mpq}$ is taken as constant.

Under this assumption, the only variable on the right hand side of equations (3.12), (3.13) or (3.14) is the argument

$$\dot{\Psi}_{\ell mpq}(t) = \dot{\Psi}_{\ell mpq}(t - t_o) + \Psi^{o}_{\ell mpq} ,$$

where $\Psi^{o}_{\ell mpq} = \Psi_{\ell mpq}(t = t_o)$.

From equation (3.12) and equation (3.16) with $\xi = a$,

$$\Delta a \approx \frac{2}{na} \sum_{\ell=2}^{\ell max} \sum_{m=0}^{\ell} \sum_{p=0}^{\ell} \sum_{q=-\infty}^{\infty} \frac{\mu R_E^{\ell}}{a^{\ell+1}} \frac{F_{\ell mp}(I)\, G_{\ell pq}(e)\, (\ell - 2p+q)}{\dot{\Psi}_{\ell mpq}}$$

$$x \left\{ \begin{pmatrix} \Delta C_{\ell m} \\ -\Delta S_{\ell m} \end{pmatrix}_{\ell-m\ odd}^{\ell-m\ even} \Big[\cos\Psi_{\ell mpq} \Big]_{\Psi^{o}_{\ell mpq}}^{\Psi_{\ell mpq}(t)} + \begin{pmatrix} \Delta S_{\ell m} \\ \Delta C_{\ell m} \end{pmatrix}_{\ell-m\ odd}^{\ell-m\ even} \Big[\sin\Psi_{\ell mpq} \Big]_{\Psi^{o}_{\ell mpq}}^{\Psi_{\ell mpq}(t)} \right\}$$

$$= \sum_{\ell=2}^{\ell max} \sum_{m=0}^{\ell} \sum_{p=0}^{\ell} \sum_{q=-\infty}^{\infty} \frac{2\mu}{a^2 n} \left(\frac{R_E}{a}\right)^{\ell} \frac{F_{\ell mp}(I)\, G_{\ell pq}(e)\, (\ell - 2p+q)}{\dot{\Psi}_{\ell mpq}} \; x$$

$$\left\{ \Delta C_{\ell m} \begin{bmatrix} \cos\Psi_{\ell mpq} - \cos\Psi^{o}_{\ell mpq} \\ \sin\Psi_{\ell mpq} - \sin\Psi^{o}_{\ell mpq} \end{bmatrix}_{\ell\text{-m odd}}^{\ell\text{-m even}} + \Delta S_{\ell m} \begin{bmatrix} \sin\Psi_{\ell mpq} - \sin\Psi^{o}_{\ell mpq} \\ -\cos\Psi_{\ell mpq} + \cos\Psi^{o}_{\ell mpq} \end{bmatrix}_{\ell\text{-m odd}}^{\ell\text{-m even}} \right\}$$

Since $G_{\ell pq}(e)$ is of the order of $e^{|q|}$, only terms with $|q| \leq 1$ may be significant for near-circular orbits, i.e. $q = 0, \pm 1$.

Now [Schrama,1989],

$$\left.\begin{aligned} G_{\ell p0}(e) &= 1 + O(e^2) \\ G_{\ell p-1}(e) &= \frac{(-\ell + 4p + 1)\, e}{2} + O(e^3) \\ G_{\ell p1}(e) &= \frac{(3\ell - 4p + 1)\, e}{2} + O(e^3) \end{aligned}\right\} \text{-(3.17)}$$

Hence only the $q = 0$ term is retained, that is to order e

$$\Delta a \approx \sum_{\ell=2}^{\ell max} \sum_{m=0}^{\ell} \sum_{p=0}^{\ell} \frac{2\mu}{a^2 n} \left(\frac{R_E}{a}\right)^{\ell} \frac{F_{\ell mp}(I)\,(\ell - 2p)}{\dot{\Psi}_{\ell mp0}} \times \left\{ \Delta C_{\ell m} \begin{bmatrix} \cos\Psi_{\ell mp0} - \cos\Psi^{o}_{\ell mp0} \\ \sin\Psi_{\ell mp0} - \sin\Psi^{o}_{\ell mp0} \end{bmatrix}_{\ell\text{-m odd}}^{\ell\text{-m even}} + \Delta S_{\ell m} \begin{bmatrix} \sin\Psi_{\ell mp0} - \sin\Psi^{o}_{\ell mp0} \\ -\cos\Psi_{\ell mp0} + \cos\Psi^{o}_{\ell mp0} \end{bmatrix}_{\ell\text{-m odd}}^{\ell\text{-m even}} \right\}$$

-(3.18)

It is this expression for the gravitational perturbation in a that creates the interaction term ΔM_{int} as given by equation (3.15). Substituting equation (3.18) into equation (3.15) and integrating gives the full expression for the interaction term as

$$\Delta M_{int} = \int -\frac{3}{2}\frac{n}{a} \sum_{\ell=2}^{\ell_{max}} \sum_{m=0}^{\ell} \sum_{p=0}^{\ell} \frac{2\mu}{a^2 n} \left(\frac{R_E}{a}\right)^{\ell} \frac{F_{\ell mp}(I)\,(\ell - 2p)}{\dot{\Psi}_{\ell mp0}}$$

$$\times \left\{ \Delta C_{\ell m} \begin{bmatrix} \cos\Psi_{\ell mp0} - \cos\overset{o}{\Psi}_{\ell mp0} \\ \sin\Psi_{\ell mp0} - \sin\overset{o}{\Psi}_{\ell mp0} \end{bmatrix}_{\ell\text{-m odd}}^{\ell\text{-m even}} + \right.$$

$$\left. \Delta S_{\ell m} \begin{bmatrix} \sin\Psi_{\ell mp0} - \sin\overset{o}{\Psi}_{\ell mp0} \\ -\cos\Psi_{\ell mp0} + \cos\overset{o}{\Psi}_{\ell mp0} \end{bmatrix}_{\ell\text{-m odd}}^{\ell\text{-m even}} \right\} dt$$

i.e.

$$\Delta M_{int} = \int -\frac{3}{2}\frac{n}{a} \sum_{\ell=2}^{\ell_{max}} \sum_{m=0}^{\ell} \sum_{p=0}^{\ell} \frac{2\mu}{a^2 n} \left(\frac{R_E}{a}\right)^{\ell} \frac{F_{\ell mp}(I)\,(\ell - 2p)}{\dot{\Psi}_{\ell mp0}}$$

$$\times \begin{bmatrix} \Delta C_{\ell m}\cos\Psi_{\ell mp0} + \Delta S_{\ell m}\sin\Psi_{\ell mp0} \\ \Delta C_{\ell m}\sin\Psi_{\ell mp0} - \Delta S_{\ell m}\cos\Psi_{\ell mp0} \end{bmatrix}$$

$$\left. \begin{matrix} - \Delta C_{\ell m}\cos\overset{o}{\Psi}_{\ell mp0} - \Delta S_{\ell m}\sin\overset{o}{\Psi}_{\ell mp0} \\ - \Delta C_{\ell m}\sin\overset{o}{\Psi}_{\ell mp0} + \Delta S_{\ell m}\cos\overset{o}{\Psi}_{\ell mp0} \end{matrix} \right]_{\ell\text{-m odd}}^{\ell\text{-m even}} dt$$

$$= -\frac{3}{2}\frac{n}{a} \sum_{\ell=2}^{\ell_{max}} \sum_{m=0}^{\ell} \sum_{p=0}^{\ell} \frac{2\mu}{a^2 n} \left(\frac{R_E}{a}\right)^{\ell} \frac{F_{\ell mp}(I)\,(\ell - 2p)}{\dot{\Psi}^2_{\ell mp0}} \times$$

$$\left\{ \begin{bmatrix} \Delta C_{\ell m}\,(\sin\Psi_{\ell mp0} - \sin\overset{o}{\Psi}_{\ell mp0}) \\ -\Delta C_{\ell m}\,(\cos\Psi_{\ell mp0} - \cos\overset{o}{\Psi}_{\ell mp0}) \end{bmatrix} \right.$$

$$
\left.
\begin{array}{l}
-\Delta S_{\ell m}\left(\cos\Psi_{\ell mp0} - \cos\overset{o}{\Psi}_{\ell mp0}\right) \\
-\Delta S_{\ell m}\left(\sin\Psi_{\ell mp0} - \sin\overset{o}{\Psi}_{\ell mp0}\right)
\end{array}
\right]_{\ell\text{-m odd}}^{\ell\text{-m even}}
\Bigg\}
$$

$$
-\left(t - t_o\right)\dot{\Psi}_{\ell mp0}\left[
\begin{array}{l}
\Delta C_{\ell m}\cos\overset{o}{\Psi}_{\ell mp0} + \Delta S_{\ell m}\sin\overset{o}{\Psi}_{\ell mp0} \\
\Delta C_{\ell m}\sin\overset{o}{\Psi}_{\ell mp0} - \Delta S_{\ell m}\cos\overset{o}{\Psi}_{\ell mp0}
\end{array}
\right]_{\ell\text{-m odd}}^{\ell\text{-m even}}
\Bigg\}
$$

Hence,

$$
\Delta M_{int} = -\frac{3}{2}\frac{n}{a}\sum_{\ell=2}^{\ell max}\sum_{m=0}^{\ell}\sum_{p=0}^{\ell}\frac{2\mu}{a^2 n}\left(\frac{R_E}{a}\right)^{\ell}\frac{F_{\ell mp}(I)\left(\ell - 2p\right)}{\dot{\Psi}_{\ell mp0}^{2}}
$$

$$
\times\Bigg\{\left[
\begin{array}{l}
\Delta C_{\ell m}\sin\Psi_{\ell mp0} - \Delta S_{\ell m}\cos\Psi_{\ell mp0} \\
-\Delta C_{\ell m}\cos\Psi_{\ell mp0} - \Delta S_{\ell m}\sin\Psi_{\ell mp0}
\end{array}
\right]_{\ell\text{-m odd}}^{\ell\text{-m even}}
$$

$$
-\left(t - t_o\right)\dot{\Psi}_{\ell mp0}\left[
\begin{array}{l}
\Delta C_{\ell m}\cos\overset{o}{\Psi}_{\ell mp0} + \Delta S_{\ell m}\sin\overset{o}{\Psi}_{\ell mp0} \\
\Delta C_{\ell m}\sin\overset{o}{\Psi}_{\ell mp0} - \Delta S_{\ell m}\cos\overset{o}{\Psi}_{\ell mp0}
\end{array}
\right]_{\ell\text{-m odd}}^{\ell\text{-m even}}
$$

$$
+\left[
\begin{array}{l}
-\Delta C_{\ell m}\sin\overset{o}{\Psi}_{\ell mp0} + \Delta S_{\ell m}\cos\overset{o}{\Psi}_{\ell mp0} \\
\Delta S_{\ell m}\sin\overset{o}{\Psi}_{\ell mp0} + \Delta C_{\ell m}\cos\overset{o}{\Psi}_{\ell mp0}
\end{array}
\right]_{\ell\text{-m odd}}^{\ell\text{-m even}}
\Bigg\}
$$

-(3.19)

To obtain the full perturbation in the mean anomaly, this term must be added to the term for ΔM due directly to gravitational field mismodelling which, from equation (3.14) and equation (3.16) with $\xi = M$, is given by

$$
\Delta M \approx \int\sum_{\ell=2}^{\ell max}\sum_{m=0}^{\ell}\sum_{p=0}^{\ell}\sum_{q=-\infty}^{\infty}\frac{\mu R_E^{\ell}}{a^{\ell+1}}\frac{F_{\ell mp}(I)}{na^2\dot{\Psi}_{\ell mpq}}\ \times
$$

$$\left\{ -\frac{1}{e}\frac{\partial G_{\ell pq}(e)}{\partial e}\left[\begin{pmatrix}\Delta C_{\ell m}\\ -\Delta S_{\ell m}\end{pmatrix}_{\ell\text{-m odd}}^{\ell\text{-m even}}\cos\Psi_{\ell mpq} + \begin{pmatrix}\Delta S_{\ell m}\\ \Delta C_{\ell m}\end{pmatrix}_{\ell\text{-m odd}}^{\ell\text{-m even}}\sin\Psi_{\ell mpq}\right]\right.$$

$$\left. + 2(\ell+1)G_{\ell pq}(e)\left[\begin{pmatrix}\Delta C_{\ell m}\\ -\Delta S_{\ell m}\end{pmatrix}_{\ell\text{-m odd}}^{\ell\text{-m even}}\cos\Psi_{\ell mpq}+\begin{pmatrix}\Delta S_{\ell m}\\ \Delta C_{\ell m}\end{pmatrix}_{\ell\text{-m odd}}^{\ell\text{-m even}}\sin\Psi_{\ell mpq}\right]\right\} d\Psi_{\ell mpq}$$

$$= \sum_{\ell=2}^{\ell max}\sum_{m=0}^{\ell}\sum_{p=0}^{\ell}\sum_{q=-\infty}^{\infty}\frac{\mu R_E^{\ell}}{a^{\ell+1}}\frac{F_{\ell mp}(I)}{na^2\dot{\Psi}_{\ell mpq}} \quad x$$

$$\left\{ -\frac{1}{e}\frac{\partial G_{\ell pq}(e)}{\partial e}\left[\begin{pmatrix}\Delta C_{\ell m}\\ -\Delta S_{\ell m}\end{pmatrix}_{\ell\text{-m odd}}^{\ell\text{-m even}}(\sin\Psi_{\ell mpq}-\sin\Psi^{o}_{\ell mpq}) - \begin{pmatrix}\Delta S_{\ell m}\\ \Delta C_{\ell m}\end{pmatrix}_{\ell\text{-m odd}}^{\ell\text{-m even}}(\cos\Psi_{\ell mpq}-\cos\Psi^{o}_{\ell mpq})\right]\right.$$

$$\left. +2(\ell+1)G_{\ell pq}(e)\left[\begin{pmatrix}\Delta C_{\ell m}\\ -\Delta S_{\ell m}\end{pmatrix}_{\ell\text{-m odd}}^{\ell\text{-m even}}(\sin\Psi_{\ell mpq}-\sin\Psi^{o}_{\ell mpq}) - \begin{pmatrix}\Delta S_{\ell m}\\ \Delta C_{\ell m}\end{pmatrix}_{\ell\text{-m odd}}^{\ell\text{-m even}}(\cos\Psi_{\ell mpq}-\cos\Psi^{o}_{\ell mpq})\right]\right\}$$

Only the terms with the eccentricity divisor will be important in terms of the radial orbit error because of the e factor of equation (3.10). Also, by equations (3.17), $\frac{\partial G_{\ell p0}(e)}{\partial e} = 0(e)$. Hence to order e^{-1}

$$\Delta M = -\sum_{\ell=2}^{\ell max}\sum_{m=0}^{\ell}\sum_{p=0}^{\ell}\sum_{\substack{q=-1\\ q\neq 0}}^{1}\frac{\partial G_{\ell pq}(e)}{\partial e}\frac{\mu R_E^{\ell}}{a^{\ell+1}}\frac{F_{\ell mp}(I)}{na^2 e\dot{\Psi}_{\ell mpq}} \quad x$$

$$\left[\begin{matrix}\Delta C_{\ell m}\sin\Psi_{\ell mpq} - \Delta S_{\ell m}\cos\Psi_{\ell mpq} - \Delta C_{\ell m}\sin\Psi^{o}_{\ell mpq} + \Delta S_{\ell m}\cos\Psi^{o}_{\ell mpq}\\ -\Delta S_{\ell m}\sin\Psi_{\ell mpq} - \Delta C_{\ell m}\cos\Psi_{\ell mpq} + \Delta S_{\ell m}\sin\Psi^{o}_{\ell mpq} + \Delta C_{\ell m}\cos\Psi^{o}_{\ell mpq}\end{matrix}\right]_{\ell\text{-m odd}}^{\ell\text{-m even}}$$

To this expression must be added the interaction term of equation (3.19), only the secular part of which is retained, since the others become insignificant when

multiplied by e. Hence the full gravitational perturbation in the mean anomaly, including the interaction terms, can be approximated by

$$\Delta M = - \sum_{\ell=2}^{\ell max} \sum_{m=0}^{\ell} \sum_{p=0}^{\ell} \sum_{\substack{q=-1 \\ q\neq 0}}^{1} \frac{\partial G_{\ell pq}(e)}{\partial e} \frac{\mu R_E^{\ell}}{a^{\ell+1}} \frac{F_{\ell mp}(I)}{na^2 e \dot{\Psi}_{\ell mpq}} \quad x$$

$$\begin{bmatrix} \Delta C_{\ell m} \sin\Psi_{\ell mpq} - \Delta S_{\ell m} \cos\Psi_{\ell mpq} - \Delta C_{\ell m} \sin\Psi^{o}_{\ell mpq} + \Delta S_{\ell m} \cos\Psi^{o}_{\ell mpq} \\ -\Delta S_{\ell m} \sin\Psi_{\ell mpq} - \Delta C_{\ell m} \cos\Psi_{\ell mpq} + \Delta S_{\ell m} \sin\Psi^{o}_{\ell mpq} + \Delta C_{\ell m} \cos\Psi^{o}_{\ell mpq} \end{bmatrix}_{\ell\text{-m odd}}^{\ell\text{-m even}}$$

$$+ \quad \frac{3}{2} \frac{n}{a} \sum_{\ell=2}^{\ell max} \sum_{m=0}^{\ell} \sum_{p=0}^{\ell} \frac{2\mu}{a^2 n} \left(\frac{R_E}{a}\right)^{\ell} F_{\ell mp}(I) \, (\ell - 2p) \, (t - t_o) \, / \, \dot{\Psi}_{\ell mp0}$$

$$x \quad \begin{Bmatrix} \Delta C_{\ell m} \cos\Psi^{o}_{\ell mp0} + \Delta S_{\ell m} \sin\Psi^{o}_{\ell mp0} \\ \Delta C_{\ell m} \sin\Psi^{o}_{\ell mp0} - \Delta S_{\ell m} \cos\Psi^{o}_{\ell mp0} \end{Bmatrix}_{\ell\text{-m odd}}^{\ell\text{-m even}}$$

-(3.20)

It is now left to obtain the expression for the eccentricity perturbation. Integrating equation (3.13) gives

$$\Delta e \approx \sum_{\ell=2}^{\ell max} \sum_{m=0}^{\ell} \sum_{p=0}^{\ell} \sum_{q=-\infty}^{\infty} \frac{\mu R_E^{\ell}}{a^{\ell+1}} \frac{F_{\ell mp}(I) \, G_{\ell pq}(e) \, q}{na^2 e \dot{\Psi}_{\ell mpq}} \quad x$$

$$\left\{ \Delta C_{\ell m} \begin{bmatrix} \cos\Psi_{\ell mpq} - \cos\Psi^{o}_{\ell mpq} \\ \sin\Psi_{\ell mpq} - \sin\Psi^{o}_{\ell mpq} \end{bmatrix}_{\ell\text{-m odd}}^{\ell\text{-m even}} \right.$$

$$\left. + \Delta S_{\ell m} \begin{bmatrix} \sin\Psi_{\ell mpq} - \sin\Psi^{o}_{\ell mpq} \\ -\cos\Psi_{\ell mpq} + \cos\Psi^{o}_{\ell mpq} \end{bmatrix}_{\ell\text{-m odd}}^{\ell\text{-m even}} \right\}$$

The q = 0 term disappears due to the factor q. Also, from equations (3.17),

$$\frac{\partial G_{\ell p\pm1}(e)}{\partial e} = \frac{G_{\ell p\pm1}(e)}{e} \quad .$$

Hence,

$$\Delta e \approx \sum_{\ell=2}^{\ell max} \sum_{m=0}^{\ell} \sum_{p=0}^{\ell} \sum_{q=-1}^{1} \frac{\partial G_{\ell pq}(e)}{\partial e} q \frac{\mu R_E^{\ell}}{a^{\ell+1}} \frac{F_{\ell mp}(I)}{n a^2 \dot{\Psi}_{\ell mpq}} \quad x$$

$$\left\{ \Delta C_{\ell m} \begin{bmatrix} \cos\Psi_{\ell mpq} - \cos\Psi^{o}_{\ell mpq} \\ \sin\Psi_{\ell mpq} - \sin\Psi^{o}_{\ell mpq} \end{bmatrix}_{\ell\text{-m odd}}^{\ell\text{-m even}} \right.$$

$$\left. + \Delta S_{\ell m} \begin{bmatrix} \sin\Psi_{\ell mpq} - \sin\Psi^{o}_{\ell mpq} \\ -\cos\Psi_{\ell mpq} + \cos\Psi^{o}_{\ell mpq} \end{bmatrix}_{\ell\text{-m odd}}^{\ell\text{-m even}} \right\}$$

-(3.21)

Equations (3.18), (3.20) and (3.21) are the perturbations Δa, ΔM and Δe, respectively, due to errors in the gravity field coefficients. Substitution into equation (3.10) results in an expression for the gravitational radial orbit error given by

$$\Delta r^{(grav)}(t) \approx \sum_{\ell=2}^{\ell max} \sum_{m=0}^{\ell} \sum_{p=0}^{\ell} \frac{2\mu}{a^2 n} \left(\frac{R_E}{a}\right)^{\ell} \frac{F_{\ell mp}(I)\,(\,\ell - 2p\,)}{\dot{\Psi}_{\ell mp0}}$$

$$x \left\{ \Delta C_{\ell m} \begin{bmatrix} \cos\Psi_{\ell mp0} - \cos\Psi^{o}_{\ell mp0} \\ \sin\Psi_{\ell mp0} - \sin\Psi^{o}_{\ell mp0} \end{bmatrix}_{\ell\text{-m odd}}^{\ell\text{-m even}} + \right.$$

$$\left. \Delta S_{\ell m} \begin{bmatrix} \sin\Psi_{\ell mp0} - \sin\Psi^{o}_{\ell mp0} \\ -\cos\Psi_{\ell mp0} + \cos\Psi^{o}_{\ell mp0} \end{bmatrix}_{\ell\text{-m odd}}^{\ell\text{-m even}} \right\}$$

$$- \cos M \sum_{\ell=2}^{\ell max} \sum_{m=0}^{\ell} \sum_{p=0}^{\ell} \sum_{q=-1}^{1} \frac{\partial G_{\ell pq}(e)}{\partial e} q \frac{\mu R_E^{\ell}}{a^{\ell+1}} \frac{F_{\ell mp}(I)}{na\,\dot{\Psi}_{\ell mpq}}$$

$$x \left\{ \Delta C_{\ell m} \begin{bmatrix} \cos\Psi_{\ell mpq} - \cos\Psi^{o}_{\ell mpq} \\ \sin\Psi_{\ell mpq} - \sin\Psi^{o}_{\ell mpq} \end{bmatrix}_{\ell-m\ odd}^{\ell-m\ even} + \right.$$

$$\left. \Delta S_{\ell m} \begin{bmatrix} \sin\Psi_{\ell mpq} - \sin\Psi^{o}_{\ell mpq} \\ -\cos\Psi_{\ell mpq} + \cos\Psi^{o}_{\ell mpq} \end{bmatrix}_{\ell-m\ odd}^{\ell-m\ even} \right\}$$

$$+ \sin M \sum_{\ell=2}^{\ell max} \sum_{m=0}^{\ell} \sum_{p=0}^{\ell} \sum_{\substack{q=-1 \\ q\neq 0}}^{1} \frac{\partial G_{\ell pq}(e)}{\partial e} \frac{\mu R_E^{\ell}}{a^{\ell+1}} \frac{F_{\ell mp}(I)}{na\,\dot{\Psi}_{\ell mpq}} \quad x$$

$$\begin{bmatrix} -\Delta C_{\ell m}\sin\Psi_{\ell mpq} + \Delta S_{\ell m}\cos\Psi_{\ell mpq} + \Delta C_{\ell m}\sin\Psi^{o}_{\ell mpq} - \Delta S_{\ell m}\cos\Psi^{o}_{\ell mpq} \\ \Delta S_{\ell m}\sin\Psi_{\ell mpq} + \Delta C_{\ell m}\cos\Psi_{\ell mpq} - \Delta S_{\ell m}\sin\Psi^{o}_{\ell mpq} - \Delta C_{\ell m}\cos\Psi^{o}_{\ell mpq} \end{bmatrix}_{\ell-m\ odd}^{\ell-m\ even}$$

$$+ \frac{3}{2}\frac{n}{a} \sum_{\ell=2}^{\ell max} \sum_{m=0}^{\ell} \sum_{p=0}^{\ell} \frac{2\mu}{a^2 n} \left(\frac{R_E}{a}\right)^{\ell} F_{\ell mp}(I)\,(\ell - 2p) \Big/ \dot{\Psi}_{\ell mp0}$$

$$x \quad (t - t_o)\, a\, e \sin M \begin{bmatrix} \Delta C_{\ell m}\cos\Psi^{o}_{\ell mp0} + \Delta S_{\ell m}\sin\Psi^{o}_{\ell mp0} \\ \Delta C_{\ell m}\sin\Psi^{o}_{\ell mp0} - \Delta S_{\ell m}\cos\Psi^{o}_{\ell mp0} \end{bmatrix}_{\ell-m\ odd}^{\ell-m\ even}$$

$$= \sum_{\ell=2}^{\ell max} \sum_{m=0}^{\ell} \sum_{p=0}^{\ell} \left(\frac{2\mu}{a^2 n} \left(\frac{R_E}{a}\right)^{\ell} \frac{F_{\ell mp}(I)\,(\ell - 2p)}{\dot{\Psi}_{\ell mp0}} \right.$$

$$x \left\{ \Delta C_{\ell m} \begin{bmatrix} \cos\Psi_{\ell mp0} - \cos\Psi^{o}_{\ell mp0} \\ \sin\Psi_{\ell mp0} - \sin\Psi^{o}_{\ell mp0} \end{bmatrix}_{\ell-m\ odd}^{\ell-m\ even} + \right.$$

$$\Delta S_{\ell m}\begin{bmatrix}\sin\Psi_{\ell mp0} - \sin\Psi^{o}_{\ell mp0}\\ -\cos\Psi_{\ell mp0} + \cos\Psi^{o}_{\ell mp0}\end{bmatrix}^{\ell\text{-m even}}_{\ell\text{-m odd}}\Bigg\}$$

$$- \sum_{q=-1}^{1} \frac{\partial G_{\ell pq}(e)}{\partial e}\, q\, \frac{\mu R_E^{\ell}}{a^{\ell+1}}\, \frac{F_{\ell mp}(I)}{na\,\dot{\Psi}_{\ell mpq}}$$

$$\times \Bigg\{ \Delta C_{\ell m}\begin{bmatrix}\cos M\cos\Psi_{\ell mpq} - \cos M\cos\Psi^{o}_{\ell mpq}\\ \cos M\sin\Psi_{\ell mpq} - \cos M\sin\Psi^{o}_{\ell mpq}\end{bmatrix}^{\ell\text{-m even}}_{\ell\text{-m odd}} +$$

$$\Delta S_{\ell m}\begin{bmatrix}\cos M\sin\Psi_{\ell mpq} - \cos M\sin\Psi^{o}_{\ell mpq}\\ -\cos M\cos\Psi_{\ell mpq} + \cos M\cos\Psi^{o}_{\ell mpq}\end{bmatrix}^{\ell\text{-m even}}_{\ell\text{-m odd}}\Bigg\}$$

$$+ \sum_{\substack{q=-1\\ q\neq 0}}^{1} \frac{\partial G_{\ell pq}(e)}{\partial e}\, \frac{\mu R_E^{\ell}}{a^{\ell+1}}\, \frac{F_{\ell mp}(I)}{na\,\dot{\Psi}_{\ell mpq}}$$

$$\times \begin{bmatrix}-\Delta C_{\ell m}\sin M\sin\Psi_{\ell mpq} + \Delta S_{\ell m}\sin M\cos\Psi_{\ell mpq}\\ \Delta S_{\ell m}\sin M\sin\Psi_{\ell mpq} + \Delta C_{\ell m}\sin M\cos\Psi_{\ell mpq}\end{bmatrix}$$

$$\begin{bmatrix}+\Delta C_{\ell m}\sin M\sin\Psi^{o}_{\ell mpq} - \Delta S_{\ell m}\sin M\cos\Psi^{o}_{\ell mpq}\\ -\Delta S_{\ell m}\sin M\sin\Psi^{o}_{\ell mpq} - \Delta C_{\ell m}\sin M\cos\Psi^{o}_{\ell mpq}\end{bmatrix}^{\ell\text{-m even}}_{\ell\text{-m odd}}$$

$$+ \frac{3}{2}\frac{n}{a}\frac{2\mu}{a^2 n}\left(\frac{R_E}{a}\right)^{\ell} F_{\ell mp}(I)\,(\ell - 2p)\,\Big/\,\dot{\Psi}_{\ell mp0}$$

$$\times (t - t_o)\, a\, e\, \sin M \begin{bmatrix}\Delta C_{\ell m}\cos\Psi^{o}_{\ell mp0} + \Delta S_{\ell m}\sin\Psi^{o}_{\ell mp0}\\ \Delta C_{\ell m}\sin\Psi^{o}_{\ell mp0} - \Delta S_{\ell m}\cos\Psi^{o}_{\ell mp0}\end{bmatrix}^{\ell\text{-m even}}_{\ell\text{-m odd}}\Bigg)$$

i.e.

$$\Delta r^{(grav)}(t) \approx \sum_{\ell=2}^{\ell_{max}} \sum_{m=0}^{\ell} \sum_{p=0}^{\ell} \left\{ \frac{2\mu}{a^2 n} \left(\frac{R_E}{a}\right)^{\ell} \frac{F_{\ell mp}(I)\,(\ell - 2p)}{\dot{\Psi}_{\ell mp0}} \right.$$

$$\times \left(\Delta C_{\ell m} \begin{bmatrix} \cos\Psi_{\ell mp0} - \cos\overset{o}{\Psi}_{\ell mp0} \\ \sin\Psi_{\ell mp0} - \sin\overset{o}{\Psi}_{\ell mp0} \end{bmatrix}_{\ell\text{-m odd}}^{\ell\text{-m even}} + \right.$$

$$\left. \left. \Delta S_{\ell m} \begin{bmatrix} \sin\Psi_{\ell mp0} - \sin\overset{o}{\Psi}_{\ell mp0} \\ -\cos\Psi_{\ell mp0} + \cos\overset{o}{\Psi}_{\ell mp0} \end{bmatrix}_{\ell\text{-m odd}}^{\ell\text{-m even}} \right) \right.$$

$$+ \sum_{\substack{q=-1 \\ q\neq 0}}^{1} \frac{\partial G_{\ell pq}(e)}{\partial e} \mu \left(\frac{R_E}{a}\right)^{\ell} \frac{F_{\ell mp}(I)}{na^2\dot{\Psi}_{\ell mpq}}$$

$$\times \left\{ \Delta C_{\ell m} \begin{bmatrix} -q\left[\cos(M - q\Psi_{\ell mpq}) - \cos(M - q\overset{o}{\Psi}_{\ell mpq})\right] \\ \sin(M - q\Psi_{\ell mpq}) - \sin(M - q\overset{o}{\Psi}_{\ell mpq}) \end{bmatrix}_{\ell\text{-m odd}}^{\ell\text{-m even}} \right.$$

$$\left. + \Delta S_{\ell m} \begin{bmatrix} \sin(M - q\Psi_{\ell mpq}) - \sin(M - q\overset{o}{\Psi}_{\ell mpq}) \\ q\left[\cos(M - q\Psi_{\ell mpq}) - \cos(M - q\overset{o}{\Psi}_{\ell mpq})\right] \end{bmatrix}_{\ell\text{-m odd}}^{\ell\text{-m even}} \right\}$$

$$+ \frac{3}{2}\frac{n}{a}\frac{2\mu}{a^2 n}\left(\frac{R_E}{a}\right)^{\ell} F_{\ell mp}(I)\,(\ell - 2p) \Big/ \dot{\Psi}_{\ell mp0}$$

$$\times \quad (t - t_o)\, a\, e \sin M \begin{bmatrix} \Delta C_{\ell m}\cos\overset{o}{\Psi}_{\ell mp0} + \Delta S_{\ell m}\sin\overset{o}{\Psi}_{\ell mp0} \\ \Delta C_{\ell m}\sin\overset{o}{\Psi}_{\ell mp0} - \Delta S_{\ell m}\cos\overset{o}{\Psi}_{\ell mp0} \end{bmatrix}_{\ell\text{-m odd}}^{\ell\text{-m even}} \Bigg\}$$

Now,

$$M + \Psi_{\ell mp-1} = M + (\ell - 2p - 1)(M + \omega) + \omega + m(\Omega - \theta_g)$$

$$= (\ell - 2p)(M + \omega) + m(\Omega - \theta_g)$$

$$= \Psi_{\ell mp0}.$$

Similarly,

$$\Psi_{\ell mp0} = (\Psi_{\ell mp1} - M) = - (M - \Psi_{\ell mp1}).$$

Hence

$$\cos (M \pm \Psi_{\ell mp\mp1}) = \cos \Psi_{\ell mp0}$$

and

$$\sin (\Psi_{\ell mp\pm1} \mp M) = \sin \Psi_{\ell mp0}.$$

Using these results, a full series expansion is obtained for the global radial orbit error of gravitational origin. This can be written

$$\Delta r^{(grav)}(t) \approx \sum_{\ell=2}^{\ell max} \sum_{m=0}^{\ell} \sum_{p=0}^{\ell} \left\{ \frac{2\mu}{a^2 n} \left(\frac{R_E}{a}\right)^{\ell} \frac{F_{lmp}(I) (\ell - 2p)}{\dot{\Psi}_{\ell mp0}} \right.$$

$$\times \left(\Delta C_{\ell m} \begin{bmatrix} \cos\Psi_{\ell mp0} - \cos\Psi^{o}_{\ell mp0} \\ \sin\Psi_{\ell mp0} - \sin\Psi^{o}_{\ell mp0} \end{bmatrix}_{\ell\text{-m odd}}^{\ell\text{-m even}} + \right.$$

$$\left. \Delta S_{\ell m} \begin{bmatrix} \sin\Psi_{\ell mp0} - \sin\Psi^{o}_{\ell mp0} \\ -\cos\Psi_{\ell mp0} + \cos\Psi^{o}_{\ell mp0} \end{bmatrix}_{\ell\text{-m odd}}^{\ell\text{-m even}} \right)$$

$$+ \sum_{\substack{q=-1 \\ q\neq0}}^{1} \frac{\partial G_{\ell pq}(e)}{\partial e} \mu \left(\frac{R_E}{a}\right)^{\ell} \frac{F_{\ell mp}(I)}{n a^2 \dot{\Psi}_{\ell mpq}}$$

$$\times \left\{ \Delta C_{\ell m} \begin{bmatrix} - q \left[\cos \Psi_{\ell mp0} - \cos \Psi^{o}_{\ell mp0} \right] \\ - q \left[\sin \Psi_{\ell mp0} - \sin \Psi^{o}_{\ell mp0} \right] \end{bmatrix}_{\ell\text{-m odd}}^{\ell\text{-m even}} \right.$$

$$\left. + \Delta S_{\ell m} \begin{bmatrix} - q \left[\sin \Psi_{\ell mp0} - \sin \Psi^{o}_{\ell mp0} \right] \\ q \left[\cos \Psi_{\ell mp0} - \cos \Psi^{o}_{\ell mp0} \right] \end{bmatrix}_{\ell\text{-m odd}}^{\ell\text{-m even}} \right\}$$

$$+ \frac{3\mu}{a^3} \left(\frac{R_E}{a}\right)^{\ell} F_{\ell mp}(I) (\ell - 2p) \Big/ \dot{\Psi}_{\ell mp0}$$

$$x \quad (t - t_o)\, a\, e \sin M \left[\begin{matrix} \Delta C_{\ell m} \cos \overset{o}{\Psi}_{\ell mp0} + \Delta S_{\ell m} \sin \overset{o}{\Psi}_{\ell mp0} \\ \Delta C_{\ell m} \sin \overset{o}{\Psi}_{\ell mp0} - \Delta S_{\ell m} \cos \overset{o}{\Psi}_{\ell mp0} \end{matrix} \right]_{\ell\text{-m odd}}^{\ell\text{-m even}} \Bigg\}$$

-(3.22)

Equation (3.22) reveals the full spectrum of periodic terms of gravitational origin with angular arguments $\dot{\Psi}_{\ell mp0}$. All the periodic terms on the right hand side contain $\dot{\Psi}_{\ell mpq}$, q=0, ±1, in the denominator, where

$$\dot{\Psi}_{\ell mpq} = (\ell - 2p + q)(\dot{M} + \dot{\omega}) - q\dot{\omega} + m(\dot{\Omega} - \dot{\theta}_g). \qquad -(3.23)$$

Therefore terms in which $\dot{\Psi}_{\ell mpq}$ is small will produce large contributions to $\Delta r^{(grav)}(t)$. Any term with frequency greater than about 2 cycles per revolution (or 2 x $\dot{M}$) turn out to be insignificant. From equation (3.23), the frequencies of the periodic terms in equation (3.22) are

$$\dot{\Psi}_{\ell mp0} = (\ell - 2p)\dot{M} + m(\dot{\Omega} - \dot{\theta}_g), \qquad -(3.24)$$

for $\dot{\omega} = 0$.

Consider the right hand side of equation (3.22). $\Delta r^{(grav)}(t)$ is made up of three main constituents: a periodic part in which q = 0, a periodic part in which q = ±1 and a secular-periodic part. Both periodic components include the divisor $\dot{\Psi}_{\ell mpq}$ .Now, the mean anomaly increases by 2π radians in the 100 minutes or so that SEASAT or ERS-1 takes to complete a revolution of the Earth. $\dot{\theta}_g \approx 2\pi$ radians/day and Ω takes a full year to complete one revolution for ERS-1 and six months for SEASAT. Hence, since $\dot{\omega} \approx 0$, the dominant term in the divisor $\dot{\Psi}_{\ell mpq}$ is that associated with $\dot{M}$. Terms exclusive of $\dot{M}$ thus provide the smallest values for $\dot{\Psi}_{\ell mpq}$ and hence the largest contributions to $\Delta r^{(grav)}(t)$. By equation (3.23), these are given by combinations of ℓ,

p, q such that $\ell - 2p + q = 0$. Since only values of q such that $|q| \leq 1$ are considered, this requires $\ell - 2p = 0, \pm 1$. For the first main constituent on the right hand side of equation (3.22), in which $q = 0$, the principal contribution would therefore occur when $\ell - 2p = 0$. However, the presence of the multiplicative factor $(\ell - 2p)$ ensures that there exists no contribution from this term for small $\dot{\Psi}_{\ell mpq}$. For the second constituent, however, in which $| q | = 1$, the main contribution to $\Delta r^{(grav)}(t)$ occurs when $\ell - 2p = \pm 1$, by equation (3.23). From equation (3.24), the corresponding frequencies of these terms are given by $\dot{\Psi}_{\ell mp0} \approx \pm \dot{M}$. The magnitude of the secular-periodic term is restricted by the factor e. Hence $\Delta r^{(grav)}(t)$ is dominated by the central term on the right hand side of equation (3.22), with the dominant frequencies centred around one cycle per revolution.

The orbits of SEASAT and ERS-1 are frozen repeat orbits, with ω held at $\frac{\pi}{2}$ radians, in which the satellites perform an integral number of revolutions, k' say, in the time taken for the Earth to revolve an integral number of times, ℓ' say, relative to the ascending node. Hence,

Time taken for satellite to complete k' revolutions

= Time taken for Earth to revolve ℓ' times with respect to the ascending node

i.e.
$$\frac{2\pi k'}{\dot{M}} = \frac{2\pi \ell'}{(\dot{\theta}_g - \dot{\Omega})}$$

Or
$$\dot{\theta}_g - \dot{\Omega} = \frac{\ell' \dot{M}}{k'} \quad . \qquad \text{-(3.25)}$$

Thus by equation (3.24),
$$\dot{\Psi}_{\ell mp0} = \left(k - \frac{m \ell'}{k'} \right) \dot{M}, \qquad \text{-(3.26)}$$

where $k = \ell - 2p$.

The frequency terms present in equation (3.22) are those spanning all the multiples of 1 cycle per revolution as given by equation (3.26). Note that the interaction term consists of a secular variation superimposed on the sinusoidal 1 cycle per revolution sinM factor, to produce a secular-periodic constituent $(t - t_o)$ sinM of $\Delta r^{(grav)}(t)$.

The theory developed so far has assumed that $\dot{\Psi}_{\ell mpq} \neq 0$. However, for certain combinations of ℓ,m,p,q this is not the case. This situation is now dealt with separately. By equation (3.23),

$$\dot{\Psi}_{\ell mpq} = 0 \quad \Rightarrow \quad (\ell - 2p + q) (\dot{M} + \dot{\omega}) - q\dot{\omega} + m (\dot{\Omega} - \dot{\theta}_g) = 0 .$$

Therefore, for $\dot{\omega} \approx 0$,

$$(\ell - 2p + q) \dot{M} + m (\dot{\Omega} - \dot{\theta}_g) = 0 . \qquad -(3.27)$$

For $m \neq 0$, from equation (3.25), equation (3.27) is satisfied when

$$\frac{(\ell - 2p + q)}{m} = \frac{\ell'}{k'} .$$

The gravity field models used here are of degree and order 36. Thus the maximum value of m is 36. Since the orbits analysed are 43 rev/3 day and 501 rev/35 day repeats, that is k'=43 or k'=501, resonance has been ignored. In practice resonance can be incorporated simply by the addition of a quadratic term in time modulated by a 1 cycle per revolution term [Rapp et al., 1991].

The alternative solution of equation (3.27) is for m = 0, in which case

$$m = \ell - 2p + q = 0 . \qquad -(3.28)$$

Hence, for $\dot{\Psi}_{\ell mpq} = 0$, the only contribution to Δr will come from errors in the zonal coefficients. The contributions are from Δa, Δe and ΔM, so they are the elements of interest here.

By equation (3.12), $\frac{da}{dt}$ contains the factor (ℓ - 2p + q), which is zero in this case. Hence

$$\dot{\Psi}_{\ell mpq} = 0 \quad \Rightarrow \quad \Delta a = 0.$$

From equation (3.13),

$$\frac{de}{dt} \approx \sum_{\ell=2}^{\ell max} \sum_{p=0}^{\ell} \sum_{q=-1}^{1} \frac{\mu R_E^{\ell}}{a^{\ell+1}} \frac{F_{\ell 0 p}(I)\, G_{\ell pq}(e)\, q}{na^2 e} \Delta C_{\ell 0} \begin{bmatrix} -\sin\Psi_{\ell 0pq} \\ \cos\Psi_{\ell 0pq} \end{bmatrix}_{\ell\ \text{odd}}^{\ell\ \text{even}} .$$

But, by equation (3.11) and equation (3.28),

$$\Psi_{\ell 0pq} = - q\omega .$$

Hence

$$\Psi_{\ell 0pq} = \begin{cases} 0 & \text{for } q = 0 \\ \mp\omega & \text{for } q = \pm 1 \end{cases} . \qquad \text{-(3.29)}$$

Moreover, for $q = \pm 1$, $\ell - 2p = \mp 1$, which is odd, hence ℓ is odd. Similarly, $q = 0$ $\Rightarrow$ ℓ is even. This leaves

$$\frac{de}{dt} \approx \sum_{\ell=2}^{\ell max} \sum_{p=0}^{\ell} \sum_{q=-1}^{1} \frac{\mu R_E^{\ell}}{a^{\ell+1}} \frac{F_{\ell 0 p}(I)\, G_{\ell pq}(e)\, q}{na^2 e} \Delta C_{\ell 0} \cos\Psi_{\ell 0pq} .$$

By equation (3.29),

$$\cos\Psi_{\ell 0p\pm 1} = \cos(\mp\omega) = \cos\omega \approx \cos\frac{\pi}{2} = 0.$$

Hence

$$\dot{\Psi}_{\ell mpq} = 0 \quad \Rightarrow \quad \Delta e = 0.$$

This is expected as for a frozen orbit e and ω are invariant under the effect of the odd zonal harmonics. Finally, by equation (3.14),

$$\frac{dM}{dt} \approx \sum_{\ell=2}^{\ell_{max}} \sum_{p=0}^{\ell} \sum_{q=-1}^{1} \frac{\mu R_E^{\ell}}{a^{\ell+1}} \frac{F_{\ell 0p}(I)}{na^2} \left\{ -\frac{1}{e} \frac{\partial G_{\ell pq}(e)}{\partial e} + 2\,(\ell+1)\, G_{\ell pq}(e) \right\}$$

$$\times \quad \Delta C_{\ell 0} \begin{pmatrix} \cos\Psi_{\ell 0pq} \\ \sin\Psi_{\ell 0pq} \end{pmatrix}_{\ell\ \text{odd}}^{\ell\ \text{even}}.$$

Using equation (3.28) and equation (3.29) gives

$$\frac{dM}{dt} \approx \sum_{\ell=2}^{\ell_{max}} \sum_{p=0}^{\ell} \sum_{q=-1}^{1} \frac{\mu R_E^{\ell}}{a^{\ell+1}} \frac{F_{\ell 0p}(I)}{na^2} \left\{ -\frac{1}{e} \frac{\partial G_{\ell pq}(e)}{\partial e} + 2(\ell+1) G_{\ell pq}(e) \right\} \Delta C_{\ell 0} \begin{bmatrix} \cos 0 \\ \sin(\mp\omega) \end{bmatrix}_{q=\pm 1}^{q=0}.$$

Therefore

$$\frac{dM}{dt} \approx -\sum_{\ell=2}^{\ell_{max}} \sum_{p=0}^{\ell} \frac{\mu R_E^{\ell}}{a^{\ell+1}} \frac{F_{\ell 0p}(I)}{ena^2} \Delta C_{\ell 0} \left[-\frac{\partial G_{\ell p-1}(e)}{\partial e} + \frac{\partial G_{\ell p1}(e)}{\partial e} \right] \qquad -(3.30)$$

There is no interaction term between the semi-major axis error and the rate of change of M this time since there is no variation in a. Equation (3.30) can now be integrated to leave the ΔM contribution as

$$\Delta M \approx - \sum_{\ell=2}^{\ell max} \sum_{p=0}^{\ell} \frac{\mu R_E^{\ell}}{a^{\ell+1}} \frac{F_{\ell 0 p}(I)}{ena^2} \Delta C_{\ell 0} \left[- \frac{\partial G_{\ell p-1}(e)}{\partial e} + \frac{\partial G_{\ell p 1}(e)}{\partial e} \right] (t - t_o)$$

-(3.31)

Since this is the only contribution to the radial orbit error for $\dot{\Psi}_{\ell 0 pq} = 0$, equation (3.31) can be substituted directly into equation (3.10) to leave

$$\Delta r \approx - \sum_{\ell=2}^{\ell max} \sum_{p=0}^{\ell} \frac{\mu R_E^{\ell}}{a^{\ell+1}} \frac{F_{\ell 0 p}(I)}{na} \Delta C_{\ell 0} \left[- \frac{\partial G_{\ell p-1}(e)}{\partial e} + \frac{\partial G_{\ell p 1}(e)}{\partial e} \right] (t - t_o) \sin M.$$

-(3.32)

From equation (3.22), (3.26) and (3.32), a final result for the gravitational radial orbit error is obtained. Gathering together terms of like frequency, the expression can be written as

$$\Delta r^{(grav)}(t) = \sum_{k=-\ell max}^{\ell max} \sum_{m=0}^{\ell max} \left\{ A_{km} \cos \dot{\Psi}_{km} t + B_{km} \sin \dot{\Psi}_{km} t \right\} + g_0 + g_1 (t - t_o) \sin M,$$

-(3.33)

where $\dot{\Psi}_{km}$ is defined by the right hand side of equation (3.26) with k replacing ℓ-2p and A_{km}, B_{km}, g_0 and g_1 can be assumed constant, since a and i vary little.

Figure (3.5) and Figure (3.6) illustrate the behaviour of the gravitational radial orbit error in SEASAT. Two orbits were constructed from the same initial starting conditions, one in the presence of the GEM-T1 gravity field, the other using the clone field described and employed in the ERS-1 simulations of chapter 7, for the six day period MJD43764 to MJD43770. The difference in the radial heights is plotted in

Figure (3.5). A spectral analysis, a breakdown of the individual frequency components, of these differences was carried out and is plotted in Figure (3.6).

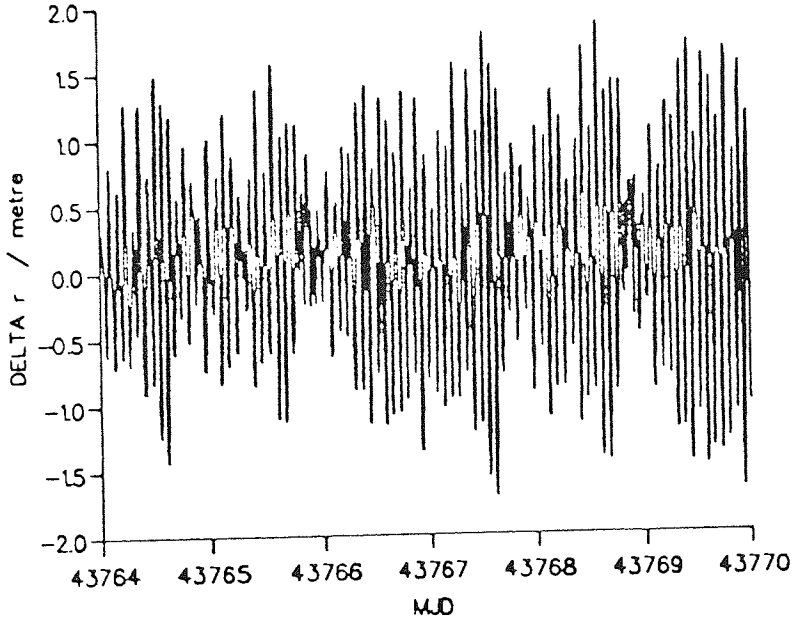

Figure (3.5)
Gravitational radial orbit error

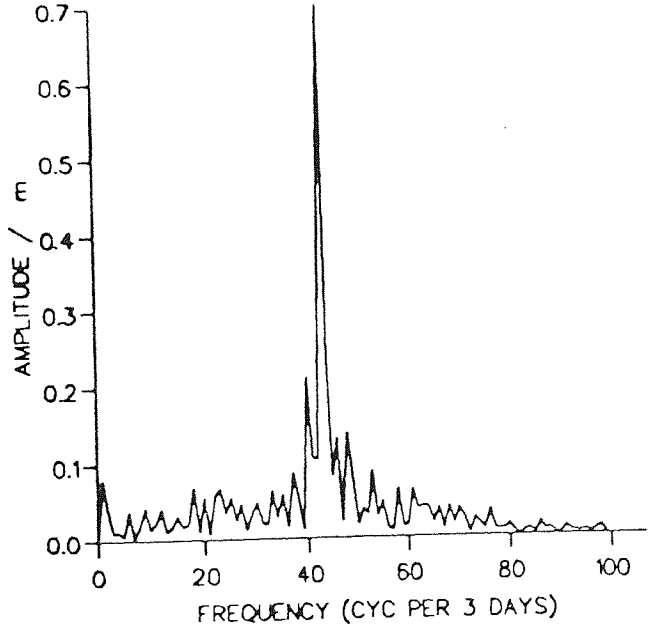

Figure (3.6)
Spectral analysis of gravitational radial orbit error

The obvious characteristic in both diagrams is the large 1 cycle per revolution signature due to the strong $\dot{M}$ frequency dependency. Being in its 43 revolution/3 day orbit, SEASAT will have revolved $6 \times \frac{43}{3} = 86$ times during the six days. This accounts for the 86 main peaks of 1 cycle per revolution appearing in the plot of Figure (3.5). Figure (7.3) and Figure (7.4) show the same pattern for ERS-1, although the orbit was a 501 revolution/35 day repeat, hence the appearance of $\left[7 \times \frac{501}{35}\right] = 100$ peaks in the seven day Δr plot, where [-] denotes the integral part.

For very low values of ℓ, the coefficients $C_{\ell m}$ are relatively well known, so that $\Delta C_{\ell m}$ is small. For satellites of high altitude, such as Lageos, the attenuation factor $\left(\frac{R_E}{a}\right)^{\ell}$ significantly reduces the effects of the other zonal and tesseral coefficients for large ℓ, but with ERS-1 and SEASAT in low orbits of near 800km, the attenuation factor is less prominent and gravitational perturbations are significant for ℓ as large as 70, say.

§ 3.7 Non-Gravitational Radial Orbit Error

Although the largest component of the radial orbit error is of gravitational origin [Tapley and Rosborough,1985], as given by equation (3.33), there is also a significant non-gravitational influence, mainly due to mismodelling of air drag and solar radiation pressure forces and errors in the initial state vector of the orbit. Errors in the calculation of tidal forces and third body attraction also contribute to a lesser extent.

§ 3.8 Mismodelling of Air Drag

A satellite moving with velocity v relative to the surrounding atmosphere will experience an atmospheric drag force, F, acting in the opposite direction to its motion, which can be expressed as [King-Hele,1987]

$$F = -\frac{1}{2}\rho v^2 \frac{A}{m} C_D \ , \qquad -(3.34)$$

where m is the satellite mass, A its cross-sectional area, ρ the air density and C_D the drag coefficient.

It has been found experimentally [King-Hele,1987] that plots of air density against geocentric height show that the density decreases approximately logarithmically with radial distance in the regions through which SEASAT travelled, that is at $r \approx 800$km. Hence

$$\ln \rho \ \alpha \ -r \ ,$$

or

$$\ln \rho \ \approx \ -\frac{r}{H} \ ,$$

where H is the approximately constant density scale height. Therefore

$$\ln \rho - \ln \rho_p \ \approx \ \left(-\frac{r}{H}\right) - \left(-\frac{r_p}{H}\right) ,$$

where ρ_p is the air density at perigee height r_p. Hence

$$\rho \approx \rho_p \exp\left[-\frac{r - r_p}{H}\right] .$$

Thus density mismodelling may be approximated by

$$\Delta\rho = \Delta\rho_p \exp\left[-\frac{r - r_p}{H}\right] , \qquad -(3.35)$$

where $\Delta\rho$, $\Delta\rho_p$ are the errors in the air density at heights r and r_p, respectively. On using equation (3.8) and from Figure (3.1),

$$\frac{r - r_p}{H} = \frac{a\,e}{H}(1 - \cos E) ,$$

which upon substitution into equation (3.35) gives

$$\Delta\rho = \Delta\rho_p \exp\left[- \frac{a\,e\,(1 - \cos E)}{H} \right] .$$

For small e, $\frac{a\,e}{H} \ll 1$, the exponential series gives

$$\Delta\rho = \Delta\rho_p \left[1 - \frac{a\,e}{H} + \frac{a\,e}{H}\cos E \right] + O(e^2) . \qquad -(3.36)$$

Thus by equation (3.5) and equation (3.2),

$$\frac{dM}{dt} = \frac{d}{dt}(E - e\sin E) = \frac{r}{a}\frac{dE}{dt} = \frac{1}{a}\sqrt{\frac{\mu}{a}} ,$$

i.e.

$$\frac{dE}{dt} = \frac{1}{r}\sqrt{\frac{\mu}{a}} \qquad -(3.37)$$

for a perturbed ellipse.

An alternative form of the Lagrange Planetary Equations given by equations (3.3) is achieved by expressing the rates of change of the elements in terms of the components of an overall disturbing force in directions tangential and transverse to the orbital motion and perpendicular to the orbital plane. From [King-Hele,1987] and [Aksnes, 1975] this leads to

$$\frac{da}{dt} = \frac{2a^2 v}{\mu} f_T , \qquad -(3.38)$$

where f_T is the tangential component of the disturbing force.

The disturbing force due to drag mismodelling, $\Delta F_{DIST}^{(drag)}$, acts tangentially and opposite to the satellite motion. By equation (3.34) and equation (3.36) it is given by

$$\Delta F_{DIST}^{(drag)} \approx -\frac{1}{2}\delta v^2 \Delta\rho_0 \left[1 - \frac{a e}{H} + \frac{a e}{H} \cos E \right],$$

where $\delta = \frac{A}{m} C_D$.

Substituting this into equation (3.38) leads to the error in a due to drag mismodelling, namely

$$\Delta a^{(drag)} \approx -\int \frac{a^2 v^3 \delta}{\mu} \Delta\rho_p \, [\, 1 - z + z \cos E \,] \, dt \;,$$

where $z = \frac{a e}{H}$.

Or, using equation (3.37),

$$\Delta a^{(drag)} \approx -a^2 \delta \Delta\rho_p \int \frac{v^3 r}{\mu} \sqrt{\frac{a}{\mu}} \, [\, 1 - z + z \cos E \,] \, dE$$

i.e.

$$\Delta a^{(drag)} \approx -a^2 \delta \Delta\rho_p \left[(1 - z) E + z \sin E \right]_{E_0}^{E} \;,$$

where $E = E_0$ at time t_0. Since $M \approx E$ and $e \approx 0$ for low eccentric orbits,

$$\Delta a^{(drag)} \approx -a^2 \delta \Delta\rho_p \, (M - M_0) \,,$$

where $M = M_0$ at time t_0. Similar expressions can be derived for $\Delta e^{(drag)}$ and $\Delta M^{(drag)}$ [Moore and Rothwell, 1990];

$$\Delta e^{(drag)} \approx -a \delta \Delta\rho_p \left[\sin M - \sin M_0 + \frac{z}{2} (M - M_0) \right]$$

and

$$\Delta M^{(drag)} \approx -a \delta \frac{\Delta\rho_p}{e} [\, \cos M - \cos M_0 \,] \,.$$

Upon substitution back into equation (3.10) the radial orbit error contribution due to drag mismodelling is derived as

$$\Delta r^{(drag)}(t) \approx - a^2 \delta \Delta\rho_p \left[(M - M_0) - \frac{z}{2} (M-M_0) \cos M - \sin(M-M_0) \right]. \quad -(3.39)$$

Since M increases linearly in time by equation (3.1), $\Delta r^{(drag)}(t)$ consists of a secular part proportional to time, t, a secular-periodic part proportional to t cosM as well as a term of frequency 1 cycle per revolution. M increases by 2π radians each orbital period, so that $\dot{M}$ is relatively large, hence $\Delta r^{(drag)}$ is dominated by the secular term. Atmospheric conditions vary over relatively short lengths of time such that this model for radial orbital drag error becomes unrealistic if applied over the whole length of an orbit of several days. For this reason the drag terms are solved for daily, or even twice daily in the event of severely changeable conditions on any particular day.

Figure (3.7) displays the radial variation due to drag error. A six day SEASAT ephemeris was converged between the dates MJD43764 and MJD43770. Each of the six daily drag coefficients within the initial state vector was changed to 3 whilst all other parameters, that is the position, velocity and solar reflectivity coefficient, were left unaltered. Using this state vector a second ephemeris was generated over the same time span. The drag coefficients used for each orbit are given in Table (3.1). The diagram depicts the radial differences between the two orbits at each ephemeris epoch. The daily linear trend is clearly visible along with the 1 cycle per revolution signature, which increases steadily due to the secular-periodic terms of equation (3.39).

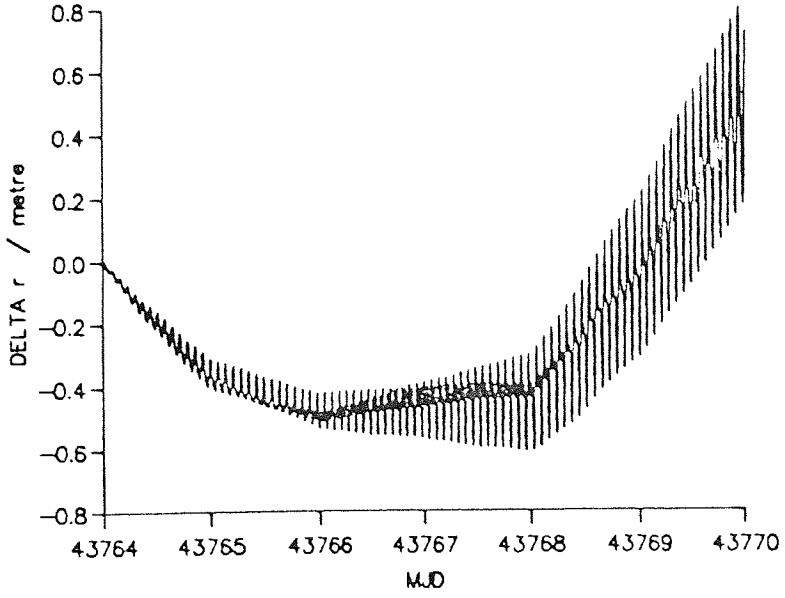

Figure (3.7)
Radial orbit error due to drag mismodelling

MJD	C_D (arc 1)	C_D (arc 2)
43764 - 43765	3.77080473450	3.00000000000
43765 - 43766	3.28768688134	3.00000000000
43766 - 43767	2.92881197582	3.00000000000
43767 - 43768	2.96105603672	3.00000000000
43768 - 43769	2.37762479766	3.00000000000
43769 - 43770	1.94292945333	3.00000000000

Table (3.1)
Drag coefficients employed in the derivation of Figure (3.7), to illustrate radial orbit error due to drag mismodelling

§ 3.9 Initial State Vector Error

From given initial conditions, an orbit of a satellite is fitted to the tracking data by solving for several parameters. During the procedure, a new estimate of the initial state vector is derived from which a new orbit will give an improved fit to the tracking data in the least squares sense. The initial state vector is repeatedly adjusted until no more significant improvement can be made.

From equation (3.10), the radial orbit error at a future time, t, due to errors in the initial values of the Keplerian elements Δa_0, Δe_0, ΔM_0 at initial time t_0 is given by

$$\Delta r^{(SI)}(t) \approx \Delta a_0 - a\,\Delta e_0 \cos M + a\,e\,\Delta M_0 \sin M \ . \qquad -(3.40)$$

As in the case of the gravitational interaction term, the initial error in the semi-major axis, Δa_0, is substituted into equation (3.15) to give the interaction term between the rate of change of M due to the gravity field and the perturbation in a due to initial state vector error as

$$\Delta M_{int}^{(SI)}(t) = -\frac{3}{2}\frac{n}{a}\,\Delta a_0\,(t - t_0) \ .$$

Thus the overall orbital error in the geocentric distance due to initial state vector error is given by

$$\Delta r^{(SI)}(t) \approx \Delta a_0 - a\,\Delta e_0 \cos M + a\,e\left[\,\Delta M_0 - \frac{3}{2}\frac{n}{a}\,\Delta a_0\,(t - t_0)\,\right]\sin M \ . \qquad -(3.41)$$

The overall radial orbit error is given by the sum of the errors due to the various perturbations described in this chapter [Moore and Gray,1991]. This means, for example, that any constant part of the error can be reduced by a suitable selection of initial value of the semi-major axis by making Δa_0 in equation (3.41) numerically equal to the negative of the sum of the constant errors due to other perturbations. Similarly, 1 cycle per revolution error and the secular-periodic sinusoidal terms can be reduced by affixing certain values to Δa_0, Δe_0 and ΔM_0.

The orbit computation minimization is carried out with respect to all three directions; radial, along-track and cross-track. Thus reducing an error term in, say, the along-track direction by adjustment of the initial starting values and other parameters, such as scale factors for drag and solar radiation pressure, may actually manufacture a larger error term in the radial direction. For example, a particular ΔM_0 may reduce a term in the along-track direction but increase the radial part $ae\Delta M_0 \sin M$

of equation (3.41), resulting in a large contribution to the radial 1 cycle per revolution perturbation.

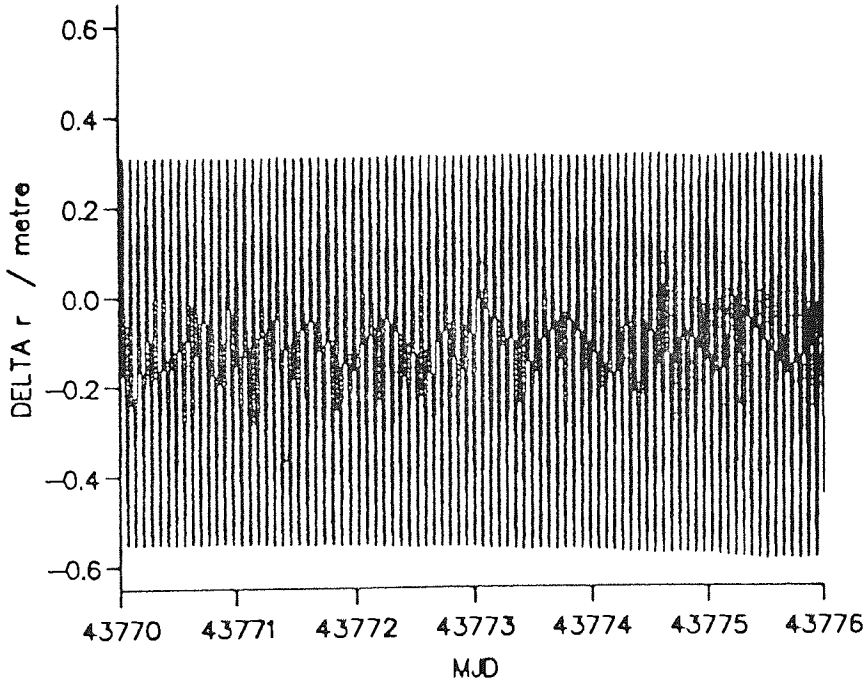

Figure (3.8)
Radial orbit error due to initial state vector error

Figure (3.8) shows the effect on a radial orbit of a change in the initial starting conditions. Two SEASAT orbits were constructed using the same drag coefficients and solar radiation pressure coefficient, under the influence of the GEM-T1 gravity field, for the six day period MJD43770 to MJD43776. One used the converged starting vector to give the best fit, the other used the end vector from the MJD43764 to MJD43770 orbit employed in the SEASAT analysis as its initial conditions. The two most striking characteristics are the relatively large 1 cycle per revolution signature due to the cosM term of equation (3.41) and the constant offset of approximately 12cm, mainly as a result of the difference in the semi-major axes, that

is the Δa_0 term of equation (3.41). A slight increase in amplitude of the 1 cycle per revolution signature is noticeable, due to the secular-periodic sinM term.

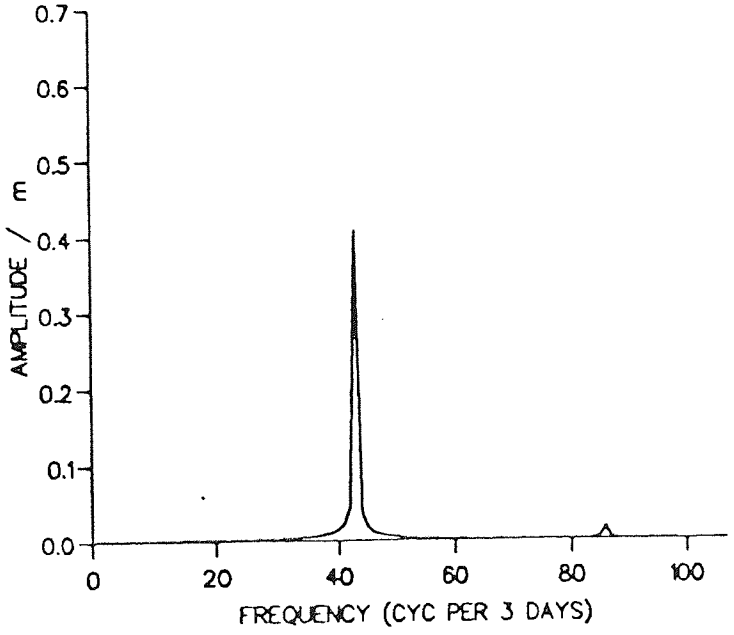

Figure (3.9)
Spectral analysis of radial orbit error due to initial state vector error

Figure (3.9) is the spectral analysis of the same radial differences and as expected shows little amplitude at any frequencies except 1 cycle per revolution, where the 41cm amplitude is consistent with Figure (3.8).

§ 3.10 Solar Radiation Pressure Mismodelling

During the sunlit portion of the orbit of a satellite, photons incident from the Sun impart momentum to the spacecraft as they strike its surface, collectively producing a perturbatory force known as the solar radiation pressure force, $F^{(SRP)}$. This depends on the cross-sectional area to mass ratio of the satellite, $\frac{A}{m}$, the solar radiation pressure, P, of the Sun on the Earth when the geocentric distance of the Sun, r_{Sun}, is equal to the mean distance of the Sun from the Earth, a_{Sun}, and a solar

reflectivity constant, C_R. The error in the force model, $\Delta F^{(SRP)}$, due to corresponding errors in the solar reflectivity constant, ΔC_R, is given by [Aksnes, 1975]

$$\mu \, \Delta F^{(SRP)} = \Delta C_R \frac{A}{m} P \left(\frac{a_{Sun}}{r_{Sun}} \right)^2 . \qquad -(3.42)$$

The Lagrange Planetary Equations can be re-written in terms of the direction cosines of $F^{(SRP)}$ at perigee in the radial direction and perpendicular to the radial direction in the orbital plane, S and T, respectively, to give the elemental variations due to solar radiation pressure force mismodelling. For example, for the semi-major axis,

$$\frac{da}{dt} = \frac{2na^3}{\sqrt{1 - e^2}} \Delta F^{(SRP)} \quad x$$

$$\left[e \sin M \, (S \cos M + T \sin M) + \frac{a (1 - e^2)}{r} (S \sin M + T \cos M) \right]$$

$$\approx 2 n a^3 \Delta F^{(SRP)} \frac{a (1 - e^2)}{r} (S \sin M + T \cos M) .$$

Hence the error in a due to solar radiation pressure mismodelling as the satellite travels through sunlight from $M = M_1$ to $M = M_2$ is given by

$$\Delta a \approx 2 a^3 \Delta F^{(SRP)} \int_{M_1}^{M_2} (S \sin M + T \cos M) \, dM$$

$$= 2 a^3 \Delta F^{(SRP)} \left[- S \cos M + T \sin M \right]_{M_1}^{M_2} .$$

Over k revolutions of the Earth, the total perturbation can be approximated by

$$\Delta a^{(k)} = \sum_{j=1}^{k} 2\, a^3\, \Delta F^{(SRP)} \left[-S \cos M + T \sin M \right]_{M_1}^{M_2} .$$

Similar expressions hold for $\Delta e^{(k)}$ and $\Delta M^{(k)}$, which can be substituted into equation (3.10) to produce the overall error in the geocentric distance of the satellite due to solar radiation pressure mismodelling, $\Delta r^{(SRP)}$. The dominant effects are cosM and sinM variations superimposed on a secular trend, although there are also significant constant and purely secular variations. That is,

$$\Delta r^{(SRP)}(t) \approx S_0 + S_1 (t - t_0) + S_2 (t - t_0) \cos M + S_3 (t - t_0) \sin M \quad , \quad -(3.43)$$

where S_0, S_1, S_2 and $S_3$are constants.

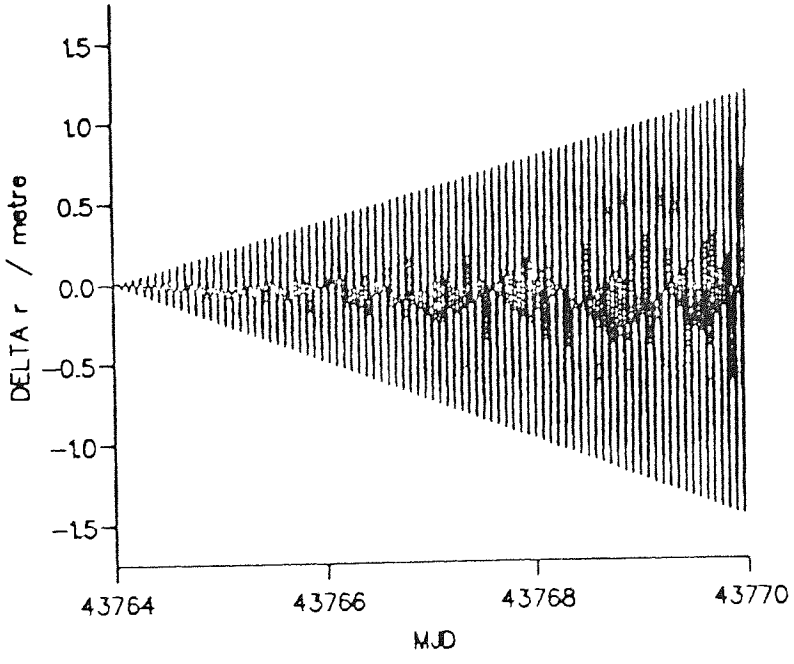

Figure (3.10)
Radial orbit error due to solar radiation pressure mismodelling

$\Delta r^{(SRP)}$ is illustrated by Figure (3.10). Two orbits were generated using the GEM-T1 gravity field model over the six days from MJD43764 to MJD43770.

Identical starting conditions were used in both cases, except for different solar reflectivity coefficients. The first arc is the GEM-T1 derived ephemeris of section §6.6 and therefore used the solar reflectivity coefficient obtained during the orbit determination procedure over the six days, whereas the second orbit used the coefficient derived during the derivation of the ephemeris for the next six days. Although the constants differ by only 4.1% (1.555 v. 1.494), a marked secular-periodic one cycle per revolution signature exists.

§ 3.11 Third Body Attraction and Tides

Satellites move in the gravitational fields of the Sun, the Moon and planets of the solar system as well as that of the Earth, which not only act directly upon the spacecraft but also indirectly through tidal forces. The Earth is gravitationally attracted to the Sun and Moon which, depending on their relative positions, alter the mass distribution of both the Earth and the water of its oceans, causing ocean and solid Earth tidal forces to act on the satellite. Errors in these force models and in the third body attraction model in the orbit determination procedure (see section §5.2) lead to perturbations in the radial direction, although these are insignificant compared to those from the geopotential error, initial state vector error and drag and solar radiation pressure mismodelling, and are consequently ignored.

§ 3.12 Overall Radial Orbit Error

The required expression for the global radial orbit error is given by the summation of all the terms described in this chapter, that is of equations (3.33), (3.39), (3.41) and (3.43). Additional terms occur from interaction between

perturbations already described and the radial perturbation due to the C_{20} harmonic term of the geopotential, which is given by [Gooding,1981]

$$\delta r \approx -\frac{1}{4} C_{20} \left(\frac{R_E}{a}\right)^2 a \sin^2 I \cos 2(\omega + M) \quad .$$

Hence

$$\Delta(\delta r) \approx \frac{1}{2} a C_{20} \left(\frac{R_E}{a}\right)^2 \sin^2 I \sin 2(\omega + M)\,(\Delta\omega + \Delta M) \quad ,$$

where ΔM is given by the term due to the particular source concerned and $\Delta\omega$ is assumed negligible since $\dot{\omega} \approx 0$. This gives rise to 2nd order effects of the form already derived, plus periodic terms of 2 cycles per revolution of not purely gravitational origin.

Thus the overall expression consists of purely periodic terms of varying frequency, along with secular, secular-periodic and constant contributions. That is,

$$\Delta r(t) \approx \Delta r^{(grav)}(t) + \Delta r^{(drag)}(t) + \Delta r^{(SRP)}(t) + \Delta r^{(SI)}(t) + \text{2nd order effects}$$

$$\Rightarrow \Delta r(t) \approx$$

$$\sum_{k=-\ell max}^{\ell max} \sum_{m=0}^{\ell max} \left\{ A_{km} \cos \dot{\Psi}_{km} t + B_{km} \sin \dot{\Psi}_{km} t \right\} + c_0 + c_1 \cos M + c_2 \sin M$$

$$+ c_3 \cos 2M + c_4 \sin 2M + c_5 (t - t_0) \cos M + c_6 (t - t_0) \sin M + c_7 (t - t_0) \sin 2M$$

$$+ c_{NDAY(t)+7} (t - t_0^{(t)}) + \left[\sum_{k=8}^{NDAY(t)+6} c_k \right]_{NDAY(t)=1}^{NDAY(t)>1} \quad ,$$

$$0$$

-(3.44)

where $c_0, \ldots, c_{NDAY(t)+7}$ are constants and $t_0^{(t)}$ is the epoch at the beginning of the NDAY(t)th day within which t falls. The summations $\sum_{k=-\ell max}^{\ell max} \sum_{m=0}^{\ell max}$ include all combinations except for the one and two cycles per revolution frequency terms, (k,m)

= (1,0) and (k,m) = (2,0), which are included separately to demonstrate that they are of both gravitational and non-gravitational origin.

CHAPTER 4

CROSSOVERS

§ 4.1 Crossover Residuals

The ground-track of a satellite is the projection of the sub-satellite points onto the surface of the Earth, as the satellite moves in its orbit. The revolution of the Earth about its axis underneath the orbit results in ascending arcs and descending arcs, those sections of the ground-track over which the satellite is travelling northwards and southwards respectively, to intersect at certain points. These points are known as crossover points.

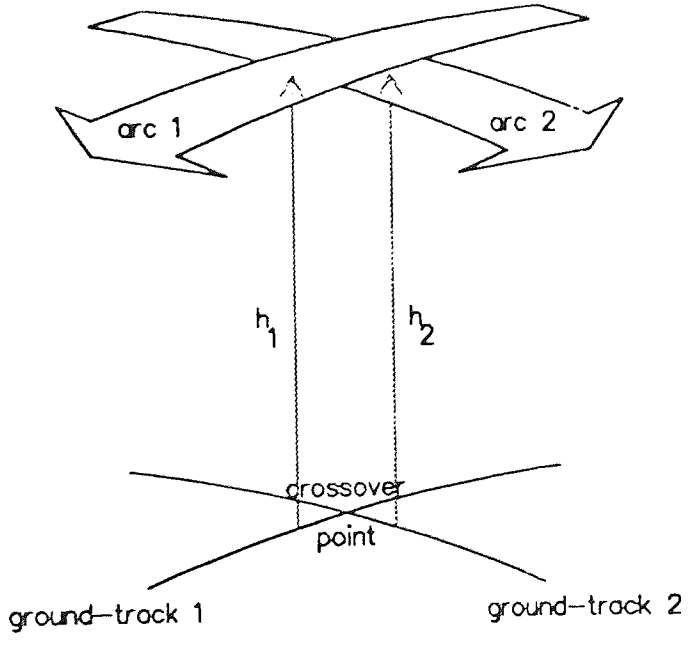

Figure (4.1)
Crossover point formed by intersecting arcs

Suppose two arcs, namely arc 1 and arc 2, intersect to form a crossover point, as shown in Figure (4.1), the satellite travelling over the crossover point on arc 1 at time t_1 and on arc 2 at time t_2. Then the crossover height difference is defined as the difference between the altitude of the satellite on arc 1 and its altitude on arc 2, at the crossover point. Thus the altimetrically measured observed crossover height difference is given by

$$C_{12}^{o} = h_1^{o} - h_2^{o} \quad , \qquad \text{-(4.1)}$$

where h_i^{o} is the observed height on arc i, i=1,2.

Similarly, the calculated crossover height difference is

$$C_{12}^{c} = h_1^{c} - h_2^{c} \quad , \qquad \text{-(4.2)}$$

where h_i^{c} is the calculated height on arc i, i=1,2.

Further, the crossover difference residual, ΔC_{12}, is the difference between the observed and the calculated crossover height differences. That is, from equation (4.1) and equation (4.2),

$$\Delta C_{12} = (h_1^{o} - h_2^{o}) - (h_1^{c} - h_2^{c}) \quad ,$$

i.e.

$$\Delta C_{12} = (h_1^{o} - h_1^{c}) - (h_2^{o} - h_2^{c}) \quad . \qquad \text{-(4.3)}$$

The observed heights, h_i^{o}, will include errors in the modelled geoid height (see chapter 2) at the location of the crossovers. However, the geoid error can be assumed time independent for $t_1 \approx t_2$, being reliant only on the position considered, and hence is common to both h_1^{o} and h_2^{o}. Thus the geoid error will cancel in the crossover difference residual equation (4.3). A data set of crossover residuals will therefore contain no error due to the geoid whilst similarly other geographically

correlated errors will cancel in the same manner [Engelis,1988]. As a result, crossover differences form a more accurate radial data set than altimetric observations, containing none of the geoid errors present in altimetry, which can exceed 1m in places. Moreover, the crossover difference residuals are dominated by the radial orbit error, although there is some contribution from dynamic sea surface topography and ocean tidal mismodelling. Crossover residuals are thus a powerful datatype for use in the modelling of radial orbit error and are used in the least squares minimization described here to reduce the global radial orbit error.

§ 4.2 Geocentric Height Approximation

The altimetric height, h, is taken to be perpendicular to the reference ellipsoid defined in section §2.2. This is known as the geodetic height. The radial height, r, however, is the geocentric height as defined in section §3.5. To a high degree of accuracy, the crossover difference residual as defined in terms of geodetic heights by equation (4.3) can also be defined in terms of geocentric, or radial heights, as will now be illustrated.

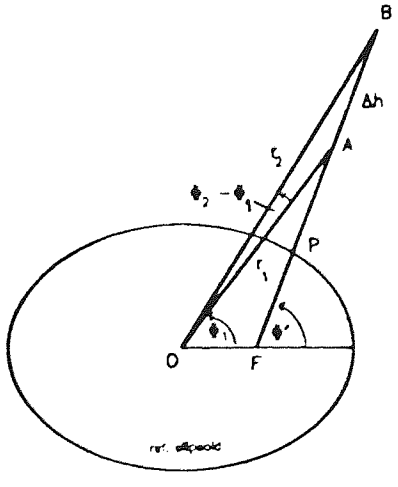

Figure (4.2)
Crossover point relative to the reference ellipsoid

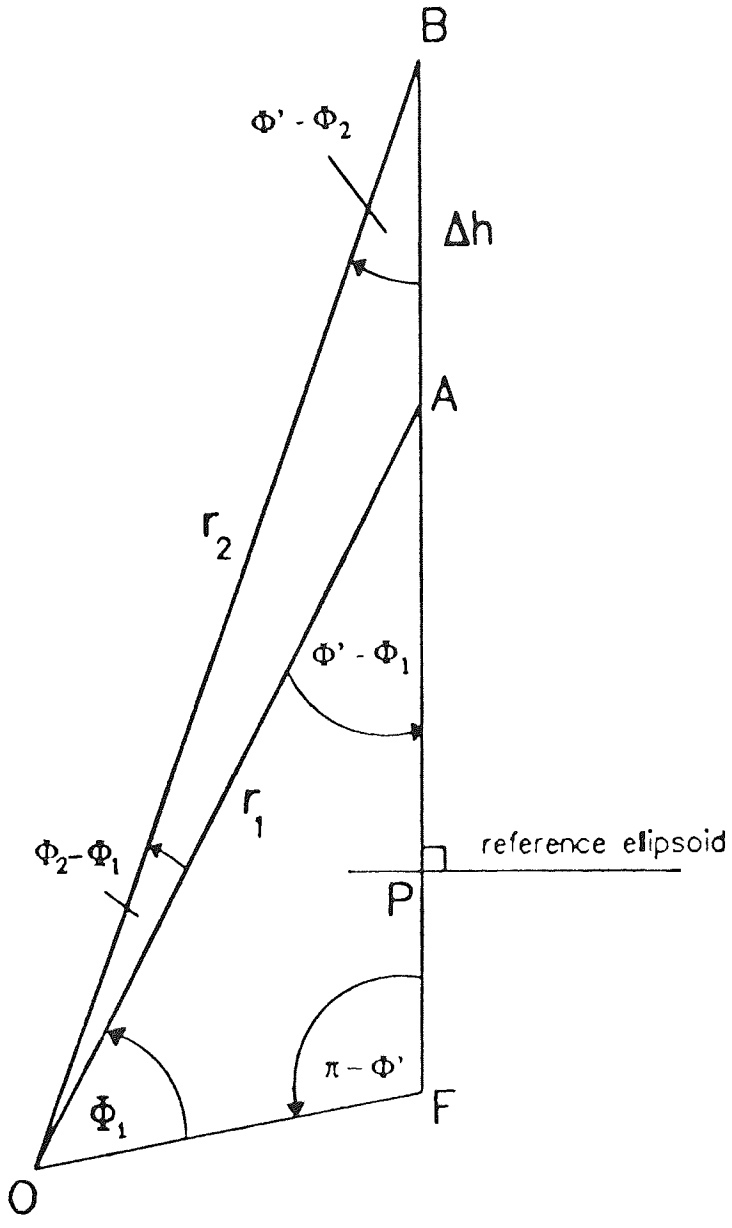

Figure (4.3)
Geocentric and geodetic representation of the crossover point of Figure (4.2)

Consider Figure (4.2) and Figure (4.3), which illustrate the geometry at a crossover point. It should be noted that the angles marked in the diagrams are exaggerated for clarity. By the definition of a crossover, the geodetic latitude is the same on both arcs = Φ', say. In Figure (4.3), Φ_1 and Φ_2 denote the geocentric

latitudes of the first and second crossover epochs, that is when the satellite is at A and B, respectively. Hence,

$$\hat{BOA} = \Phi_2 - \Phi_1$$

and

$$\hat{OBA} = \Phi' - \Phi_2.$$

Applying the sine rule to triangle BOA,

$$\frac{\Delta h}{\sin(\Phi_2 - \Phi_1)} = \frac{r_2}{\sin(\Phi' - \Phi_1)} = \frac{r_1}{\sin(\Phi' - \Phi_2)} ,$$

whence

$$r_1 = \Delta h \frac{\sin(\Phi_2 - \Phi')}{\sin(\Phi_1 - \Phi_2)} \qquad \text{-(4.4)}$$

and

$$r_2 = \Delta h \frac{\sin(\Phi_1 - \Phi')}{\sin(\Phi_1 - \Phi_2)} . \qquad \text{-(4.5)}$$

Subtracting equation (4.5) from equation (4.4) gives

$$r_1 - r_2 = \Delta h \frac{[\sin(\Phi_2 - \Phi') - \sin(\Phi_1 - \Phi')]}{\sin(\Phi_1 - \Phi_2)}$$

$$= \Delta h \frac{\cos\left[\Phi' - \frac{(\Phi_1 + \Phi_2)}{2}\right] \sin\left[\frac{(\Phi_2 - \Phi_1)}{2}\right]}{\cos\left[\frac{(\Phi_2 - \Phi_1)}{2}\right] \sin\left[\frac{(\Phi_1 - \Phi_2)}{2}\right]} .$$

Hence

$$|\Delta r| = |r_1 - r_2| = \Delta h \frac{\cos\left[\Phi' - \frac{(\Phi_1 + \Phi_2)}{2}\right]}{\cos\left[\frac{(\Phi_2 - \Phi_1)}{2}\right]} . \qquad \text{-(4.6)}$$

Let Φ_P be the geocentric latitude of P, the point of intersection between the reference ellipsoid and its normal through B. Then

$$\hat{OPB} = \pi - \Phi' + \Phi_P \ .$$

Applying the sine rule to ΔOBP,

$$\frac{\sin (\Phi_P - \Phi')}{r_2} = \frac{\sin (\Phi' - \Phi_2)}{r_P} \ ,$$

where r_P is the geocentric distance of P. Hence

$$\frac{r_P}{r_2} \sin (\Phi_P - \Phi') = \sin (\Phi' - \Phi_2) \ . \qquad -(4.7)$$

Now [Bomford, 1980]

$$\Phi_P = \Phi' - \frac{e^2}{(2 - e^2)} \sin 2\Phi' + \frac{1}{2}\left[\frac{e^2}{(2 - e^2)}\right]^2 \sin 4\Phi' + \ldots,$$

where e (≈ 0.082) is the eccentricity of the reference ellipsoid. Hence $\Phi_P - \Phi' = O(e^2) \approx 0.0067$.

Also, using small angle approximations, equation (4.7) becomes

$$\frac{r_P}{r_2} (\Phi_P - \Phi') \approx (\Phi' - \Phi_2) \ ,$$

i.e.

$$\Phi_2 \approx \Phi' - \frac{r_P}{r_2} (\Phi_P - \Phi') \ .$$

Since $r_P < r_2$, the second term on the right hand side is negligible. A similar expression holds for Φ_1 and r_1. Thus $\Phi_1 \approx \Phi_2 \approx \Phi'$ and

$$\frac{\cos\left[\,\Phi' - \frac{(\Phi_1 + \Phi_2)}{2}\,\right]}{\cos\left[\frac{(\Phi_2 - \Phi_1)}{2}\right]} \approx 1,$$

as illustrated by Table (4.1), which shows this ratio calculated from every 100th crossover obtained from the SEASAT long arc spanning MJD43764 to MJD43770. The error incurred in the crossover differences as a result of approximation of the geodetic height differences to geocentric is given, from equation (4.6), by

$$\Delta h - \Delta r = \Delta h \left(1 - \frac{\cos\left[\,\Phi' - \frac{(\Phi_1 + \Phi_2)}{2}\,\right]}{\cos\left[\frac{(\Phi_2 - \Phi_1)}{2}\right]} \right).$$

Φ_1 /deg	Φ_2 /deg	Φ' /deg	Δh	ratio	$\lvert\Delta h - \Delta r\rvert$ /m
10.373	10.375	10.436	138.451	0.9999994	0.000080
-65.341	-65.341	-65.470	-44.308	0.9999975	0.000112
-61.668	-61.668	-61.811	-157.024	0.9999969	0.000487
52.743	52.744	52.908	77.118	0.9999959	0.000319
-52.748	-52.748	-52.912	77.796	0.9999959	0.000319
63.669	63.670	63.805	-48.902	0.9999972	0.000137
-20.234	-20.233	-20.344	42.852	0.9999981	0.000080
-61.667	-61.668	-61.811	-9.282	0.9999969	0.000029
71.927	71.928	72.028	29.206	0.9999985	0.000045
71.936	71.930	72.031	-37.674	0.9999985	0.000055
-29.062	-29.065	-29.210	68.624	0.9999967	0.000224
71.263	71.262	71.366	135.523	0.9999984	0.000220
56.313	56.311	56.469	-87.701	0.9999963	0.000328
52.744	52.745	52.910	58.263	0.9999959	0.000242
-63.674	-63.674	-63.809	-115.251	0.9999972	0.000321

Table (4.1)
Geocentric approximation to geodetic crossover residuals

Taken over all 1,547 residuals derived between the above dates, the maximum magnitude is less than 1 millimetre and 0.042% of the original geodetic value of

approximately 229.951m. Clearly the accuracy of the approximation is sufficient to allow the crossover difference residual equation (4.3) to be re-defined as

$$\Delta C_{12} = \Delta r\,(t_1) - \Delta r\,(t_2) \quad . \qquad \text{-(4.8)}$$

This definition shall be henceforth assumed. A crossover residual is therefore the difference between the radial errors. Thus differencing equation (3.44) at $t = t_1$ and $t = t_2$ will produce an analytical expression for a crossover difference residual. As for the radial error model, the expression is comprised of both gravitational and non-gravitational effects.

§ 4.3 Periodic Gravitational Crossover Difference Error

The purely periodic gravitational contribution to ΔC_{12} of equation (4.8) is given by the difference between the purely periodic gravitational contribution to the radial orbit error at the two crossover epochs, that is

$$\Delta C_{12}^{(p)} = \Delta r^{(p)}(t_1) - \Delta r^{(p)}(t_2) \ ,$$

where the $\Delta r^{(p)}(t_i)$, i=1,2 are expressed by all periodic terms of equation (3.44) of purely gravitational origin. Thus

$$\Delta C_{12}^{(p)} =$$

$$\sum_{k=-\ell max}^{\ell max} \sum_{m=0}^{\ell max} \left\{ A_{km} \left(\cos \dot{\Psi}_{km} t_1 - \cos \dot{\Psi}_{km} t_2 \right) + B_{km} \left(\sin \dot{\Psi}_{km} t_1 - \sin \dot{\Psi}_{km} t_2 \right) \right\} \qquad \text{-(4.9)}$$

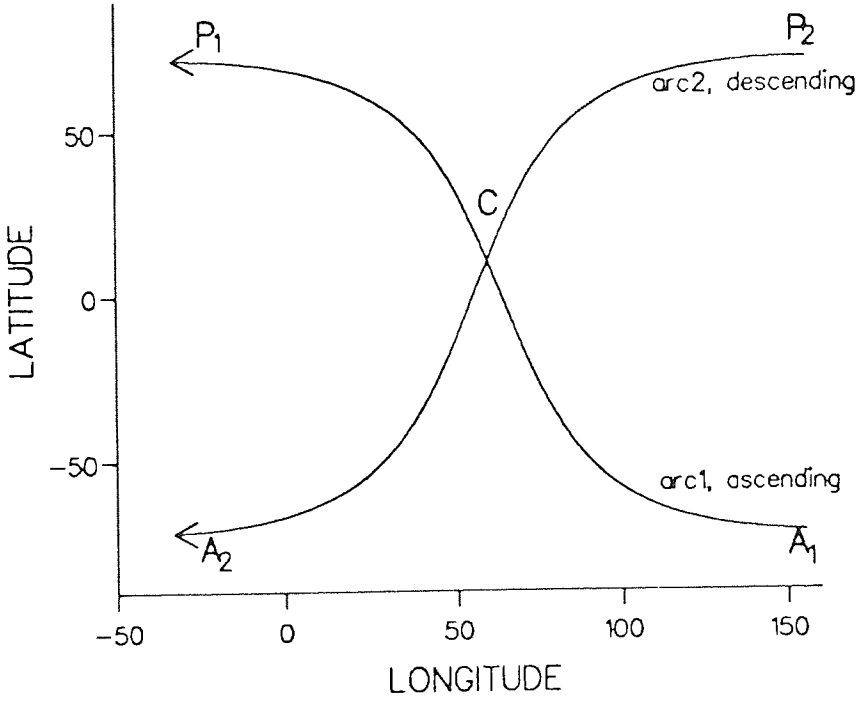

Figure (4.4)
Arc 1 and arc 2 intersect to form the crossover point, C

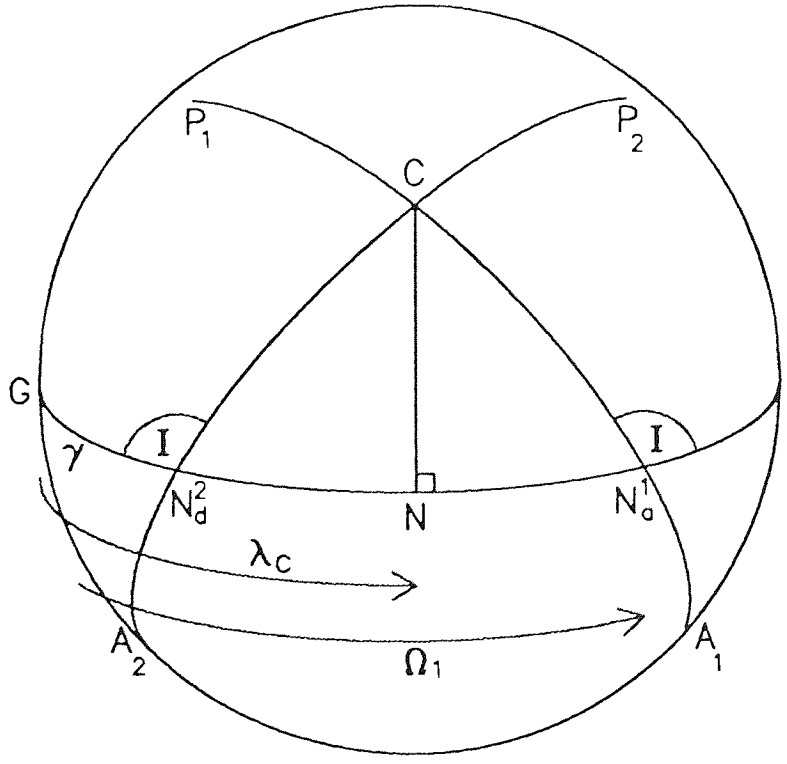

Figure (4.5)
Projection of crossover point of Figure (4.4) onto the Earth-fixed unit sphere

The altimetric satellites SEASAT and ERS-1 are in frozen orbits with perigee fixed at 90°. Thus the sub-satellite point corresponding to mean perigee is always at the point of maximum latitude, and apogee corresponds to the point of minimum, or maximum southern latitude, as shown in Figure (4.4) and Figure (4.5), in which P_i is the point on the ground-track of arc i at which the satellite is at perigee, A_i the point on the ground-track of arc i at which the satellite is at apogee, N_a^i and N_d^i the ascending and descending nodes of arc i, respectively, and G the point of intersection between the Greenwich meridian and the equator.

Let ω_i be the argument of perigee on arc i. Then

$$\omega_1 \approx \omega_2 \approx \frac{\pi}{2} \text{ radians.}$$

Now the inclination, I, can be considered fixed for a particular satellite. Hence

$$C\hat{N}_d^2 G = \pi - C\hat{N}_a^1 G = I .$$

Therefore, assuming a near circular orbit,

$$C N_d^2 = C N_a^1$$

and

$$P_2 C = C P_1$$

i.e.

$$M_2 = 2\pi - M_1 , \qquad -(4.10)$$

where M_i is the mean anomaly at C for arc i.

Equation (4.10) leads to the following fundamental results:

$$\cos M_2 = \cos (- M_1) = \cos M_1 \qquad -(4.11)$$

$$\sin M_2 = \sin (- M_1) = - \sin M_1 \qquad -(4.12)$$

Substituting $M_2 = - M_1$ into equation (4.9) and using equation (3.25) and equation (3.26) gives the purely periodic contribution to the crossover difference error due to gravity field mismodelling as

$$\Delta C_{12}^{(p)} = \sum_{k=-\ell max}^{\ell max} \sum_{m=0}^{\ell max}$$

$$\left\{ A_{km}\left(\cos\left[kM_1 + m\left(\Omega(t_1) - \theta_g(t_1)\right)\right] - \cos\left[-kM_1 + m\left(\Omega(t_2) - \theta_g(t_2)\right)\right]\right)\right.$$

$$\left. +B_{km}\left(\sin\left[kM_1 + m\left(\Omega(t_1) - \theta_g(t_1)\right)\right] - \sin\left[-kM_1 + m\left(\Omega(t_2) - \theta_g(t_2)\right)\right]\right)\right\}$$

-(4.13)

§ 4.4 Other Crossover Residual Contributions

Differencing each of the other radial orbit error effects given by equation (3.44) yields the other significant contributions to ΔC_{12}. Now, from equation (4.11), the 1 and 2 cycles per revolution cosine contributions cancel, as

$$\cos M_1 - \cos M_2 = \cos 2M_1 - \cos 2M_2 = 0.$$

By equation (4.12), the 1 cycle per revolution sine contribution is

$$c_2 [\sin M_1 - \sin M_2] = 2 c_2 \sin M_1. \qquad -(4.14)$$

Similarly the 2 cycles per revolution sine contribution is

$$2 c_4 \sin 2M_1 . \qquad -(4.15)$$

The constant term will cancel.

By equation (4.12), the secular-periodic sinM contribution is

$$c_6 [(t_1 - t_0) \sin M_1 - (t_2 - t_0) \sin M_2]$$

$$= c_6 [(t_1 - t_0) \sin M_1 + (t_2 - t_0) \sin M_1]$$

$$= c_6 (t_1 + t_2 - 2t_0) \sin M_1 \qquad \text{-(4.16)}$$

The effects modelled by terms (4.13), (4.14), (4.15) and (4.16) are due primarily to gravitational mismodelling. Other effects, due to drag and solar radiation pressure, are the secular-periodic cosine contribution which, using equation (4.11), is given by

$$c_5 [(t_1 - t_0) \cos M_1 - (t_2 - t_0) \cos M_2] = c_5 (t_1 - t_2) \cos M_1 \quad , \text{-(4.17)}$$

the secular-periodic sin2M contribution,

$$c_7 (t_1 + t_2 - 2t_0) \sin 2M_1 \quad , \qquad \text{-(4.18)}$$

and a secular contribution given by

$$\begin{cases} (t_1 - t_0^{(t_1)}) c_{NDAY(t_1)+7} - (t_2 - t_0^{(t_2)}) c_{NDAY(t_2)+7} - \sum_{k=NDAY(t_1)+7}^{NDAY(t_2)+6} c_k & \begin{matrix} NDAY(t_1) \\ \neq NDAY(t_2) \end{matrix} \\ c_{NDAY(t_1)+7} (t_1 - t_2) & \begin{matrix} NDAY(t_1) \\ = NDAY(t_2) \end{matrix} \end{cases} \qquad \text{-(4.19)}$$

As in the case of the radial error formula given by equation (3.44), an overall crossover difference error model is obtained by addition of all the above terms, (4.13) to (4.19). That is,

$$\Delta C_{12} = \sum_{k=-\ell max}^{\ell max} \sum_{m=0}^{\ell max}$$

$$\Big\{ A_{km} \Big(\cos\Big[kM_1 + m\big(\Omega(t_1) - \theta_g(t_1)\big)\Big] - \cos\Big[-kM_1 + m\big(\Omega(t_2) - \theta_g(t_2)\big)\Big] \Big)$$

$$+ B_{km} \Big(\sin\Big[kM_1 + m\big(\Omega(t_1) - \theta_g(t_1)\big)\Big] - \sin\Big[-kM_1 + m\big(\Omega(t_2) - \theta_g(t_2)\big)\Big] \Big) \Big\}$$

$$+ 2c_2 \sin M_1 + 2c_4 \sin 2M_1 + c_6 (t_1 + t_2 - 2t_0) \sin M_1 + c_5 (t_1 - t_2) \cos M_1 + c_7 (t_1 + t_2 - 2t_0) \sin 2M_1 +$$

$$\begin{cases} (t_1 - t_0^{(t_1)})\, c_{NDAY(t_1)+7} - (t_2 - t_0^{(t_2)})\, c_{NDAY(t_2)+7} - \sum_{k=NDAY(t_1)+7}^{NDAY(t_2)+6} c_k & \begin{matrix} NDAY(t_1) \\ \neq NDAY(t_2) \end{matrix} \\ c_{NDAY(t_1)+7} (t_1 - t_2) & \begin{matrix} NDAY(t_1) \\ = NDAY(t_2) \end{matrix} \end{cases}$$

§ 4.5 Unobservables and Linear Combinations

It is apparent that several periodic terms of the radial orbit error are unobservable in crossover residuals. The constant term will vanish along with all zonal (m = 0) cosine contributions. Thus an important consequence is that all purely periodic terms of zonal origin are unobservable in crossovers.

The least squares minimization of the crossover residuals described in chapter 5 involves the solution for each cosine and sine frequency coefficient A_{km}, B_{km} of equation (4.13). However, several frequency terms will be seen to be linear combinations of others, which leads to singularity of the normal equation matrix if an attempt is made to simultaneously estimate all coefficients of the combination.

Let the Earth-fixed longitude and latitude of the crossover point C of Figure (4.5) be λ_C and ϕ_C, respectively. Then

$$\lambda_C = \frac{1}{2}\left\{ GN_a^1 + GN_d^2 \right\}$$

$$= \frac{1}{2}\left\{ \left[\Omega(t_1) - \theta_g(t_1) \right] + \left[\Omega(t_2) + \pi - \theta_g(t_2) \right] \right\}$$

$$= \frac{1}{2}\left\{ \Phi(t_1) + \Phi(t_2) + \pi \right\} , \qquad -(4.20)$$

where $\Phi(t_i) = \Omega(t_i) - \theta_g(t_i)$, i = 1, 2.

Let N be the point of intersection between the meridian through C and the equatorial plane. Then

$$CN = \phi_C \qquad \text{and} \qquad N_a^1C = M_1 - \frac{3\pi}{2}.$$

Applying the cotangent rule to the spherical triangle N_a^1CN, in which

$$NN_a^1 = \Phi(t_1) - \lambda_C ,$$

$$\hat{CNN}_a^1 = \frac{\pi}{2} ,$$

and

$$\hat{NN}_a^1C = \pi - I$$

gives

$$\cot\left(M_1 - \frac{3\pi}{2}\right) \sin\left(\Phi(t_1) - \lambda_C\right) = \cot\left(\frac{\pi}{2}\right)\sin(\pi - I) + \cos\left(\Phi(t_1) - \lambda_C\right) \cos(\pi - I)$$

$\Rightarrow$

$$\tan\left(\Phi(t_1) - \lambda_C\right) = \tan\left(M_1 - \frac{3\pi}{2}\right) \cos(\pi - I) ,$$

$\therefore$

$$\tan\left\{ \frac{\Phi(t_1) - \Phi(t_2)}{2} + \frac{3\pi}{2} \right\} = \cot M_1 \cos I \ ,$$

using equation (4.20). That is

$$\tan M_1 \cot\left\{ \frac{\Phi(t_2) - \Phi(t_1)}{2} \right\} = \cos I \ . \qquad \text{-(4.21)}$$

Employing compound angle formulae, a particular k,m term of equation (4.13) is

$$\Delta C_{12}^{(p)}{}_{(k,m)} = 2 \sin\left\{ - kM_1 + m\left(\frac{\Phi(t_2) - \Phi(t_1)}{2}\right) \right\} \ x$$
$$\left\{ A_{km} \sin\left[m\left(\frac{\Phi(t_2) + \Phi(t_1)}{2}\right)\right] - B_{km} \cos\left[m\left(\frac{\Phi(t_2) + \Phi(t_1)}{2}\right)\right] \right\}.$$

Consider the term for which (k,m) = (1,1). That is

$$\Delta C_{12}^{(p)}{}_{(1,1)} = 2 \sin\left\{ - M_1 + \left(\frac{\Phi(t_2) - \Phi(t_1)}{2}\right) \right\} \ x$$
$$\left\{ A_{11} \sin\left(\frac{\Phi(t_2) + \Phi(t_1)}{2}\right) - B_{11} \cos\left(\frac{\Phi(t_2) + \Phi(t_1)}{2}\right) \right\}$$

-(4.22)

Now,

$$\sin\left\{ - M_1 + \left(\frac{\Phi(t_2) - \Phi(t_1)}{2}\right) \right\} =$$
$$- \sin M_1 \cos\left(\frac{\Phi(t_2) - \Phi(t_1)}{2}\right) + \cos M_1 \sin\left(\frac{\Phi(t_2) - \Phi(t_1)}{2}\right)$$

$$= \cos M_1 \sin\left(\frac{\Phi(t_2) - \Phi(t_1)}{2}\right)\left\{ 1 - \tan M_1 \cot\left(\frac{\Phi(t_2) - \Phi(t_1)}{2}\right) \right\}$$

Therefore, by equation (4.21),

$$\sin\left\{ - M_1 + \left(\frac{\Phi(t_2) - \Phi(t_1)}{2}\right)\right\} = \cos M_1 \sin\left(\frac{\Phi(t_2) - \Phi(t_1)}{2}\right)\{ 1 - \cos I \}.$$

Substituting this into equation (4.22) gives

$$\Delta C^{(p)}_{12(1,1)} = 2 \sin\left(\frac{\Phi(t_2) - \Phi(t_1)}{2}\right)\cos M_1 \{ 1 - \cos I \} \times \left\{ A_{11} \sin\left(\frac{\Phi(t_2) + \Phi(t_1)}{2}\right) - B_{11} \cos\left(\frac{\Phi(t_2) + \Phi(t_1)}{2}\right) \right\}. \quad -(4.23)$$

Similarly for the (k,m) = (-1,1) term yields

$$\Delta C^{(p)}_{12(-1,1)} = 2 \sin\left(\frac{\Phi(t_2) - \Phi(t_1)}{2}\right)\cos M_1 \{ 1 + \cos I \} \times \left\{ A_{-11} \sin\left(\frac{\Phi(t_2) + \Phi(t_1)}{2}\right) - B_{-11} \cos\left(\frac{\Phi(t_2) + \Phi(t_1)}{2}\right) \right\}. \quad -(4.24)$$

Hence, by equation (4.23) and equation (4.24),

$$\Delta C^{(p)}_{12(1,1)A} = \left(\frac{1 - \cos I}{1 + \cos I}\right)\Delta C^{(p)}_{12(-1,1)A}$$

and

$$\Delta C^{(p)}_{12(1,1)B} = \left(\frac{1 - \cos I}{1 + \cos I}\right)\Delta C^{(p)}_{12(-1,1)B},$$

where $\Delta C^{(p)}_{12(k,m)A}$ and $\Delta C^{(p)}_{12(k,m)B}$ represent terms associated with A_{km} and B_{km}, respectively, i.e. $\Delta C^{(p)}_{12(k,m)} = A_{km}\Delta C^{(p)}_{12(k,m)A} + B_{km}\Delta C^{(p)}_{12(k,m)B}$.

Thus the (k,m) = (1,1), (-1,1) frequency terms are mutually linearly dependent and the corresponding coefficients cannot all be simultaneously resolved.

Table (4.2) verifies the linear combinations discussed when applied to the crossover residuals examined in section §4.3 and Table (4.1). The arguments of the (k,m) = (1,1) and (k,m) = (-1,1) frequency terms of equation (4.13) were calculated for every 100th crossover residual. The inclination of SEASAT remained steady at around 108.0^{o}, so that

$$\frac{1 - \cos I}{1 + \cos I} \approx \frac{1 - \cos 108.0^{o}}{1 + \cos 108.0^{o}} \approx 1.894,$$

the value about which the ratio of the (k,m) = (1,1) to (k,m) = (-1,1) arguments remains approximately constant.

Other such combinations exist for the (k,m) = (-2,2), (0,2), (2,2) frequencies and for (k,m) = (-2,1), (0,1), (2,1). In order to overcome the problem and recover the unobservable and linearly dependent combinations of frequency terms, a number of direct radial height measurements must be included [Sandwell et al.,1986].

(1,1) cos	(1,1) sin	(-1,1) cos	(-1,1) sin	(1,1)/ (-1,1) cos	(1,1)/ (-1,1) sin
0.341	0.364	0.185	0.198	1.893	1.893
-1.525	-0.887	-0.809	-0.470	1.886	1.886
-1.699	0.921	-0.901	0.488	1.886	1.886
-1.713	-0.996	-0.902	-0.525	1.899	1.899
1.669	-1.068	0.877	-0.561	1.903	1.903
-1.842	0.241	-0.977	0.128	1.885	1.885
0.118	-0.939	0.063	-0.497	1.890	1.890
-1.860	0.529	-0.977	0.278	1.905	1.905
-0.119	-0.147	-0.059	-0.073	2.015	2.015
-0.173	0.078	-0.086	0.039	2.014	2.014
1.106	-0.709	0.579	-0.371	1.912	1.912
0.703	0.223	0.366	0.116	1.923	1.923
1.906	0.606	1.011	0.321	1.886	1.886
-1.840	-0.736	-0.969	-0.387	1.899	1.899
0.366	-1.822	0.193	-0.965	1.889	1.889

Table (4.2)
Linear combinations of the (k,m)=(1,1), (k,m)=(-1,1) frequency terms

§ 4.6 Attainment of the Crossover Data Set

To construct the crossover data sets used in the analyses, the calculated crossover differences were found by first separating the calculated ephemeris into its northern and southern hemisphere arcs, then comparing each arc with all others in the same hemisphere. A geometrical method was applied to achieve an initial estimate of the longitude of each crossover point, from which approximations for the epochs were derived. These were then refined using Lagrangian interpolation.

Consider one such crossover for which approximate positions P_1 and P_2 on arc 1 and arc 2, respectively, have been estimated by this process. Suppose P_1 is the point (λ_1,ϕ_1), P_2 is the point (λ_2,ϕ_2) and the epochs at which the satellite is at P_1 and P_2 are t_{P1} and t_{P2}, respectively. Let C be the true position of the crossover point sought, at the position (λ,ϕ). Assuming that P_1 and P_2 are sufficiently close estimates of C that the variations of the longitude and latitude of the ground-track with time over the distances CP_1 and CP_2 can be considered constant, then [Rowlands,1981]

$$\frac{d\lambda_i}{dt} = \frac{\lambda_i - \lambda}{t_{Pi} - t_i} \quad , i = 1,2,$$

where t_1, t_2 are the epochs at which the satellite is at C along arc 1 and arc 2, respectively. Hence,

$$\lambda = \lambda_i - (t_{Pi} - t_i)\frac{d\lambda_i}{dt} \quad ,$$

where i = 1 or i = 2.

Equating the two expressions for i = 1 and i = 2 gives

$$\lambda_1 - (t_{P1} - t_1)\frac{d\lambda_1}{dt} = \lambda_2 - (t_{P2} - t_2)\frac{d\lambda_2}{dt} \quad ,$$

i.e.

$$(t_{P1} - t_1)\frac{d\lambda_1}{dt} - (t_{P2} - t_2)\frac{d\lambda_2}{dt} = \lambda_1 - \lambda_2 \quad . \qquad -(4.25)$$

Similarly for the latitudes,

$$(t_{P1} - t_1)\frac{d\phi_1}{dt} - (t_{P2} - t_2)\frac{d\phi_2}{dt} = \phi_1 - \phi_2 \quad . \qquad -(4.26)$$

Expressing (4.25) and (4.26) in matrix form,

$$\begin{bmatrix} \frac{d\lambda_1}{dt} & -\frac{d\lambda_2}{dt} \\ \frac{d\phi_1}{dt} & -\frac{d\phi_2}{dt} \end{bmatrix} \begin{bmatrix} t_{P1} - t_1 \\ t_{P2} - t_2 \end{bmatrix} = \begin{bmatrix} \lambda_1 - \lambda_2 \\ \phi_1 - \phi_2 \end{bmatrix},$$

i.e.

$$\begin{bmatrix} t_1 \\ t_2 \end{bmatrix} = \begin{bmatrix} t_{P1} \\ t_{P2} \end{bmatrix} - \begin{bmatrix} \frac{d\lambda_1}{dt} & -\frac{d\lambda_2}{dt} \\ \frac{d\phi_1}{dt} & -\frac{d\phi_2}{dt} \end{bmatrix}^{-1} \begin{bmatrix} \lambda_1 - \lambda_2 \\ \phi_1 - \phi_2 \end{bmatrix}.$$

Thus new estimates are made for t_1 and t_2, and hence for the latitude and longitude of C. The process is repeated until convergence.

On finding accurate locations, interpolation in the ephemeris at the epochs leads to a value for the crossover height, which is differenced at both times to produce the calculated crossover height difference. The observed crossover height differences are similarly determined by interpolation in the GDR altimetric height measurements, applying the appropriate corrections as described in chapter 2, at the same epochs. Subtraction of the two measurements yields the crossover height residual.

Altimeters take a measurement over the area of the footprint on the surface beneath. Measurements over land are of downgraded accuracy, if available at all and

precise comparison of the waveform is essential. Although altimetry over land is currently under investigation by several authors [Katsgris and Dixon,1990], the methodology is still at a preliminary stage and in this study was discounted. The land altimetry has been filtered out of the SEASAT data set. Observations taken over deserts or inland lake regions could be used, but since the number of such crossovers is small relative to the total number over the oceans, their inclusion would have only a marginal effect at best.

Another improvement in the accuracy of the data set is made by the elimination of spurious data points. Some individual residuals are unusually large, especially those due to the altimeter readings being taken over sea ice. A large proportion of such points are found near to the southern extremes of latitude, as discussed later in section §6.11. To diminish the problem, any crossover residuals taking a numerical value greater than a particular threshold magnitude were discarded.

For the ERS-1 simulations, in which a derived ephemeris is assumed to represent the true satellite orbit, a simulated set of observed crossover differences was constructed in a manner analogous to the calculated values and a continental global map was computed to eliminate any crossover points deemed to have fallen over land.

CHAPTER 5

SOFTWARE SUMMARY

The theory and methods behind some of the software employed in the research are outlined in this chapter. All programs are written in FORTRAN and applied using a VAX 8650 mainframe computer.

§ 5.1 Radial Orbit Error Recovery

The possibility of global radial orbit error reduction has been investigated under a number of different circumstances. This is achieved by the creation of software for the simultaneous retrieval of all coefficients contributing to equation (3.44). A least squares fit is carried out through a set of crossover residual data supplemented by direct radial height measurements in order to produce a solution for each coefficient.

Equation (4.10) is applied to estimate the mean anomaly of the second epoch and the assumptions of a single revolution of the right ascension per year in the case of the Sun-synchronous ERS-1 orbits and a near twice annual rate for SEASAT are made in order to calculate the right ascension. The Greenwich Mean Sidereal angle is calculated at each epoch and thus the angular arguments of all significant periodic terms are determined for every residual. Hence estimates are made for all coefficients of the radial orbit error formula.

Measures of the accuracy and of the ill-conditioning of the overall solution are made by determination of the standard error of each coefficient and of the eigenvalues of the inverse normal equation matrix, respectively.

§ 5.2 Orbit Determination

The satellite ephemerides determined throughout the following chapters have been generated using the satellite analysis package of programs currently in use at Aston University, known as SATAN-A.

Orbits are computed by integrating the equation of motion of the satellite using an 8th order Gauss Jackson numerical method, beginning from an initial estimate of the position and velocity of the spacecraft. A least squares differential correction procedure is applied in order to minimize the discrepancies between the derived ranges and observations of ranges from laser ranging stations, by solving for new estimates of the starting vector and drag and solar reflectivity coefficients. Another orbit is generated from the updated parameters and the process is repeated in an iterative procedure until no more significant improvement is observed in terms of fitting the calculated ephemeris to the observational tracking data.

The equation of motion of a satellite is given by

$$\ddot{\underline{x}} = -\frac{\mu \underline{x}}{r^3} + \underline{F},$$

where $\underline{x}$ is the position of the spacecraft in an inertial reference frame and r is its geocentric distance.

The first term on the right hand side occurs from the inverse square law of attraction due to the gravitational field of the Earth and $\underline{F}$ comprises all other forces acting on the satellite. Several parameters are included in $\underline{F}$ and modelled within the orbit generation program.

The non-spherical geopotential components create a gravitational force on the satellite which is expressed in terms of the coefficients of the gravity field model being used.

Retarding drag forces due to air resistance of the atmosphere are given by equation (3.34) and a solar radiation pressure force arising from the bombardment of the spacecraft by photons incident both directly from the Sun and indirectly after reflection from the surface of the Earth is modelled by equation (3.42) with $F^{(SRP)}$ and C_R replacing $\Delta F^{(SRP)}$ and ΔC_R, respectively.

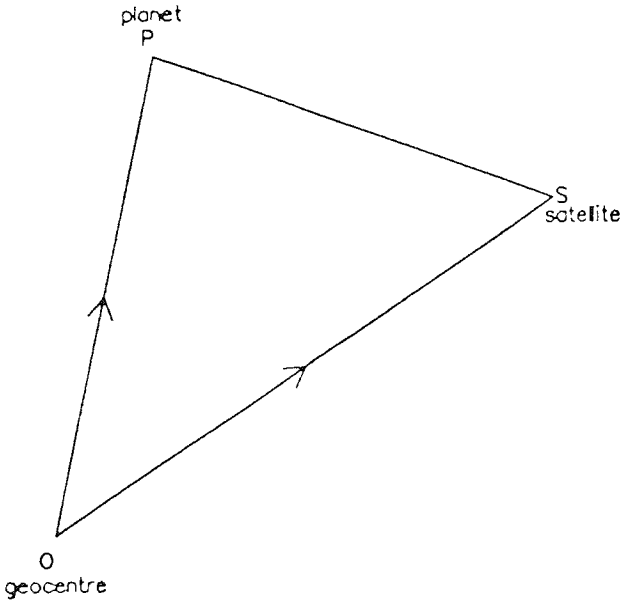

Figure (5.1)
Third body gravitational attraction configuration

The presence of other planets within the solar system create gravitational third body attraction forces, $\underline{F}_{TBA}$, given for each in terms of the relative distances between the planet, Earth and satellite by the equation [Brouwer and Clemence,1961]

$$\underline{F}_{TBA} = G M_P \left\{ \frac{(\underline{OP} - \underline{OS})}{SP^3} - \frac{\underline{OP}}{OP^3} \right\},$$

where O, S, P are defined by Figure (5.1), M_P is the mass of the particular planet concerned and G is the Universal Gravitational Constant. Venus, Mars, Jupiter and Saturn have significant effects, as well as the Sun and Moon. Finally, solid Earth and ocean tidal forces are included. These are found from existing standard sources [Lambeck,1977].

Thus $\underline{F}$ is dependent on a number of parameters, several of which may be corrected for during the least squares differential procedure that immediately follows the orbit calculation. The corrections are determined in a manner similar to that in which the constant radial, along-track and orbit normal corrections are derived during the short arc determination described later in section §6.4, except that for the long arc orbit determination, the laser ranges are minimized with respect to the parameters that affect the orbit described above. For the SEASAT studies and the ERS-1 orbits derived from laser ranging data, these were the six position and velocity components of the initial state vector, daily drag coefficients and a solar reflectivity constant. The simulations of ERS-1 did not involve drag and solar radiation corrections as no data was available pertaining to the atmospheric density or incident solar radiation and the simulations are purely gravitational.

§ 5.3 Spectral Analyses

Several spectral analyses of residual data sets are illustrated throughout. Frequency signatures present can be estimated by separating out and determining each individual term. Ignoring linear and secular-periodic effects, it can be reasonably assumed that a radial residual at epoch t can be expressed by [Ponman,1979]

$$\Delta r\,(t) \;=\; N(t) + \sum_{m=1}^{mmax} \left\{ \;\alpha_m \cos\left(2\pi \upsilon^{(m)}\, t \right) + \beta_m \sin\left(2\pi \upsilon^{(m)}\, t \right) \right\} \qquad \text{-(5.1)}$$

where $N(t)$ is random noise, $\upsilon^{(m)}$ are the frequencies of the periodic terms present in the data, mmax is the maximum significant value of m and α_m and β_m are the amplitudes of the terms required for solution.

In the case of the 43 revolution/3 day repeat orbits of SEASAT and ERS-1, m_{max} is taken as 107 and for the ERS-1 simulations of the 501 revolution/35 day repeat orbit, $m_{max} = 1072$. If υ' is the reciprocal of the number of revolutions of the Earth during one repeat period, then $\upsilon^{(m)}$ is given by

$$\upsilon^{(m)} = m\,\upsilon' = \begin{cases} \frac{m}{43} & \text{SEASAT and ERS-1 43 rev/3 day repeat orbits} \\ \frac{m}{501} & \text{ERS-1 501 rev/35 day repeat orbit} \end{cases}$$

Suppose there are NRES residuals in the data set and t_n is the epoch of the nth residual. Let

$$A(\upsilon) = \frac{\sum_{n=1}^{NRES} \Delta r\,(t_n) \cos\,(2\pi\upsilon t_n)}{\sum_{n=1}^{NRES} \cos^2(2\pi\upsilon t_n)}. \qquad -(5.2)$$

Then, from equation (5.1),

$$A(\upsilon) = \sum_{n=1}^{NRES} \Big\{ N(t_n)\cos(2\pi\upsilon t_n) + \alpha_1 \cos(2\pi\upsilon^{(1)}t_n)\cos(2\pi\upsilon t_n) + \ldots + \alpha_{mmax} \cos(2\pi\upsilon^{(mmax)}t_n)\cos(2\pi\upsilon t_n) + \beta_1 \sin(2\pi\upsilon^{(1)}t_n)\cos(2\pi\upsilon t_n) + \ldots + \beta_{mmax} \sin(2\pi\upsilon^{(mmax)}t_n)\cos(2\pi\upsilon t_n) \Big\} \Big/ \sum_{n=1}^{NRES} \cos^2(2\pi\upsilon t_n) \qquad -(5.3)$$

Taken over all NRES residuals, for any particular frequency υ, it can be assumed that

$$\overline{\cos^2(2\pi\upsilon t_n)} \approx \frac{1}{2},$$

i.e.

$$\sum_{n=1}^{NRES} \cos^2(2\pi\upsilon t_n) \approx \frac{N}{2} \quad . \qquad -(5.4)$$

Also, in general,

$$\overline{\cos(X)\cos(Y)} = \frac{1}{2}\left\{ \overline{\cos(X+Y)} + \overline{\cos(X-Y)} \right\} \approx \begin{cases} 0 & X \neq Y \\ \frac{1}{2} & X = Y \end{cases} ,$$

i.e.

$$\sum_{n=1}^{NRES} \cos(X)\cos(Y) \approx \begin{cases} 0 & X \neq Y \\ \frac{N}{2} & X = Y \end{cases} . \qquad -(5.5)$$

Applying equations (5.4) and (5.5) to equation (5.3) and assuming $\overline{N(t_n)} \approx 0$ gives

$$A(\upsilon) \approx \begin{cases} 0 & \upsilon \neq \upsilon^{(m)} \\ \alpha_m & \upsilon = \upsilon^{(m)} \end{cases} ,$$

with a similar expression holding for $B(\upsilon)$ and β_m, where $B(\upsilon)$ is given by equation (5.2) with sines replacing the cosine terms.

Hence $A(\upsilon^{(m)})$ and $B(\upsilon^{(m)})$ are estimates of the coefficients α_m and β_m, respectively. These expressions are derived from the radial residuals to produce the final spectrum of amplitudes given for each frequency $\upsilon^{(m)}$ by

$$P(\upsilon^{(m)}) = \sqrt{A(\upsilon^{(m)})^2 + B(\upsilon^{(m)})^2} \quad .$$

The theory so far has been carried out assuming a data set of radial residuals. However, an extension of the method is now developed to accommodate spectral analyses of crossover residuals, for use during this study.

It is assumed that each of the two radial residuals that make up a crossover can be expressed in the form of equation (5.1). The ith crossover residual, ΔC_i, is given by the difference between the two at each crossover epoch t_{i1} and t_{i2}. That is,

$$\Delta C_i = [N(t_{i1}) - N(t_{i2})] + \sum_{m=1}^{mmax} \{ \alpha_m [\cos (2\pi\upsilon^{(m)} t_{i1}) - \cos (2\pi\upsilon^{(m)} t_{i2})] + \beta_m [\sin (2\pi\upsilon^{(m)} t_{i1}) - \sin (2\pi\upsilon^{(m)} t_{i2})] \},$$

-(5.6)

where α_m and β_m are the amplitudes of the frequency terms as before. Solving for α_m and β_m using crossover residuals will produce an estimate of the power spectrum from crossover data. Let

$$A(\upsilon) = \frac{\sum_{n=1}^{NRES} \Delta C_n \{ \cos (2\pi\upsilon t_{n1}) - \cos (2\pi\upsilon t_{n2}) \}}{\sum_{n=1}^{NRES} \{ \cos^2(2\pi\upsilon t_{n1}) + \cos^2(2\pi\upsilon t_{n2}) \}}.$$

Then, by equation (5.6),

$$\begin{aligned} A(\upsilon) = & \sum_{n=1}^{NRES} \{ [N(t_{n1}) - N(t_{n2})] \left(\cos(2\pi\upsilon t_{n1}) - \cos(2\pi\upsilon t_{n2}) \right) \\ & + \alpha_1 [\cos (2\pi\upsilon^{(1)} t_{n1}) - \cos (2\pi\upsilon^{(1)} t_{n2})] \left(\cos(2\pi\upsilon t_{n1}) - \cos(2\pi\upsilon t_{n2}) \right) + \ldots \\ & + \alpha_{mmax} [\cos (2\pi\upsilon^{(mmax)} t_{n1}) - \cos (2\pi\upsilon^{(mmax)} t_{n2})] \\ & \qquad \times \left(\cos(2\pi\upsilon t_{n1}) - \cos(2\pi\upsilon t_{n2}) \right) \\ & + \beta_1 [\sin (2\pi\upsilon^{(1)} t_{n1}) - \sin (2\pi\upsilon^{(1)} t_{n2})] \left(\cos(2\pi\upsilon t_{n1}) - \cos(2\pi\upsilon t_{n2}) \right) + \ldots \\ & + \beta_{mmax} [\sin (2\pi\upsilon^{(mmax)} t_{n1}) - \sin (2\pi\upsilon^{(mmax)} t_{n2})] \\ & \qquad \times \left(\cos(2\pi\upsilon t_{n1}) - \cos(2\pi\upsilon t_{n2}) \right) \} \\ & / \sum_{n=1}^{NRES} \{ \cos^2(2\pi\upsilon t_{n1}) + \cos^2(2\pi\upsilon t_{n2}) \} \end{aligned}$$

From equation (5.5) and since for all n, $t_{n1} \neq t_{n2}$,

$$\sum_{m=1}^{mmax} \alpha_m \cos(2\pi\upsilon^{(m)}t_{n1}) \cos(2\pi\upsilon t_{n2}) \approx \sum_{m=1}^{mmax} \alpha_m \cos(2\pi\upsilon^{(m)}t_{n2}) \cos(2\pi\upsilon t_{n1}) \approx 0$$

for all υ.

Hence the only non-zero terms remaining are given by

$$A(\upsilon^{(m)}) \approx \frac{\sum_{n=1}^{NRES} \alpha_m \{ \cos^2(2\pi\upsilon^{(m)}t_{n1}) + \cos^2(2\pi\upsilon^{(m)}t_{n2})\}}{\sum_{n=1}^{NRES} \{ \cos^2(2\pi\upsilon^{(m)}t_{n1}) + \cos^2(2\pi\upsilon^{(m)}t_{n2})\}},$$

i.e.

$$A(\upsilon^{(m)}) \approx \alpha_m .$$

Similarly, $B(\upsilon^{(m)}) \approx \beta_m$, where

$$B(\upsilon) = \frac{\sum_{n=1}^{NRES} \Delta C_n \left\{ \sin (2\pi\upsilon t_{n1}) - \sin (2\pi\upsilon t_{n2}) \right\}}{\sum_{n=1}^{NRES} \left\{ \sin^2(2\pi\upsilon t_{n1}) + \sin^2(2\pi\upsilon t_{n2}) \right\}}.$$

Hence calculation of $A(\upsilon^{(m)})$ and $B(\upsilon^{(m)})$ for each frequency $\upsilon^{(m)}$ produces estimates of α_m and β_m and the power, $P(\upsilon^{(m)})$, can be deduced for each term as for the radial residuals. Unobservable frequency terms will not contribute to the power spectra as no crossover data will be present at those frequencies, a fact demonstrated by crossover spectral analyses depicted within this study, derived from the above analysis.

CHAPTER 6

SEASAT ANALYSIS

The radial error reduction procedure developed in the preceding chapters is now applied to SEASAT, in order to demonstrate the validity of the method. Crossover observations derived from SEASAT altimetry are employed and problems encountered with the data set discussed. The concept of arc aggregates is introduced and applied to successive six day orbits.

§ 6.1 SEASAT Mission

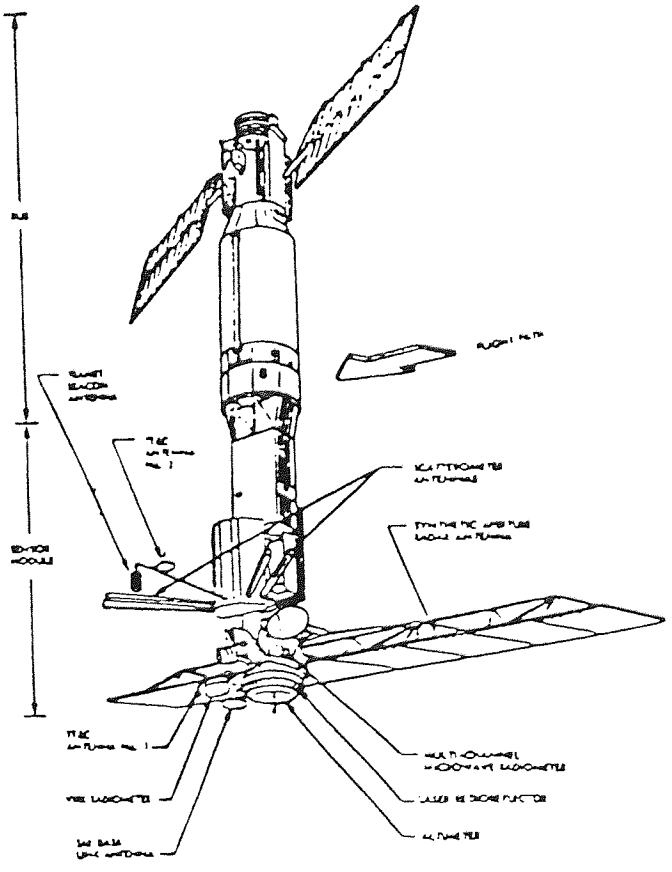

Figure (6.1)
SEASAT

On June 16th, 1978, SEASAT was launched by NASA to become the first satellite entirely devoted to the study of the oceans of the world. As shown in Figure (6.1), it carried on board five main instruments for use in measuring atmospheric and oceanographic phenomena, including a radar altimeter, the data from which is of most interest here.

SEASAT initially performed a near 17 day repeat period, until being manoeuvred into its 3 day repeat orbit on September 10th, 1978. On October 9th, a disastrous electrical power failure occurred, terminating its operational lifetime months earlier than anticipated. Throughout the last month of operation, SEASAT performed a near perfect repeat orbit with negligible drift of the ground-track between successive points 43 revolutions apart. Altimetric readings were taken approximately every second, so that much useful information has still been gathered and a good global coverage was achieved. This is shown in Figure (6.2), which displays the derived ground-track for the three days from MJD43764 to MJD43767.

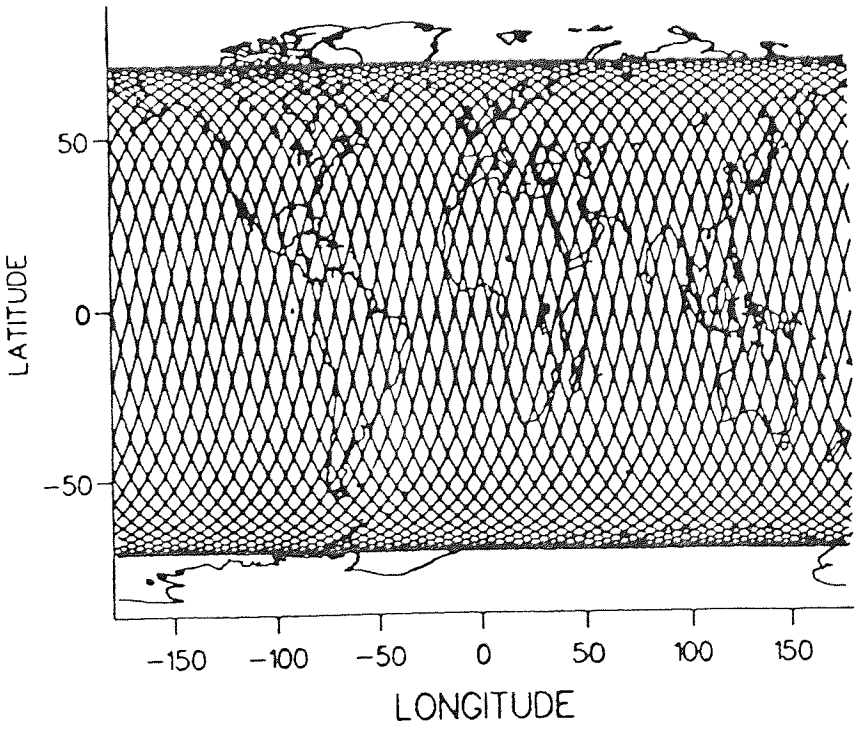

Figure (6.2)
SEASAT 3-day repeat orbit ground-track

The data analysed is that returned between 13th September (MJD43764) and 1st October (MJD43782), during which time SEASAT performed six full repeat cycles. Values for the eccentricity of the near circular orbit, semi-major axis and inclination were approximately 0.001, 7163km and 108°, respectively. Its repeat period was approximately 3.008859 days in which time it performed 43 complete revolutions of the Earth.

Before proceeding to analyse real observational data, it is necessary to establish the credibility of the method. An initial investigation is made here to show that the coefficients of equation (3.44) can be retrieved with reasonable certainty whilst approximating the radial orbit error due to atmospheric density mismodelling by daily linear drag coefficients.

§ 6.2 Non-Gravitational Solution

A non-gravitational solution has been attempted. A SEASAT ephemeris was converged between the dates MJD43770 and MJD43776 under the influence of the GEM-T1 gravity field, using all existing laser ranging data. The CIRA72 model [Jacchia,1972] was assumed to represent the atmospheric density. A second ephemeris, also using the GEM-T1 field, was generated between the same dates, this time with the MSIS83A atmospheric density model [Hedin,1983]. The radial differences at each common epoch between the two arcs have been derived over the region of study and are plotted in Figure (6.3). The differences are due entirely to non-gravitational causes since both arcs were generated using the same gravity field. Thus, eliminating all purely gravitational contributions, from equation (3.44), the radial orbit difference between the two arcs at any epoch t, where $t \in$ [MJD43770,MJD43776], is given by

$$\Delta r\,(t) = a_0 + a_1\,\cos M + a_2\,\sin M + a_3\,\cos 2M + a_4\,\sin 2M + a_5\,(t - t^*)\cos M$$

$$+ a_6\,(t - t^*)\sin M + a_7\,(t - t^*)\sin 2M + a_{NDAY(t)+7}\,(t - t_0^{(t)}) + \left[\begin{array}{c} \sum_{k=8}^{NDAY(t)+6} a_k \\ 0 \end{array}\right]_{NDAY(t)=1}^{NDAY(t)>1}$$

-(6.1)

where a_0, ..., $a_{NDAY(t)+7}$ are the constant coefficients to be found and t^* is a fixed epoch within the arc.

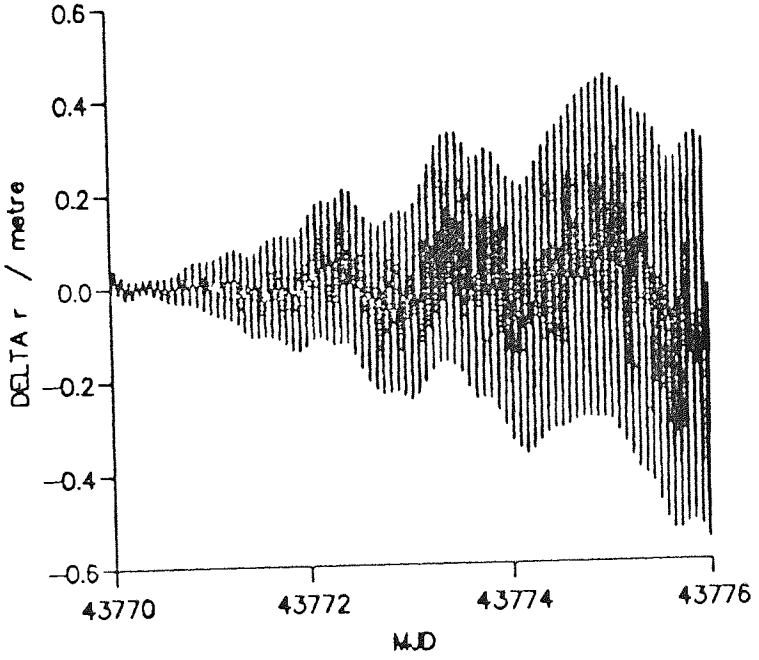

Figure (6.3)
Radial differences between orbits generated from CIRA72 and MSIS83A atmospheric density models

A set of crossover differences was derived for each arc in turn by the method described in section §4.6. The epochs of the crossover points will be approximately the same according to both sets. Consider a particular crossover, the earlier epoch of which is t_1 and the later t_2. Then, if the subscripts CIRA and MSIS represent values

associated with the arcs derived from the CIRA72 and MSIS83A density models, respectively, from equation (4.8) the crossover difference residuals are given by

$$\Delta C_{MSIS} = [\, r^{OBS}(t_1) - r_{MSIS}(t_1) \,] - [\, r^{OBS}(t_2) - r_{MSIS}(t_2) \,] \qquad -(6.2)$$

and

$$\Delta C_{CIRA} = [\, r^{OBS}(t_1) - r_{CIRA}(t_1) \,] - [\, r^{OBS}(t_2) - r_{CIRA}(t_2) \,] , \qquad -(6.3)$$

where $r^{OBS}(t_i)$ is the observed geocentric distance at time (t_i), i = 1,2.

Subtracting equation (6.3) from equation (6.2) gives

$$\Delta C_{MSIS} - \Delta C_{CIRA} = [\, r_{CIRA}(t_1) - r_{MSIS}(t_1) \,] - [\, r_{CIRA}(t_2) - r_{MSIS}(t_2) \,] . \qquad -(6.4)$$

If the crossover difference residuals according to each separate arc are differenced, then equation (6.4) is analogous to equation (4.8), where the CIRA72 derived arc can be considered as an observed ephemeris and the MSIS83A derived arc the calculated ephemeris. Equation (6.1) is an expression for non-gravitational radial orbit error and equation (6.4) can be re-written as

$$\Delta C = \Delta r\,(t_1) - \Delta r\,(t_2)$$

where $\Delta r\,(t_i)$, i = 1,2 is as in equation (6.1) and

$$\Delta C = \Delta C_{MSIS} - \Delta C_{CIRA} .$$

Each crossover residual was differenced in this way and a data set comprising 2,849 crossovers was obtained. From equation (6.4) and using equation (6.1), each is given by

$$\Delta C = 2\, a_2 \sin M + 2\, a_4 \sin 2M + a_5 (t_1 - t_2) \cos M + a_6 (t_1 + t_2 - 2\, t^{*}) \sin M + a_7 (t_1 + t_2 - 2\, t^{*}) \sin 2M +$$

$$\left[(t_1 - t_0^{(t_1)})\, a_{NDAY(t_1)+7} - (t_2 - t_0^{(t_2)})\, a_{NDAY(t_2)+7} - \sum_{k=NDAY(t_1)+7}^{NDAY(t_2)+6} a_k \right]_{\neq NDAY(t_2)}^{NDAY(t_1)}$$

$$a_{NDAY(t_1)+7}\,(t_1 - t_2)\Big]_{=NDAY(t_2)}^{NDAY(t_1)}$$

The a_0, a_1 and a_3 coefficients, associated with the constant, cosM and cos2M terms, respectively, are thus unobservable in the crossover data set. No deficient linear combination of coefficients exist since those are caused by gravitational effects. Figure (6.4) and Figure (6.5) show the spectral analyses of the radial differences of Figure (6.3) and the crossover data, respectively. The main aspect of Figure (6.4) is the large 1 cycle per revolution signature due to the cosM and, to a lesser extent, sinM coefficients of equation (6.1). Although the cosM term cancels out of the crossover differences and is not present in Figure (6.5), there is a significant purely periodic term of frequency 1 cycle per revolution within the radial error due to the sinM contribution. Additional direct radial heights need to be included for the resolution of the cosM coefficient.

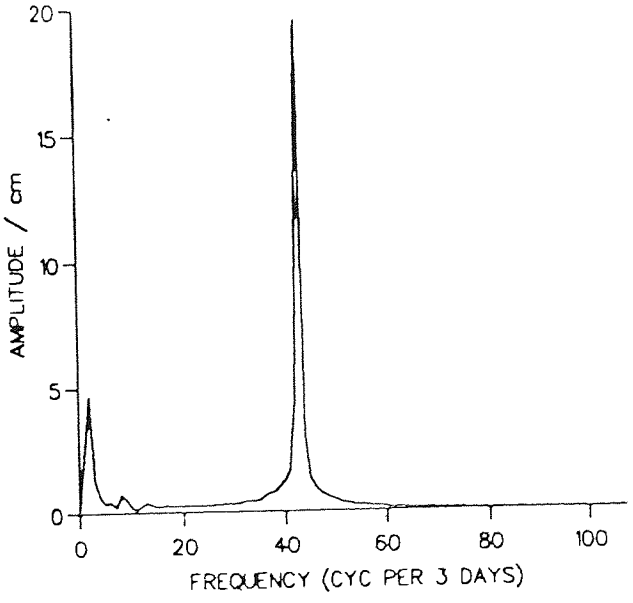

Figure (6.4)
Spectral analysis of radial differences of Figure (6.3)

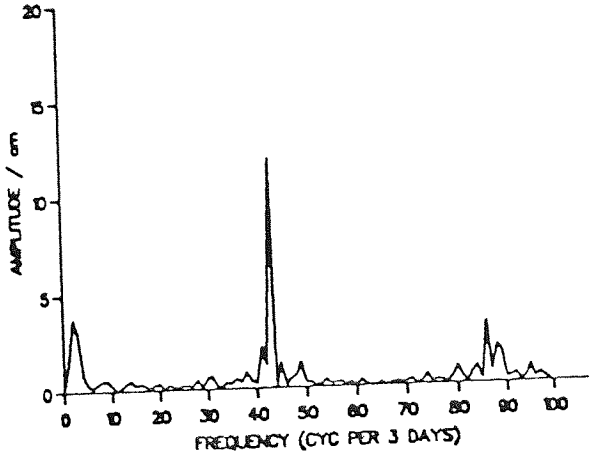

Figure (6.5)
Spectral analysis of crossover differences generated between orbits derived from CIRA72 and MSIS83A atmospheric density models

The direct radial measurements required were found by selecting a particular epoch, t_{ep}, say, and interpolating linearly in each of the two ephemerides, to find the respective radial distances of each. These were then differenced such that

$$\Delta r(t_{ep}) = r_{CIRA}(t_{ep}) - r_{MSIS}(t_{ep})$$

to produce the required radial correction. A wide spread of epochs and mean anomaly, which was also derived by interpolation in one of the ephemerides, was chosen, as shown in Table (6.1).

MJD	Δr /m	s.e./m	M/deg
43770.381597	-0.005	0.05	197.1
43771.796181	-0.036	0.05	274.9
43773.560764	0.278	0.05	353.3
43774.690972	0.349	0.05	48.0
43775.196528	-0.158	0.05	129.1

Table (6.1)
Direct radial measurements for SEASAT non-gravitational analysis

A standard error of 5cm was assigned to each direct measurement, compared with 50cm for each crossover residual, corresponding to weights of 400 and 4, respectively, to reflect the relative accuracies of the data types and the fourteen coefficients of equation (6.1) were determined. The results are displayed in Table (6.2), Figure (6.6) and Figure (6.7). The square roots of the eigenvalues of the inverse normal equation matrix give a guide as to how accurately the system of coefficients as a whole has been determined and represent the combined effects of the individual standard errors of the estimated coefficients on the overall solution.

coefficient	associated term	estimated value (cm)	standard error (cm)
1	constant	2.1	0.4
2	cosM	22.9	0.3
3	sinM	5.3	0.1
4	cos2M	2.1	0.4
5	sin2M	0.0	0.1
6	Δt cosM	2.1	0.1
7	Δt sinM	1.5	0.1
8	Δt sin2M	-0.1	0.1
9	Δt	-1.6	4.8
10	Δt	1.3	3.6
11	Δt	-0.3	3.2
12	Δt	-1.7	3.3
13	Δt	6.9	4.0
14	Δt	-21.9	5.6

Table (6.2)
Calculated coefficients and standard errors of SEASAT non-gravitational solution

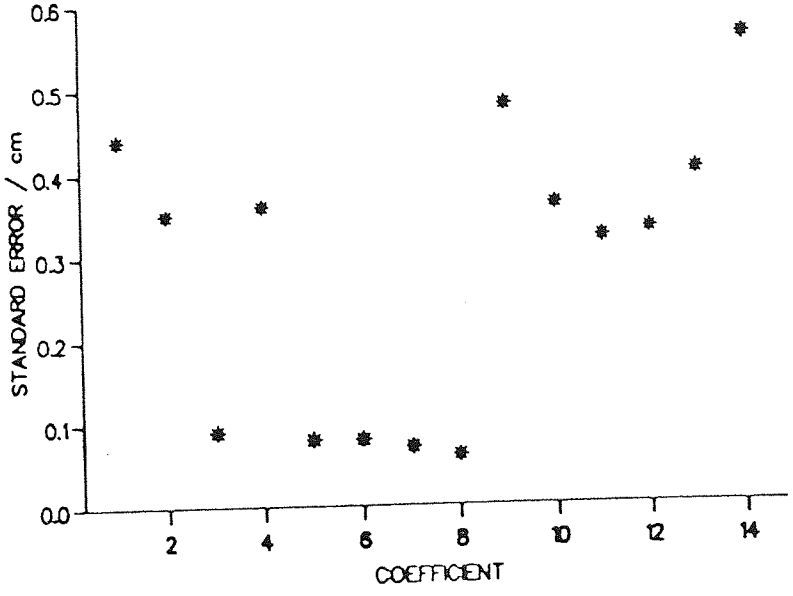

Figure (6.6)
Standard errors of estimated coefficients of SEASAT non-gravitational solution

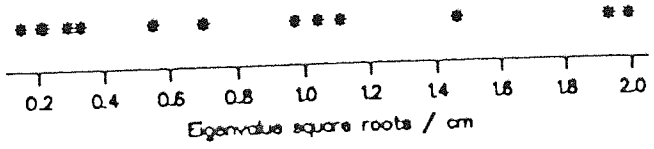

Figure (6.7)
Eigenvalue square roots of SEASAT non-gravitational solution

By substituting the values of the estimated coefficients into equation (6.1), a derived value for Δr (t) is obtained which was subtracted from the radial difference $r_{CIRA}(t) - r_{MSIS}(t)$ at each epoch t within the three day time span. The residuals that remain are the radial orbit errors after application of the method and are plotted in Figure (6.8).

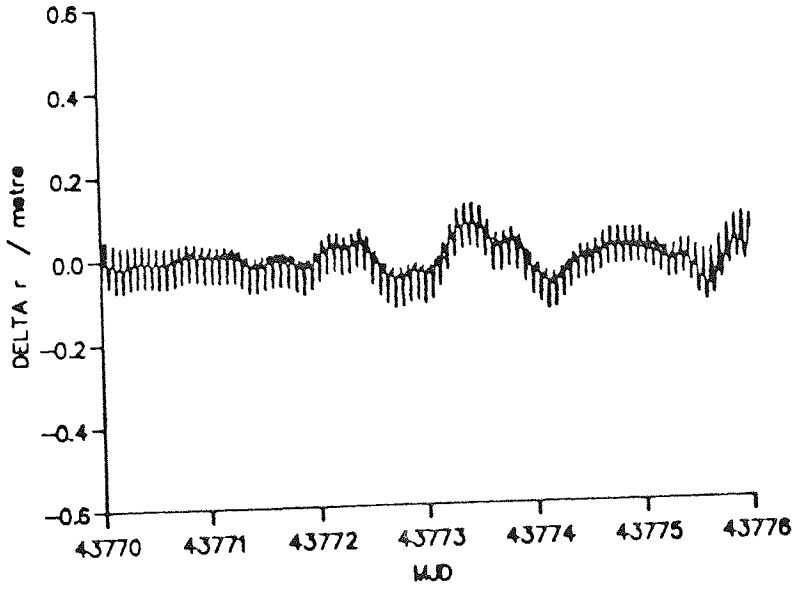

Figure (6.8)
Radial orbit error after fit of SEASAT non-gravitational solution

The error has been substantially reduced, from an rms value of 18.0 cm and maximum value of 55.3 cm (see Figure (6.3)) to an rms of 4.4cm and maximum value of 13.6cm. The diminished one cycle per revolution signature shows that, like the constant coefficient, the cosM term has been well resolved by the direct height measurements, evidence of which is borne out in the spectral analysis of these final radial residuals shown in Figure (6.9).

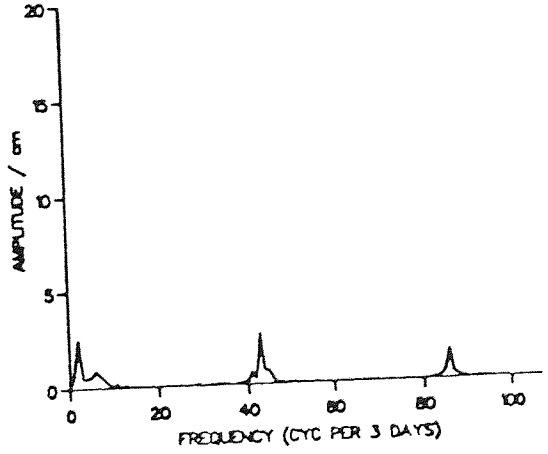

Figure (6.9)
Spectral analysis of radial orbit error after fit of SEASAT non-gravitational solution

The geographical distribution of the radial orbit error is worthy of investigation. The surface of the Earth was subdivided into 288 15° x 15° regions. The latitude and longitude of the radial differences before application of the reduction method, that is those shown in Figure (6.3), were calculated at each epoch and sorted into their relevant geographical bin. Figure (6.10) and Figure (6.11) plot the mean and rms about the mean of the differences in each section, respectively.

All descending SEASAT arcs have approximately the same value of mean anomaly, M, at a particular latitude, at which all ascending arcs have mean anomaly -M. From Figure (6.4) and Table (6.2), the dominant frequency term of the radial error is the cosM term. From equation (6.1), taken over all latitudes, in any particular 15° x 15° section, the cosM term will tend to dominate when calculating the mean values. This is clearly seen in the north to south sloped effect apparent in Figure (6.10), where the cosM term changes with M from a high value down to a similar value but of opposite sign. | cosM | is highest at the latitudinal extremes, diminishing around the equator where the mean anomaly, M = 90° and cosM = 0.

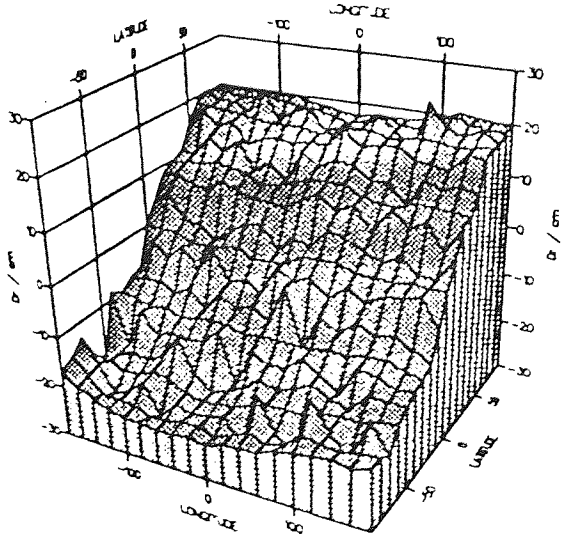

Figure (6.10)
Geographical distribution of mean radial orbit error before fit of SEASAT non-gravitational solution

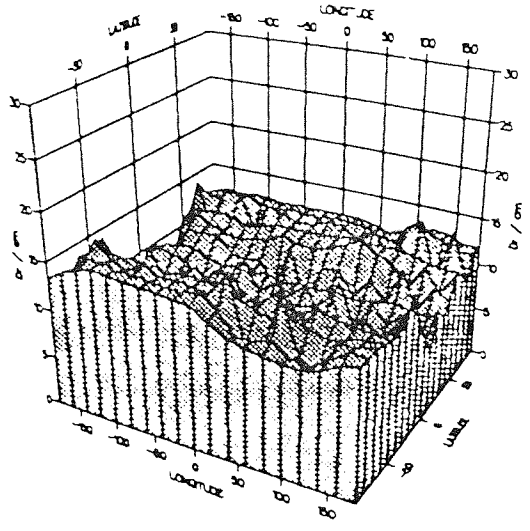

Figure (6.11)
Geographical distribution of radial orbit error rms about the mean before fit of SEASAT non-gravitational solution

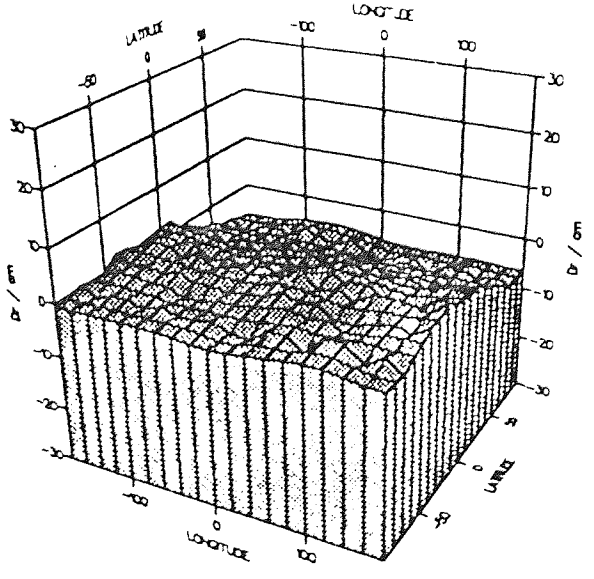

Figure (6.12)
Geographical distribution of mean radial orbit error after fit of SEASAT non-gravitational solution

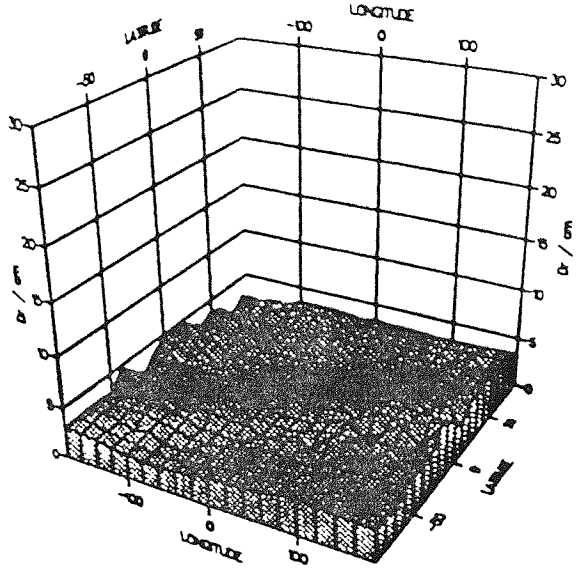

Figure (6.13)
Geographical distribution of radial orbit error rms about the mean after fit of SEASAT non-gravitational solution

Figure (6.9) shows the amplitudes of the remaining frequency terms after application of the method, with all frequency terms reduced to less than 2.7cm. The slight signatures that remain, at $\frac{2}{43}$ cycles per revolution, or 1 cycle per 1.5 days, which is not well resolved and at 1 cycle per revolution, manifest themselves in the peaks and troughs of Figure (6.8). The 1 cycle per revolution signature is also visible in the post-solution geographical plot of radial residuals of Figure (6.12), in which slight increases in magnitude of the mean values after solution at the extremes of latitude are present. Figure (6.8) shows that the solution holds good over the full length of the time span, and the low values in Figure (6.12) and Figure (6.13) verify that it is entirely global. Thus it appears that each coefficient has been well independently determined and the theoretical model for the non-gravitational radial orbit error seems to hold up well experimentally. It remained to investigate the validity of the gravitational model by moving on to complete real solutions.

§ 6.3 SEASAT Tracking Network

SEASAT was tracked by eleven laser ranging stations over the eighteen day period of study. However, several of the stations produced insufficient data, or data of poor quality. During the calibration phase of the mission, observations were taken that enabled numerical values to be placed on the accuracies of the readings from each. The stations involved and the standard errors assigned to each are shown in Figure (6.14) and Table (6.3).

The most accurate stations are those with an assigned standard error of 0.15m and all are in North America. This is most problematical in terms of achieving a highly accurate global set of tracking data. The weights applied to each observation used in the orbit determination procedure are given by the reciprocal of the square of the standard error given to the station concerned.

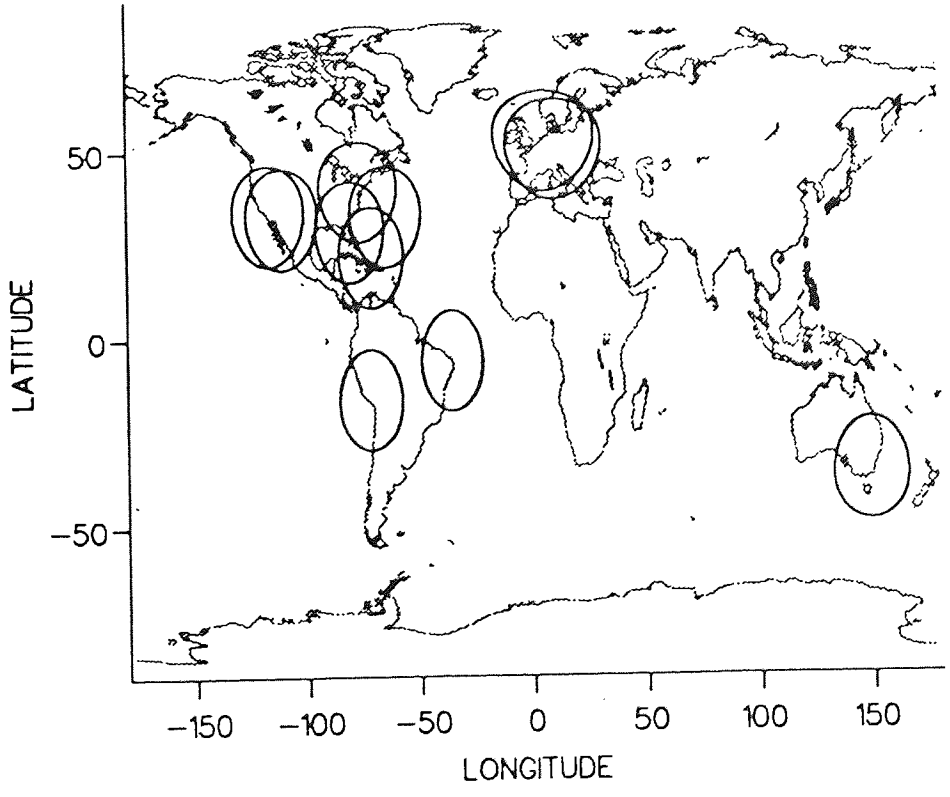

Figure (6.14)
SEASAT laser ranging station network

station number	longitude(deg)	latitude(deg)	s.e.(m)
7062	243.2	32.6	0.15
7063	283.2	39.0	0.15
7067	295.3	32.4	0.15
7068	288.9	21.5	0.15
7069	279.4	28.2	0.15
7833	5.8	52.2	0.70
7834	10.0	50.0	0.70
7907	288.5	-16.5	0.50
7921	249.1	31.7	0.70
7929	324.8	-5.9	0.70
7943	149.0	-35.6	0.70

Table (6.3)
SEASAT laser tracking stations

§ 6.4 Short Arc Direct Height Observations

The unobservable constant, cosM and cos2M coefficients require direct radial measurements for their determination and separation. Direct radial data also permits determination of those coefficients of the mutual linear combinations in the crossover equations. The direct heights were found for SEASAT by the method of short arc determination. The differences between laser range observations obtained from a pass over a tracking station and the calculated ranges obtained from the corresponding arc of the global ephemeris, are minimized over the pass in the least squares sense. Another arc is thus generated over the short time span during which the satellite is within the viewing circle of the station. This new arc is known as a short arc. In this SEASAT analysis, constant corrections Δr, Δa and Δn were made to the original calculated ephemeris at each epoch of the short arc, the minimization having been carried out with respect to the three mutually perpendicular radial, along-track and cross-track directions r, a and n, respectively.

Consider one such pass over a station in which NOBS observations were taken. Let R_i^{OBS} and R_i^{CAL} be the ith observed and calculated ranges, respectively,

where i = 1,..., NOBS. In the short arc determination procedure, I is minimized where

$$I = \sum_{i=1}^{NOBS} \left(R_i^{OBS} - R_i^{CAL} \right)^2 .$$

It is desired to find R_i^{CAL} such that

$$\frac{\partial I}{\partial p_j} = 0$$

where $p_j \in \{ r , a , n \}$.

i.e.

$$\sum_{i=1}^{NOBS} \left(R_i^{OBS} - R_i^{CAL} \right) \frac{\partial R_i^{CAL}}{\partial p_j} = 0. \qquad -(6.5)$$

Suppose the new short arc calculated range values are $R_i^{CAL}(sh)$ and the originals $R_i^{CAL}(orig)$. Then the constant corrections Δr, Δa and Δn are sought such that

$$R_i^{CAL}(sh) = R_i^{CAL}(orig) + \sum_{j=1}^{3} \underline{\nabla} (R_i^{CAL}) \underline{\Delta p}_j , \qquad -(6.6)$$

where $\underline{\nabla}$ is the operator

$$\underline{\nabla} = \left(\hat{\underline{r}} \frac{\partial}{\partial r} + \hat{\underline{a}} \frac{\partial}{\partial a} + \hat{\underline{n}} \frac{\partial}{\partial n} \right) ,$$

$\underline{\Delta p}_j$, j = 1,2,3 is the jth term of the vector of desired corrections

$$\underline{\Delta p} = \begin{bmatrix} \Delta r \\ \Delta a \\ \Delta n \end{bmatrix},$$

and it is assumed that $\underline{\nabla}\,(R_i^{CAL})$ is constant over the length of the short arc. That is

$$\frac{\partial R_i^{CAL(sh)}}{\partial p_j} = \frac{\partial R_i^{CAL(orig)}}{\partial p_j} \quad . \qquad -(6.7)$$

Substituting equation (6.6) and equation (6.7) into equation (6.5) gives

$$\sum_{i=1}^{NOBS}\left(R_i^{OBS} - R_i^{CAL(orig)} - \sum_{k=1}^{3} \underline{\nabla}\,(R_i^{CAL})\,\underline{\Delta p}_k \right) \frac{\partial R_i^{CAL(orig)}}{\partial p_j} = 0 ,$$

i.e.

$$\sum_{i=1}^{NOBS}\sum_{k=1}^{3} \frac{\partial R_i^{CAL(orig)}}{\partial p_j}\,\underline{\nabla}(R_i^{CAL})\,\underline{\Delta p}_k = \sum_{i=1}^{NOBS}\left(R_i^{OBS} - R_i^{CAL(orig)} \right) \frac{\partial R_i^{CAL(orig)}}{\partial p_j} .$$

Or, in matrix form,

$$N\,\underline{\Delta p} = \underline{b} \ ,$$

i.e.

$$\underline{\Delta p} = N^{-1}\,\underline{b} \ ,$$

where

$$N_{jk} = \sum_{i=1}^{NOBS} \frac{\partial R_i^{CAL(orig)}}{\partial p_j} \frac{\partial R_i^{CAL(orig)}}{\partial p_k} \ ,$$

$$b_j = \sum_{i=1}^{NOBS} \left(R_i^{OBS} - R_i^{CAL(orig)} \right) \frac{\partial R_i^{CAL(orig)}}{\partial p_j} \ .$$

The standard errors of the calculated corrections are found by the usual method of estimating standard errors using the least squares procedure, that is

$$\sigma_j = \sqrt{\frac{\sum_{i=1}^{NOBS} v_i^2}{NOBS - 4} N_{jj}^{-1}} \quad ,$$

where N_{jj}^{-1} is the jth diagonal element of N^{-1} and $\sum_{i=1}^{NOBS} v_i^2$ is the post-solution sum of squares of the range residuals.

The correction Δr in the radial direction is used in the direct radial height observations. Note that Δr is the difference between the new calculated short arc radial position of SEASAT and the original position according to the calculated ephemeris. Thus, for the purposes of this analysis, it is assumed that the new short arc positions are those of observational data, so that the value estimated in the short arc determination can be directly substituted for $\Delta r(t)$ in the direct height equations of the form of equation (3.44) as used to supplement the crossover data set. The epoch of the short arc correction was assumed to be its mean epoch.

§ 6.5 Gravitational Coefficient Recovery

The analyses that follow seek the simultaneous recovery of all the significant coefficients included in equation (3.44), both gravitational and non-gravitational. All the orbits generated have been computed using the GEM-T1 model of the gravity field. This is complete up to degree and order 36. That is, $\ell max = 36$. The arguments put forward in section §3.6 suggest that the significant contributions arise from terms of frequency less than about 2.5 cycles per revolution. That is

$$\dot{\Psi}_{km} < 2.5 \dot{M} \quad .$$

Or, by equation (3.26),

$$k k' - m \ell' < 2.5 k' \quad . \qquad -(6.8)$$

SEASAT was in a 43 revolution per 3 day repeat orbit, that is k'=43 and ℓ'=3. Thus the significant gravitational coefficients and therefore those sought in the following radial error reduction analyses are those for which k and m are such that

$$43\,k - 3\,m < 2.5 \times 43 = 107.5 \quad .$$

These are shown in Table (6.4). All discrete values of $\dot{\Psi}_{km}$ in steps of $\frac{1}{43}$ cycles per revolution, up to and including $\dot{\Psi}_{km} = \frac{107}{43}\ \dot{M}$, are covered.

k	m	fq	k	m	fq	k	m	fq	k	m	fq
1	14	1	1	5	28	-1	4	55	-1	13	82
1	15	2	2	19	29	2	10	56	2	1	83
0	1	3	0	10	30	0	19	57	3	15	84
1	13	4	1	4	31	-1	5	58	-1	14	85
1	16	5	2	18	32	2	9	59	2	0	86
0	2	6	0	11	33	0	20	60	3	14	87
1	12	7	1	3	34	-1	6	61	-1	15	88
1	17	8	2	17	35	2	8	62	2	1	89
0	3	9	0	12	36	0	21	63	3	13	90
1	11	10	1	2	37	-1	7	64	-1	16	91
1	18	11	2	16	38	2	7	65	2	2	92
0	4	12	0	13	39	3	21	66	3	12	93
1	10	13	1	1	40	-1	8	67	-1	17	94
1	19	14	2	15	41	2	6	68	2	3	95
0	5	15	0	14	42	3	20	69	3	11	96
1	9	16	1	0	43	-1	9	70	-1	18	97
1	20	17	2	14	44	2	5	71	2	4	98
0	6	18	0	15	45	3	19	72	3	10	99
1	8	19	-1	1	46	-1	10	73	-1	19	100
1	21	20	2	13	47	2	4	74	2	5	101
0	7	21	0	16	48	3	18	75	3	9	102
1	7	22	-1	2	49	-1	11	76	-1	20	103
2	21	23	2	12	50	2	3	77	2	6	104
0	8	24	0	17	51	3	17	78	3	8	105
1	6	25	-1	3	52	-1	12	79	-1	21	106
2	20	26	2	11	53	2	2	80	2	7	107
0	9	27	0	18	54	3	16	81			

Table (6.4)
Frequencies of the periodic gravitational coefficients recovered in analyses of 43 rev/3 day repeat orbits. fq is in units of $\frac{1}{43}$ cycles per revolution.

§ 6.6 Six Day Long Arc Analysis

Crossover residuals from the full six days from MJD43764 to MJD43770 were obtained from an ephemeris generated using the GEM-T1 gravity field model of degree and order 36. All crossovers with epochs separated by more than the precise SEASAT period of 3.008859 days were discarded, to avoid using the same altimetric measurements more than once. The short arc determination for direct height observations was carried out using the laser passes over the time studied. It was found that most of the arcs were not well determined. Only four have been derived with standard errors of less than 10cm. Previous studies [Sinclair,1988] have shown that unless the satellite passes almost directly overhead of a station, then a well determined short arc is never achieved using the data from one station alone. No such passes over one station were recorded. Thus, in order to obtain reasonable reliability, the satellite must have been tracked simultaneously by two or more stations. This compounds the problem of lack of global distribution of the stations mentioned earlier.

From Figure (6.14), the only reliable stations whose viewing circles overlap are also those confined to North America. The spread of available short arcs is thus limited to this relatively small area. For the six days analysed, only five such passes occurred, of which one was rejected due to its high standard error being above the threshold value used here of 10cm. This left only those displayed in Table (6.5) to be included as the direct radial height observations. The corresponding short arcs are shown in Figure (6.15), which highlights the global deficiencies.

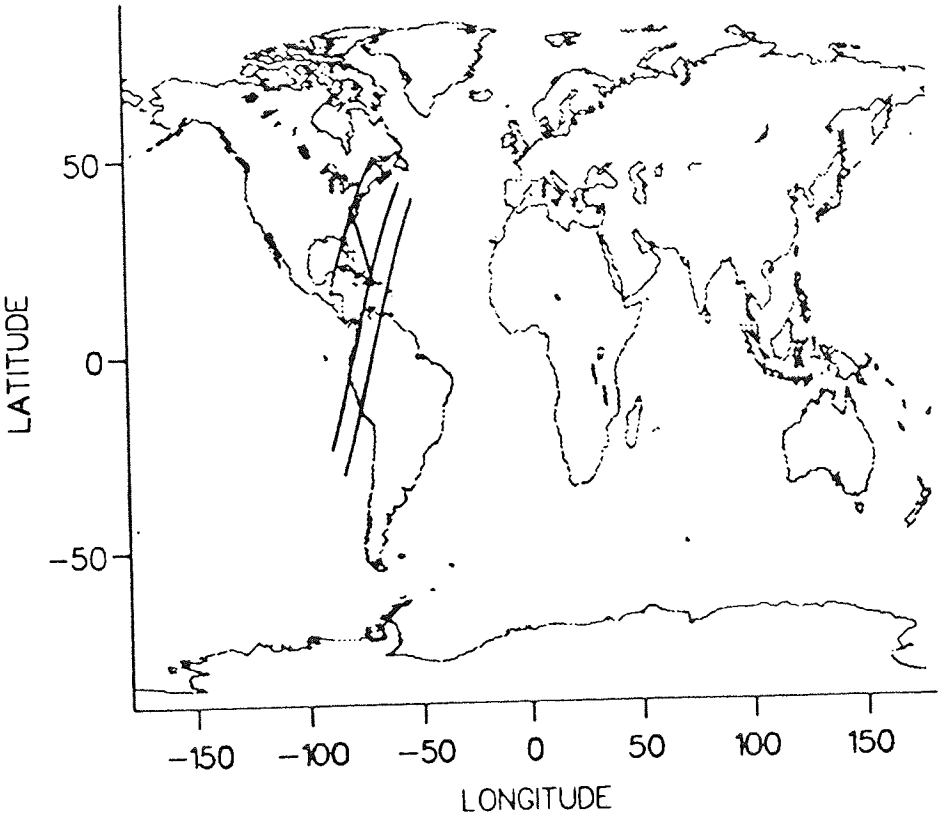

Figure (6.15)
Short arcs derived from SEASAT laser ranging data, MJD43764 to MJD43770

epoch (MJD)	long. (deg)	lat. (deg)	Δr (m)	s.e. (cm)	weight (cm^{-2})	M (deg)
43764.127480	292.8	27.3	-0.012	2.7	0.14	60.9
43765.109862	243.9	45.6	-0.148	9.4	0.01	75.1
43767.139197	286.6	13.5	-0.331	3.3	0.09	75.6
43767.602342	286.4	26.9	-0.138	2.2	0.21	298.5

Table (6.5)
SEASAT short arc data, MJD43764 to MJD43770

Each crossover was assigned an a priori standard error of 0.5m, that is a weight of $\frac{1}{0.5^2} = 4$ was applied to each of the 1,547 residuals generated. The direct height weights, shown in Table (6.5), were derived during the short arc determination.

The error reduction procedure was carried out in an attempt to recover the 224 coefficients required. The standard errors of the derived coefficients and the square roots of the eigenvalues of the solution, shown in Figure (6.16) and Figure (6.17), illustrate the extent of the ill-conditioning.

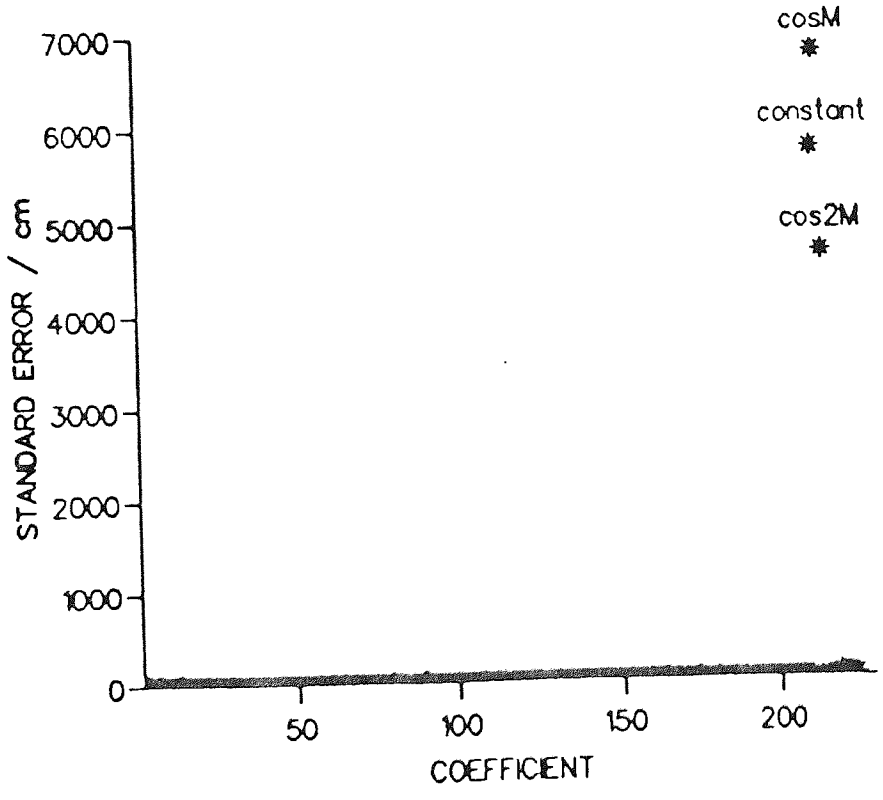

Figure (6.16)
Standard errors of estimated coefficients of unconstrained SEASAT 6-day solution

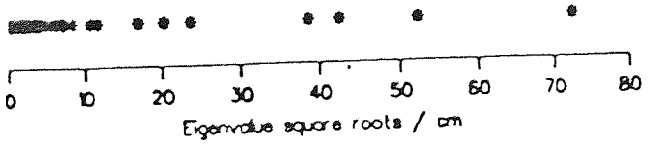

Figure (6.17)
Eigenvalue square roots of unconstrained SEASAT 6-day solution

The terms unobservable in the crossover data have been particularly poorly determined. This is due partly to the fact that the short arcs used are all situated in a region in which the mean anomaly, crucial in solving for the cosM and cos2M terms, takes a similar value in all four, which means that little new information is gleaned from each additional observation. The difficulty in separating out the combination terms and frequencies close together reveals the need for constraints to be applied to the coefficients. These have the effect of weighting the solutions in a manner dependent on the constraints imposed.

§ 6.7 Frequency Dependent Weights

It is well known that a typical frequency spectrum of radial orbit error for altimetric satellites using current knowledge takes the general form of a peak of the order of 1 metre at one cycle per revolution, gradually diminishing at higher and lower frequencies to around 10cm [Wagner and Melchioni,1989]. Thus a frequency dependent constraint weighting scheme was devised to mirror the general shape of the expected distribution. The errors in the frequency terms before fit were assumed to take the form of Figure (6.18), which is a linear increase from 10cm for the constant term to 1m at one cycle per revolution, then decreasing linearly to 10cm at two cycles per revolution. All frequency terms above this were given the minimum a priori standard error of 10cm. The weighting system was applied by adding the inverse of the square of the assumed standard error of each coefficient to the appropriate diagonal element of the normal equation matrix. Each weight, W, is given by

$$W = \frac{1}{\sigma^2} \ ,$$

where

$$\sigma = \begin{cases} 0.9\,\dot{\Psi}_{km} + 0.1 & \text{for} \quad 0 \leq \dot{\Psi}_{km} < 1\,\text{cyc/rev} \\ -0.9\,\dot{\Psi}_{km} + 1.9 & \text{for} \quad 1\,\text{cyc/rev} \leq \dot{\Psi}_{km} \leq 2\,\text{cyc/rev} \\ 0.1 & \text{for} \quad \dot{\Psi}_{km} \geq 2\,\text{cyc/rev} \end{cases}$$

All drag terms were assigned a standard error of 10cm.

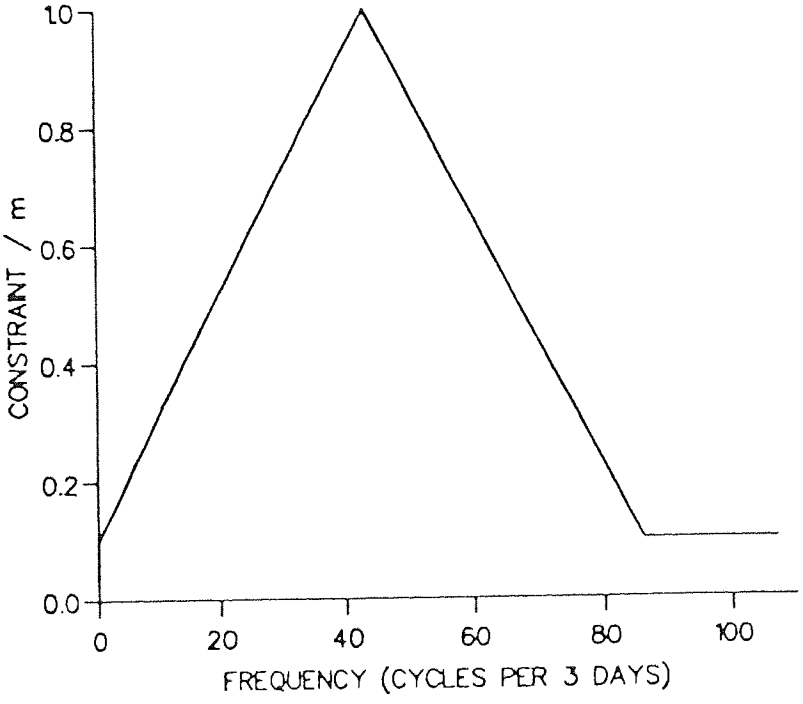

Figure (6.18)
Constraints applied to periodic frequency coefficients

The application of the constraints had a dramatic effect on the solution, as Figure (6.19) and Figure (6.20) illustrate. The cosM term is still not satisfactorily recovered, due to the lack of global short arcs, but the frequency terms have been well separated, apart from the (k,m) = (1,1), (-1,1) combinations, the inseparability of which remains unaffected by the weighting strategy which places the same constraints on both frequencies.

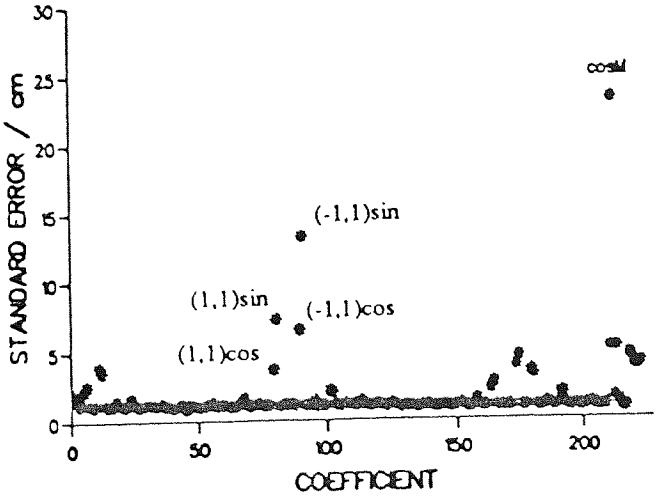

Figure (6.19)
Standard errors of estimated coefficients of constrained SEASAT 6-day solution, using real short arc derived direct radial heights

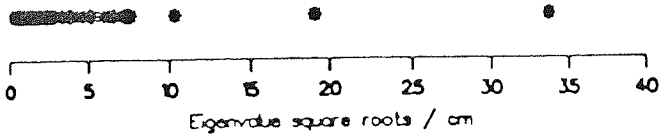

Figure (6.20)
Eigenvalue square roots of constrained SEASAT 6-day solution, using real short arc derived direct radial heights

§ 6.8 Fictitious Short Arcs

Future altimetric missions should have a far better global network of accurate tracking stations than available for SEASAT. This should help to overcome the problems experienced here, especially in the recovery of the cosM frequency term. The introduction of fictitious short arc observations at this stage gives some insight into the possible improvement of the solution if a wider geographical spread of short arc data was available.

Several locations were selected to give a wide range in time and in the mean anomaly. Fictitious direct heights were positioned at each. Anticipating that good

short arcs will become available, a value of 5cm was assumed to be realistic for the standard error of the radial correction.

Successive single fictitious short arcs were added to the real short arc data. The effect of the additional observation on the solution was monitored in an attempt to gain insight into the maximum number of direct height measurements necessary to improve the solution beyond which any extra data become superfluous. The standard error of the worst determined coefficient and the square root of the maximum eigenvalue of the inverse normal equation matrix were recorded each time. These are plotted in Figure (6.21). The results suggest that after the addition of approximately five or six extra terms, no really significant improvement is observed. The fact that all four real short arcs are situated in the same geographical area probably implies that more are required in this study, since the first four provide similar information about the crucial mean anomaly and cannot be assumed independent.

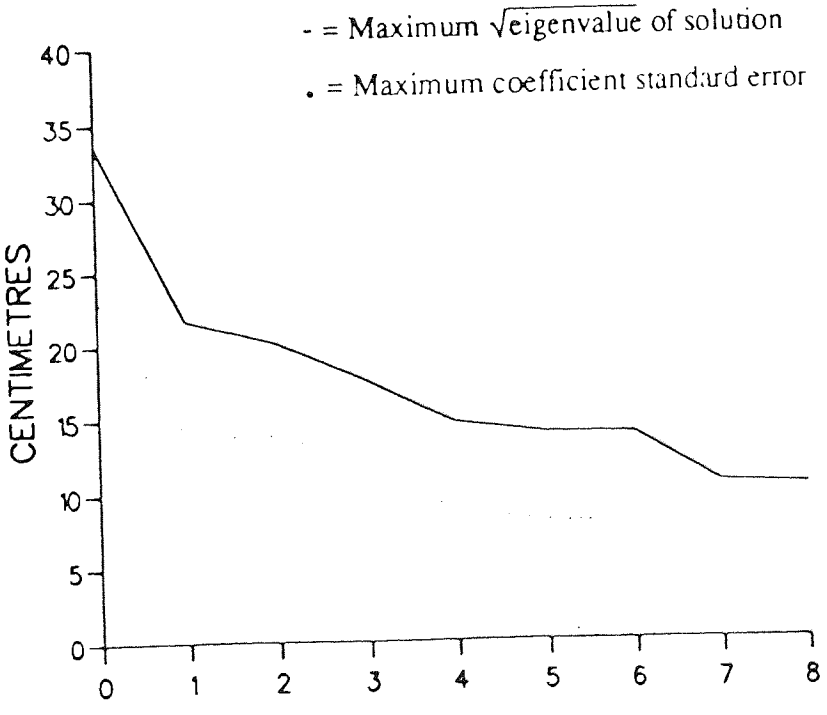

Figure (6.21)
Effect on constrained SEASAT 6-day solution of additional direct height data

Six fictitious values were introduced to supplement the short arc determined radial corrections and crossover residuals used to obtain the results of Figure (6.19) and Figure (6.20). The locations of the direct heights, both real and fictitious, are plotted in Figure (6.22). The frequency dependent constraints were applied as before. The solution, plotted in Figure (6.23) and Figure (6.24), has been strikingly improved. The coefficients have all been simultaneously well determined while at the same time the spectral analyses of the crossover residuals shown in Figure (6.25) and Figure (6.26) verify that error terms at all frequencies have been reduced from those initially present. Figures (6.27) to (6.30) illustrate that the error has diminished in all geographical regions.

Thus, given a good global distribution of high quality tracking data and applying a priori frequency dependent constraints to the solutions, the proposed radial orbit error reduction method has been demonstrably vindicated. The original crossover residual rms error has been reduced globally from 70.8cm before fit to a post-solution rms error of 23.9cm. This represents a radial orbit error reduction of from 50.1cm rms to 16.9cm, the radial rms being approximately equal to a factor of $\frac{1}{\sqrt{2}}$ less than the crossover equivalent for a large sample of data [Rothwell,1989].

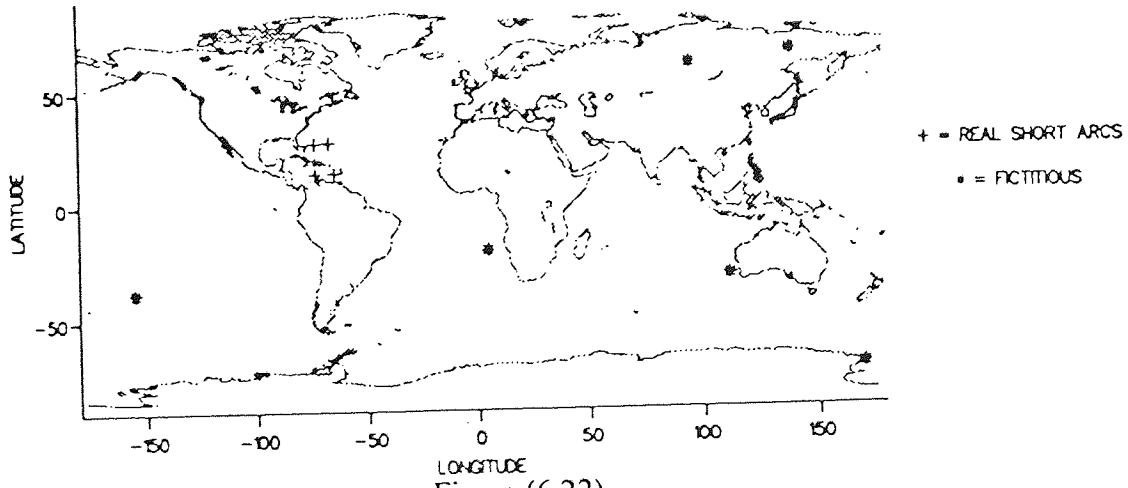

Figure (6.22)
Locations of direct height data employed in SEASAT 6-day analyses

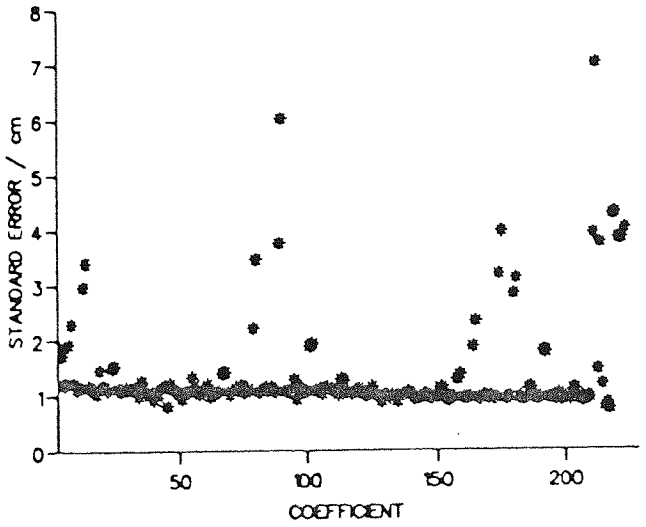

Figure (6.23)
Standard errors of estimated coefficients of SEASAT 6-day solution, using real and fictitious direct height data

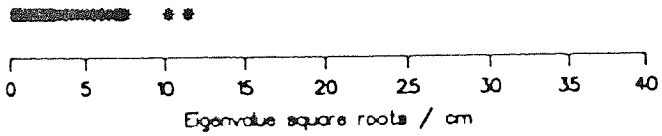

Figure (6.24)
Eigenvalue square roots of SEASAT 6-day solution, using real and fictitious direct height data

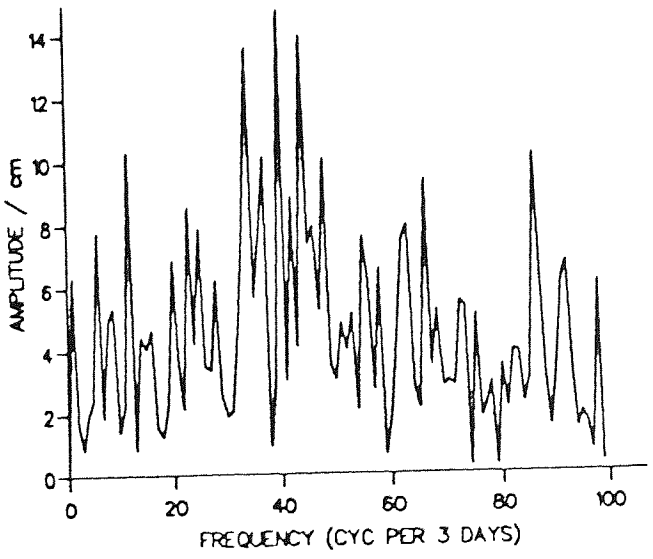

Figure (6.25)
Spectral analysis of crossover residuals before fit of SEASAT 6-day solutions

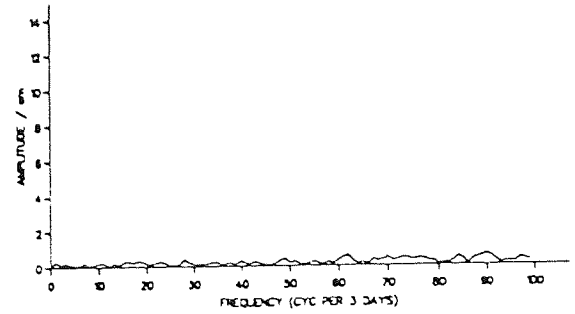

Figure (6.26)
Spectral analysis of crossover residuals after fit of SEASAT 6-day solution, using real and fictitious direct height data

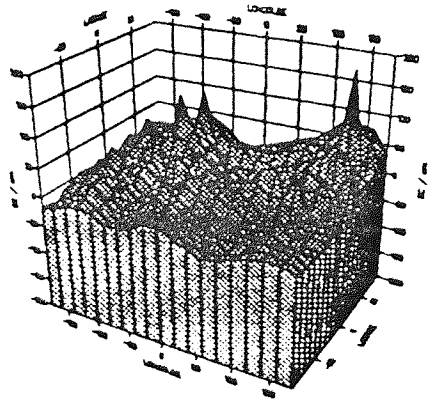

Figure (6.27)
Geographical distribution of mean crossover residuals before fit of SEASAT 6-day solutions

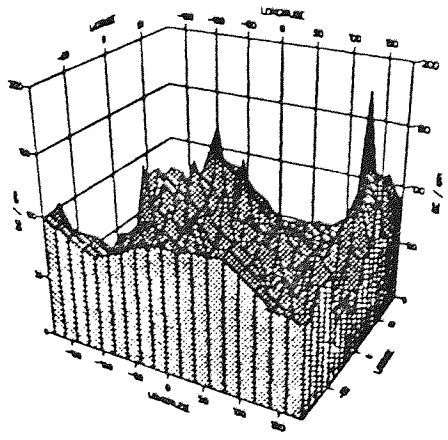

Figure (6.28)
Geographical distribution of crossover residual rms error about the mean before fit of SEASAT 6-day solution

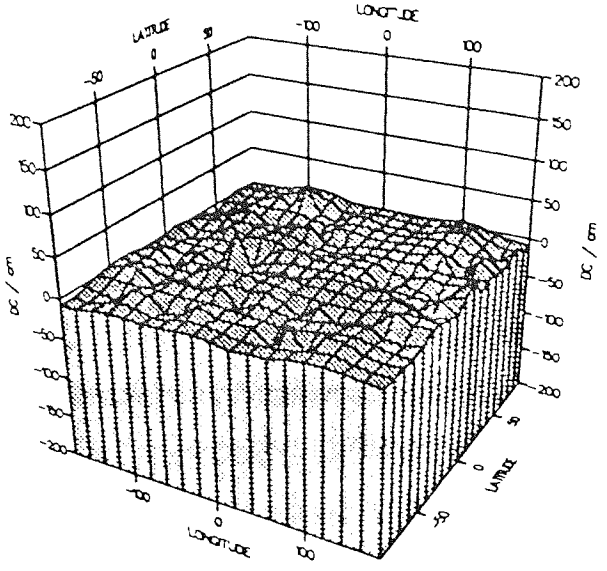

Figure (6.29)
Geographical distribution of mean crossover residuals after fit of SEASAT 6-day solution, using real and fictitious direct height data

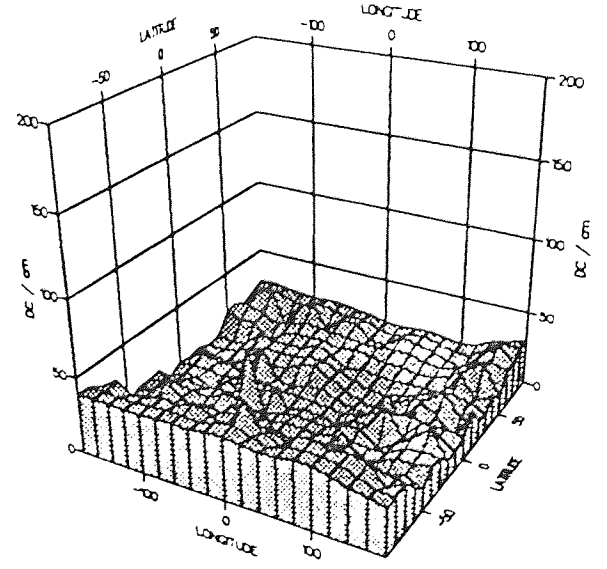

Figure (6.30)
Geographical distribution of crossover residual rms error about the mean after fit of SEASAT 6-day solution, using real and fictitious direct height data

§ 6.9 Importance of the Direct Radial Height Observations

The crucial role played by the radial height data is demonstrated by investigating a crossovers-only study. The constant, cosM and cos2M terms are not present in the crossover data, but it is difficult, even with the frequency dependent constraints applied, to separate out the linear combination terms. Figure (6.25) shows the amplitudes of the frequency terms present within the initial crossover residuals. 212 frequency coefficients need to be retrieved for a complete solution, plus the six daily drag coefficients and three time dependent terms, making a total of 221. The (badly determined) solution obtained without constraints is shown below in Figure (6.31) and Figure (6.32).

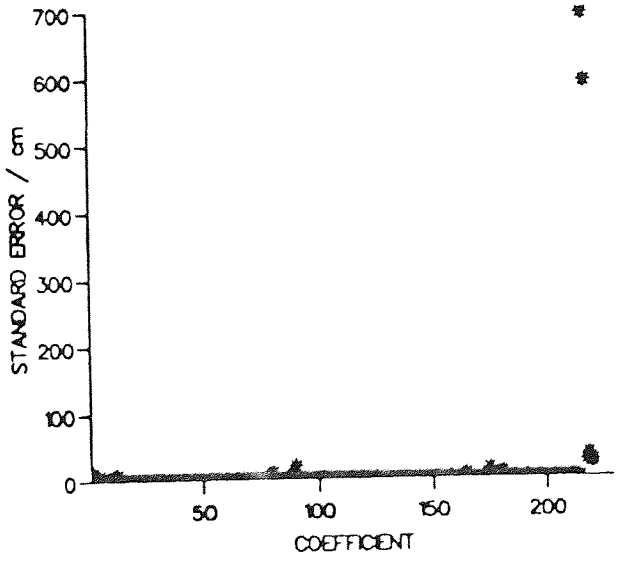

Figure (6.31)
Standard errors of unconstrained SEASAT crossovers-only solution

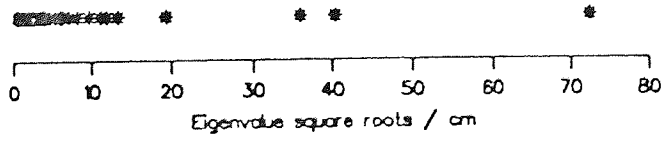

Figure (6.32)
Eigenvalue square roots of unconstrained SEASAT crossovers-only solution

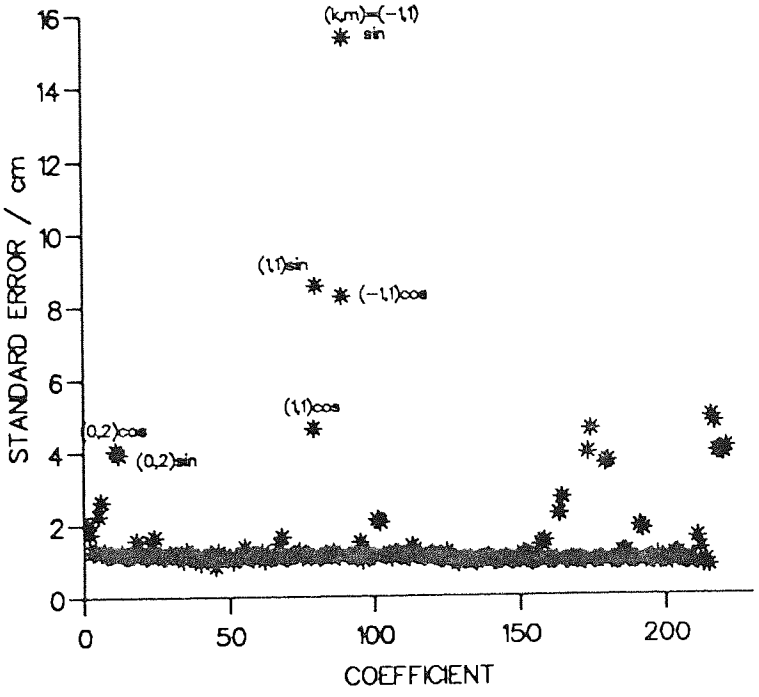

Figure (6.33)
Standard errors of constrained SEASAT crossovers-only solution

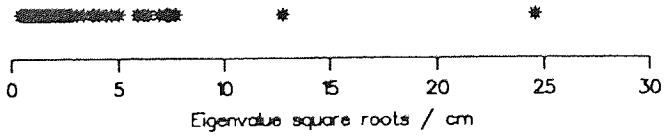

Figure (6.34)
Eigenvalue square roots of constrained SEASAT crossovers-only solution

Although Figure (6.33) and Figure (6.34) verify that a meaningful solution is obtainable using the constraints, the inclusion of the short arcs, the sole purpose of which in this instance of no constant, cosM or cos2M coefficients to be found is to aid separation of the frequency terms, both for similar frequencies and the linear

combinations, produced far better results. These are displayed in Figures (6.35) to (6.37) and include the fictitious data used earlier.

Hence it is concluded that not only are the direct height observations the only information available to resolve the three unobservable terms, but their aid in overcoming the ill-conditioning of the periodic frequency coefficients is indispensible.

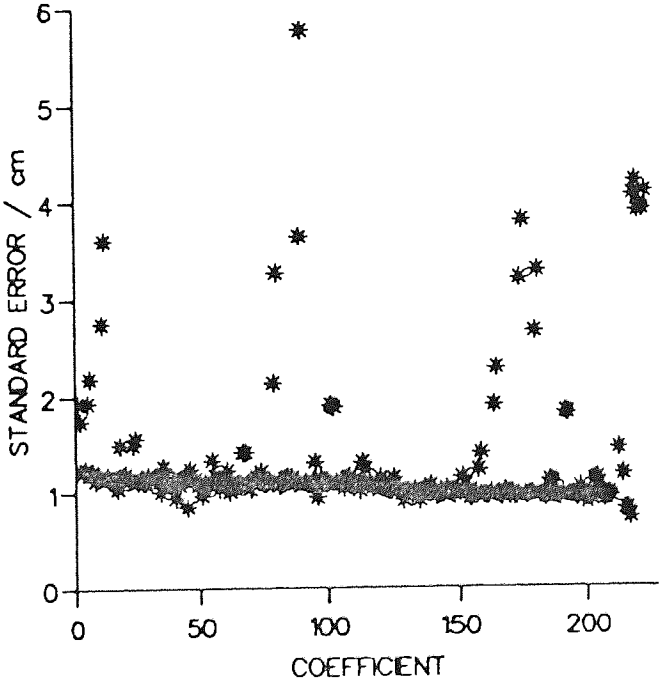

Figure (6.35)
Standard errors of SEASAT crossovers-only coefficient solution using direct height data to separate the frequency terms

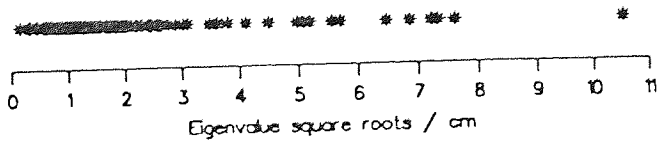

Figure (6.36)
Eigenvalue square roots of SEASAT crossovers-only coefficient solution using direct height data to separate the frequency terms

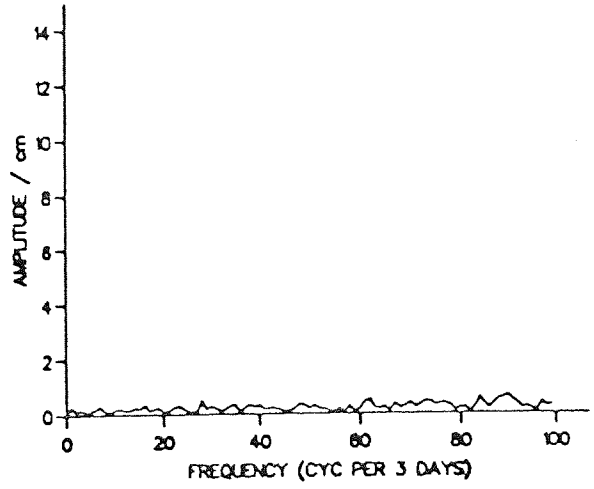

Figure (6.37)
Spectral analysis of residuals after fit of SEASAT crossovers-only coefficient solution using direct height data to separate the frequency terms

§ 6.10 Double Arc Aggregate

The results derived in the previous sections, in which the crossover residuals are generated from one single six day ephemeris, imply that the proposed radial orbit error reduction procedure appears to work well over the length of two successive repeat periods. After this time span, errors are gradually built up in the force model used in the orbit determination and the derived ephemerides are of insufficient accuracy. In order to span longer periods, separate orbits are generated. An investigation is now undertaken to determine the feasibility of extension of the method to reduce the global error over the complete length of two successive ephemerides, that is four successive repeat periods.

A second six day orbit was computed from MJD43770 to MJD43776. All the crossover residuals within this arc were found as for the previous six days. Since both ephemerides were of six days duration (twice the SEASAT repeat period), the satellite will pass over each crossover point four times during the course of each ephemeris. Suppose these times are t_1, t_2, t_3 and t_4, respectively, for the first six day

arc. Then the repeat period, $\tau_P = t_3 - t_1 = t_4 - t_2$. Three crossover residuals are given by $\Delta r\ (t_1) - \Delta r\ (t_2)$, $\Delta r\ (t_2) - \Delta r\ (t_3)$ and $\Delta r\ (t_3) - \Delta r\ (t_4)$. At first glance an additional possibility might appear to be $\Delta r\ (t_1) - \Delta r\ (t_4)$. However, since

$$[\ \Delta r\ (t_1) - \Delta r\ (t_2)\ ] + [\ \Delta r\ (t_2) - \Delta r\ (t_3)\ ] + [\ \Delta r\ (t_3) - \Delta r\ (t_4)\ ] = \Delta r\ (t_1) - \Delta r\ (t_4),$$

this last residual is already implicitly included through the other three and its addition to the data set is unnecessary. For this reason, any such crossovers with epochs greater than the repeat period of SEASAT are discarded.

Suppose the next epoch at which the satellite passes the crossover point is t_5. This epoch falls within the second six day arc. The problem arises of calculating such crossover residuals whose epochs straddle the discontinuity between the two ephemerides.

A third six day ephemeris was generated, over the period MJD43767 to MJD43773, to overlap the other two. All the times of crossovers within this orbit having epochs either side of MJD43770 were logged, to form the set of crossover epochs that straddled the discontinuity. Their crossover residuals were found by interpolation using epochs t_4 and t_5, to find the calculated geocentric distances required. In this manner a complete crossover residual data set of 5,439 crossovers, comprising of 1,034 across the discontinuity and 2,858 within the second six days to be added to the original 1,547 of the first six days, was generated.

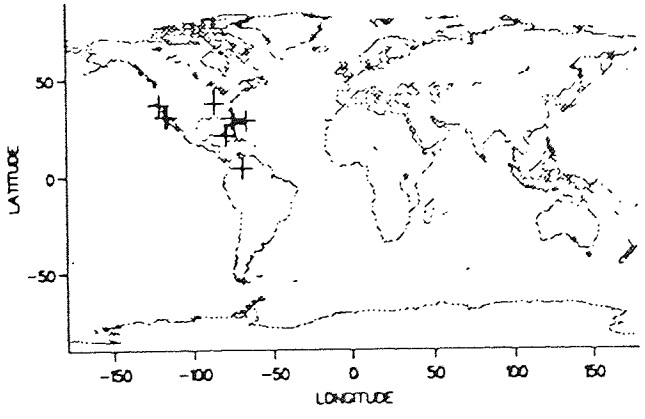

Figure (6.38)
Direct height locations derived from SEASAT short arcs, MJD43770 to MJD43776

epoch (MJD)	long. (deg)	lat. (deg)	Δr (m)	s.e. (cm)	weight (cm^{-2})	M (deg)
43770.611840	284.8	30.0	-0.238	5.5	0.03	301.7
43771.129604	291.1	4.1	-0.067	8.5	0.01	85.5
43771.732873	239.1	37.0	0.014	3.9	0.07	309.2
43772.639197	280.8	20.9	0.414	6.5	0.02	292.1
43773.153821	293.4	28.5	-0.217	3.2	0.10	59.6
43773.221867	273.4	37.7	-0.107	9.5	0.01	49.7
43773.293411	244.1	30.2	0.292	4.4	0.05	57.8
43773.620091	286.3	27.1	0.073	3.2	0.10	298.6
43774.740413	242.6	30.7	-0.148	6.0	0.03	302.4

Table (6.6)
SEASAT short arc data, MJD43770 to MJD43776

Short arcs were found using the later ephemeris in the same way as for the earlier orbit in the single arc study. There were more reliable arcs recorded this time, with nine having a derived post-solution standard error of less than 10cm, although the problem of lack of global coverage remained. Those used are shown in Figure (6.38) and Table (6.6) and were added to the original four used in the single arc studies.

The fact that the two ephemerides were derived with respect to two different starting vectors implies that several coefficients to be recovered in the analysis are arc dependent and separate parameters must be recovered for each orbit. Any coefficients arising due to errors in the initial state vector will be different for each arc. Also six daily, linear drag terms need to be resolved for each ephemeris. Hence, by equation (3.44), the total radial orbit error expression to be estimated is given by

$$\Delta r\,(t) = \sum_{k=-\ell_{max}}^{\ell_{max}} \sum_{m=0}^{\ell_{max}} \left\{ A_{km}\cos \dot{\Psi}_{km} t + B_{km}\sin \dot{\Psi}_{km} t \right\}$$

$$+ a_0^{(i)} + a_1^{(i)} \cos M + a_2^{(i)} \sin M + a_3^{(i)} \cos 2M + a_4^{(i)} \sin 2M + a_5^{(i)} (t - t^{*(i)}) \cos M$$

$$+ a_6^{(i)} (t - t^{*(i)}) \sin M + a_7^{(i)} (t - t^{*(i)}) \sin 2M$$

$$+ \; a^{(i)}_{NDAY(t)+7} \left(t - t_0^{(t)} \right) + \left[\begin{matrix} \sum_{k=8}^{NDAY(t)+6} a_k^{(i)} \\ 0 \end{matrix} \right]_{NDAY(t)=1}^{NDAY(t)>1}$$

-(6.9)

where the (i) superscripts denote arc dependent parameters for the ith arc, i = 1, 2.

Hence 238 coefficients need to be found for the complete radial recovery; 210 frequency coefficients, 12 drag terms and 16 other arc dependent coefficients. The one and two cycles per revolution cosine and sine parameters are considered as arc dependent although they are contributed to by gravity field mismodelling, an error common to both ephemerides, since the coefficients due to non-gravitational sources will absorb the gravitational terms at these frequencies in the least squares coefficient recovery.

By equation (6.9), each crossover residual is given by

$$\begin{aligned}
\Delta C \; = \; & \sum_{k=-\ell max}^{\ell max} \sum_{m=0}^{\ell max} \left\{ A_{km} \cos \dot{\Psi}_{km} t + B_{km} \sin \dot{\Psi}_{km} t \right\} \\
& + [a_0^{(i)} - a_0^{(j)}] + [a_1^{(i)} - a_1^{(j)}] \cos M + [a_2^{(i)} + a_2^{(j)}] \sin M + [a_3^{(i)} - a_3^{(j)}] \cos 2M \\
& + [a_4^{(i)} + a_4^{(j)}] \sin 2M + [a_5^{(i)} (t_1 - t^{*(i)}) - a_5^{(j)} (t_2 - t^{*(j)})] \cos M \\
& + [a_6^{(i)} (t_1 - t^{*(i)}) + a_6^{(j)} (t_2 - t^{*(j)})] \sin M + [a_7^{(i)} (t_1 - t^{*(i)}) + a_7^{(j)} (t_2 - t^{*(j)})] \sin 2M \\
& + (t_1 - t_0^{(t_1)}) \, a^{(i)}_{NDAY(t_1)+7} - (t_2 - t_0^{(t_2)}) \, a^{(j)}_{NDAY(t_2)+7} \\
& + \left[\begin{matrix} \sum_{k=8}^{NDAY(t_1)+6} a_k^{(i)} \\ 0 \end{matrix} \right]_{NDAY(t_1)=1}^{NDAY(t_1)>1} - \left[\begin{matrix} \sum_{k=8}^{NDAY(t_2)+6} a_k^{(j)} \\ 0 \end{matrix} \right]_{NDAY(t_2)=1}^{NDAY(t_2)>1} - \left[\begin{matrix} \sum_{k=8}^{13} a_k^{(i)} \\ 0 \end{matrix} \right]_{i=j}^{i \neq j},
\end{aligned}$$

-(6.10)

where t_1, t_2 fall within arc i and arc j , respectively.

Note that although for i = j, that is when both crossover epochs lie within the same ephemeris, three of the coefficients present in equation (6.9) are unobservable in the crossover residuals given by equation (6.10) (the constant, cosM and cos2M terms for that arc), there will be some signature at the usually unobservable frequencies this time when the epochs are from different arcs. This is because the appropriate radial orbit error coefficients are different for each orbit.

The radial misclosure, Δr_{MISC} between the two calculated orbits is given by the difference in the geocentric distances at MJD43770 according to each ephemeris. Before application of the correction procedure, this was

$$\Delta r_{MISC} = r_{7076}(\text{MJD43770}) - r_{6470}(\text{MJD43770}) \approx -0.498\text{metres} ,$$

where $_{6470}$ denotes values associated with the ephemeris covering the time span from MJD43764 to MJD43770, etc.

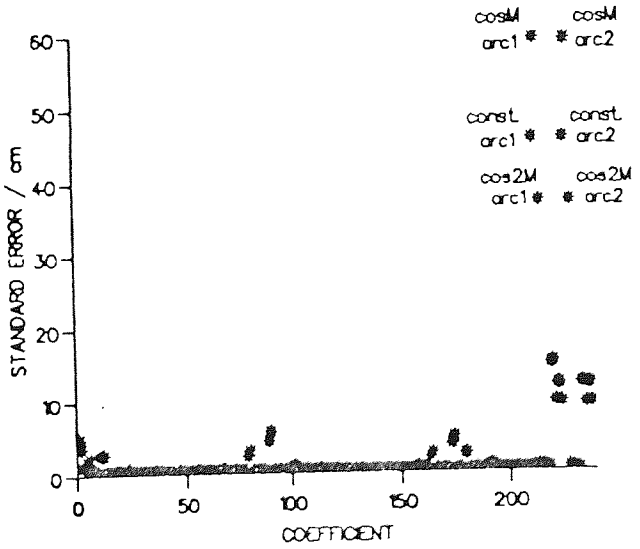

Figure (6.39)
Standard errors of estimated coefficients of unconstrained SEASAT 12-day solution

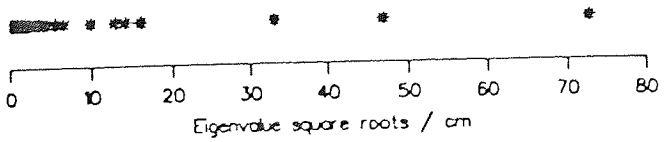

Figure (6.40)
Eigenvalue square roots of unconstrained SEASAT 12-day solution

The coefficients were estimated, initially without constraints, using the 13 short arcs from Table (6.5) and Table (6.6). The unreliable solution is depicted in Figure (6.39) and Figure (6.40). The extra crossover residuals have proved insufficient to separate the ill-determined coefficients, whose poor standard errors have combined to produce the square root eigenvalue of over 73cm. The solution is barely an improvement on the unconstrained single arc results of Figure (6.16) and Figure (6.17). Therefore the frequency dependent constraints were applied as before.

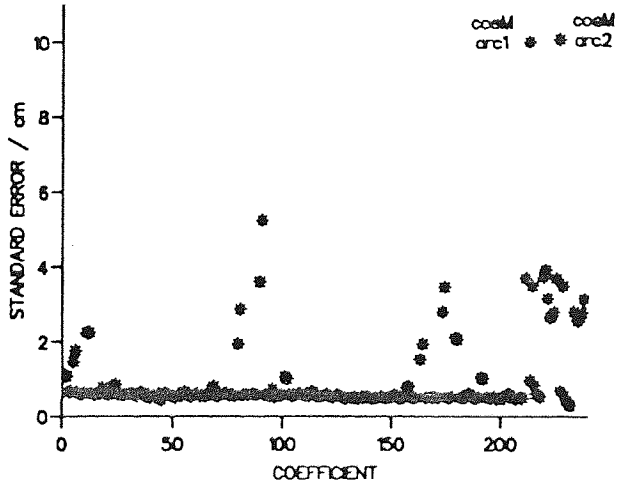

Figure (6.41)
Standard errors of estimated coefficients of constrained SEASAT 12-day solution, using real short arc derived direct height data only

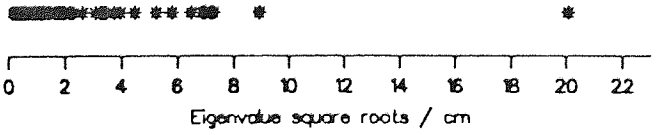

Figure (6.42)
Eigenvalue square roots of constrained SEASAT 12-day solution , using real short arc derived direct height data only

The desired effect was achieved. Figure (6.41) and Figure (6.42) show that an adequate solution has been returned. The frequency terms have all been well resolved, except the two cosM coefficients, the solutions of which are again impeded

by the lack of global distribution of the direct radial height data and which once more combine to corrupt the solution. This accounts for the relatively large value of around 20cm for the maximum square root eigenvalue.

It was deemed necessary at this point to produce extra fictitious short arc data, in order to discover how the arc aggregate solution would improve if a better global distribution was available. Six extra terms were assumed to be ample to separate out the coefficients, judging from Figure (6.21) and bearing in mind the extra crossover data. Three were included for each ephemeris; a total of nineteen direct radial heights were now included, with a wide spread in the mean anomaly. With the additional data the solution is seen to improve as anticipated. The final coefficient standard errors and square roots of eigenvalues are shown in Figure (6.43) and Figure (6.44).

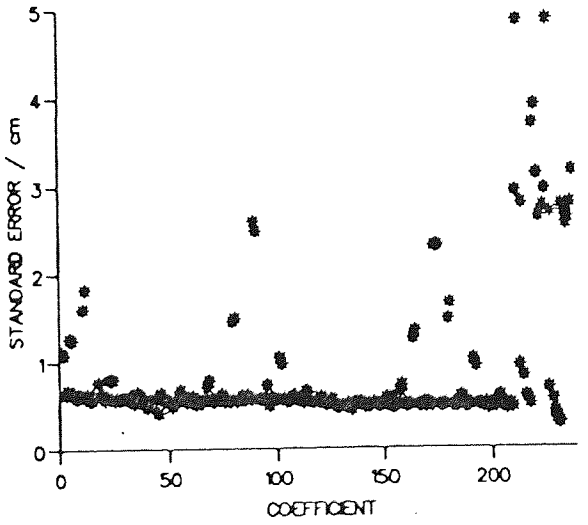

Figure (6.43)
Standard errors of estimated coefficients of SEASAT 12-day solution, using real and fictitious direct height data

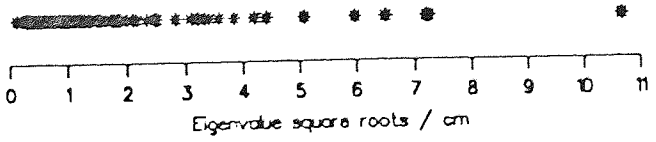

Figure (6.44)
Eigenvalue square roots of SEASAT 12-day solution, using real and fictitious direct height data

Figures (6.45) and (6.46) show spectral analyses of the pre- and post-solution crossover residual data, respectively. All frequency terms have been well recovered and reduced. The initial crossover residual rms error of 71.7cm has been reduced after fit to 25.4cm, equivalent to a radial reduction of from 50.7cm to 17.9cm over the whole length of the two arcs, that is a 64.7% reduction. The extra data included has served to increase the stability of this solution still further than for the single ephemeris solution.

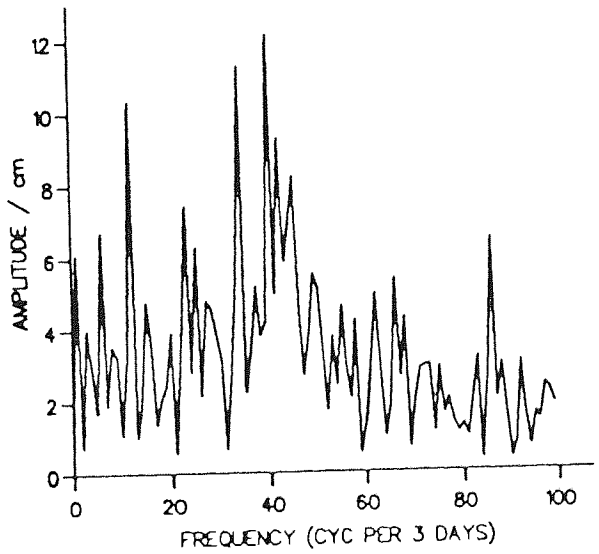

Figure (6.45)
Spectral analysis of SEASAT crossover residuals, MJD43764 to MJD 43776

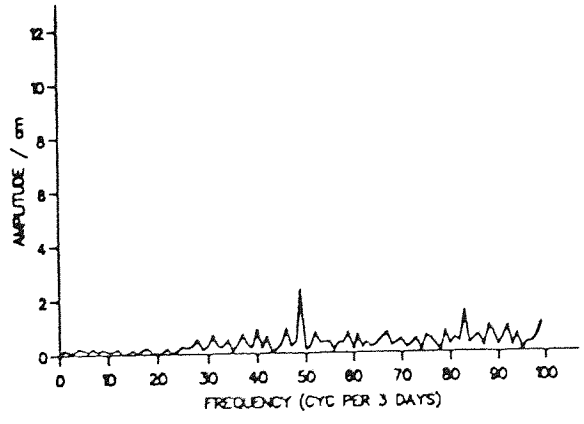

Figure (6.46)
Spectral analysis of crossovers after solution of SEASAT 12-day analysis, using real and fictitious direct height data

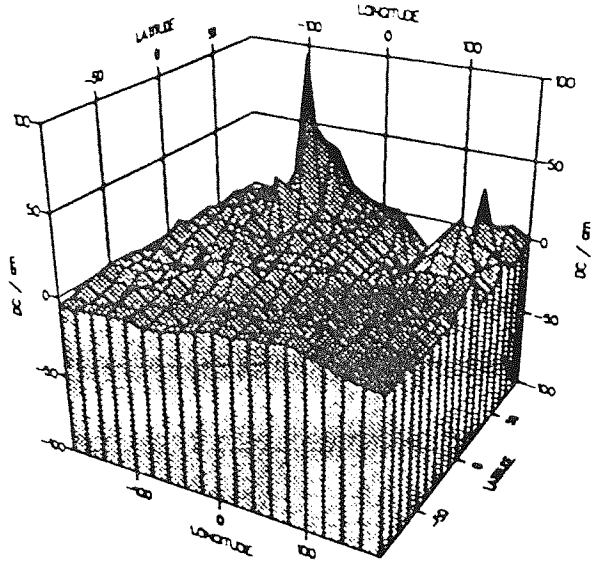

Figure (6.47)
Geographical distribution of mean crossover residuals for SEASAT, MJD43764 to MJD43776

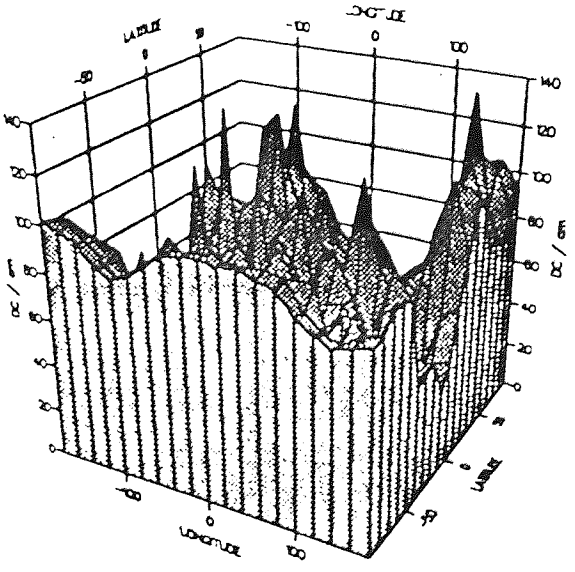

Figure (6.48)
Geographical distribution of SEASAT crossover residual rms error about the mean, MJD43764 to MJD43776

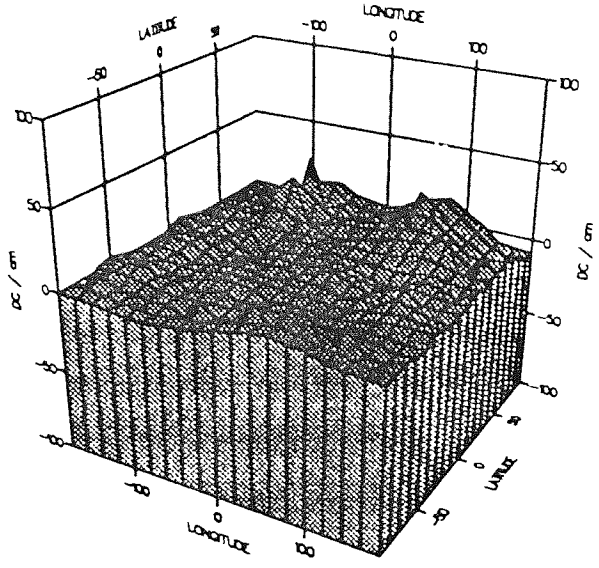

Figure (6.49)
Geographical distribution of mean crossover residuals after fit of SEASAT 12-day solution, using real and fictitious direct height data

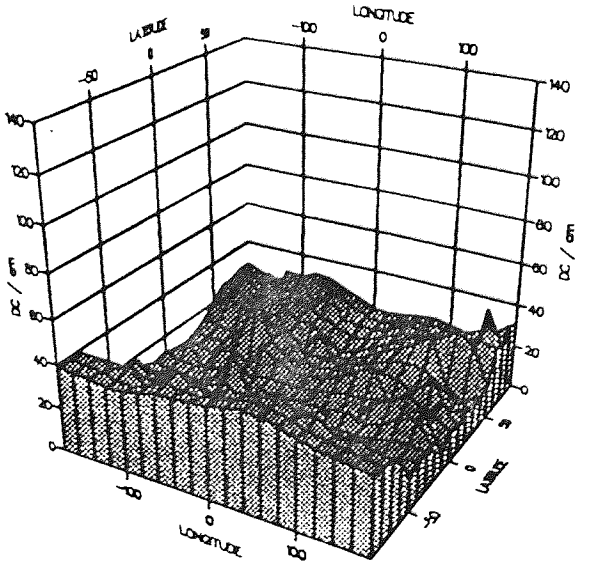

Figure (6.50)
Geographical distribution of crossover residual rms error about the mean after fit of SEASAT 12-day solution, using real and fictitious direct height data

The fact that the overall rms error has fallen substantially globally, as shown in Figures (6.47) to (6.50), reinforces the suggestion that the method is even more reliable for two arcs than for the single arc solution. Now

$$\Delta r_{MISC} = r_{7076}(MJD43770) - r_{6470}(MJD43770)$$

$$= r^{OBS}(MJD43770) - r_{6470}(MJD43770) - r^{OBS}(MJD43770) + r_{7076}(MJD43770)$$

$$= \Delta r_{6470}(MJD43770) - \Delta r_{7076}(MJD43770).$$

This is the difference in the radial orbit errors of each arc at the misclosure epoch. Hence subtracting the estimated radial orbit error differences from the original radial height differences at the discontinuity will yield the final, after fit, misclosure value.

$\Delta r(MJD43770)$ for each arc is found by substituting the calculated coefficients into equation (6.9). The frequency dependent terms will cancel and the estimated misclosure equation becomes

$$\Delta r_{MISC} = [a_0^{(1)} - a_0^{(2)}] + [a_1^{(1)} - a_1^{(2)}] \cos M_{70} + [a_2^{(1)} - a_2^{(2)}] \sin M_{70} + [a_3^{(1)} - a_3^{(2)}] \cos 2M_{70} + [a_4^{(1)} - a_4^{(2)}] \sin 2M_{70} + 3[a_5^{(1)} + a_5^{(2)}] \cos M_{70} + 3[a_6^{(1)} + a_6^{(2)}] \sin M_{70} + 3[a_7^{(1)} + a_7^{(2)}] \sin 2M_{70} + \sum_{k=8}^{13} a_k^{(i)} \quad -(6.11)$$

where M_{70} is the mean anomaly at the misclosure epoch MJD43770.

The relevant recovered coefficient values are given in Table (6.7). The mean anomaly at MJD43770 is calculated to be approximately $33.84° \approx 0.59$ rad. Equation (6.11) is applied to these values to give the estimation of the radial orbit differences as ≈ -0.627m. Hence the misclosure has been reduced from -0.498m before fit down to

-0.498 - (-0.627) = 0.129m after application of the radial error reduction procedure.

coefficient	associated term	estimated value/cm
$a_0^{(1)}$	constant	-21.3
$a_1^{(1)}$	cosM	28.5
$a_2^{(1)}$	sinM	-0.8
$a_3^{(1)}$	cos2M	3.1
$a_4^{(1)}$	sin2M	-10.8
$a_5^{(1)}$	Δt cosM	-15.5
$a_6^{(1)}$	Δt sinM	-1.6
$a_7^{(1)}$	Δt sin2M	-1.0
$a_8^{(1)}$	Δt	-13.1
$a_9^{(1)}$	Δt	16.6
$a_{10}^{(1)}$	Δt	-0.1
$a_{11}^{(1)}$	Δt	1.0
$a_{12}^{(1)}$	Δt	3.1
$a_{13}^{(1)}$	Δt	-18.6
$a_0^{(2)}$	constant	-4.4
$a_1^{(2)}$	cosM	25.6
$a_2^{(2)}$	sinM	-2.6
$a_3^{(2)}$	cos2M	6.2
$a_4^{(2)}$	sin2M	-13.4
$a_5^{(2)}$	Δt cosM	-0.8
$a_6^{(2)}$	Δt sinM	-2.3
$a_7^{(2)}$	Δt sin2M	-0.1

Table (6.7)
Coefficients estimated in SEASAT 12-day analysis using real and fictitious direct height data

The radial misclosure can be removed altogether by inclusion in the data set as an infallible observation. This forces the solution to precisely satisfy the misclosure equation and has the desirable effect of providing a continuous, smooth running orbit over the full twelve day time span.

Suppose the misclosure equation can be expressed in matrix notation by

$$A_2 \underline{x} = \underline{b}_2 \qquad \text{-(6.12)}$$

where $\underline{x}$ consists of the 238 coefficients of equation (6.9), $\underline{b}_2$ the misclosure value and A_2 the design matrix for the misclosure equation. If A_1 is the normal equation matrix for all other residuals and $\underline{b}_1$ the vector of residuals, then the misclosure equation can be introduced as infallible in the least squares procedure by minimizing ζ with respect to χ and all the coefficients in $\underline{x}$, where [Bomford,1980]

$$\zeta = (A_1 \underline{x} - \underline{b}_1)^T W (A_1 \underline{x} - \underline{b}_1) - 2 (A_2 \underline{x} - \underline{b}_2)^T \chi$$

with χ being such that $\frac{\partial \zeta}{\partial \chi} = 0$ and W being the diagonal weight matrix of constraints.

Then

$$\frac{\partial \zeta}{\partial \underline{x}} = 2 A_1^T W A_1 \underline{x} - 2 A_1^T W \underline{b}_1 - 2 A_2^T \chi .$$

Setting this to zero for minimum ζ gives

$$A_1^T W A_1 \underline{x} - A_1^T W \underline{b}_1 - A_2^T \chi = 0$$

$\Rightarrow$

$$\underline{x} = \left(A_1^T W A_1 \right)^{-1} \left[A_1^T W \underline{b}_1 + A_2^T \chi \right] . \qquad \text{-(6.13)}$$

Substituting equation (6.13) into equation (6.12) gives

$$A_2 \left(A_1^T W A_1 \right)^{-1} \left[A_1^T W \underline{b}_1 + A_2^T \chi \right] = \underline{b}_2$$

$\Rightarrow$

$$\chi = \left[A_2 \left(A_1^T W A_1 \right)^{-1} A_2^T \right]^{-1} \left\{ \underline{b}_2 - A_2 \left(A_1^T W A_1 \right)^{-1} A_1^T W \underline{b}_1 \right\} . \quad -(6.14)$$

Finally, substituting equation (6.14) into equation (6.13) yields the solution of the coefficients as

$$\underline{x} = \left(A_1^T W A_1 \right)^{-1} \left\{ A_1^T W \underline{b}_1 + A_2^T \left[A_2 \left(A_1^T W A_1 \right)^{-1} A_2^T \right]^{-1} \left[b_2 - A_2 \left(A_1^T W A_1 \right)^{-1} A_1^T W b_1 \right] \right\} .$$

This solution satisfies equation (6.12), so that the misclosure is removed and the two orbits become continuous after solution.

The infallible observation was incorporated into the analysis and the radial error reduction method otherwise carried out under the same conditions as those that produced the results shown in Figures (6.39) to (6.44). The solutions are similar, with the most reliable being those in which the six fictitious direct heights were employed. In this instance, the crossover residual rms has fallen from 71.7cm to 25.4cm, equivalent to a radial reduction of approximately 64.5%, from 50.7cm initially to 18.0cm after fit, with a continuous final radial ephemeris over the full twelve days. Figures (6.51) to (6.56) depict the final standard errors and square roots of eigenvalues of the solution and Figure (6.57) is a spectral analysis of the post-solution crossover residuals.

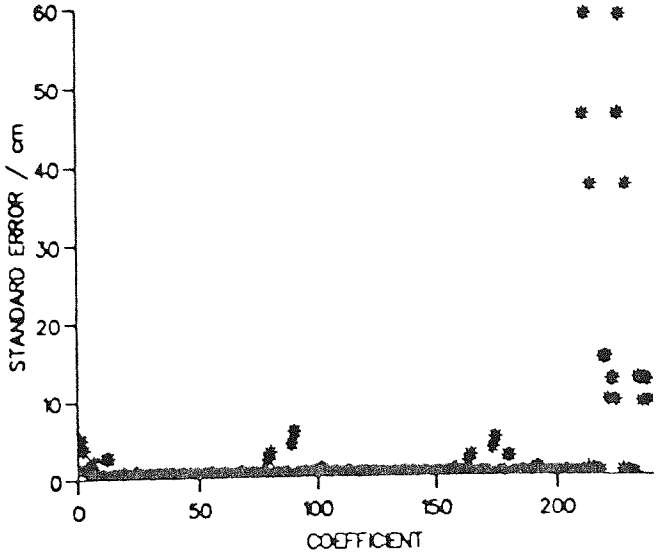

Figure (6.51)
Standard errors of estimated coefficients of unconstrained SEASAT 12-day solution, incorporating infallible misclosure expression

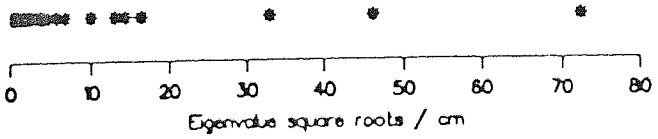

Figure (6.52)
Eigenvalue square roots of unconstrained SEASAT 12-day solution, incorporating infallible misclosure expression

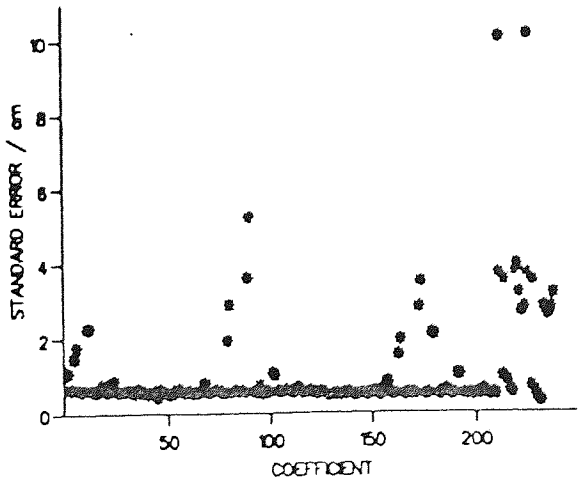

Figure (6.53)
Standard errors of estimated coefficients of constrained SEASAT 12-day solution, using real short arc derived direct height data only, incorporating infallible misclosure expression

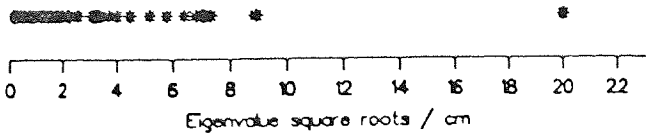

Figure (6.54)
Eigenvalue square roots of constrained SEASAT 12-day solution, using real short arc derived direct height data only, incorporating infallible misclosure expression

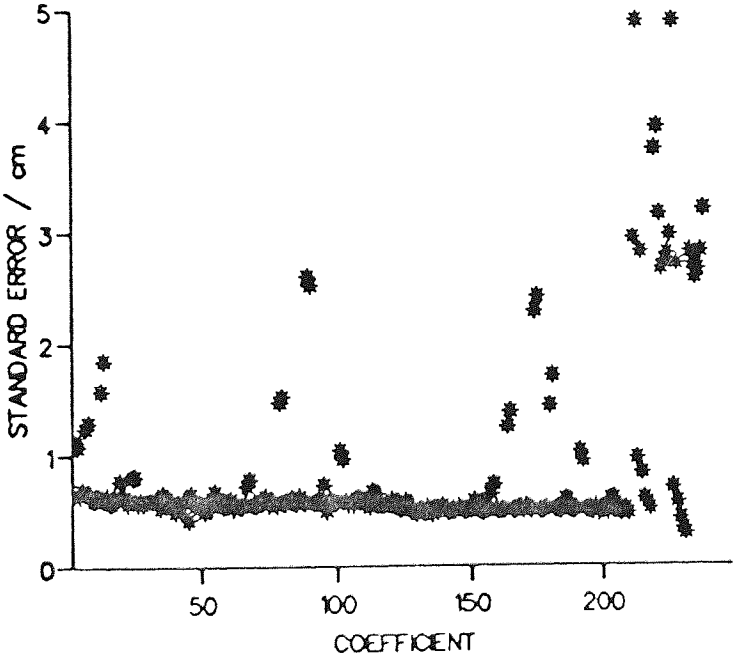

Figure (6.55)
Standard errors of estimated coefficients of SEASAT 12-day solution, using real and fictitious direct height data, incorporating infallible misclosure expression

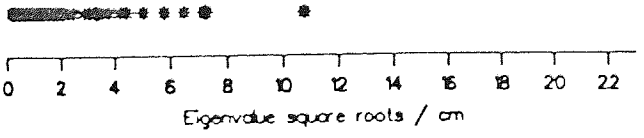

Figure (6.56)
Eigenvalue square roots of SEASAT 12-day solution, using real and fictitious direct height data, incorporating infallible misclosure expression

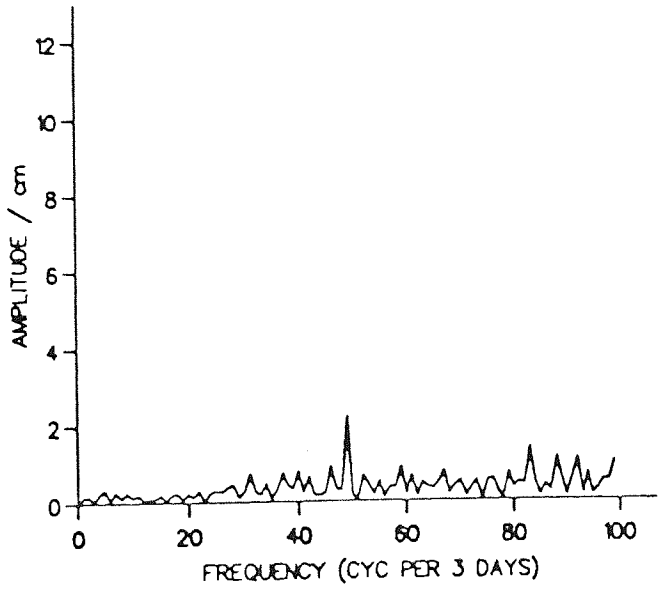

Figure (6.57)
Spectral analysis of crossover residuals after fit of SEASAT 12-day solution, using real and fictitious direct height data, incorporating infallible misclosure expression

§ 6.11 Triple Arc Aggregate

If the procedure can be applied successfully to a third six day arc, then it can be reasonably assumed that the possibility would exist of producing a complete, continuous solution for a longer repeat period, such as the 35 day repeat of ERS-1, with better tracking data. Bearing this ultimate goal in mind, a third successive six day arc, from MJD43776 to MJD43782, was generated. All the crossover residuals within the eighteen day time span from MJD43764 to MJD43782, including those across both discontinuities, at MJD43770 and MJD43776, were calculated. A total of 9,188 crossovers was obtained.

The radial residual equation for the whole eighteen days consists of both arc independent and arc dependent contributions, as before (see Figure (6.69)). Owing to a severe geomagnetic storm that occurred between MJD43780 and MJD43781, a far greater variation in atmospheric density took place during this day than usual . This

prompted the derivation of two linear 12-hourly drag coefficients instead of one daily term, both in the orbit generation and the radial error reduction process.

The radial error and crossover residual equations are of the form of equation (6.9) and equation (6.10), respectively, with i and j running from 1 to 3. A total of 253 coefficients were found. The short arcs from the $_{7682}$ ephemeris were derived and a further four fictitious heights created. Figure (6.58) and Table (6.8) show the locations of direct radial height observations for the three arc study. The positions of the fictitious data are unrealistic. Their inclusion has served only to illustrate the potential of the error reduction procedure and is not intended to be taken as a literal example of possible data points.

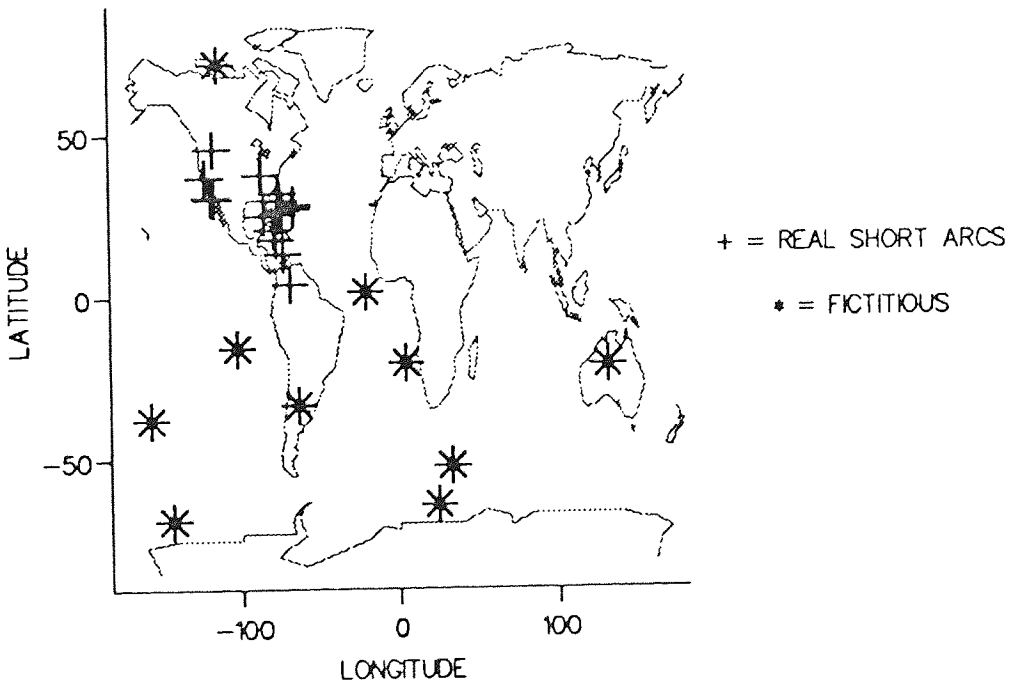

Figure (6.58)
Direct radial height data locations for 18-day SEASAT analyses

	epoch /MJD	long. /deg	lat. /deg	Δr /m	s.e. /cm	weight /cm^{-2}	M /deg
	43764.127480	-67.2	27.3	-0.012	2.7	0.14	60.9
	43765.109862	-116.1	45.6	-0.148	9.4	0.01	75.1
F	43766.310069	-154.9	-37.8	0.000	5.0	0.04	130.0
	43767.139197	-73.4	13.5	-0.331	3.3	0.09	75.6
	43767.602342	-73.6	26.9	-0.138	2.2	0.21	298.5
F	43768.895486	4.7	-20.5	0.000	5.0	0.04	111.4
F	43769.405208	33.5	-52.2	0.000	5.0	0.04	213.7
	43770.611840	-75.2	30.0	-0.238	5.5	0.03	301.7
	43771.129604	-68.9	4.1	-0.067	8.5	0.01	85.5
	43771.732873	-120.9	37.0	0.014	3.9	0.07	309.2
	43772.639197	-79.2	20.9	0.414	6.5	0.02	292.1
	43773.153821	-66.6	28.5	-0.217	3.2	0.10	59.6
F	43773.175000	-141.7	-68.9	0.000	5.0	0.04	168.7
	43773.221867	-86.6	37.7	-0.107	9.5	0.01	49.7
	43773.293411	-115.9	30.2	-0.292	4.4	0.05	57.8
	43773.620091	-73.7	27.1	0.073	3.2	0.10	298.6
F	43774.100000	130.9	-21.2	0.000	5.0	0.04	247.5
	43774.740413	-117.4	30.7	-0.148	6.0	0.03	302.4
F	43775.504167	-21.0	1.7	0.000	5.0	0.04	271.8
	43776.629994	-76.3	32.1	-0.033	6.5	0.02	304.0
	43777.213000	-85.0	25.0	0.521	5.8	0.03	63.3
	43778.192495	-76.4	25.7	-0.255	6.2	0.03	62.7
	43778.656272	-77.8	17.8	0.331	3.5	0.08	288.8
F	43779.510069	-113.2	71.9	0.000	5.0	0.04	1.4
F	43780.230208	-102.1	-15.8	0.000	5.0	0.04	106.4
F	43780.675000	-64.1	-33.2	0.000	5.0	0.04	234.7
F	43781.780208	24.9	-64.1	0.000	5.0	0.04	160.9

Table (6.8)
Direct height data employed in 18-day SEASAT analyses. (F = Fictitious value).

The results of the triple arc analysis are displayed in Figures (6.59) to (6.64).

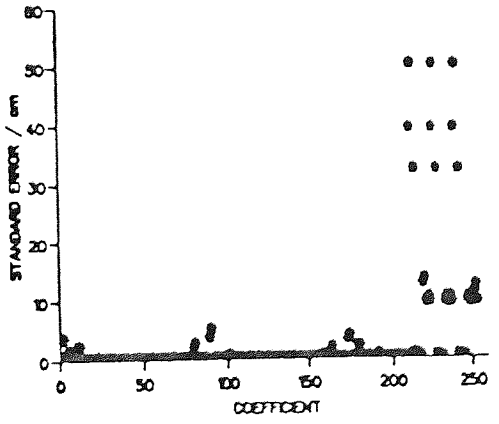

Figure (6.59)
Standard errors of estimated coefficients of unconstrained SEASAT 18-day solution, incorporating infallible misclosure expression

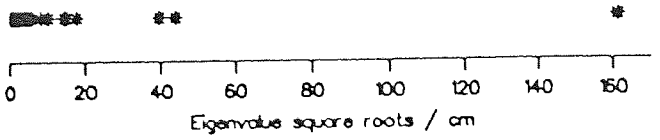

Figure (6.60)
Eigenvalue square roots of unconstrained SEASAT 18-day solution, incorporating infallible misclosure expression

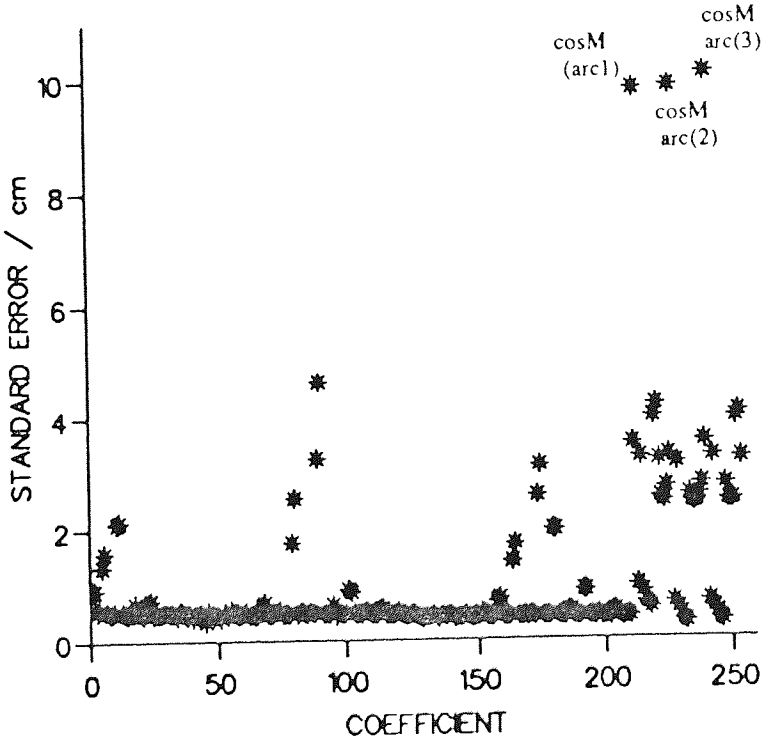

Figure (6.61)
Standard errors of estimated coefficients of constrained SEASAT 18-day solution, using real short arc derived direct height data only, incorporating infallible misclosure expression

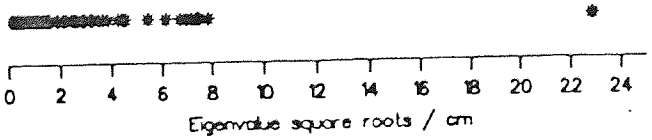

Figure (6.62)
Eigenvalue square roots of constrained SEASAT 18-day solution, using real short arc derived direct height data only, incorporating infallible misclosure expression

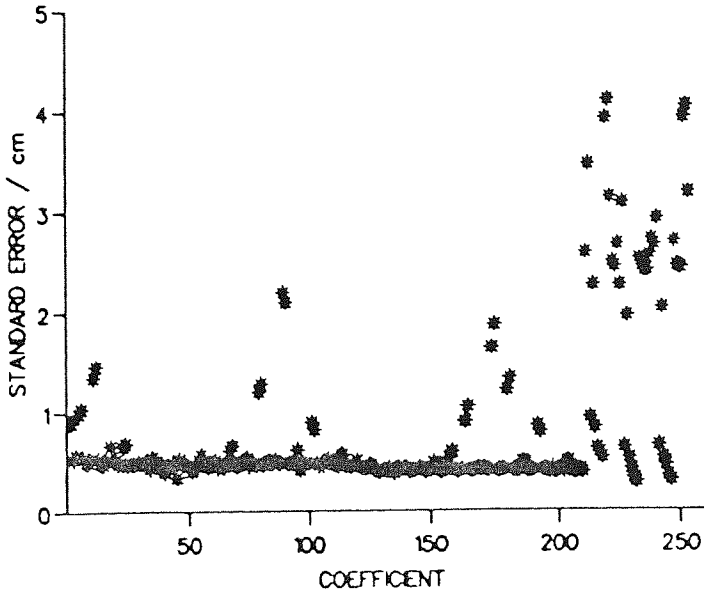

Figure (6.63)
Standard errors of estimated coefficients of SEASAT 18-day solution, using real and fictitious direct height data, incorporating infallible misclosure expression

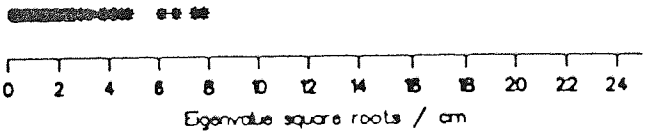

Figure (6.64)
Eigenvalue square roots of SEASAT 18-day solution, using real and fictitious direct height data, incorporating infallible misclosure expression

Although the additional crossover residuals in the full triple arc aggregate have gone some way towards separating out the periodic frequency terms, the coefficients are still badly determined and constraints are required. Figure (6.61) and Figure (6.62) plot the resolution of the coefficients after all the real short arc data has been included, with no fictitious short arcs. Derived entirely from real data, the cosM coefficients from each of the three arcs are not well resolved; the large square root of eigenvalue of around 23cm is due to the combination of the three badly resolved cosM coefficients. Figure (6.63) and Figure (6.64) provide encouraging evidence of

the success of the method. Again a full global solution has been achieved, as deduced from Figures (6.65) to (6.68), reliable in terms of the resolution of the coefficients.

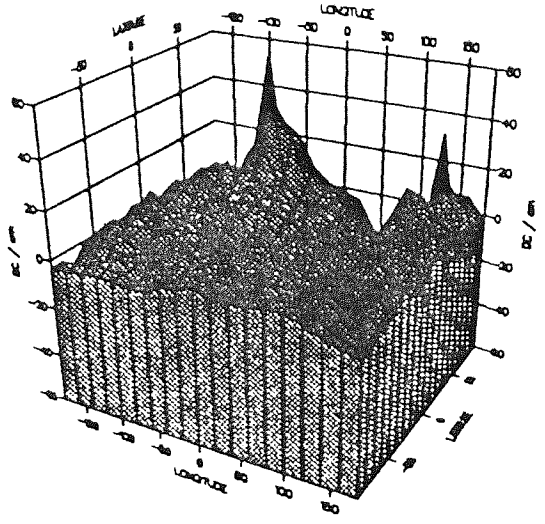

Figure (6.65)
Geographical distribution of mean crossover residuals for SEASAT, MJD43764 to MJD43782

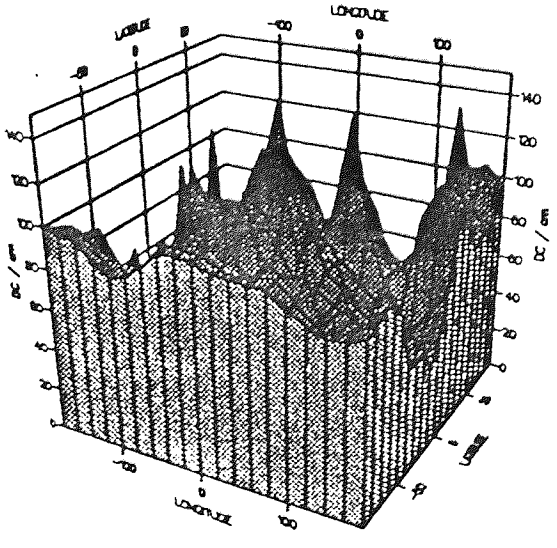

Figure (6.66)
Geographical distribution of SEASAT crossover residual rms error about the mean, MJD43764 to MJD43782

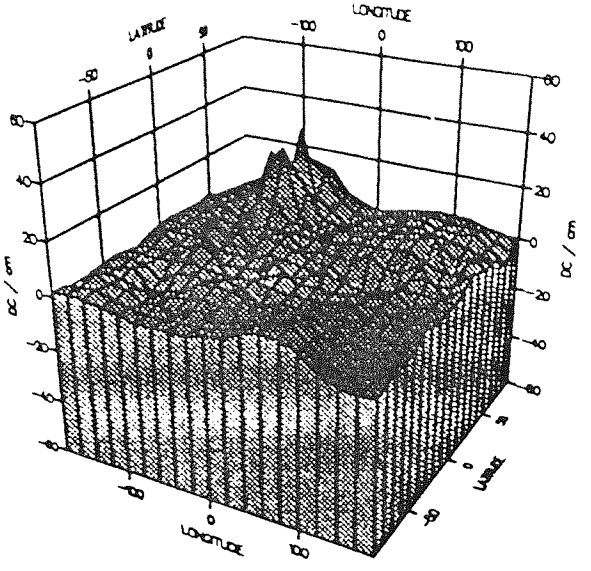

Figure (6.67)
Geographical distribution of mean crossover residuals after fit of SEASAT 18-day solution, using real and fictitious direct height data

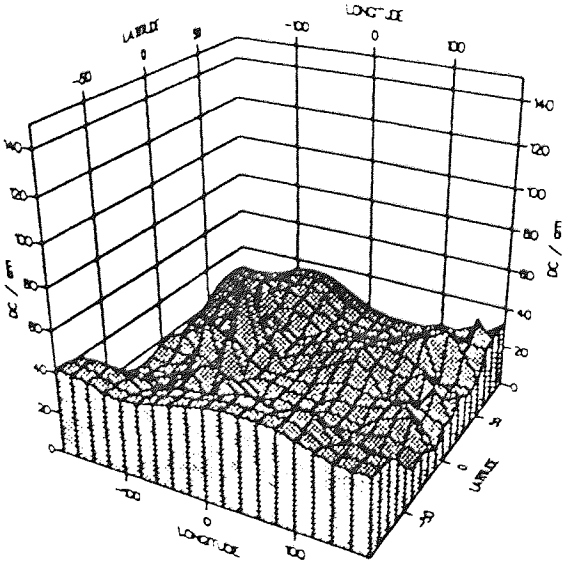

Figure (6.68)
Geographical distribution of crossover residual rms error about the mean after fit of SEASAT 18-day solution, using real and fictitious direct height data

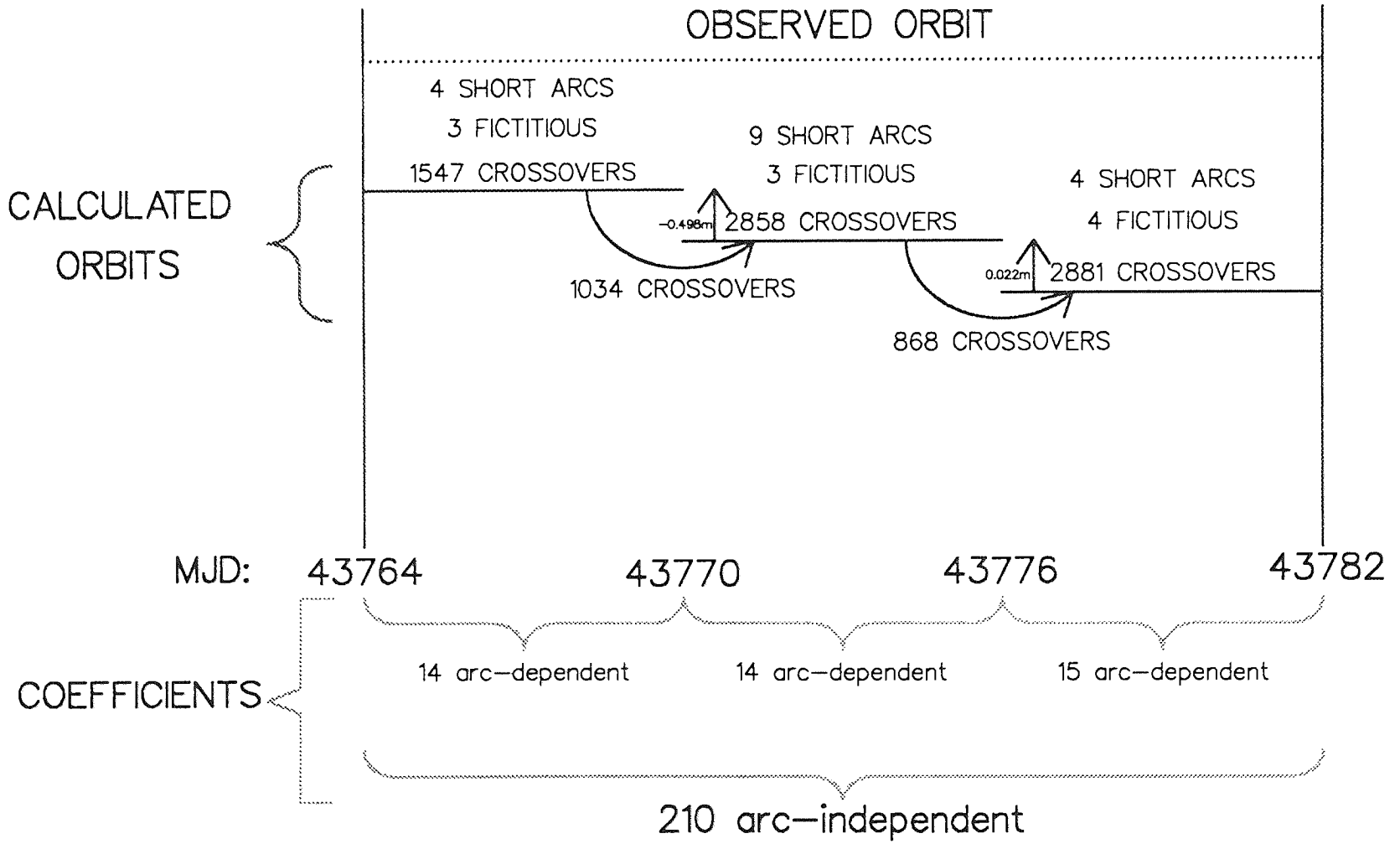

Figure (6.69)
Triple arc solution summary

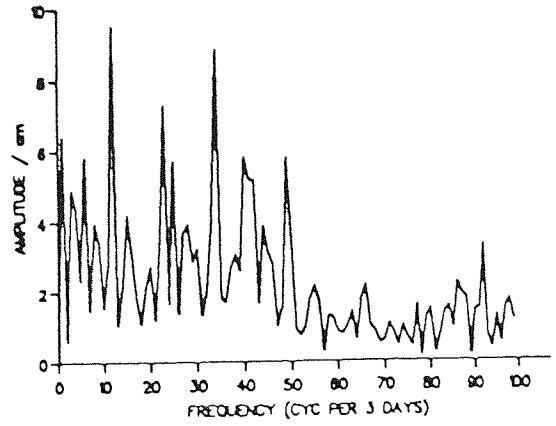

Figure (6.70)
Spectral analysis of SEASAT crossover residuals, MJD43764 to MJD 43782

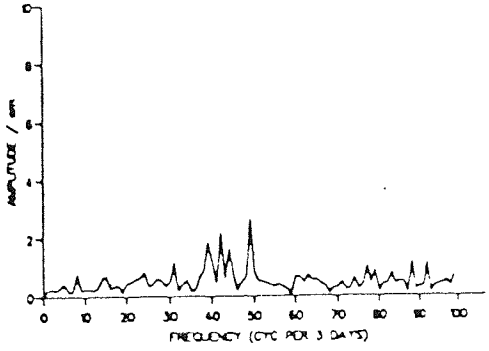

Figure (6.71)
Spectral analysis of crossover residuals after fit of SEASAT 18-day solution, using real and fictitious direct height data

The rms error of the crossover residuals has fallen from 72.1cm initially to 27.8cm after final convergence of the procedure, while at the same time producing a smooth, continuous 18 day radial ephemeris. The equivalent reduction in the radial orbit error is from 51.0cm rms to 19.6cm (≈ 61.6% reduction). Figure (6.70) and Figure (6.71) show that terms of all frequency have been substantially reduced. Figure (6.69) summarizes the 3 arc aggregate solution, illustrating the breakdown of the crossover residuals and short arc data, the misclosures included as infallible observations and the nature of the 253 coefficients recovered.

Table (6.9) and Figure (6.72) compare solutions obtained for the single, double and triple arc studies. The fictitious data has been included in each. The equivalent radial orbit rms error is reduced in all cases to below 20cm, including the complete 18 day triple arc analysis. At the same time all coefficients have been accurately resolved. The extra crossovers in the arc aggregates provide more

information with which to separate out gravitational terms of similar frequency and accounts for the gradual reduction in the standard error of the worst determined coefficients. It follows that each solution overall will have greater reliability, hence the reduction in the square roots of the maximum eigenvalues. The final radial reduction to 19.6cm for the triple arc solution is as good as can be reasonably expected by fitting data obtained from three separate arcs to the same radial orbit error model.

NO. OF ARCS		1	2	3
Crossovers	Total	1,547	5,439	9,188
	Rejected	165	755	1,339
	Retained	1,382	4,684	7,849
Direct Heights	Real	4	13	17
	Fictitious	3	6	10
	Total	7	19	27
Max. standard error of solution/cm		7.0	4.9	4.1
Max. $\sqrt{\text{eigenvalue}}$/cm		11.5	10.7	7.8
ΔC_{rms} before solution/cm		70.8	71.7	72.1
ΔC_{rms} after solution/cm		23.9	25.4	27.8
Equivalent Δr_{rms} before solution/		50.1	50.7	51.0
Equivalent Δr_{rms} after solution/cr		16.9	18.0	19.6

Table (6.9)
Comparison of SEASAT arc aggregate solutions

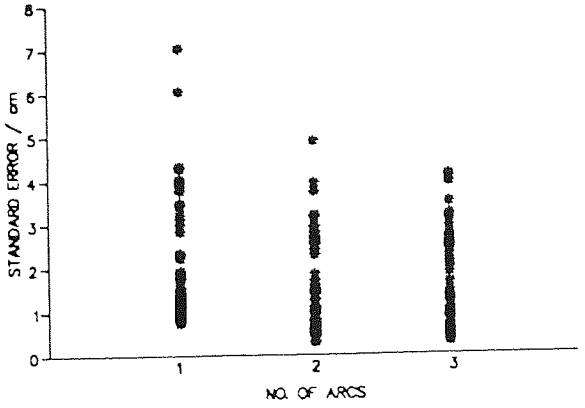

(i) Standard errors of estimated coefficients

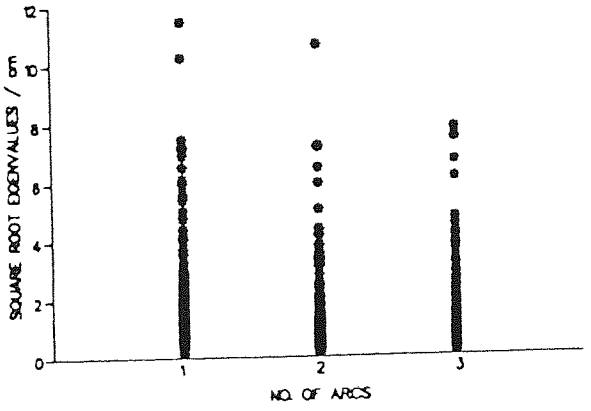

(ii) Eigenvalue square roots of solutions

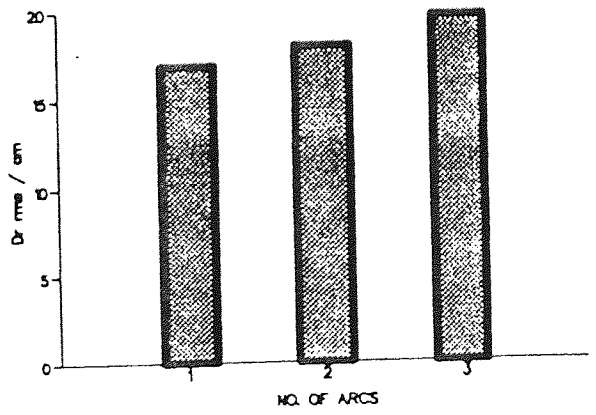

(iii) Post-solution equivalent rms radial orbit error

Figure (6.72)
Comparison of SEASAT arc aggregate solutions

The SEASAT studies have been hampered not only by the disappointing returns from the laser ranging stations, but also because a relatively large percentage of the altimetry used in the derivation of the crossover heights is inaccurate due to the presence of sea ice. Prior to the month of September, over which the analyses were carried out, winter had fallen on the southern hemisphere. The locations of the 1,339 data points rejected during the triple arc analysis from which Figure (6.63) and Figure (6.64) were derived, namely those having a post-solution crossover residual greater than 0.75m, are plotted in Figure (6.73). As expected, most appear over the southern oceans where sea ice has contaminated the altimeter returns.

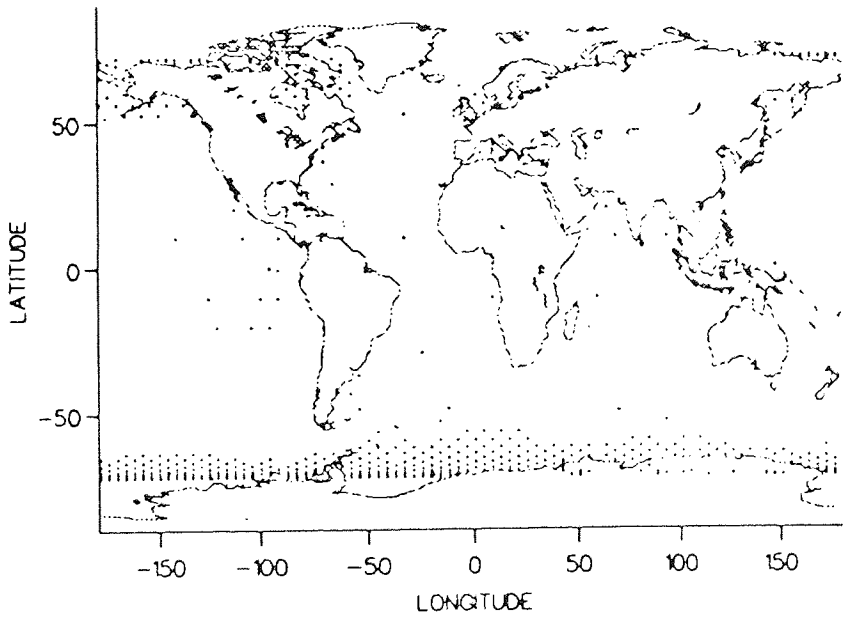

Figure (6.73)
Crossover residuals rejected during SEASAT triple arc analysis

§ 6.12 Conclusions

Using the radial reduction arc aggregate techniques introduced, the SEASAT analyses have served to validate the proposed radial orbit error reduction procedure. Given a greater spread of direct radial height observations and altimetric data less

corrupted by sea ice, it should be possible to reduce the global radial orbit error of similar altimetric satellites to less than 20cm over a prolonged period of time, such as the 35 day repeat orbit proposed for ERS-1.

CHAPTER 7

ERS-1 SIMULATIONS

§ 7.1 ERS-1 Mission

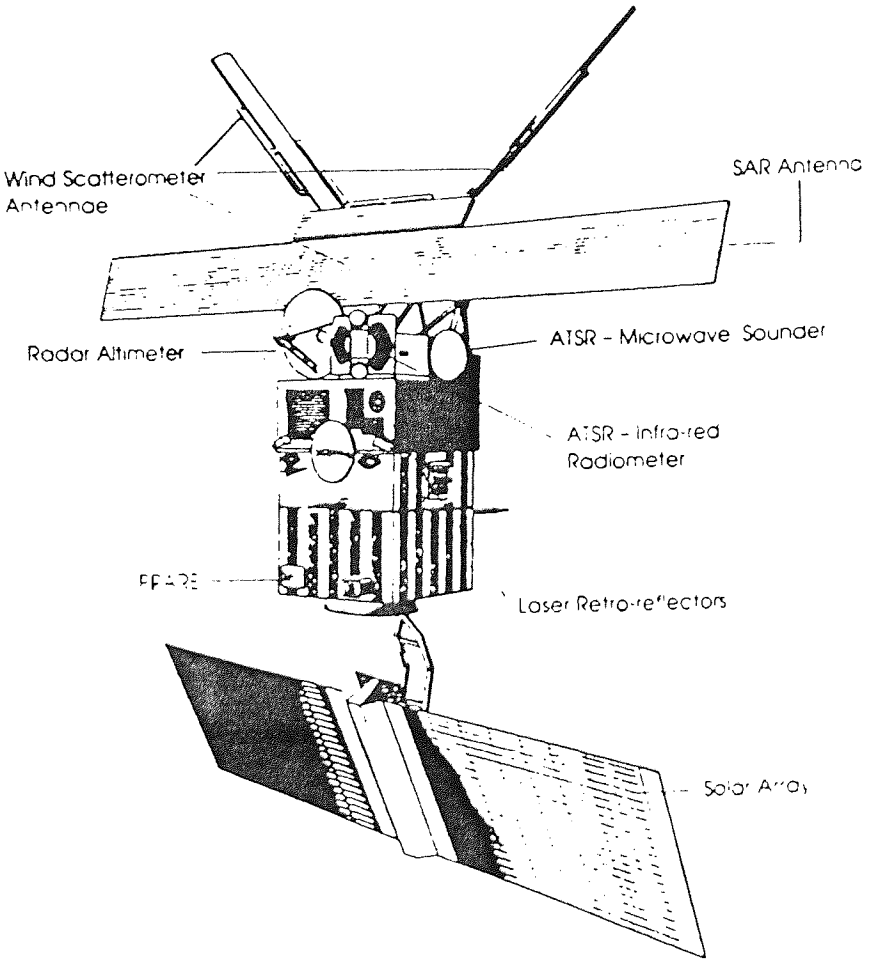

Figure (7.1)
ERS-1

Figure (7.1) shows the European Remote Sensing satellite, ERS-1, launched on July 17th, 1991. The main mission objectives of the most highly sophisticated remote sensing satellite ever launched are to monitor the environment, ice and oceans of the Earth, using the five active microwave instruments on board.

A radar altimeter is employed in the study of the sea surfaces, as for SEASAT, although the satellites differ in that the high inclination of the polar orbit of ERS-1 enables an unprecedented global distribution of data to be gathered, with the spacecraft reaching extremes of latitude 82° north and 82° south. This is 10° further north and south than SEASAT, from which many of the observations of the southern regions were rejected due to the prevalence of sea ice, as described in section §6.11. For precise orbit determination ERS-1 carried a laser retroreflector array and an on-board microwave tracking system, PRARE.

On April 14th, 1992, ERS-1 entered its 35 day repeat orbit, during which the satellite performs 501 nodal revolutions of the Earth in the time taken for the Earth to revolve 35 times relative to the precessing orbital plane. This large number of revolutions coupled with the polar orbit ensures that a dense and almost complete coverage of the ocean surfaces is achieved. This is demonstrated by Figure (7.2), which compares the ground-tracks of the 501 rev/35 day ERS-1 repeat orbit, obtained by amalgamation of the five GEM-T1 derived arcs used in the arc aggregate of section §7.7 and the 3 day SEASAT repeat orbit of Figure (6.2), over the United Kingdom and a section of the North Sea. The highly dense coverage of the ERS-1 orbit is well illustrated.

§ 7.2 Obtaining the Initial Orbit

In order to be able to generate simulated orbits, an initial estimate must be made of the position and velocity of the satellite. The orbit chosen for analysis was the 501 rev/35 day repeat, so it was necessary to construct an orbit that would perform this motion as precisely as possible. That is, over the length of an ephemeris, it was required that the average mean motion, $\bar{n} = \frac{501}{35} \approx 14.314$ revolutions per

day. An estimate can then be made, using equation (3.4), for the initial semi-major axis from this value, i.e.

$$a = \left(\frac{\mu}{\bar{n}^2} \right)^{\frac{1}{3}} \Rightarrow \quad a \approx 7.165097 \text{ MM.}$$

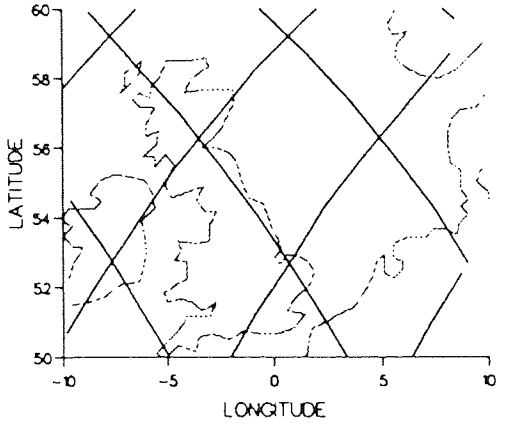

(a) SEASAT 3-day repeat orbit

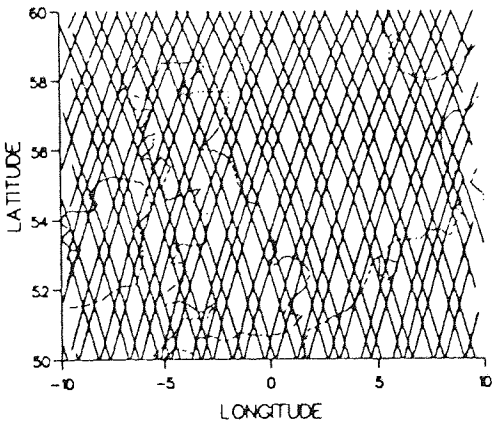

(b) ERS-1 35-day repeat orbit

Figure (7.2)
Ground-track comparison of 43 rev/3 day SEASAT and 501 rev/35 day ERS-1 repeat orbits

The low eccentric, frozen, Sun-synchronous orbit of ERS-1 was planned to have a near circular orbit with values of argument of perigee and right ascension of ascending node given approximately by 90° and 247.07°, respectively, at the beginning of its 35 day repeat orbit. Taking these values as initial estimates and setting the mean anomaly to zero at time t = 0, a value for the inclination was calculated by consideration of the gravitational influence of the Earth on the right ascension [Kaula,1966] and using

$$\dot{\Omega} \approx \frac{2\pi}{365.24 \times 86400} \approx 0.0172 \text{ revs/day},$$

appropriate to a Sun-synchronous orbit, that is an annual revolution of the orbital plane. Expressions for each of the Keplerian elements [Gooding,1981] were then used in an iterative procedure to obtain the initial osculating values given in Table (7.1) for the elements of the simulated orbit.

element	initial value
a	7.1503768 MM
e	0.0019
I	98.53°
ω	90.00°
Ω	247.07°
M	0.00
n	14.359 revs/day

Table (7.1)
Initial osculating elements for ERS-1 simulated orbit

An initial state vector was formed in terms of the position and velocity of the satellite by transforming these elements to rectangular co-ordinates, from which a simulated seven day ephemeris was computed using the GEM-T1 gravity field model. No drag or solar radiation pressure was modelled for this gravitational simulation.

The time elapsed during each complete revolution was recorded. By averaging these over the full seven days, the mean value of the mean motion was obtained. 9959.26 minutes were taken to complete 99 full revolutions of the Earth, with the satellite orbiting at an average mean motion of approximately 14.3143 revs/day ≈ 501.001 revs/35 days, a close approximation to the actual 501 revs/35 day orbit proposed. The duration of individual orbits varied between 100.59 minutes and 100.60 minutes.

§ 7.3 Derivation of the GEM-T1 Clone Gravity Field Model

A simulated data set was completed by calculation of a second ephemeris over the same seven day period, using a different gravity field model, but starting from the same initial conditions and again ignoring drag and solar radiation pressure. The difference between the two orbits is thus due entirely to gravitational effects.

Firstly it was necessary to establish a second gravitational field model. In order to make the simulation as realistic as possible, a clone of the GEM-T1 model was sought which reflected the known covariances of GEM-T1. The standard errors of all the GEM-T1 coefficients up to degree and order 36 were considered. Random perturbations were applied to each, then added to the original coefficient concerned to produce a new set of coefficients which represent the clone gravity field model. Each coefficient is given by

$$COE_{cl} = COE_{GT1} + R\,\sigma \quad , \qquad -(7.1)$$

where COE_{GT1} and σ are the value and standard error, respectively, of a coefficient of the GEM-T1 field model, COE_{cl} is the new derived value of the corresponding coefficient of the clone field and R is a random number.

By creating the clone in this manner, the coefficients that are the source of the greatest gravitational orbit error in arcs derived from real data are likely to be the main contributors to the radial orbit error of the simulation. The perturbations applied to the GEM-T1 field coefficients were adjusted by scaling R such that the radial differences between the new ephemeris derived from the clone and that derived from GEM-T1 reflected values that could realistically be assumed to simulate radial orbit errors.

Identical initial elements to those of Table (7.1) were used to construct a 7 day ephemeris using the clone field model. The average time over all complete revolutions of the Earth of the clone derived orbit was calculated in the same way as for the GEM-T1 derived orbit and was found to be such that the satellite performed an average mean motion of approximately 501.001 revs per 35 days, again a close approximation to the desired orbit.

Two orbits had now been generated. The clone orbit was assumed to represent a calculated ephemeris, while the GEM-T1 represented the corresponding observed orbit. The radial differences between the two over the seven day period are plotted in Figure (7.3).

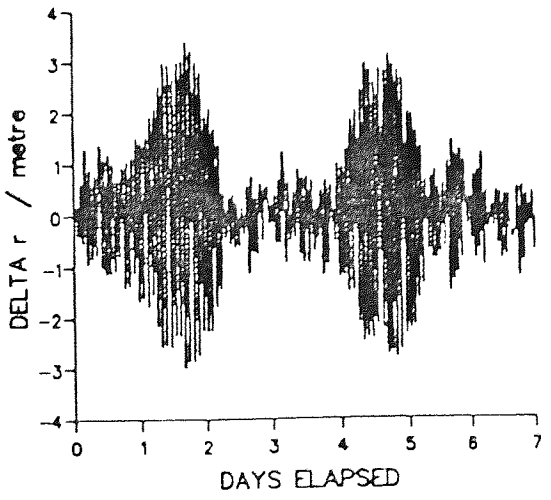

Figure (7.3)
Radial orbit error of 7-day simulation of ERS-1 501 rev/35 day repeat orbit

The (gravitational) radial differences are modelled by equation (3.33) plus a 2nd order secular periodic $\Delta t \sin 2M$ effect. Using equation (6.8), the significant periodic frequency terms less than 2.5 cycles per revolution present for ERS-1 in its 501 rev / 35 day orbit are all those for which k, m satisfy

$$501\,k - 35\,m < 2.5 \times 501 = 1250.$$

This consists of 179 discrete frequencies.

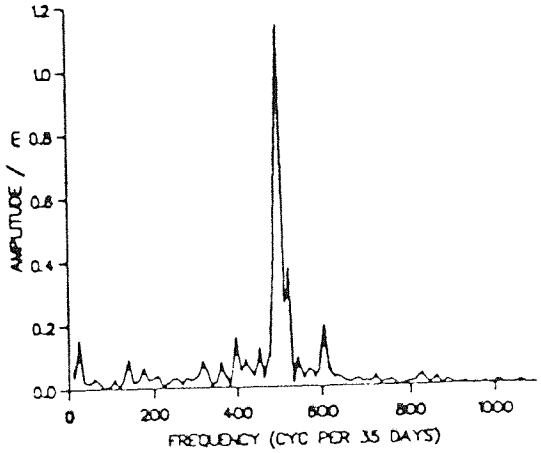

Figure (7.4)
Spectral analysis of radial differences before fit of 7-day ERS-1 simulation solution

A spectral analysis is plotted in Figure (7.4), which was carried out through the radial differences of Figure (7.3) solving for terms at each of these frequencies. As expected the main term present is that at 1 cycle per revolution. No significant contribution is made to the radial differences by terms of frequency greater than approximately 2.14 cycles per revolution, so it was decided that solving for any frequencies above $\frac{1072}{501}$ cyc/rev would be trivial. Thus 308 periodic gravitational coefficients, at the frequencies given in Table (7.2), remained to be recovered by the radial error reduction procedure, plus the constant and two secular periodic terms, making a total of 311 in all. Note that, from Table (7.2), not all periodic frequency multiples of $\frac{1}{501}$ cycles per revolution are present .

k	m	fq	k	m	fq	k	m	fq
1	14	11	2	18	372	1	35	724
2	29	13	1	25	374	3	22	733
2	28	22	3	32	383	0	21	735
1	15	24	0	11	385	4	36	744
0	1	35	1	3	396	-1	7	746
1	13	46	2	17	407	2	7	757
2	30	48	1	26	409	3	21	768
2	27	57	3	31	418	0	22	770
1	16	59	0	12	420	4	35	779
0	2	70	1	2	431	-1	8	781
1	12	81	2	16	442	2	6	792
2	31	83	1	27	444	3	20	803
2	26	92	3	30	453	0	23	805
1	17	94	0	13	455	4	34	814
0	3	105	1	1	466	-1	9	816
1	11	116	2	15	477	2	5	827
2	32	118	1	28	479	3	19	838
2	25	127	3	29	488	0	24	840
1	18	129	0	14	490	4	33	849
0	4	140	1	0	501	-1	10	851
1	10	151	2	14	512	2	4	862
2	33	153	1	29	514	3	18	873
2	24	162	3	28	523	0	25	875
1	19	164	0	15	525	4	32	884
0	5	175	-1	1	536	-1	11	886
1	9	186	2	13	547	2	3	897
2	34	188	1	30	549	3	17	908
2	23	197	3	27	558	0	26	910
1	20	199	0	16	560	4	31	919
0	6	210	-1	2	571	-1	12	921
1	8	221	2	12	582	2	2	932
2	35	223	1	31	584	3	16	943
2	22	232	3	26	593	0	27	945
1	21	234	0	17	595	4	30	954
0	7	245	-1	3	606	-1	13	956
1	7	256	2	11	617	2	1	967
2	36	258	1	32	619	3	15	978
2	21	267	3	25	628	0	28	980
1	22	269	0	18	630	4	29	989
3	35	278	-1	4	641	-1	14	991
0	8	280	2	10	652	2	0	1002
1	6	291	1	33	654	3	14	1013
2	20	302	3	24	663	0	29	1015
1	23	304	0	19	665	4	28	1024
3	34	313	-1	5	676	-1	15	1026
0	9	315	2	9	687	-2	1	1037
1	5	326	1	34	689	3	13	1048
2	19	337	3	23	698	0	30	1050
1	24	339	0	20	700	4	27	1059
3	33	348	-1	6	711	-1	16	1061
0	10	350	2	8	722	-2	2	1072
1	4	361						

Table (7.2)

Frequencies, fq, associated with the periodic gravitational coefficients recovered in analyses of 501 rev/35 day repeat orbits. fq is in units of $\frac{1}{501}$ cycles per revolution.

§ 7.4 Simulated Crossovers

The crossover residuals were found in a similar manner as for the non-gravitational SEASAT analysis of section §6.2. The crossover heights derived within each arc were differenced at each crossover epoch to leave a set of residuals of the form of equation (4.8), with

$$\Delta r (t_i) = r_{GT1} (t_i) - r_{cl} (t_i), \qquad i = 1, 2,$$

and

$$\Delta C = \Delta C_{cl} - \Delta C_{GT1},$$

where the cl and GT1 subscripts represent values associated with the clone ("calculated") and GEM-T1 ("observed") derived ephemerides, respectively.

The crossovers generated are spread across the whole globe. In reality, when crossovers are found from altimetric data, only those over the ocean regions are retained. In order to further increase the realism, it was decided that only points where real altimetric crossovers could become available should be used in the simulation, that is only those over the seas. Hence the results obtained give guidance as to the possibility of obtaining solutions from real data available from similar regions.

Various coastal points over the surface of the Earth were connected along lines of constant latitude or longitude to give an approximate guide as to the location of the continental regions. Thus an approximate map of the world was constructed. Any crossover points falling within the continental boundaries of the map were considered to represent unreliable crossover residuals over land and consequently discarded. Of the 5,731 residuals originally calculated, 4,269 marine crossovers remained.

Prior to launch it was anticipated that ERS-1 would be tracked using PRARE, a satellite-ground-satellite system developed in order to provide a comprehensive global coverage of high quality data. However, shortly after launch the PRARE system failed. Since this study was undertaken before the launch, it has focused on the possibility of using PRARE data to produce the direct radial measurements required to supplement the crossover data. As a result, the locations of the ground stations were selected from those included in the PRARE network. A much better coverage of the Earth would have been achieved using PRARE than that obtained from the laser stations that tracked SEASAT. Six stations were chosen for the simulation, those situated at the Falkland Islands, Greenbelt (U.S.A.), Hartebeestoek (South Africa), Townsville (Australia), Tromsoe (Norway) and Ulan Bator (Mongolia). These are widely distributed to eliminate the problems that arose in the SEASAT study. Ulan Bator in particular was taken deep into the continental regions, where the crossover data had been eliminated. Figure (7.5) and Table (7.3) show the sites selected.

Site	Location	Long. /deg	Lat. /deg
1	Falkland Is.	-57.8	-51.5
2	Ulan Bator	107.1	47.7
3	Hartebeestoek	27.7	-25.7
4	Greenbelt	-76.8	38.8
5	Townsville	146.8	-19.2
6	Tromsoe	18.9	69.5

Table (7.3)
Direct height data sites used in ERS-1 35 day repeat orbit simulations

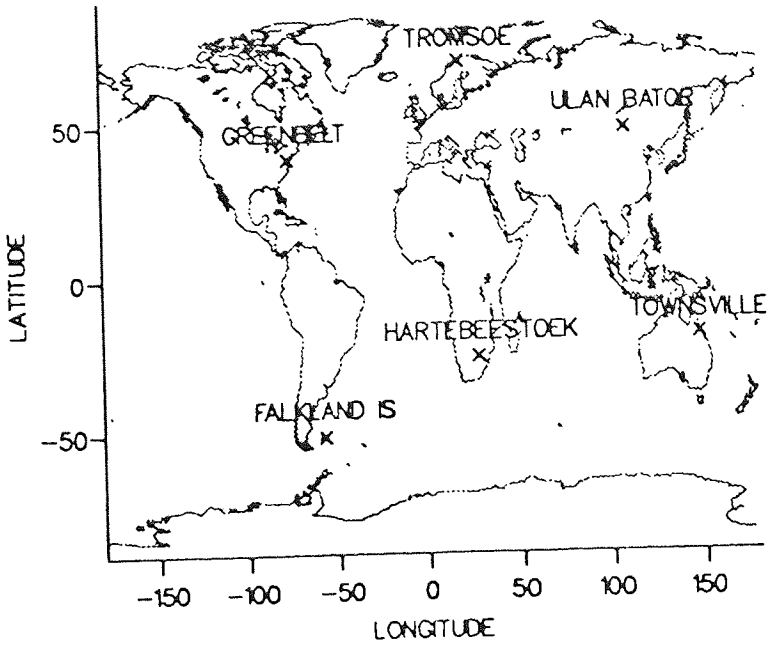

Figure (7.5)
Direct height data sites used in ERS-1 35 day repeat orbit simulations

Figure (7.6) shows the configuration of a satellite at P_{SAT} and PRARE site at P_{STN} relative to the centre of the Earth, O. Angle $\hat{OP}_{STN}P_{SAT}$ ($=\beta$, say) was derived for each ephemeris epoch whenever the satellite passed within the vicinity of a station of Table (7.3). The ephemeris epochs for which the zenith angle ($180° - \beta$) was minimum for each station over the seven days was recorded. The radial distances r_{cl} and r_{GTI} were calculated at each. Then the radial height difference, $\Delta r = r_{GTI} - r_{cl}$ was taken as the direct radial height measurement. Those derived are given in Table (7.4). The six observations, one from each station, were used with an assumed a priori standard error of 5cm to supplement the crossover residuals, to which was applied a standard error of 50cm.

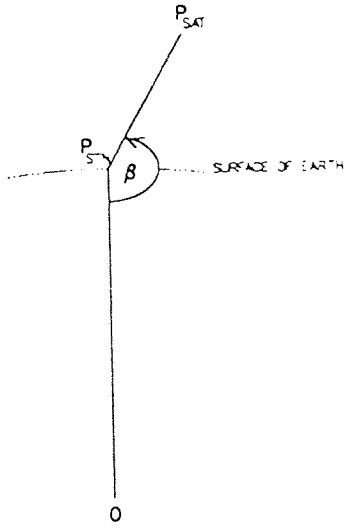

Figure (7.6)
Geometrical configuration used to obtain direct radial height data for ERS-1 35 day repeat orbit simulations

Site	Days Elapsed	Δr/m	s.e. /m	Long. /deg	Lat. /deg	M /deg
2	0.007986	-0.049	0.05	105.4	47.8	49.9
4	0.968403	-1.144	0.05	-76.8	39.6	-51.5
5	1.376042	1.103	0.05	146.4	-19.2	-102.3
3	2.188194	1.169	0.05	26.9	-26.2	117.1
1	2.402778	0.270	0.05	-56.9	-51.4	141.9
6	6.290972	-0.101	0.05	17.6	69.7	18.3

Table (7.4)
Direct radial height data derived for ERS-1 7-day simulation analysis

§ 7.6 Seven Day Long Arc Radial Error Reduction

The 4,269 crossovers and six direct radial height observations were taken as the residual data set and each of the 311 coefficients estimated using the radial error reduction procedure. The results of the converged solution are displayed in Figures (7.7) to (7.14). A good solution has been achieved in terms of the reliability of the

recovered coefficients, with the largest standard error of any derived coefficient being less than 1.5cm.

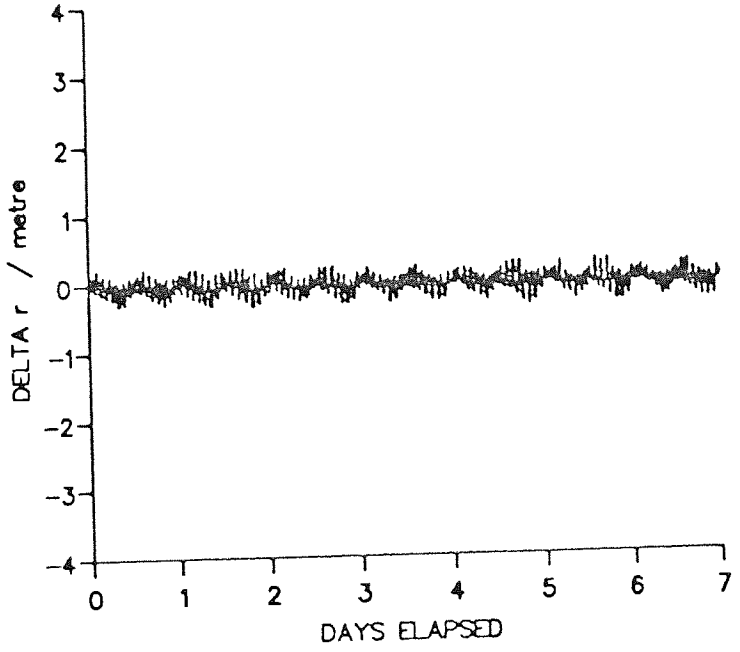

Figure (7.7)
Radial orbit error remaining after fit of ERS-1 7-day simulation solution

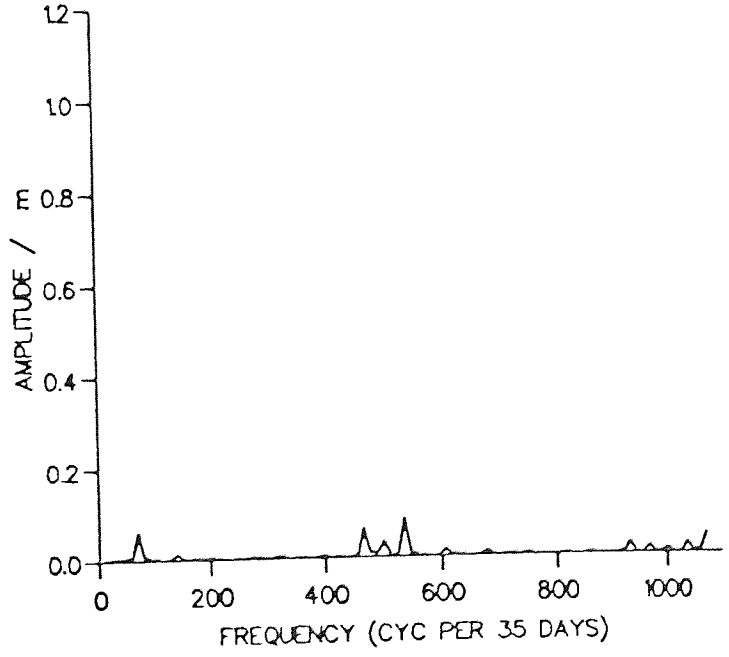

Figure (7.8)
Spectral analysis of radial orbit error remaining after fit of ERS-1 7-day simulation solution

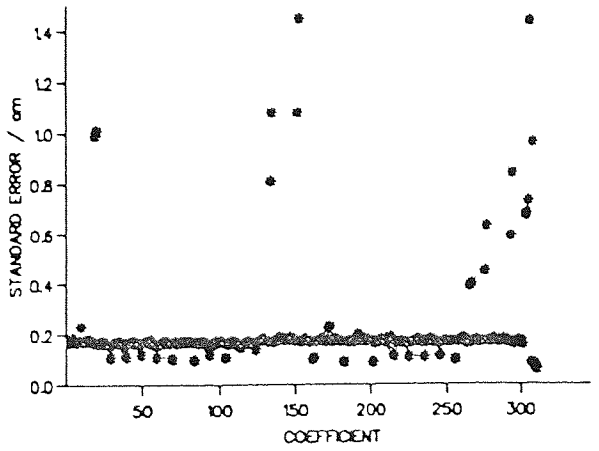

Figure (7.9)
Standard errors of estimated coefficients of ERS-1 7-day simulation solution

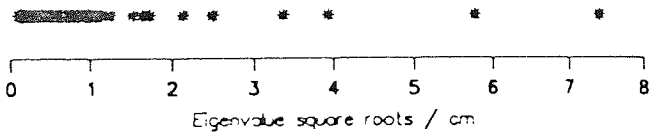

Figure (7.10)
Eigenvalue square roots of ERS-1 7-day simulation solution

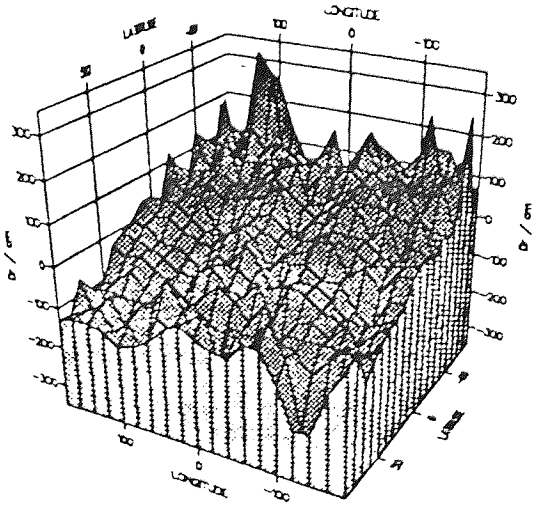

Figure (7.11)
Geographical distribution of mean radial residuals before fit of ERS-1 7-day simulation solution

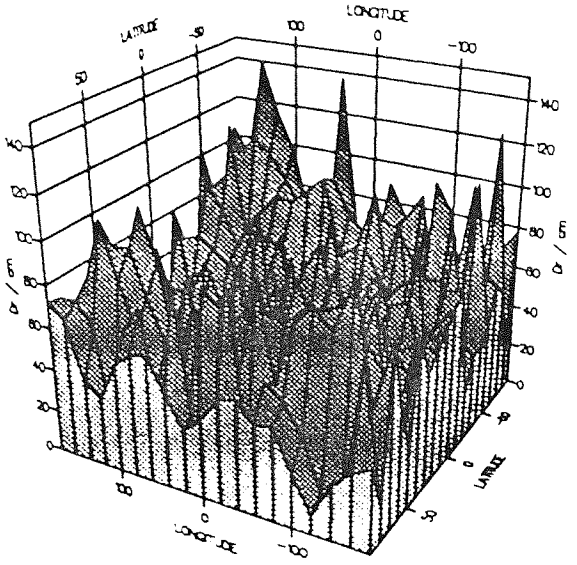

Figure (7.12)
Geographical distribution of radial residual rms error about the mean, before fit of ERS-1 7-day simulation solution

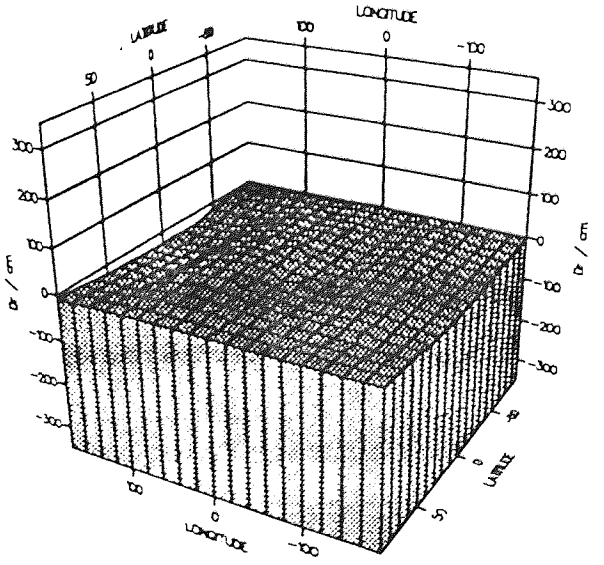

Figure (7.13)
Geographical distribution of mean radial residuals after fit of ERS-1 7-day simulation solution

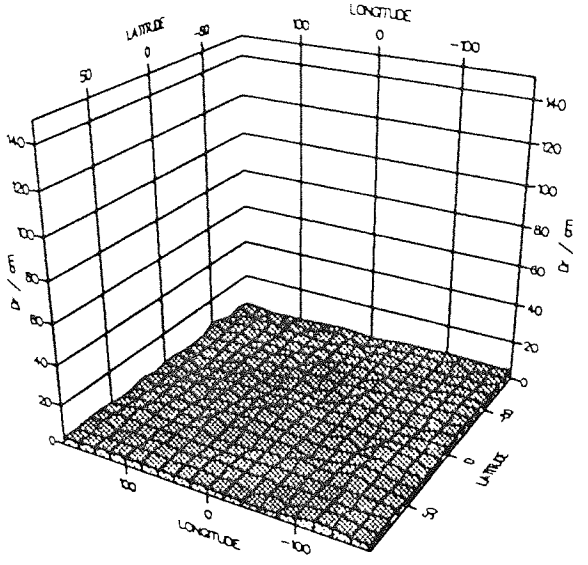

Figure (7.14)
Geographical distribution of radial residual rms error about the mean, after fit of ERS-1 7-day simulation solution

The estimates of each coefficient were substituted back into the radial correction formula and added to the radial differences at each ephemeris epoch of Figure (7.3) to produce the final post-solution radial residuals shown in Figure (7.7). The radial error has been greatly reduced at all frequencies, as demonstrated by comparison of the spectral analysis of the post-solution residuals of Figure (7.8) with that of the pre-solution residuals of Figure (7.4). The radial residuals have been reduced from a pre-solution rms of 1.09 metres before applying the method to only 11.8cm afterwards, with the maximum of 3.58m reduced to 38.4cm. The geographical plots of Figures (7.11) to (7.14) illustrate how well reduced the errors are over all regions of the world. Although more coefficients were recovered than for the SEASAT single arc analysis, that is 311 instead of 224, the extra crossover data

and the lack of corrupt data points provided by the 35 day repeat orbit simulation have served to produce an even more stable global solution over the seven days.

§ 7.7 Arc Aggregates

In order to extend the simulations to more than one arc, further ephemerides were derived in the same manner as before. The initial state values used to generate a successive "observed" ephemeris using the GEM-T1 gravity field model were taken as the final state values from the previous GEM-T1 arc. Thus continuous observational arcs were simulated. The absence of drag modelling means that a successive generation can be carried out in which the simulated orbit under the influence of the GEM-T1 field will still result in a close approximation to the 501 rev / 35 day repeat orbit.

A similar situation would arise using the "calculated" clone derived orbit. However, a misclosure was introduced to simulate the misclosure that would invariably arise using real data, by taking the initial state vector of the second clone derived ephemeris to be the mean of the differences in position and velocity between the endpoints of the GEM-T1 and clone derived ephemerides of the earlier arcs, that is the initial position and velocity, respectively, of the second clone derived orbit, are given by

$$\underline{s}_I = \frac{1}{2}\left(\underline{x}_{cl} + \underline{x}_{GT1} \right)$$

and

$$\dot{\underline{s}}_I = \frac{1}{2}\left(\dot{\underline{x}}_{cl} + \dot{\underline{x}}_{GT1} \right) ,$$

where $\underline{x}_{cl}$ and $\underline{x}_{GT1}$ denote the final satellite positions of the previous arc according to the clone and GEM-T1 derived orbits, respectively. The radial differences over the full 14 days are depicted in Figure (7.15), which includes the

radial misclosure after 7 days. Figure (7.16) is a spectral analysis through these residuals. The equation of the misclosure is found by substituting the appropriate values into an expression of the form of equation (6.11) and is included as an infallible observation in a similar manner to that of the SEASAT analysis. Seven days after the start of the analysis, the radial misclosure was calculated to be approximately -0.203m and the mean anomaly approximately 70.2°.

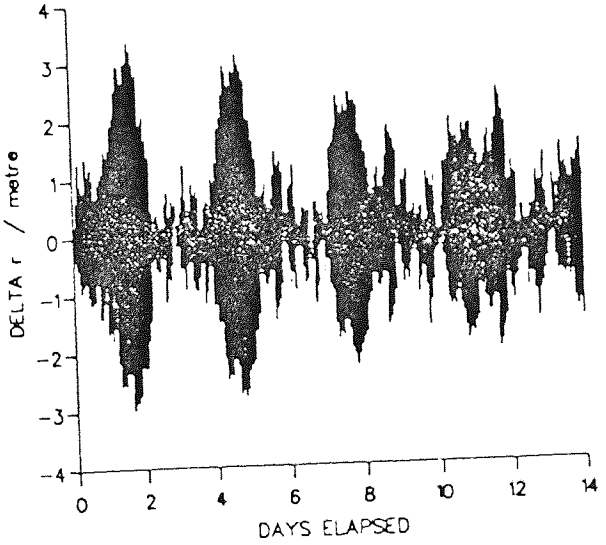

Figure (7.15)
Radial orbit error before fit of ERS-1 14-day simulation solution

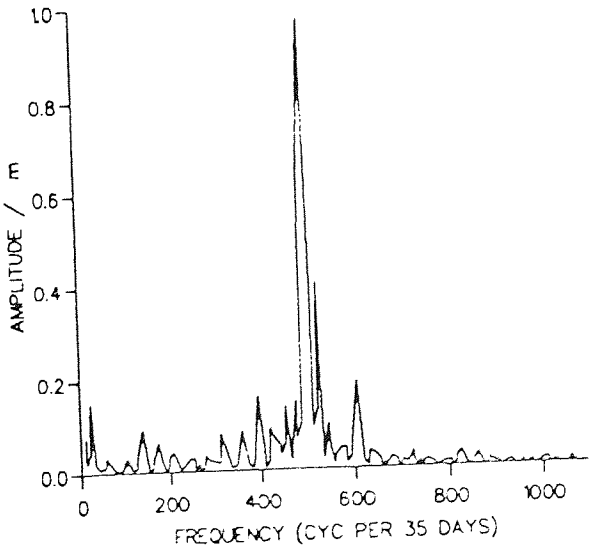

Figure (7.16)
Spectral analysis of radial orbit error before fit of ERS-1 14-day simulation solution

A second direct radial measurement was derived from each of the sites included in Table (7.3). The crossover residuals within the second arc were produced in the usual manner. In order to obtain the crossovers that straddle the misclosure, the successive ephemerides were compared by effectively superimposing the complete global ground-track from which the first seven day orbit was derived onto the corresponding ground-track for the following seven days. Any points of intersection between the two separate ground-tracks represent the positions of crossover points across the discontinuity between the successive orbits. The radial height differences according to the clone and the GEM-T1 derived ephemerides were calculated, then differenced to produce the desired residuals of the form of equation (4.8). Those over land areas were filtered out as before to leave 7,386 across the misclosure to be added to the 4,269 from the first seven day simulation and the 4,297 within the second seven days, a total of 16,952 crossovers altogether, supplemented by the 12 direct radial height measurements derived. An additional seven arc dependent coefficients were included in the 318 terms sought by the radial error reduction carried out.

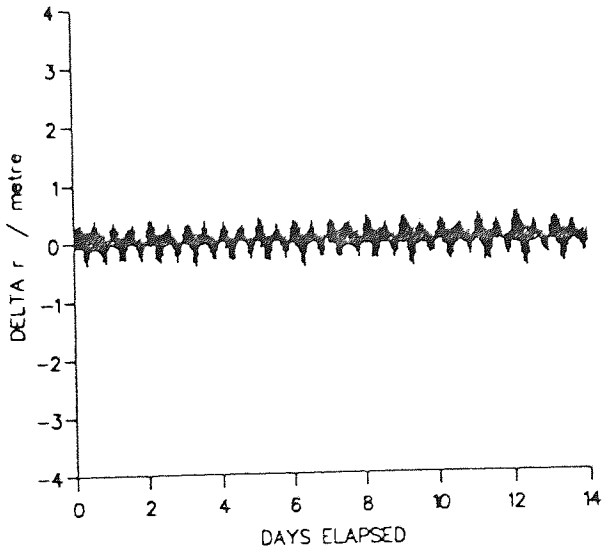

Figure (7.17)
Radial orbit error after fit of ERS-1 14-day simulation solution

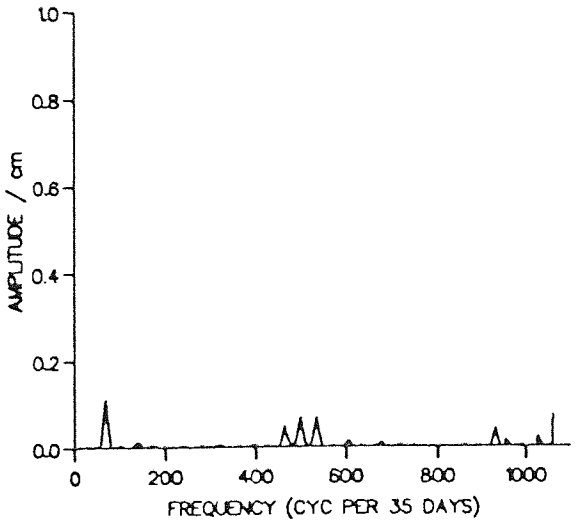

Figure (7.18)
Spectral analysis of radial orbit error after fit of ERS-1 14-day simulation solution

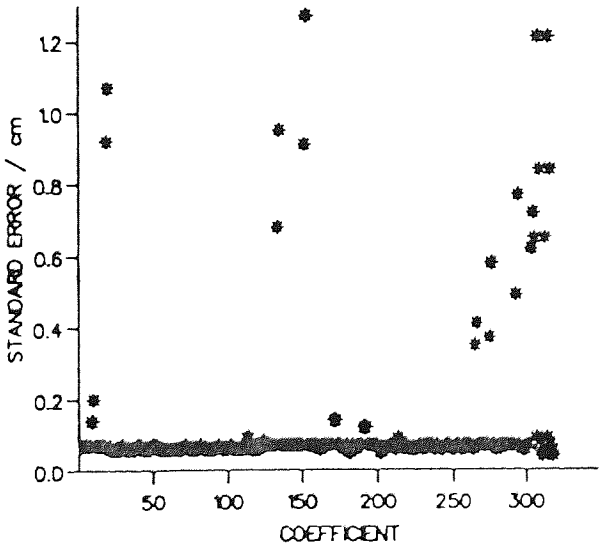

Figure (7.19)
Standard errors of estimated coefficients of ERS-1 14-day simulation solution

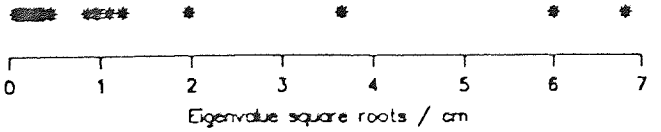

Figure (7.20)
Eigenvalue square roots of ERS-1 14-day simulation solution

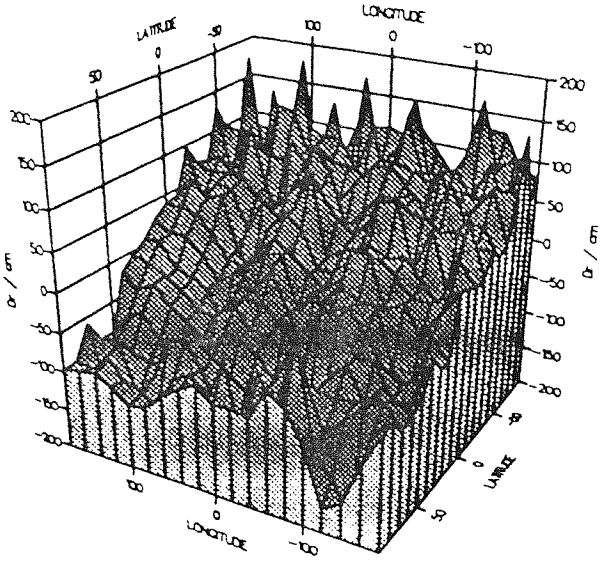

Figure (7.21)
Geographical distribution of mean radial residuals before fit of ERS-1 14-day simulation solution

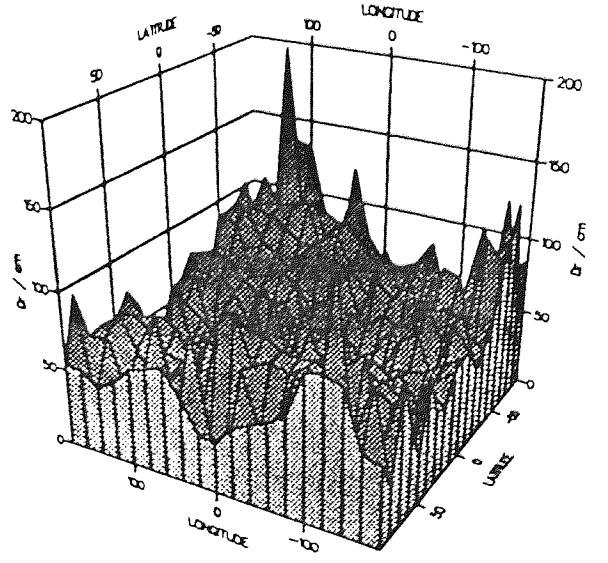

Figure (7.22)
Geographical distribution of radial residual rms error about the mean, before fit of ERS-1 14-day simulation solution

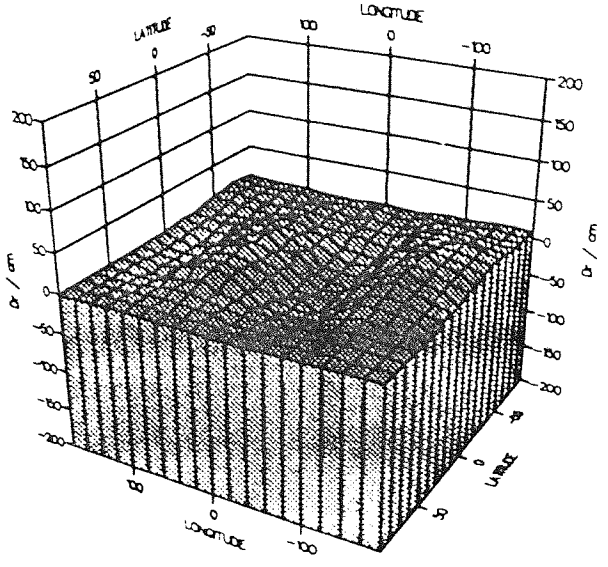

Figure (7.23)
Geographical distribution of mean radial residuals after fit of ERS-1 14-day simulation solution

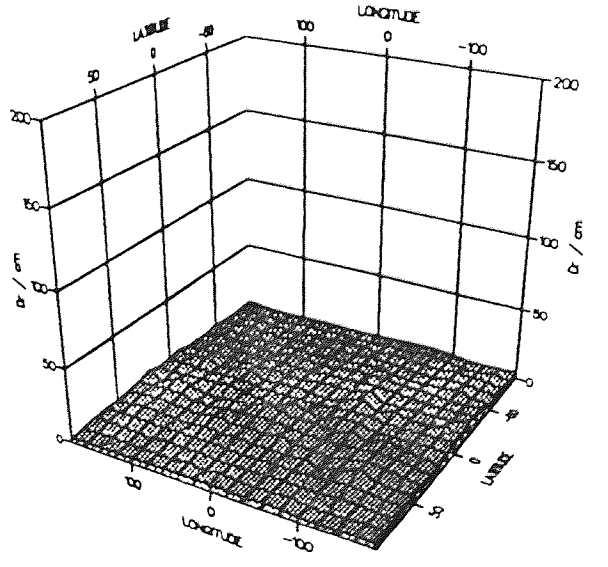

Figure (7.24)
Geographical distribution of radial residual rms error about the mean, after fit of ERS-1 14-day simulation solution

The results displayed in Figures (7.17) to (7.24) confirm the success of the double arc aggregate. Over the full 14 days, the radial orbit error after fit has fallen by 86.2%, from 100.5cm to 13.9cm. Terms at all frequencies have been resolved globally and the standard error of the worst determined coefficient is only 1.3cm. The square root of the maximum eigenvalue is 6.8cm, due to the cumulative effects of the errors from each of the 318 coefficients.

The extension of the arc aggregate method to three arcs results in a relatively poor recovery of the global error. After convergence of the solution, the rms has fallen from 94.1cm to 27.3cm, a less dramatic reduction than was the case for two arcs (see Figure (7.25) and Figure (7.26)).

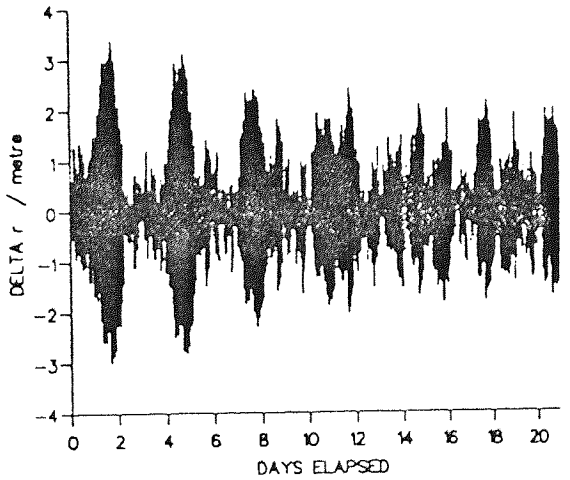

Figure (7.25)
Radial orbit error before fit of ERS-1 21-day simulation solution

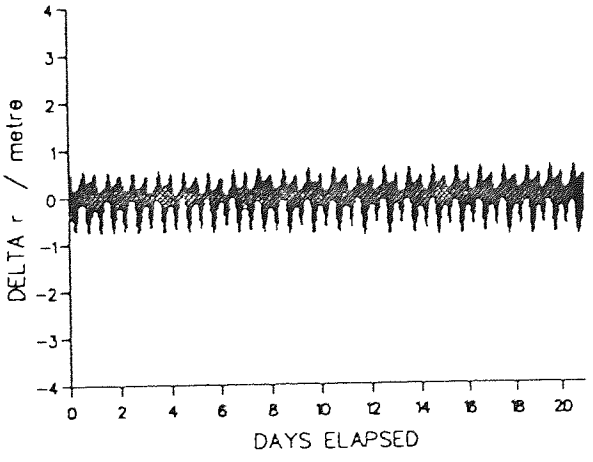

Figure (7.26)
Radial orbit error after fit of ERS-1 21-day simulation solution

Figure (7.27) and Figure (7.28) portray the spectral analyses of the pre- and post-solution radial residuals, respectively. Significant signatures remain at several frequencies after solution. In particular, coefficients of terms at the frequency of the linear combinations described in section §4.5 have not been well retrieved. Confirmation of this is provided by Figure (7.29), which shows that the coefficients of these frequencies are ill-determined.

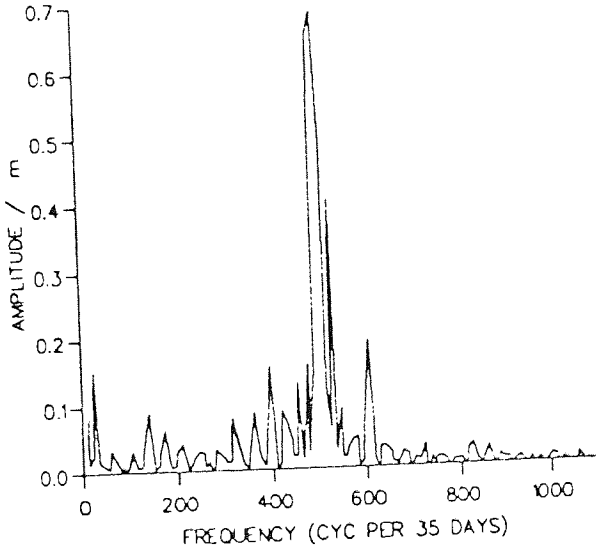

Figure (7.27)
Spectral analysis of radial orbit error before fit of ERS-1 21-day simulation solution

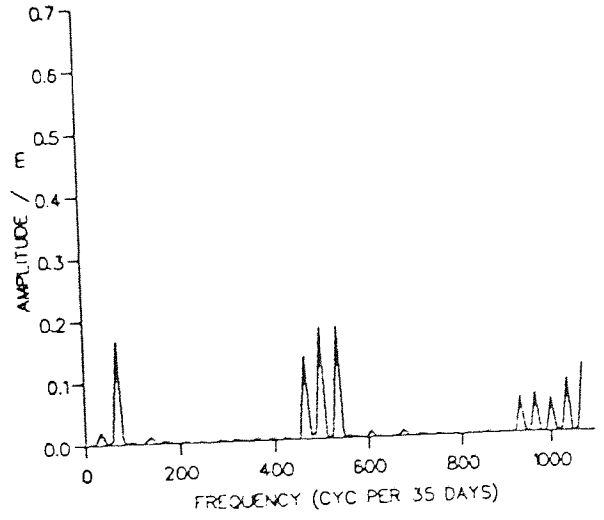

Figure (7.28)
Spectral analysis of radial orbit error after fit of ERS-1 21-day simulation solution

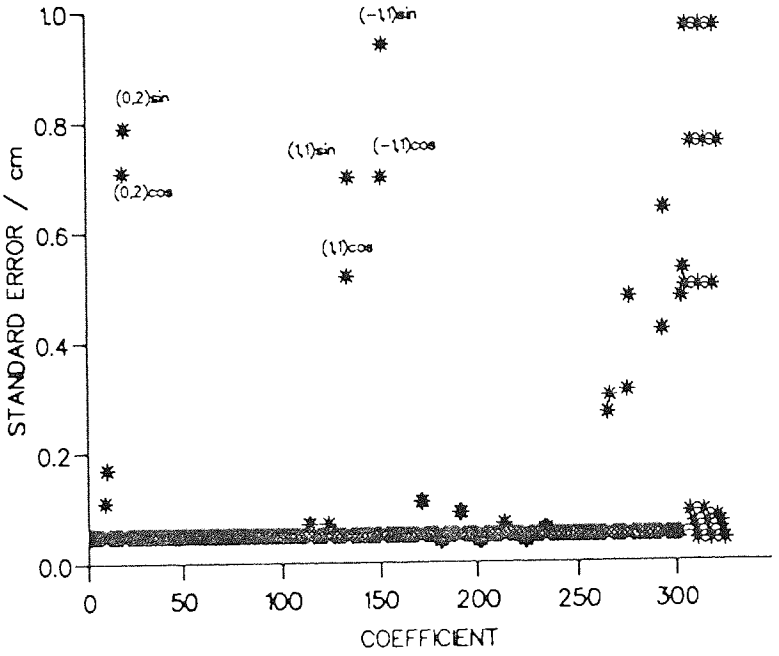

Figure (7.29)
Standard errors of estimated coefficients of ERS-1 21-day simulation solution

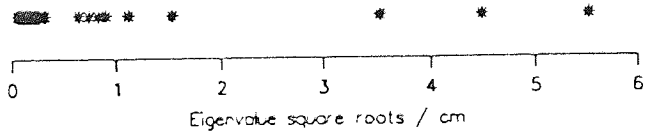

Figure (7.30)
Eigenvalue square roots of ERS-1 21-day simulation solution

Consequently it was suspected that the extra six direct radial height measurements introduced have provided insufficient information to combat the problems associated with the linear combinations arising from the additional 21,091 crossovers. Therefore the procedure was repeated with the (k,m) = (0,2) frequency terms suppressed. This had the desired effect and as Figures (7.31) to (7.38) illustrate, a good solution has been achieved, with all coefficients well determined.

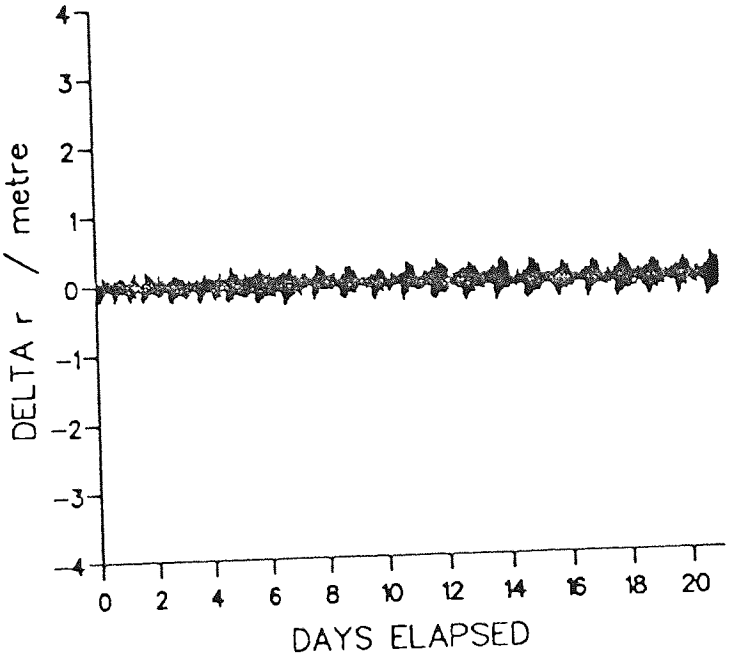

Figure (7.31)
Radial orbit error remaining after fit of ERS-1 21-day simulation solution, with (k,m) = (0,2) frequency terms suppressed

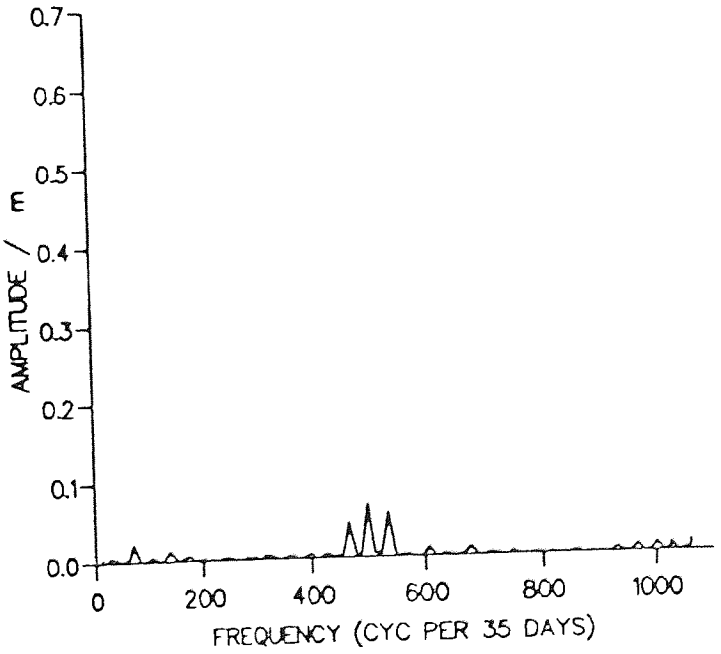

Figure (7.32)
Spectral analysis of radial orbit error remaining after fit of ERS-1 21-day simulation solution, with (k,m) = (0,2) frequency terms suppressed

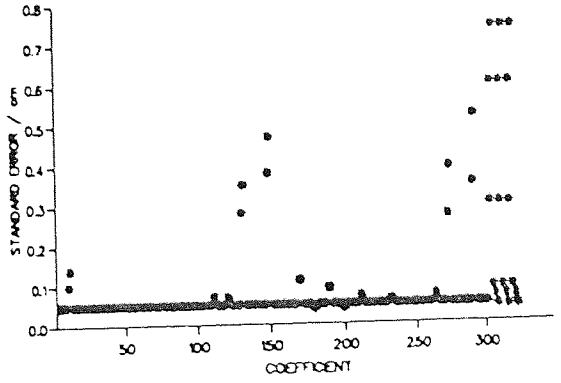

Figure (7.33)
Standard errors of estimated coefficients of ERS-1 21-day simulation solution, with (k,m) = (0,2) frequency terms suppressed

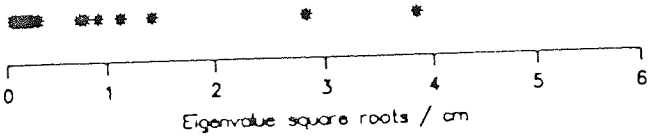

Figure (7.34)
Eigenvalue square roots of ERS-1 21-day simulation solution, with (k,m) = (0,2) frequency terms suppressed

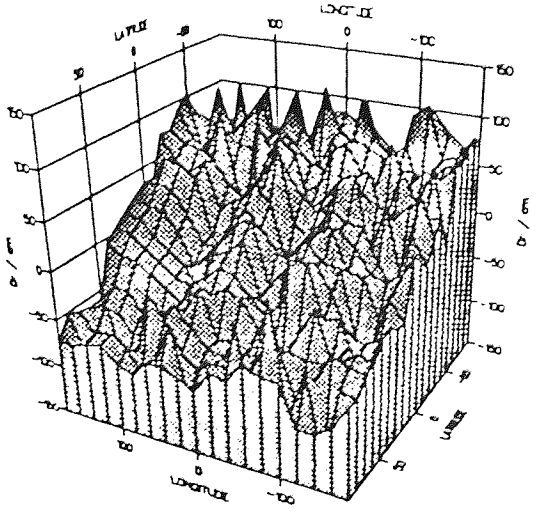

Figure (7.35)
Geographical distribution of mean radial residuals before fit of ERS-1 21-day simulation solution

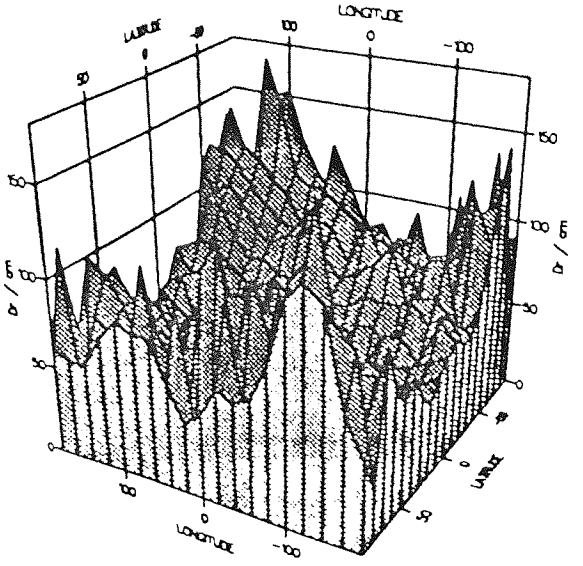

Figure (7.36)
Geographical distribution of radial residual rms error about the mean, before fit of ERS-1 21-day simulation solution

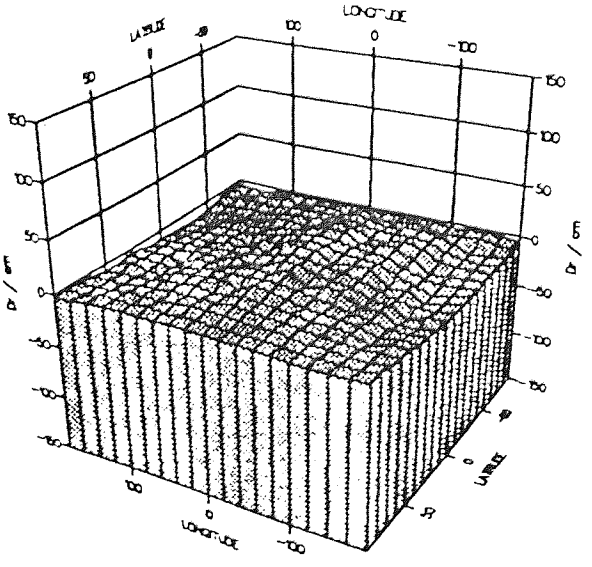

Figure (7.37)
Geographical distribution of mean radial residuals after fit of ERS-1 21-day simulation solution, with (k,m) = (0,2) frequency terms suppressed

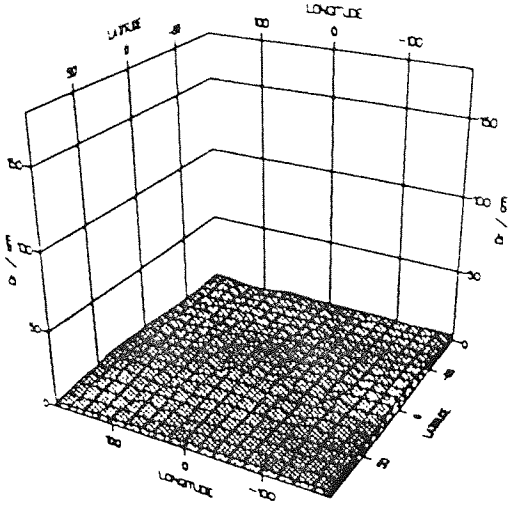

Figure (7.38)
Geographical distribution of radial residual rms error about the mean, after fit of ERS-1 21-day simulation solution, with (k,m) = (0,2) frequency terms suppressed

The quadruple arc aggregate analysis was similarly problematical with suppression of the (0,2) frequency terms again necessary to overcome the ill-conditioning. Eventually the solution is comparable with the previous results involving one, two and three arcs. The eventual results for the four successive arc aggregate are shown in Figures (7.39) to (7.48).

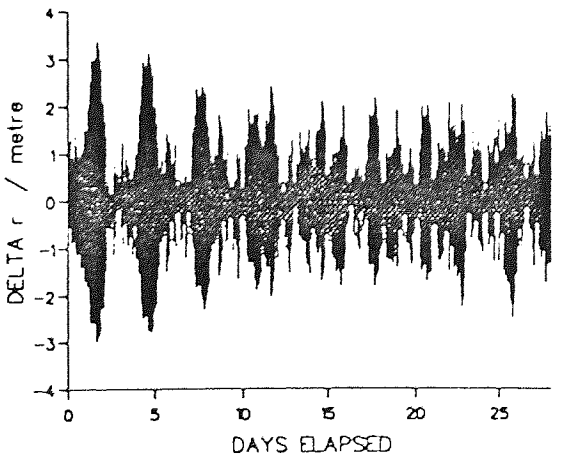

Figure (7.39)
Radial orbit error before fit of ERS-1 28-day simulation solution

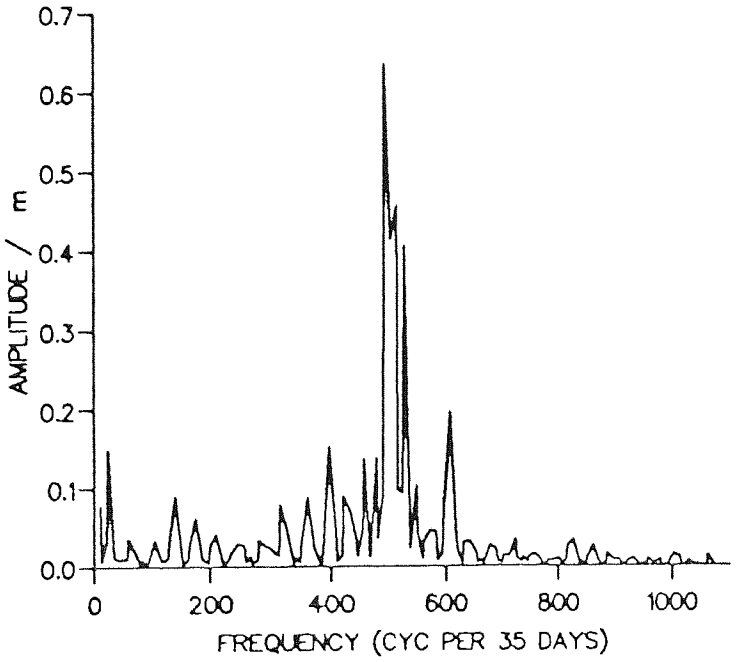

Figure (7.40)
Spectral analysis of radial orbit error before fit of ERS-1 28-day simulation solution.

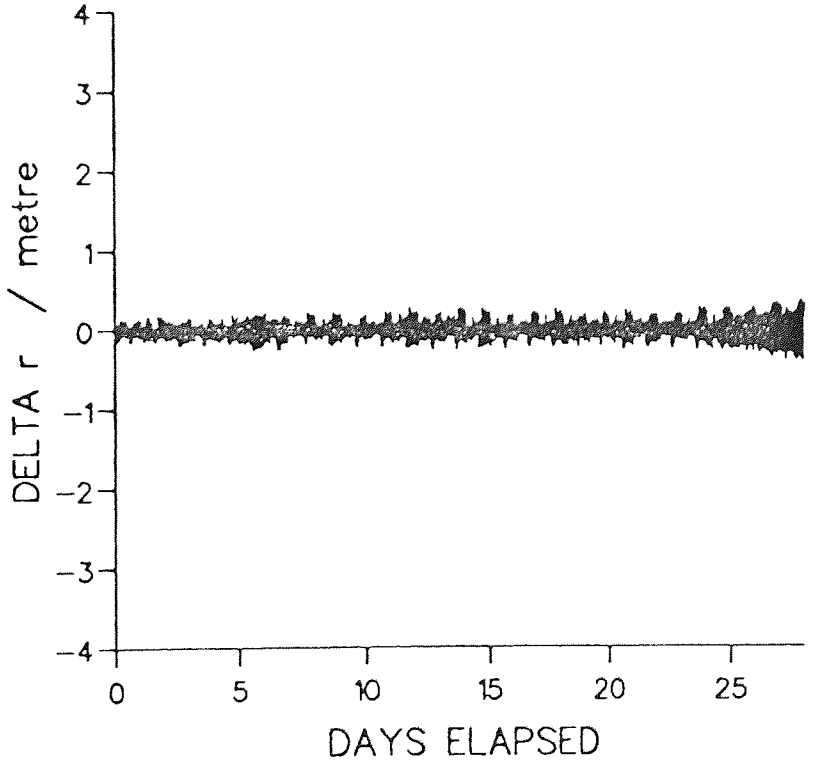

Figure (7.41)
Radial orbit error remaining after fit of ERS-1 28-day simulation solution, with (k,m) = (0,2) frequency terms suppressed

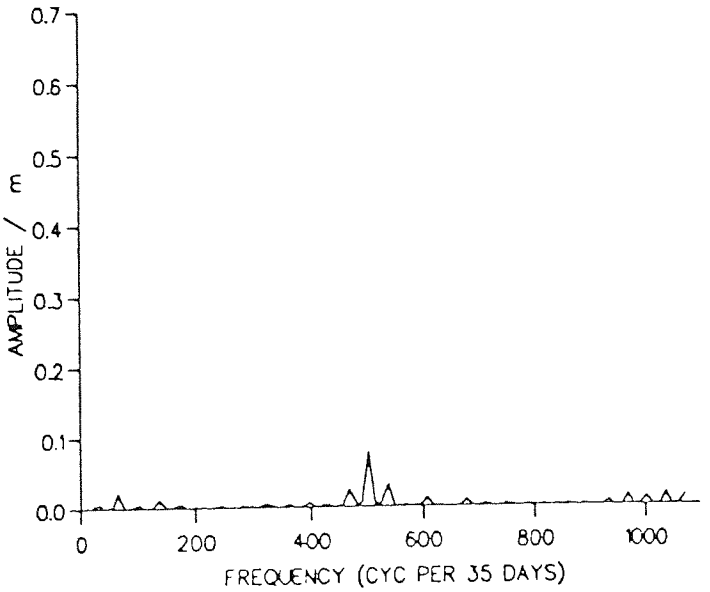

Figure (7.42)
Spectral analysis of radial orbit error remaining after fit of ERS-1 28-day simulation solution, with (k,m) = (0,2) frequency terms suppressed

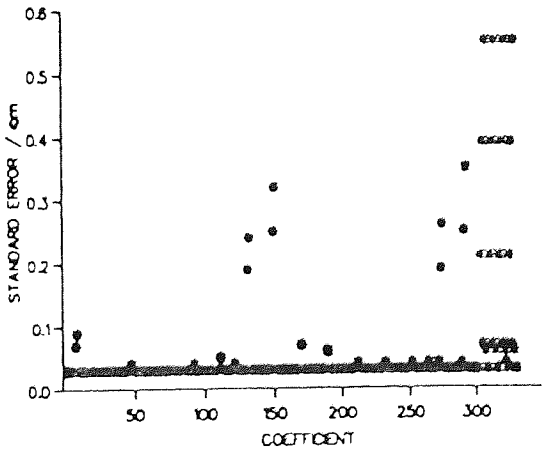

Figure (7.43)
Standard errors of estimated coefficients of ERS-1 28-day simulation solution, with (k,m) = (0,2) frequency terms suppressed

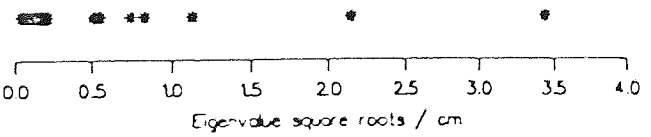

Figure (7.44)
Eigenvalue square roots of ERS-1 28-day simulation solution, with (k,m) = (0,2) frequency terms suppressed

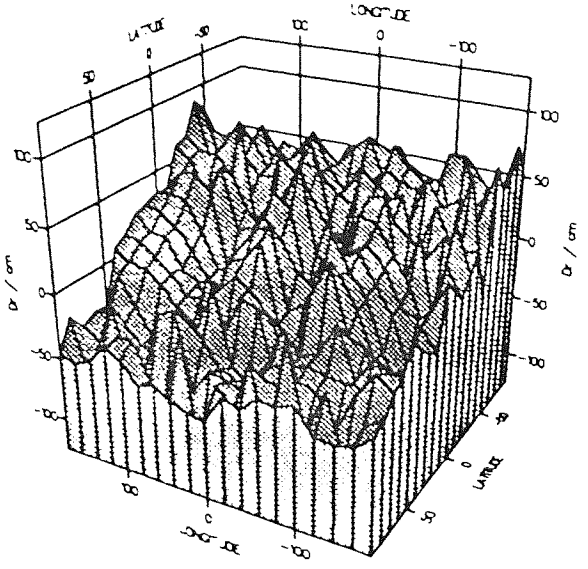

Figure (7.45)
Geographical distribution of mean radial residuals before fit of ERS-1 28-day simulation solution

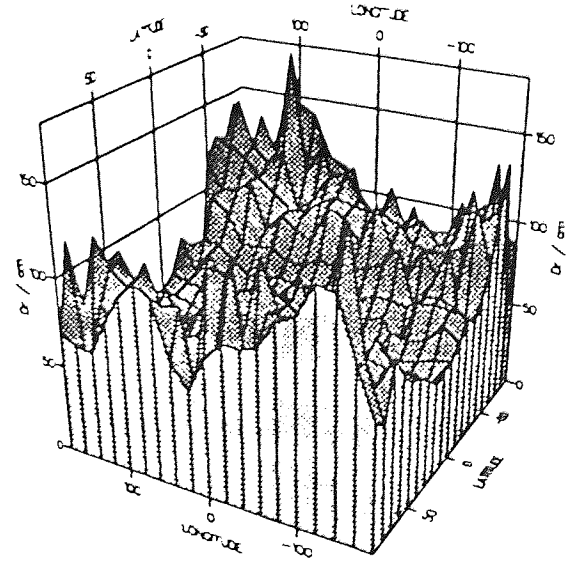

Figure (7.46)
Geographical distribution of radial residual rms error about the mean, before fit of ERS-1 28-day simulation solution

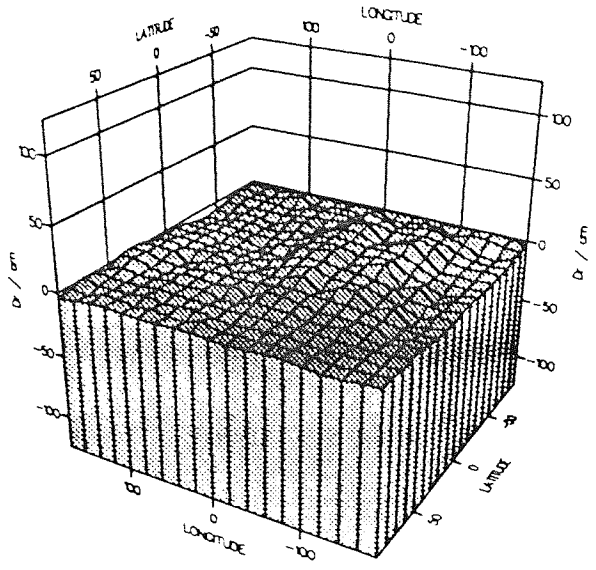

Figure (7.47)
Geographical distribution of mean radial residuals after fit of ERS-1 28-day simulation solution, with (k,m) = (0,2) frequency terms suppressed

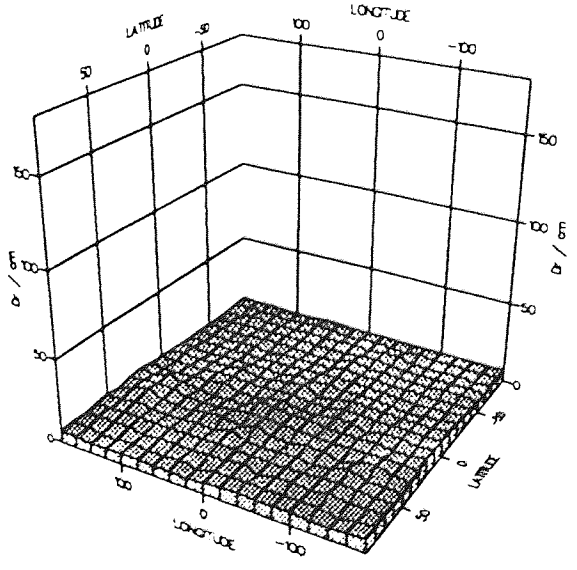

Figure (7.48)
Geographical distribution of radial residual rms error about the mean, after fit of ERS-1 28-day simulation solution, with (k,m) = (0,2) frequency terms suppressed

Finally, the full 35 day repeat orbit, incorporating 4 misclosures, was analysed. This time there was no requirement for suppression of any coefficient and the full solution is shown in Figures (7.49) to (7.58). A highly reliable reduction of the radial orbit error to 16.4cm (≈ 82%) has been achieved.

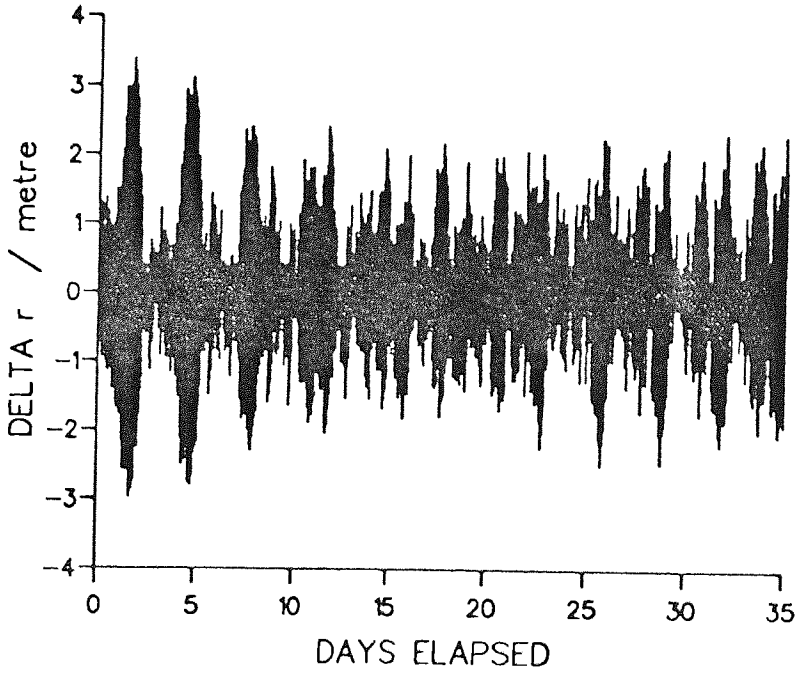

Figure (7.49)
Radial orbit error before fit of complete ERS-1 35-day repeat orbit simulation solution

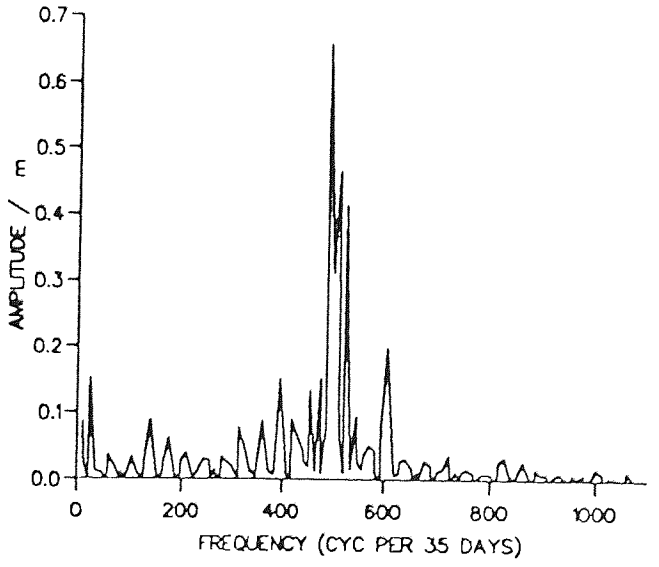

Figure (7.50)
Spectral analysis of radial orbit error before fit of complete ERS-1 35-day repeat orbit simulation

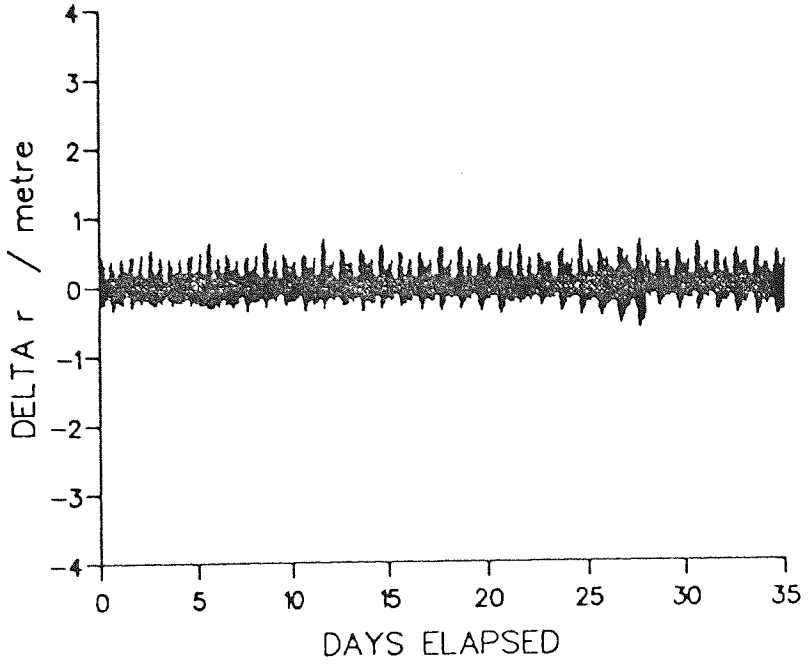

Figure (7.51)
Radial orbit error remaining after fit of complete ERS-1 35-day repeat orbit simulation solution

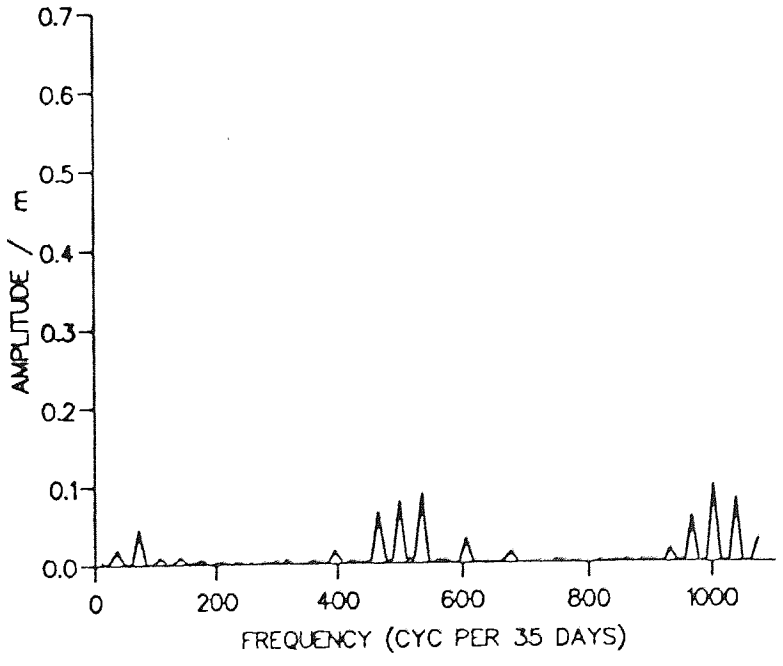

Figure (7.52)
Spectral analysis of radial orbit error remaining after fit of complete ERS-1 35-day repeat orbit simulation solution

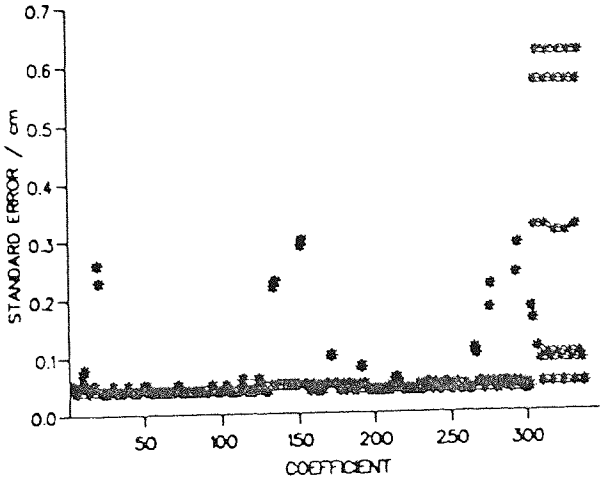

Figure (7.53)
Standard errors of estimated coefficients of complete ERS-1 35-day repeat orbit simulation solution

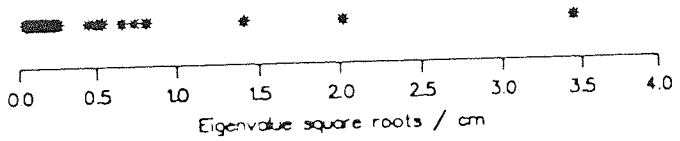

Figure (7.54)
Eigenvalue square roots of complete ERS-1 35-day repeat orbit simulation solution

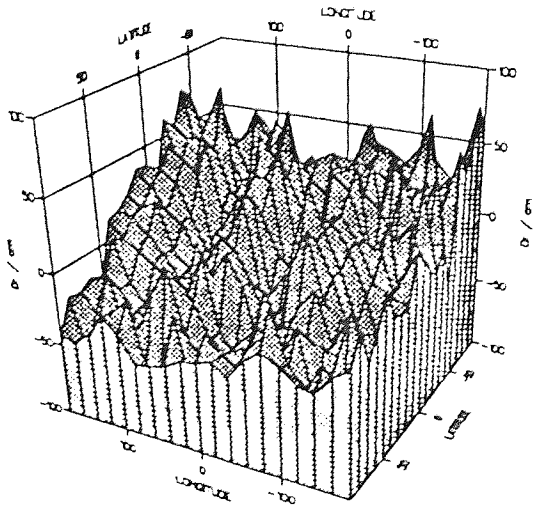

Figure (7.55)
Geographical distribution of mean radial residuals before fit of complete ERS-1 35-day repeat orbit simulation solution

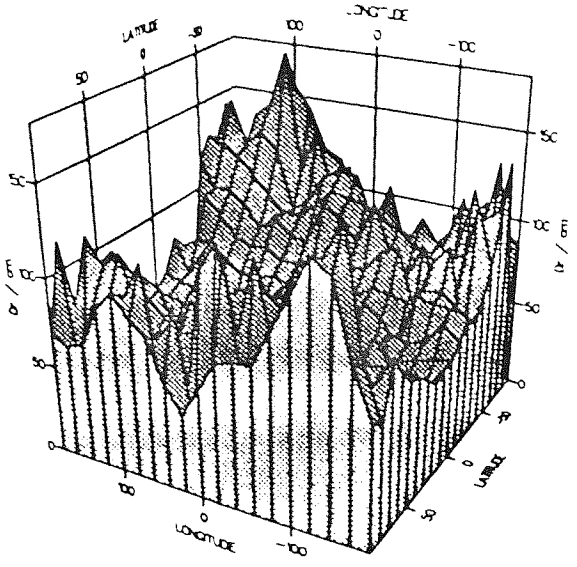

Figure (7.56)
Geographical distribution of radial residual rms error about the mean, before fit of complete ERS-1 35-day repeat orbit simulation solution

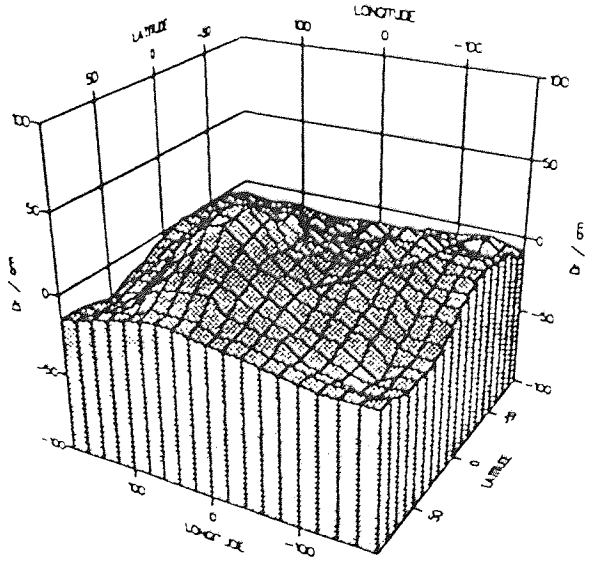

Figure (7.57)
Geographical distribution of mean radial residuals after fit of complete ERS-1 35-day repeat orbit simulation solution

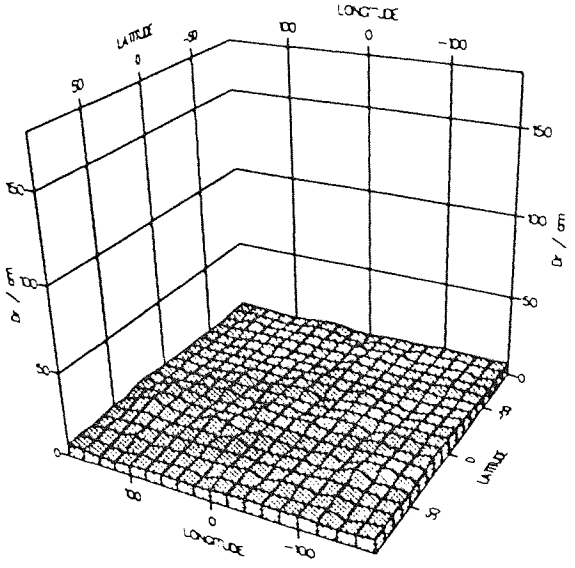

Figure (7.58)
Geographical distribution of radial residual rms error about the mean, after fit of complete ERS-1 35-day repeat orbit simulation solution

The arc aggregate solutions are summarised in Table (7.5) and all the solutions culminating in that of the complete repeat orbit of 35 days are compared in Figure (7.59). The overall stability is improved as more crossover residuals are introduced to the data set. The full 35 days is one repeat period and thus all crossovers are not included until the final five arc aggregate. Progressively more time will have elapsed between crossover epochs as more arcs are added. Therefore the tesseral frequency terms which, through the right ascension of the ascending node, Ω, and the Greenwich mean sidereal angle, θ_g, depend on the time elapsed between the crossover epochs and the explicitly time dependent terms of the radial correction expression will benefit not only from the additional data but because any slight miscalculations in individual crossover epochs, Ω or θ_g should become less significant over longer time spans and when more data is included. The solutions

shown for the 3 and 4 arc aggregates are those obtained upon suppression of the (k,m) = (0,2) frequency terms.

Arcs	Total Crossovers	Direct Heights	Δr_{rms} /cm (before)	Δr_{rms} /cm (after)	$s.e._{max}$ /cm	$\sqrt{ev}_{max}$ /cm
1	4,269	6	109.4	11.8	1.5	7.4
2	16,952	12	100.5	13.9	1.3	6.8
3	38,043	18	94.1	9.3	0.8	3.8
4	67,827	24	91.3	9.7	0.5	3.4
5	106,026	30	90.9	16.4	0.6	3.5

Table (7.5)
ERS-1 simulated five arc aggregate summary

§ 7.8 Conclusions

The ERS-1 simulations have been a resounding success. All 35 days of the repeat period have been analysed and the simultaneous recovery of each of the 339 coefficients has been achieved with high accuracy, using only six of the proposed sites anticipated for use in PRARE. The spacial distribution and magnitude of the residuals employed in the study are realistic and should be agreeable with actual data when it becomes available. Therefore it can be reasonably assumed that application of the radial orbit error reduction procedure will produce similar results to those derived here, over the whole continuous time span of lengthy repeat orbits.

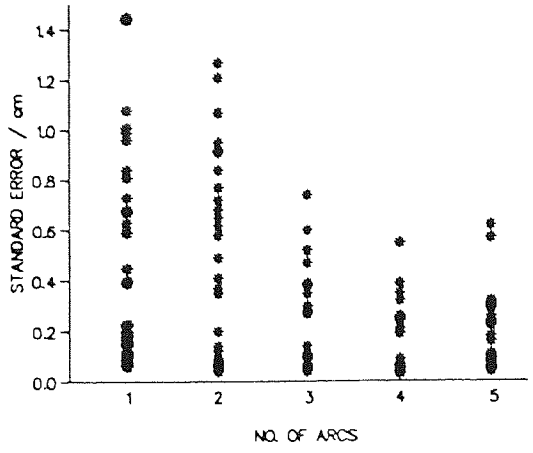

(i) Standard errors of estimated coefficients

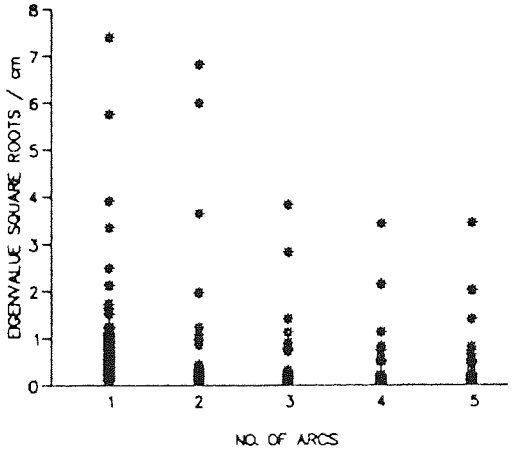

(ii) Eigenvalue square roots of solutions

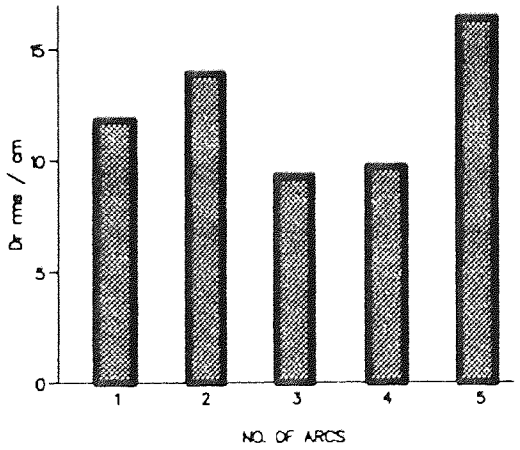

(iii) Post-solution rms radial orbit error

Figure (7.59)
Comparison of ERS-1 simulated arc aggregate solutions

CHAPTER 8

ERS-1 TRANSPONDER ANALYSIS

The altimeter on board ERS-1 can be programmed to receive altimetric radar pulses returned by transponders placed at known locations about the surface of the Earth. Transponders are electronic instruments that receive radar signals, amplify and then re-transmit the signal. Previously only employed on board communication satellites for the purposes of tracking from radars on Earth, ground-based transponders were originally intended for use with ERS-1 primarily as an experiment to provide tracking data to compare range measurements with PRARE and laser ranging observations and to observe slippage of the ground-track over successive repeat orbits. The experiment is being used to demonstrate the basic concept of making precise observations of satellite altitude by "reflecting" the ERS-1 altimeter pulse as the spacecraft passes overhead, as shown in Figure (8.1). Given the lack of short arc data, a study is now undertaken to provide comparisons of the effects of different geographical locations of transponders on the global radial orbit error reduction procedure.

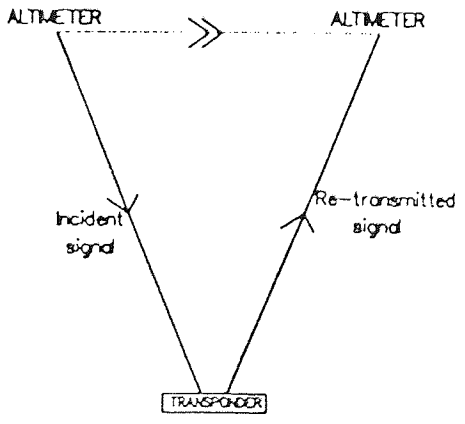

Figure (8.1)
Principle of using a transponder to obtain direct radial height observations

§ 8.1 Short Arc Solution

Phase	Dates	Repeat Period
1 Launch and Early Orbit	July 1991 - Sept 1991	3 days
2 Commissioning	Sept 1991 - Dec 1991	3 days
3 1st Ice	Dec 1991 - April 1992	3 days
4 Multi-Disciplinary	April 1992 - Dec 1993	35 days
5 2nd Ice	Jan 1994 - March 1994	3 days
6 Geodetic	April 1994 - end of mission	176 days

Table (8.1)
ERS-1 mission schedule

The different phases of the ERS-1 mission are given in Table (8.1) [Vass and Handoll,1991]. Following the Launch and Early Orbit Phase, during which various instrument calibrations were carried out, ERS-1 entered its commissioning phase, in which it remained until 12th December, 1991. Early in this period laser ranging data was available from the network of tracking stations. Data from six days during August, 1991, from MJD48469 (1st August) until MJD48475 (7th August) has been considered. Two six day orbits were generated over this time, the first using the GEM-T1 gravity field model and the second using a clone field similar to that included in the 35 day repeat orbit simulations. The GEM-T1 derived ephemeris was considered as the observed orbit and the clone derived ephemeris as the calculated orbit throughout the quasi-simulated analyses that follow.

One of the main purposes of the commissioning phase was to ensure the consistency of oceanographic and meteorological data returned from ERS-1 instruments with those from other sources. As the first new experiments commenced during the first ice phase, including in particular Arctic and Antarctic ice investigations, it was decided to manipulate the data to produce compatibility with that period.

Epoch /MJD	Long. /deg	Epoch /MJD	Long. /deg	Epoch /MJD	Long. /deg
48469.00941	334.13 d	48471.03268	325.76 d	48473.02100	149.96 a
48469.04425	141.59 a	48471.06751	133.22 a	48473.05593	317.38 d
48469.07918	309.02 d	48471.10244	300.64 d	48473.09077	124.84 a
48469.11401	116.47 a	48471.13728	108.10 a	48473.12570	292.27 d
48469.14895	283.90 d	48471.17221	275.52 d	48473.16054	99.73 a
48469.18378	91.36 a	48471.20705	82.99 a	48473.19547	267.15 d
48469.21872	258.78 d	48471.24198	250.41 d	48473.23030	74.61 a
48469.25355	66.24 a	48471.27681	57.87 a	48473.26524	242.04 d
48469.28849	233.67 d	48471.31175	225.29 d	48473.30007	49.50 a
48469.32332	41.12 a	48471.34658	32.75 a	48473.33501	216.92 d
48469.35825	208.55 d	48471.38152	200.18 d	48473.36984	24.38 a
48469.39309	16.01 a	48471.41635	7.64 a	48473.40477	191.80 d
48469.42802	183.43 d	48471.45128	175.06 d	48473.43961	359.26 a
48469.46285	350.89 a	48471.48612	342.52 a	48473.47454	166.69 d
48469.49779	158.32 d	48471.52105	149.94 d	48473.50937	334.15 a
48469.53262	325.78 a	48471.55588	317.40 a	48473.54431	141.57 d
48469.56756	133.20 d	48471.59082	124.83 d	48473.57914	309.03 a
48469.60239	300.66 a	48471.62565	292.29 a	48473.61407	116.45 d
48469.63732	108.08 d	48471.66059	99.71 d	48473.64891	283.91 a
48469.67216	275.54 a	48471.69542	267.17 a	48473.68384	91.37 d
48469.70709	82.97 d	48471.73035	74.59 d	48473.71868	258.80 a
48469.74193	250.43 a	48471.76519	242.05 a	48473.75361	66.22 d
48469.77686	57.85 d	48471.80012	49.48 d	48473.78844	233.68 a
48469.81169	225.31 a	48471.83496	216.94 a	48473.82338	41.10 d
48469.84663	32.73 d	48471.86989	24.36 d	48473.85821	208.56 a
48469.88146	200.19 a	48471.90472	191.82 a	48473.89315	15.99 d
48469.91640	7.62 d	48471.93966	359.24 d	48473.92798	183.45 a
48469.95123	175.08 a	48471.97449	166.70 a	48473.96291	350.87 d
48469.98616	342.50 d	48472.00942	334.13 d	48473.99774	158.33 a
48470.02099	149.96 a	48472.04426	141.59 a	48474.03268	325.76 d
48470.05593	317.39 d	48472.07919	309.01 d	48474.06751	133.22 a
48470.09076	124.85 a	48472.11402	116.47 a	48474.10245	300.64 d
48470.12570	292.27 d	48472.14896	283.90 d	48474.13728	108.10 a
48470.16053	99.73 a	48472.18379	91.36 a	48474.17221	275.52 d
48470.19547	267.15 d	48472.21873	258.78 d	48474.20705	82.98 a
48470.23030	74.61 a	48472.25356	66.24 a	48474.24198	250.41 d
48470.26523	242.04 d	48472.28849	233.66 d	48474.27681	57.87 a
48470.30007	49.50 a	48472.32333	41.12 a	48474.31175	225.29 d
48470.33500	216.92 d	48472.35826	208.55 d	48474.34658	32.75 a
48470.36983	24.38 a	48472.39309	16.01 a	48474.38152	200.18 d
48470.40477	191.80 d	48472.42803	183.43 d	48474.41635	7.64 a
48470.43960	359.26 a	48472.46286	350.89 a	48474.45128	175.06 d
48470.47454	166.69 d	48472.49780	158.31 d	48474.48612	342.52 a
48470.50937	334.15 a	48472.53263	325.77 a	48474.52105	149.94 d
48470.54430	141.57 d	48472.56756	133.20 d	48474.55588	317.40 a
48470.57914	309.03 a	48472.60240	300.66 a	48474.59082	124.83 d
48470.61407	116.46 d	48472.63733	108.08 d	48474.62565	292.29 a
48470.64890	283.92 a	48472.67216	275.54 a	48474.66058	99.71 d
48470.68384	91.34 d	48472.70710	82.96 d	48474.69542	267.17 a
48470.71867	258.80 a	48472.74193	250.42 a	48474.73035	74.59 d
48470.75361	66.22 d	48472.77687	57.85 d	48474.76519	242.05 a
48470.78844	233.68 a	48472.81170	225.31 a	48474.80012	49.48 d
48470.82338	41.10 d	48472.84663	32.73 d	48474.83495	216.94 a
48470.85821	208.56 a	48472.88147	200.19 a	48474.86989	24.36 d
48470.89314	15.99 d	48472.91640	7.62 d	48474.90472	191.82 a
48470.92798	183.45 a	48472.95123	175.08 a	48474.93965	359.24 d
48470.96291	350.87 d	48472.98617	342.50 d	48474.97449	166.71 a
48470.99774	158.33 a				

Table (8.2)
Equator crossings of 6-day ERS-1 "observed" orbit. a,d signify ascending and descending crossings, respectively.

Throughout both phases ERS-1 transcribed a 43 revolution per 3 day repeat orbit. Table (8.2) shows the equator crossing times and longitudes of the "observed" orbit generated from the commissioning phase laser ranging data. The tenth crossing occurs with the satellite travelling northwards at an Earth-fixed longitude of 41.12° east of the Greenwich Meridian. This is approximately 1.88° further east than the proposed ice phase northwards crossing of longitude 39.24° east. Hence the ephemerides were both effectively rotated from the commissioning phase to the first ice phase by applying a 1.88° eastwards rotation. That is, new ice phase ephemeris values X_{ICE}, Y_{ICE}, Z_{ICE} were derived at each epoch from the original commission phase values X_{COM}, Y_{COM}, Z_{COM} using

$$\begin{pmatrix} X_{ICE} \\ Y_{ICE} \\ Z_{ICE} \end{pmatrix} = R \begin{pmatrix} X_{COM} \\ Y_{COM} \\ Z_{COM} \end{pmatrix} ,$$

where R is the rotation matrix given by

$$R = \begin{pmatrix} \cos\theta & -\sin\theta & 0 \\ \sin\theta & \cos\theta & 0 \\ 0 & 0 & 1 \end{pmatrix}$$

and $\theta = 1.88°$.

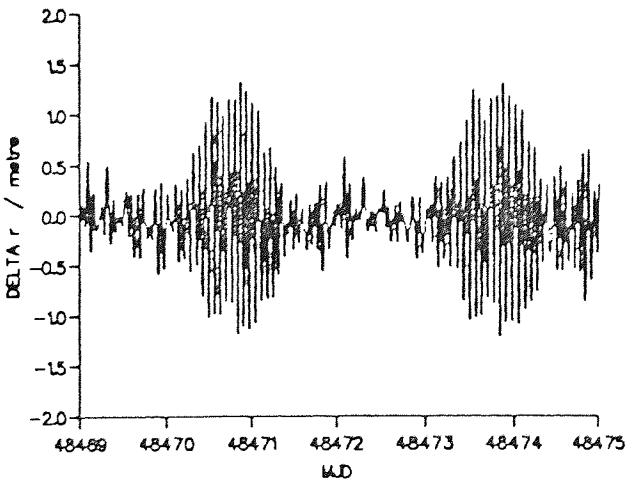

Figure (8.2)
Radial differences of ERS-1 6-day orbits before solution

The radial differences between the new ice phase observed and calculated orbits are illustrated in Figure (8.2), with the typical spectral analysis and geographical distributions of these residuals depicted in Figures (8.3), (8.4) and (8.5). Both orbits were generated from the same initial state vector using identical daily drag coefficients. Thus no linear drag terms were resolved in the orbit error reduction process, although secular periodic terms and small periodic one cycle per revolution terms with amplitude proportional to the square of the time elapsed, which arise from resonance, were solved for. That is, the radial residual equation was given by

$$\Delta r(t) = \sum_{k=-\ell_{max}}^{\ell_{max}} \sum_{m=0}^{\ell_{max}} \left\{ A_{km} \cos \dot{\Psi}_{km} t + B_{km} \sin \dot{\Psi}_{km} t \right\}$$

$$+ a_0 + a_1 \cos M + a_2 \sin M + a_3 \cos 2M + a_4 \sin 2M + a_5 (t - t^*) \sin M$$

$$+ a_6 (t - t^*) \sin 2M + a_7 (t - t^*)^2 \cos M + a_8 (t - t^*)^2 \sin M \; . \qquad -(8.1)$$

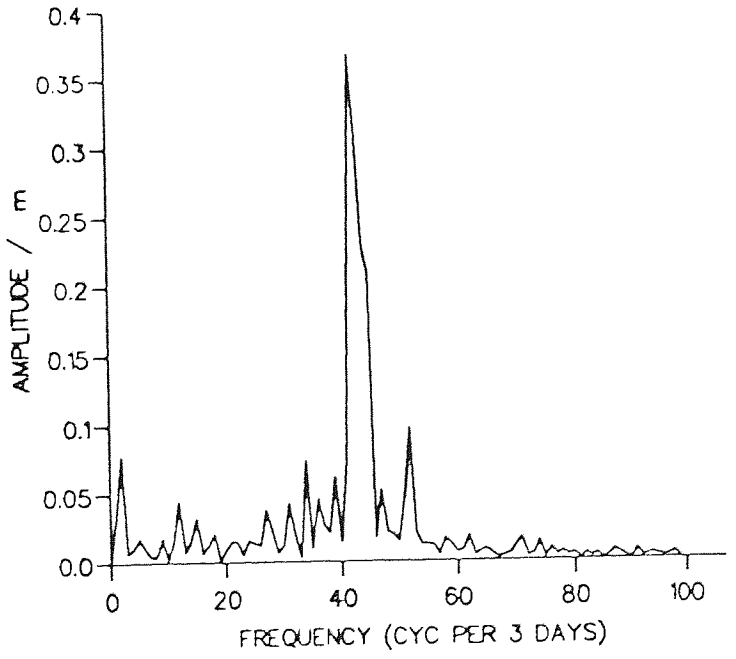

Figure (8.3)
Spectral analysis of radial differences of ERS-1 6-day orbits before solution

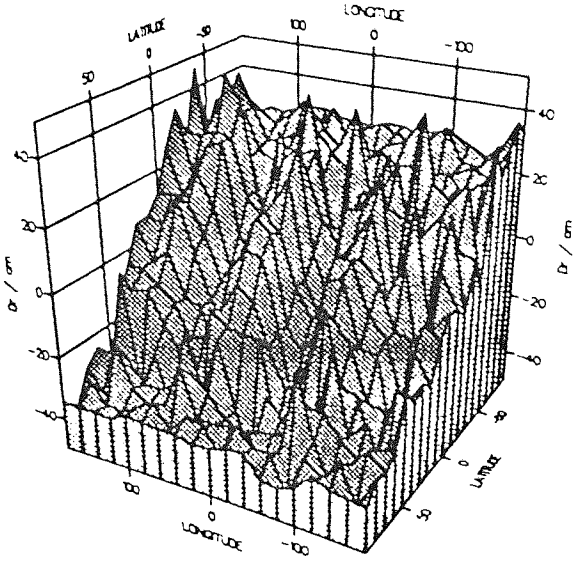

Figure (8.4)
Geographical distribution of mean radial residuals before fit of ERS-1 6-day solutions

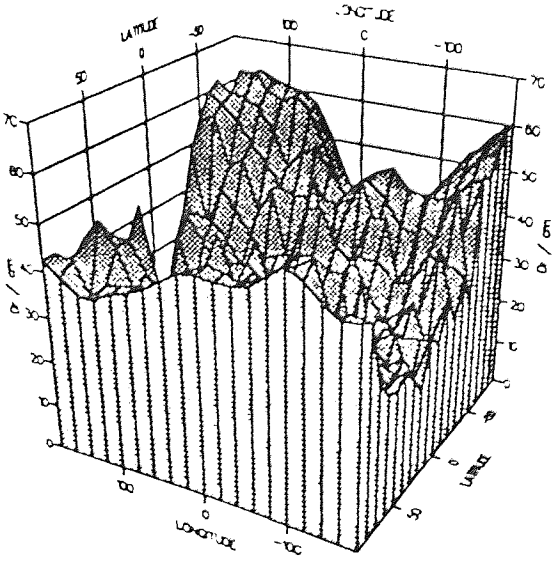

Figure (8.5)
Geographical distribution of radial residual rms error about the mean before fit of ERS-1 6-day solutions

A more detailed map of the global continents was applied than for the 35 day repeat orbit simulations in order to separate the crossovers into marine and land residuals. The map used and crossover positions are shown in Figure (8.6). After the derivation each of the 3,279 marine residuals was given a random perturbation of between -20cm and +20cm to take account of any noise that would be present in real altimetrically derived crossovers.

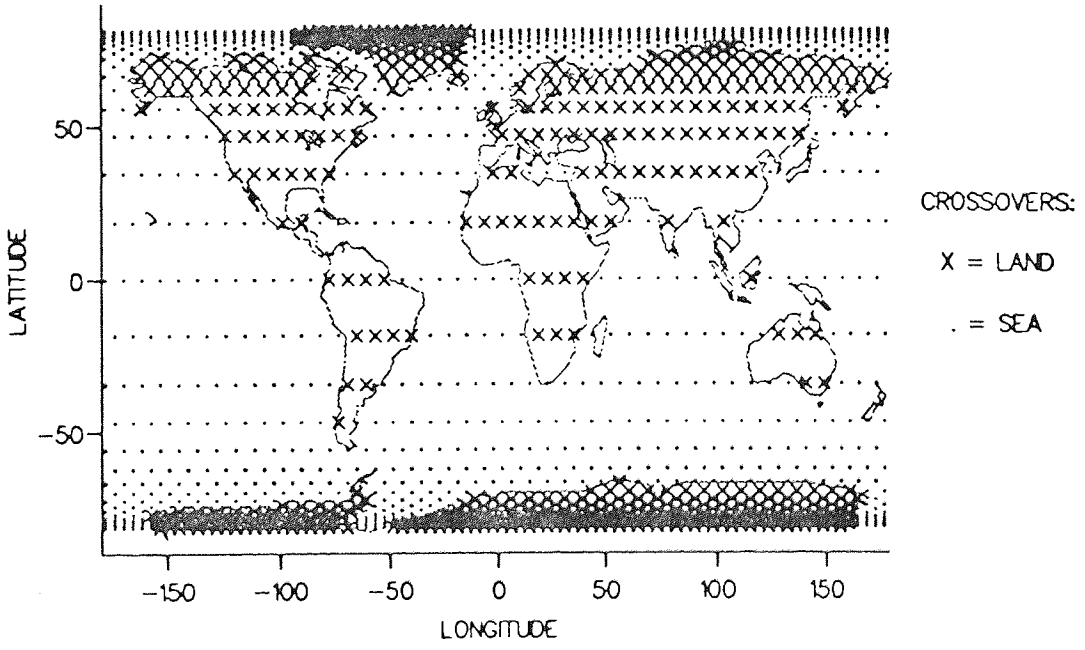

Figure (8.6)
Crossover locations for ERS-1 6-day analysis

The laser station network of ERS-1 is far more comprehensive than for SEASAT, with the 26 stations shown in Figure (8.7) viewing over the time span analysed. Six of these sites were chosen to provide a realistic simulation of short arc determined radial corrections that might be obtained from data extracted from the ice phase. Their positions were selected where simultaneous tracking by more than one station is probable and to supply a reasonable global distribution. Direct radial height measurements were derived in the same manner as for the 35 day repeat simulations and these are given in Table (8.3).

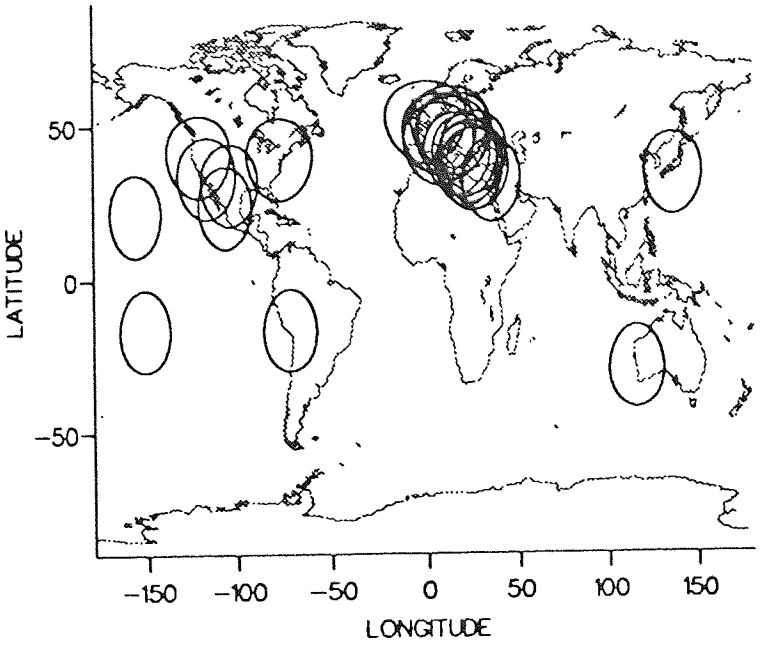

Figure (8.7)
Laser ranging station tracking network for ERS-1

Station	Epoch /MJD	Δr /m	Long. /deg	Lat. /deg	M /deg
7517	48469.386111	0.011	22.8	35.6	53.8
7834	48470.429861	-0.656	11.0	49.6	39.6
7109	48471.249653	-0.756	238.8	39.1	309.8
7105	48472.664583	0.007	283.3	38.6	50.7
7086	48472.736111	0.153	255.5	29.7	59.8
7840	48473.903125	-0.875	359.9	50.8	321.7

Table (8.3)
Direct radial height measurements used in ERS-1 6-day analyses

Each direct height was assigned an a priori standard error of 10cm, after a random perturbation of magnitude up to 5cm was added to each. The crossovers and direct height data were amalgamated and the radial error reduction procedure applied to solve for the 219 coefficients of equation (8.1).

A good solution was achieved, with the radial rms falling to 10.4cm, that is approximately 23% of its original value of 44.6cm. The results are displayed in Figures (8.8) to (8.13).

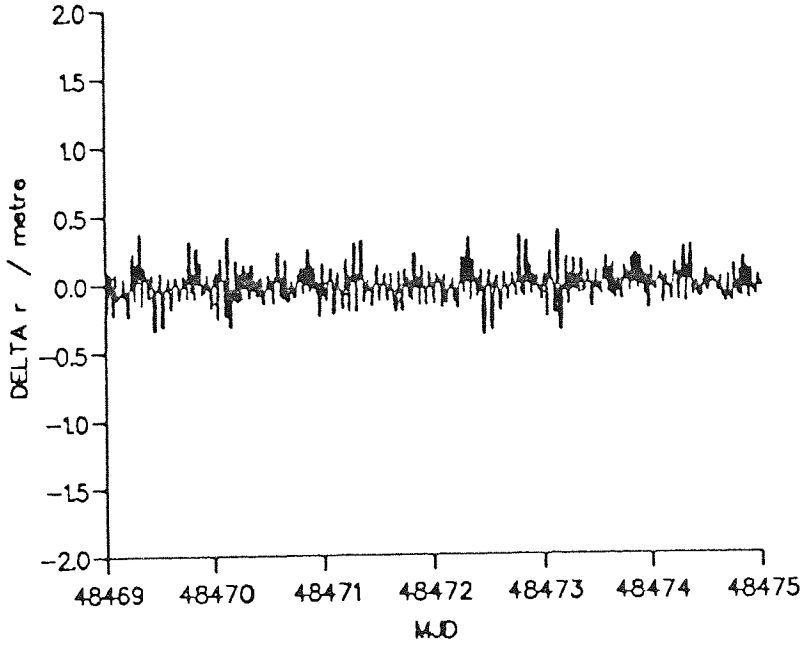

Figure (8.8)
Radial orbit error remaining after fit of ERS-1 6-day solution, using direct height data from laser station locations only

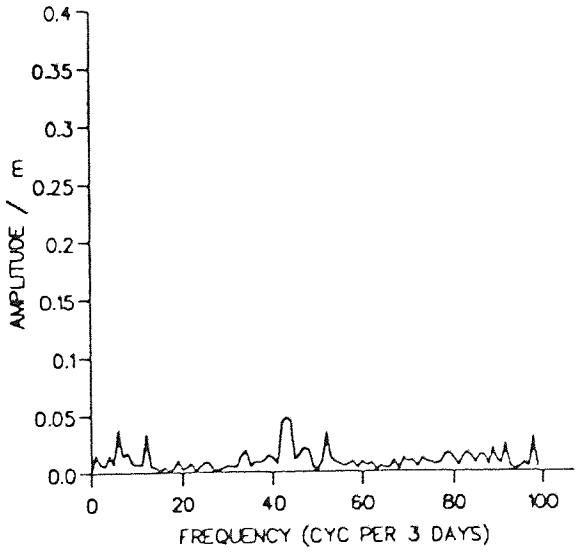

Figure (8.9)
Spectral analysis of radial orbit error remaining after fit of ERS-1 6-day solution using direct height data from laser station locations only

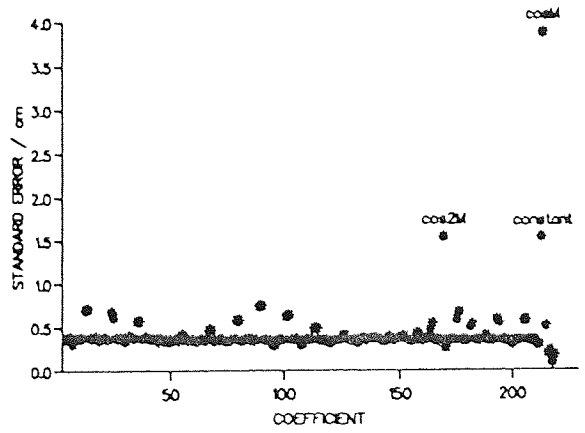

Figure (8.10)
Standard errors of estimated coefficients of ERS-1 6-day solution using direct height data from laser station locations only

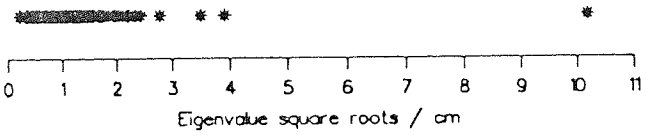

Figure (8.11)
Eigenvalue square roots of ERS-1 6-day solution using direct height data from laser station locations only

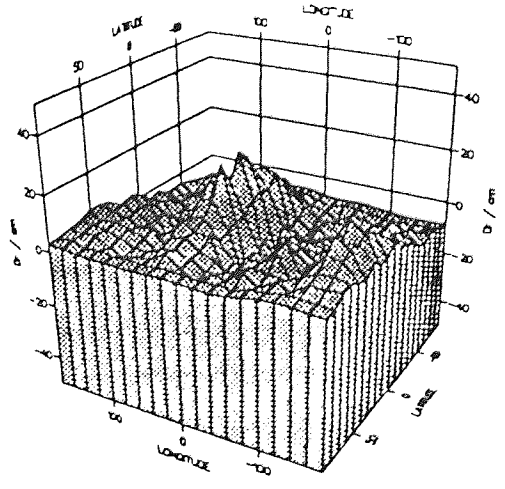

Figure (8.12)
Geographical distribution of mean radial residuals after fit of ERS-1 6-day solution using direct height data from laser station locations only

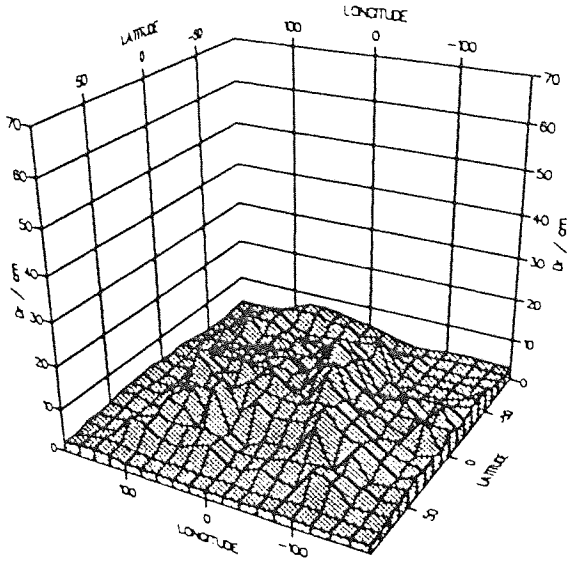

Figure (8.13)
Geographical distribution of radial residual rms error about the mean, after fit of ERS-1 6-day solution using direct height data from laser station locations only

§ 8.2 Transponder Observations

Several locations were proposed as possible sites for the transponder deployment with ERS-1. Having obtained a solution using realistic short arc estimates, the effects of the various propositions on the radial orbit error reduction are now explored.

Of the initial proposals, one transponder would be placed at Venice (Italy) for use in calibrations throughout the commissioning phase, with others at Scott Base, Ross Island (Antarctica), Bulawayo (Zimbabwe), and Fairbanks (Alaska) for polar experiments and to monitor passes over Antarctica and Greenland. An additional site at Easter Island was also under consideration for use in the first ice phase. When used in conjunction with the short arc locations, a good global distribution of tracking sites is achieved. The positions of the proposed sites are given in Figure (8.14) in addition

to those of the laser ranging stations used and the fictitious transponder locations described later (see section §8.4).

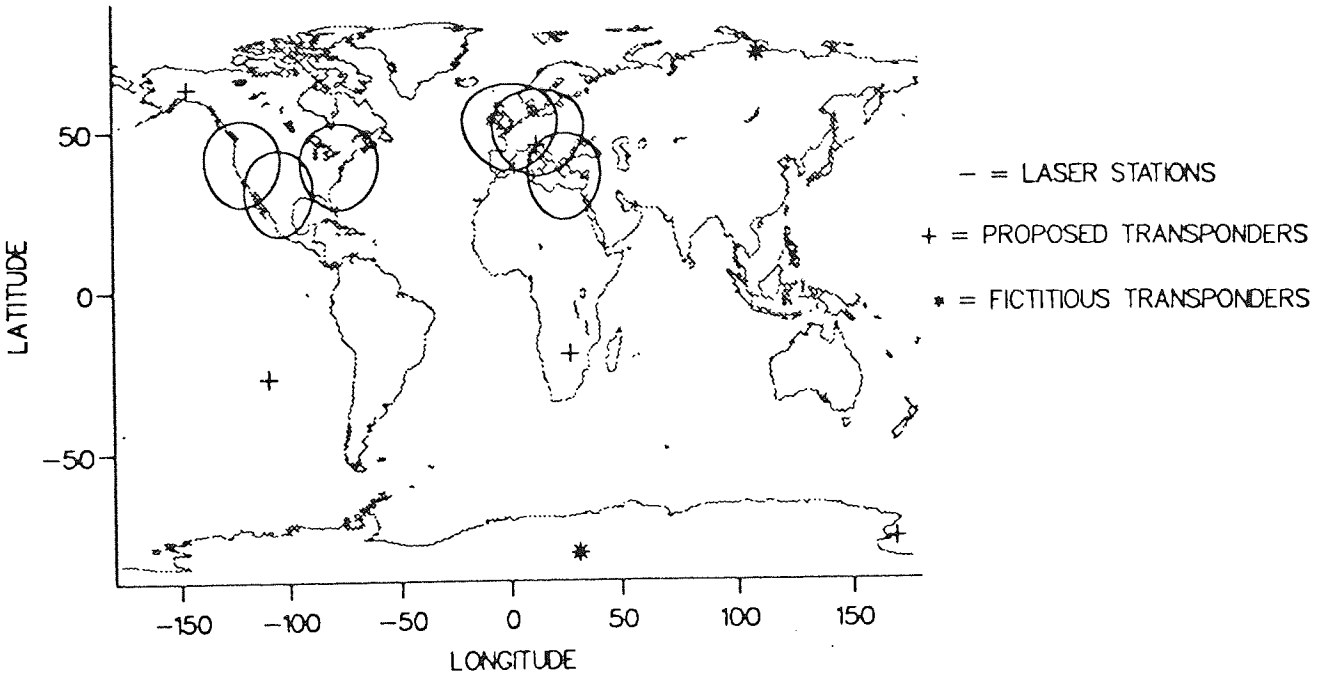

Figure (8.14)
Direct radial height data locations used in the ERS-1 6-day analyses

In order for the illumination of a transponder by the altimeter radar pulse to be sufficient for a reliable reading, the spacecraft must pass almost directly overhead. Thus the transponders must all be located in the vicinity of the ground-track. The epoch of a transponder reading is here estimated by assuming a linear variation in the position of the satellite between successive ephemeris epochs.

Consider Figure (8.15), which depicts the spacecraft passing a transponder at T by moving from position A at time t_1 to B at time t_2. Let the satellite be at P, its closest position to T, at time t.

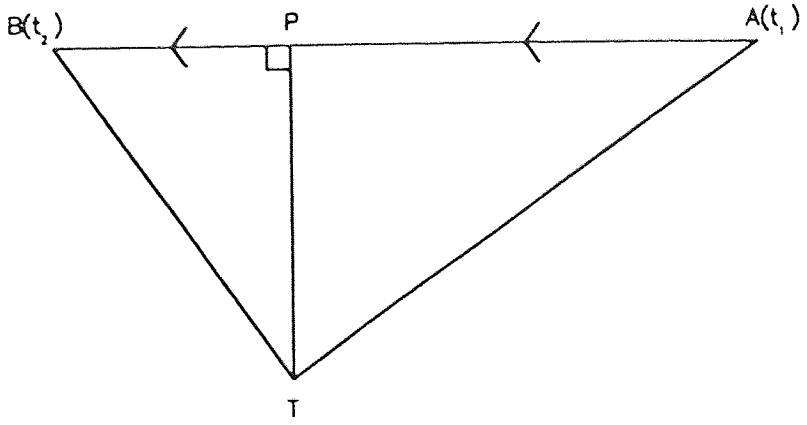

Figure (8.15)
Geometrical configuration used in obtaining the simulated transponder observations

By the cosine rule,

$$\cos \hat{A} = \frac{AT^2 + AB^2 - BT^2}{2\,AT\,AB} \quad \text{and} \quad \cos \hat{B} = \frac{BT^2 + AB^2 - AT^2}{2\,BT\,AB} .$$

But,

$$\cos \hat{A} = \frac{AP}{AT} \quad \text{and} \quad \cos \hat{B} = \frac{BP}{BT} .$$

Hence

$$AP = \frac{AT^2 + AB^2 - BT^2}{2\,AB} \quad \text{and} \quad BP = \frac{BT^2 + AB^2 - AT^2}{2\,AB} .$$

Therefore

$$\frac{AP}{BP} = \frac{AT^2 + AB^2 - BT^2}{BT^2 + AB^2 - AT^2} .$$

Hence, under the assumption of linear variation in position over AB,

$$\frac{t - t_1}{t_2 - t} = \frac{AT^2 + AB^2 - BT^2}{BT^2 + AB^2 - AT^2}$$

$\Rightarrow$

$$t = \frac{t_2 \left(AT^2 + AB^2 - BT^2\right) + t_1 \left(BT^2 + AB^2 - AT^2\right)}{2\,AB^2} .$$

which is the epoch required.

The radial distances at time t were calculated by interpolation in each ephemeris, then differenced to obtain an estimate for the radial residual over a transponder. Creating the observations in this manner ensures that the estimate is derived when the satellite position on the ground-track is close enough to the transponder location for a realistic observation to have been taken. Table (8.4) gives the derived values. During the two repeat orbits made over the six days, the satellite passes over each transponder twice, the second pass three days after the first, so that a pair of observations is obtained from each transponder. Note that the three transponders at Zimbabwe, Italy and Alaska have been situated such that their observations are taken from the same arc as the satellite travelling northwards passes Bulawayo and Venice, then back southwards over Fairbanks. A random noise perturbation of between ±5cm has been applied to each transponder residual.

Site	Location	Epoch/MJD	Δr/m	M/deg
4	Easter Is.	48470.723681	0.710	115.8
2	Scott Base	48471.575095	-0.084	189.0
1	Bulawayo	48471.866226	0.336	251.2
5	Venice	48471.878619	0.153	315.2
3	Fairbanks	48471.892202	-0.183	25.2
4	Easter Is.	48473.723680	0.599	115.8
2	Scott Base	48474.575096	-0.049	186.6
1	Bulawayo	48474.866228	0.616	251.2
5	Venice	48474.878619	0.353	315.3
3	Fairbanks	48474.892203	-0.358	25.3

Table (8.4)
Direct height data from transponder locations

§ 8.3 Transponder Solutions

Each pair of transponder observations was added in turn to the original short arc data set and assumed an a priori standard error of 5cm in the radial error reduction procedure. The solutions are compared in Table (8.5) and Figure (8.16).

Solution no.	Site	Δr_{rms} /cm	$s.e._{max}$ /cm	$\sqrt{ev}_{max}$ /cm
1	1	10.4	3.6	9.5
2	2	10.0	2.1	5.8
3	3	9.8	3.0	8.1
4	4	9.8	3.3	8.6
5	5	11.9	3.7	9.7

Table (8.5)
ERS-1 6-day solutions using single transponder locations

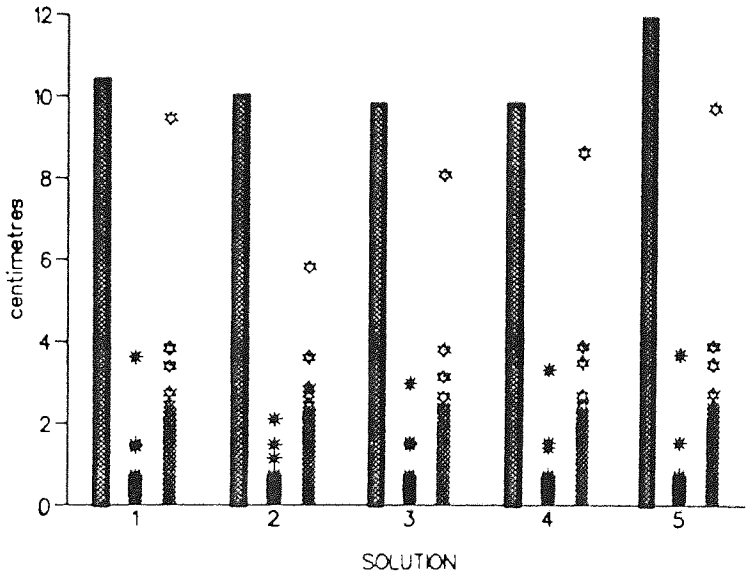

Figure (8.16)
Comparison of single transponder solutions

In Figures (8.16) to (8.19), bars represent Δr_{rms}, asterisks standard errors and stars $\sqrt{\text{eigenvalue}}$. The solution numbers in the tables correspond to those in the diagrams. The outstanding feature is the improvement made upon introduction of the Antarctic transponder, in terms of the resolution of the coefficients. Although the radial rms error is barely affected, the solution is of far greater reliability, with the standard error of the worst determined parameter being reduced to 2.1cm, nearly half the value of that derived in the short arc only analysis. Further, the value of the square root of the maximum eigenvalue is reduced from 10.2cm to 5.8cm. Scott Base is located at the most extreme latitude of all the transponder sites, where the radial

orbit error is particularly dependent on the cosM term, which tends towards its maximum value in this region. Figure (8.10) has shown that the cosM coefficient is the worst determined in the short arc only analysis. Hence high resolution of this parameter, from the heavily cosM dependent radial data supplied at the Scott Base site, has not only reduced the standard error of the cosM term, but in the process has reduced the aliasing of this term into the other coefficients.

Conversely, the Bulawayo transponder, which is close to the equator and therefore provides data which is less dependent on cosM, adds little to the resolution of the cosM term and is thus relatively ineffectual. Venice is situated close to three of the European laser ranging stations. Consequently its latitude, and therefore the mean anomaly of the orbit of the passing satellite, is similar to all three. Hence little new information is acquired from the Venice site over that achieved from short arc estimations.

The simultaneous inclusion of two transponders (i.e. four extra observations) in the data set further improves the solution. Comparisons of the solutions obtained using each of the ten possible pairs appear in Table (8.6) and Figure (8.17). Any pair inclusive of the Antarctic site produces the greatest improvement.

Solution no.	Sites	Δr_{rms} /cm	$s.e._{max}$ /cm	$\sqrt{ev}_{max}$ /cm
1	1,2	9.9	2.0	5.6
2	1,3	9.8	2.9	7.7
3	1,4	9.8	3.2	8.2
4	1,5	12.9	3.2	8.5
5	2,3	9.8	1.7	4.7
6	2,4	9.9	2.0	5.5
7	2,5	10.2	2.0	5.7
8	3,4	9.8	2.7	7.3
9	3,5	10.3	2.8	7.7
10	4,5	10.1	3.2	8.3

Table (8.6)
ERS-1 6-day solutions using pairs of transponder locations

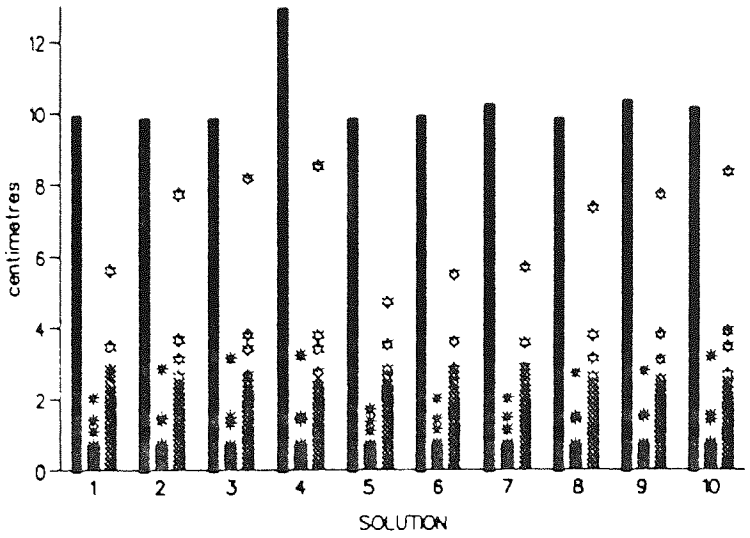

Figure (8.17)
Comparison of solutions obtained using pairs of transponder locations

The three transponders originally planned for the first ice phase orbit were near to Scott Base, Fairbanks and Bulawayo. The solution in which all these are included is given in Table (8.7) and Figure (8.18), along with all other triple combinations. The marked improvement on the short arc only solution provides some guidance as to the results that could have been expected from actual readings.

Solution no.	Sites	Δr_{rms} /cm	$s.e._{max}$ /cm	$\sqrt{ev}_{max}$ /cm
1	1,2,3	9.7	1.7	4.6
2	1,2,4	9.9	2.0	5.3
3	1,2,5	10.5	1.9	5.3
4	1,3,4	9.7	2.6	7.1
5	1,3,5	11.1	2.5	7.0
6	1,4,5	10.7	2.8	7.5
7	2,3,4	9.9	1.7	4.6
8	2,3,5	9.8	1.6	4.6
9	2,4,5	10.1	2.0	5.4
10	3,4,5	9.9	2.6	7.1

Table (8.7)
ERS-1 6-day solutions using three transponder locations

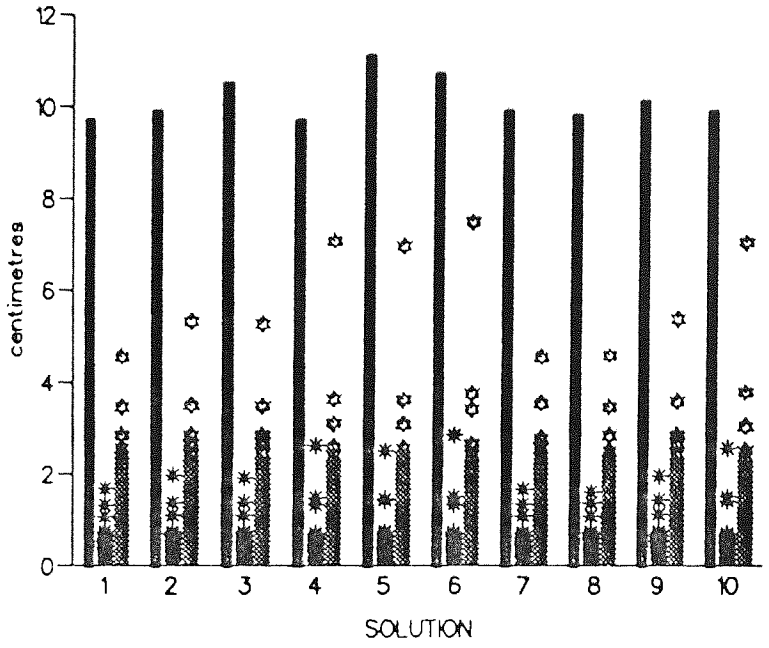

Figure (8.18)
Comparison of solutions obtained using three transponder locations

Although it is unlikely that ERS-1 will be tracked using four or more transponders, solutions derived from each combination of quartets and using all five transponders are included to complete the comparisons. These are shown in Table (8.8) and Figure (8.19).

Solution no.	Sites	Δr_{rms} /cm	$s.e._{max}$ /cm	$\sqrt{ev}_{max}$ /cm
1	1,2,3,4	9.9	1.6	4.4
2	1,2,3,5	9.8	1.5	4.1
3	1,2,4,5	10.2	1.8	5.0
4	1,3,4,5	10.1	2.3	6.4
5	2,3,4,5	9.9	1.6	4.4
6	1,2,3,4,5	9.8	1.5	3.9

Table (8.8)
ERS-1 6-day solutions using four and five transponder locations

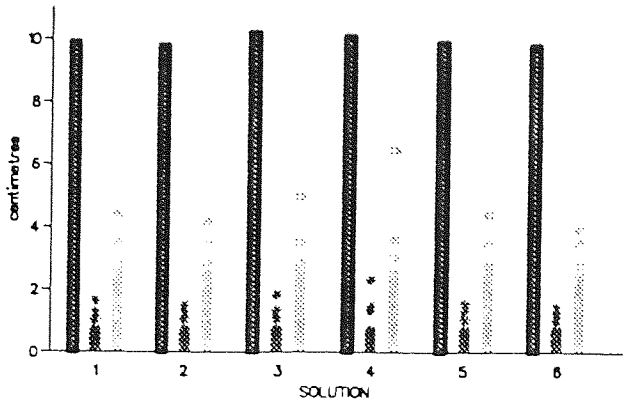

Figure (8.19)
Comparison of solutions obtained using four and five transponder locations

§ 8.4 Fictitious Transponders

Considering the impact of the Scott Base site, extra fictitious polar transponders were created to emphasize the importance of readings available from high latitudes. All the locations considered thus far will generate one observation per repeat period. However, placing a transponder under a crossover point will double this number as the satellite passes overhead on both ascending and descending tracks during each repeat orbit. One fictitious site was set up beneath the land crossover point at latitude 81.3° south, longitude 30.8° east and a second was introduced in the Arctic region. The positions are shown in Figure (8.14). Observations were derived from each, as given in Table (8.9).

Site	Epoch/MJD	Δr/m	M/deg
1	48469.062075	-0.108	181.9
1	48469.131116	-0.342	178.1
2	48470.215625	-0.341	14.1
1	48472.062075	-0.108	181.8
1	48472.131116	-0.296	178.1
2	48473.215625	-0.405	14.1

Table (8.9)
Direct height data from fictitious transponder locations

Adding all three polar transponders (the fictitious sites plus Scott Base) to the short arc data produced the highly reliable results of Figures (8.20) to (8.25), whilst the radial orbit error rms reduced to 10.0cm. In fact, Figures (8.10), (8.11), (8.26) and (8.27) show that using only the data returned from the crossover site produced a considerable improvement on the short arc only solution in terms of the resolution of the coefficients, while reducing the radial orbit error to 10.6cm rms.

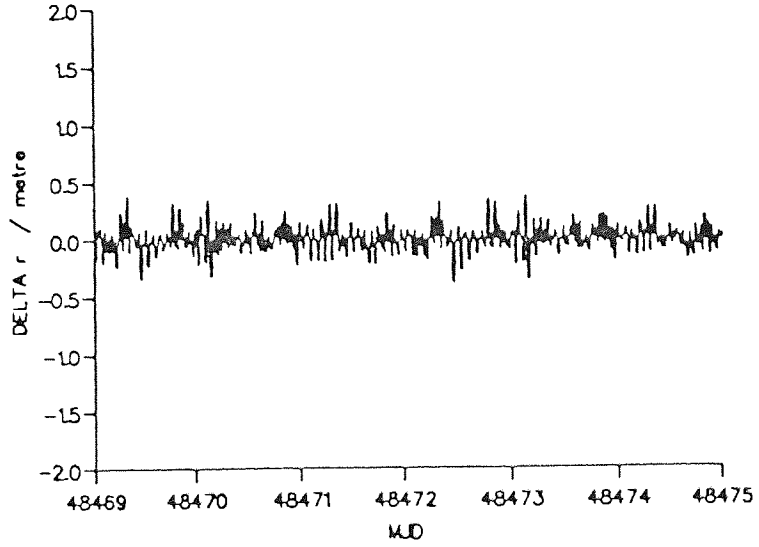

Figure (8.20)
Radial orbit error remaining after fit of ERS-1 6-day solution using direct height data from laser station locations plus all three polar transponder locations

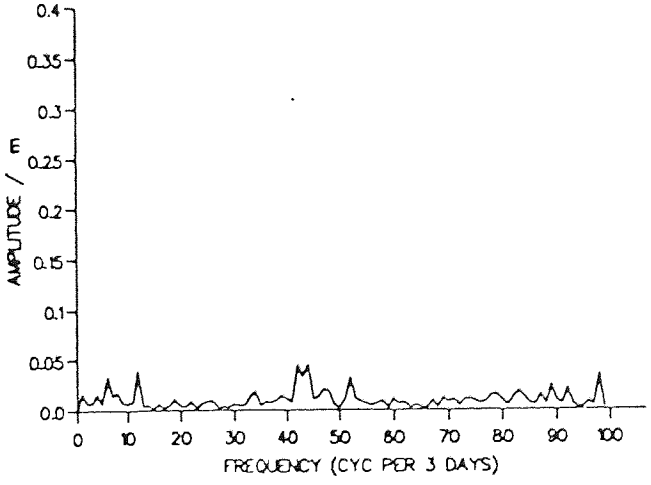

Figure (8.21)
Spectral analysis of radial orbit error remaining after fit of ERS-1 6-day solution using direct height data from laser station locations plus all three polar transponder locations

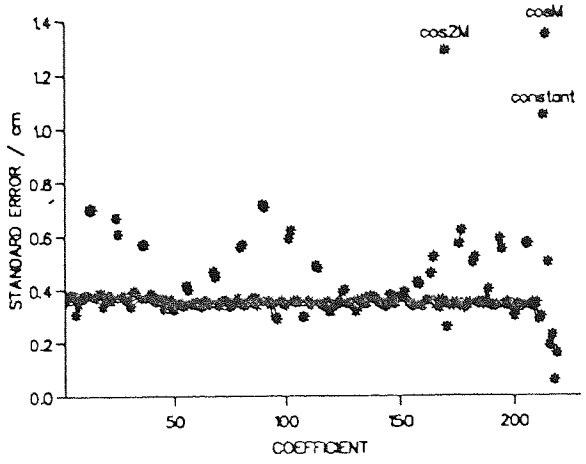

Figure (8.22)
Standard errors of estimated coefficients of ERS-1 6-day solution using direct height data from laser station locations plus all three polar transponder locations

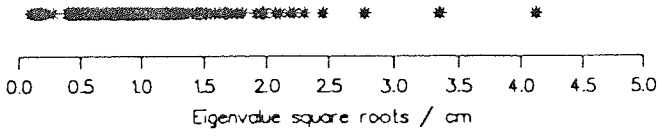

Figure (8.23)
Eigenvalue square roots of ERS-1 6-day solution using direct height data from laser station locations plus all three polar transponder locations

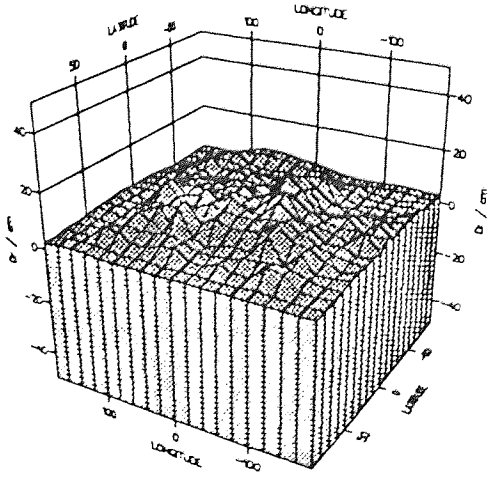

Figure (8.24)
Geographical distribution of mean radial residuals after fit of ERS-1 6-day solution using direct height data from laser station locations plus all three polar transponder locations

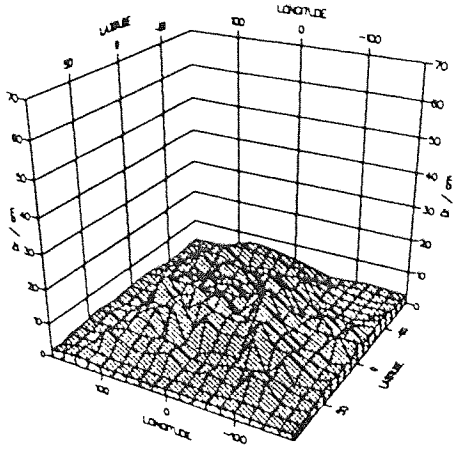

Figure (8.25)
Geographical distribution of radial residual rms error about the mean, after fit of ERS-1 6-day solution using direct height data from laser station locations plus all three polar transponder locations

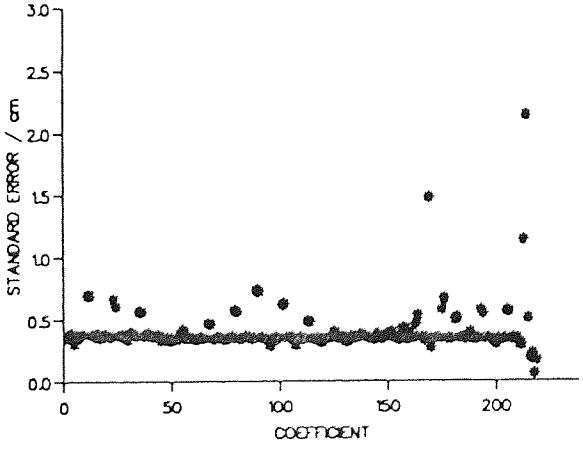

Figure (8.26)
Standard errors of estimated coefficients of ERS-1 6-day solution using direct height data from laser station locations plus the sub-crossover polar transponder location

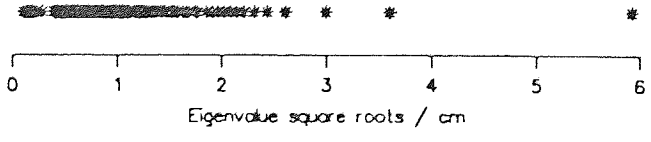

Figure (8.27)
Eigenvalue square roots of ERS-1 6-day solution using direct height data from laser station locations plus the sub-crossover polar transponder location

Finally, Figures (8.28) to (8.33) display the results of inclusion of all transponder locations, real and fictitious, in the data. The excellent solution has been achieved in reducing the radial orbit error to 9.6cm.

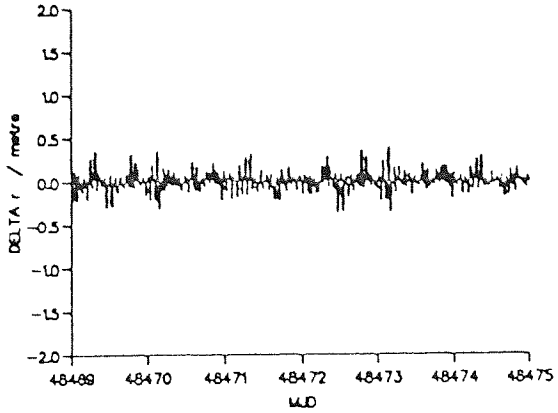

Figure (8.28)
Radial orbit error remaining after fit of ERS-1 6-day solution using direct height data from laser station locations plus all transponder locations

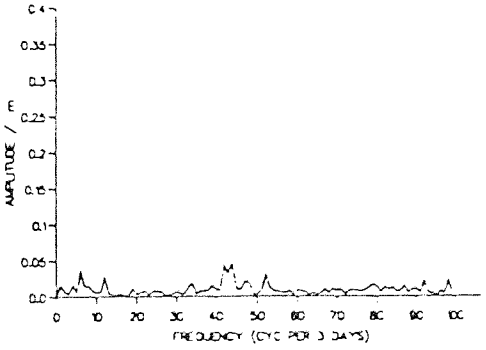

Figure (8.29)
Spectral analysis of radial orbit error remaining after fit of ERS-1 6-day solution using direct height data from laser station locations plus all transponder locations

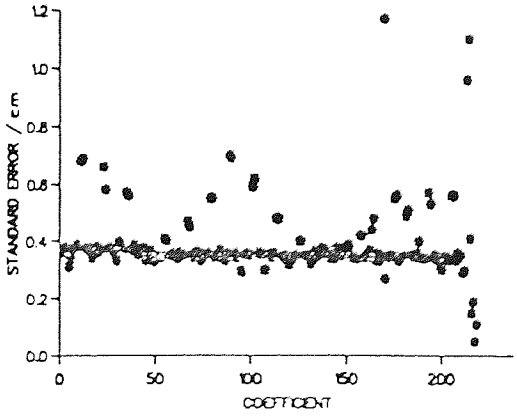

Figure (8.30)
Standard errors of estimated coefficients of ERS-1 6-day solution using direct height data from laser station locations plus all transponder locations

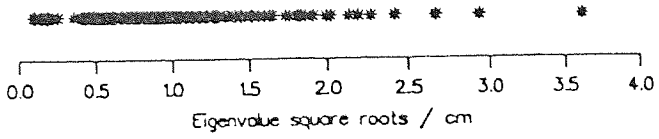

Figure (8.31)
Eigenvalue square roots of ERS-1 6-day solution using direct height data from laser station locations plus all transponder locations

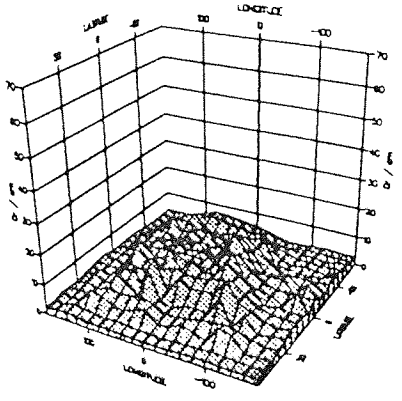

Figure (8.32)
Geographical distribution of mean radial residuals after fit of ERS-1 6-day solution using direct height data from laser station locations plus all transponder locations

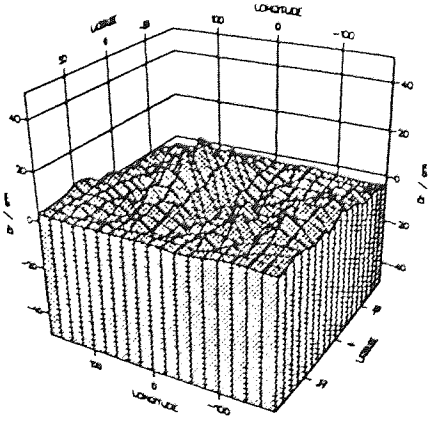

Figure (8.33)
Geographical distribution of radial residual rms error about the mean, after fit of ERS-1 6-day solution using direct height data from laser station locations plus all transponder locations

§ 8.5 Conclusions

The results accentuate the strong dependence of the radial orbit error reduction on the position of the radial data and illustrate the value of placing transponders in polar regions. Although the short arc solution is improved by inclusion of any of the transponders, the Antarctic location is clearly the most influential due to its high latitudinal magnitude. Indeed, the solution involving only the Scott Base transponder is better than that achieved from the simultaneous inclusion of all the other four. These analyses, coupled with the relative robustness, low cost and manoeuvrability of transponders strengthens the case for their installation in hostile polar regions in the future, from where vital radial data could be obtained and where the deployment of other tracking devices is impractical.

CHAPTER 9

CONCLUSIONS

A non-dynamic procedure for reducing the global radial orbit error of dynamic long arc altimetric ephemerides has been proposed. This involves the refinement of a set of crossover difference residuals derived from the long arcs.

An overall global radial correction expression due to both gravitational and non-gravitational causes has been analytically developed. Mismodelling of the gravitational field of the Earth provides the main component, although corrections due to air drag and solar radiation pressure mismodelling and initial state vector errors are also significant. The separate effects of each of these constituents has been illustrated. The one cycle per revolution frequency term has been identified as supplying the principal contribution to the overall correction.

A crossover difference residual expression has been formulated by differencing the radial expressions at the two ground-track points of intersection. The important one cycle per revolution cosine parameter is included in those of the radial correction unobservable in crossover data. Particular sets of other frequency terms have been established as mutual linear combinations. The unobservable and linearly combined coefficients require for their recovery a number of direct radial height observations.

The feasibility of the method has been vindicated upon application to data from the three day repeat orbit of the NASA satellite SEASAT (1978-64A). An initial check was successfully carried out using orbits generated from separate atmospheric density models, thus validating the non-gravitational part. Using short arc derived radial corrections as the direct height data, it was found that frequency dependent

constraints are required for the simultaneous recovery of all gravitational coefficients. The inclusion of the constraints produced an adequate solution, although the deficiency of globally distributed SEASAT tracking data was found to be an impediment. Several additional fictitious direct measurements were consequently added. The results are most promising, with the crossover residual error reduced to less than 34% of its initial value. An equivalent global radial orbit error reduction of from 50.1cm to 16.9cm was achieved, which gives insight into the possible reduction that could be reasonably expected from a more extensive global coverage of tracking data.

The concept of arc aggregates has been devised. Including the radial misclosure between successive arcs as an infallible observation effectively creates a continuous smooth orbit over the whole time span. Having identified arc-dependent and arc-independent parameters within the radial correction expression, the arc aggregate technique was successfully applied to several consecutive SEASAT three day repeat periods. The reliable eighteen day global solution has substantially reduced the equivalent radial orbit error from 51.0cm to 19.6cm, a highly satisfactory resolution for fitting data from three separate arcs to a single radial correction model.

A clone of the GEM-T1 gravity field model was constructed and employed in a full simulation of the 501 revolution per 35 days repeat orbit of ERS-1. Using the arc aggregate procedure, the reduction method was progressively applied until the full repeat period was covered. Highly promising results were returned, using six of the sites originally anticipated for use in PRARE. The final 35 consecutive day radial reduction was from 90.9cm to 16.4cm, or 81.9%.

The validity of the radial orbit error correction method has been firmly established. Given the comprehensive spread of high quality tracking data that should become available, the possibility exists of reducing the global radial orbit error of similar altimetric missions using the techniques proposed. A global reduction to less

than 20cm rms over periods of time spanning several long arc orbits should be achievable.

The effects of varying the geographical locations of the direct height observations has been investigated. Laser ranging data from an early ERS-1 three day repeat orbit was employed and various proposed locations for ground-based transponder sites considered. The results accentuate the strong dependence of the radial ephemeris correction on the positions of the direct height data. The site at Scott Base, Antarctica, situated at the most extreme latitude, was found to have the greatest influence. Fictitious transponders were set up in other polar regions in order to provide data which was heavily dependent on the fundamental cosM coefficient of the radial orbit error expression. The solutions obtained have served to illustrate the potential impact of tracking data situated in positions of high latitudinal magnitude. Hence the future installation of transponders in hostile polar territory could provide vital data from regions where the deployment of other less manoeuvrable tracking devices such as lasers is impractical.

References

Aksnes, K., Short-period and long-period perturbations of a spherical satellite due to direct solar radiation, Celestial Mechanics **13**, 89-104, 1976.

Bomford, G., Geodesy (4th edition), Clarendon Press, Oxford, 1980.

Brouwer, D. and Clemence, G.M., Methods of Celestial Mechanics, Academic Press, New York and London, 1961.

Colombo, O.L., Altimetry, Orbits and Tides, NASA Technical Memorandum 86180, National Aeronautics and Space Administration, Goddard Space Flight Center, Greenbelt, Maryland 20771, U.S.A., 1984.

Cook, G.E., Perturbations of near-circular orbits by the Earth's gravitational potential, Planet. Space Sci., **14**, 433-444, 1966.

Engelis, T., On the simultaneous improvement of a satellite orbit and determination of sea surface topography using altimeter data, manuscripta geodaetica, **13**, 180-190, 1988.

Gooding, R.H., A second-order satellite orbit theory, with compact results in cylindrical co-ordinates, Proc. R. Soc. Lond.,A **299**, 425-474, 1981.

Hedin, A.E., A revised thermospheric model based on mass spectrometer and incoherent scatter data:MSIS-83, J. Geophys. Res., **88**, 10170-10188, 1983.

Jacchia, L.G., Atmospheric Models in the Region from 110 to 2000km. In CIRA72, COSPAR Working Group 4, Akademie-Verlag, Berlin, 1972.

Katsgris, E.C. and Dixon, T.H., Special processing of wide beam altimeter data to improve resolution in high relief terrain, Proceedings of the Consultative Meeting on Imaging Altimeter Requirements and Techniques, held on 30th May-1st June 1990, at the Mullard Space Science Laboratory, University College London, III.5, Final Report, 1990.

Kaula, W.M., Theory of Satellite Geodesy, Blaisdell Publishing Company, Waltham, Massachusetts, 1966.

King-Hele, D.G., Satellite Orbits in an Atmosphere: Theory and Applications, Blackie and Son Ltd., Glasgow and London, 1987.

Lambeck, K., Tidal Dissipation in the Oceans: Astronomical, Geophysical and Oceanographic Consequences, Proc. R. Soc. Lond.,A **287**, 545-594, 1977.

Moore, P. and Gray, R.D., Global non-dynamic improvement of radial positioning for altimeter satellites, Adv. Space Res., **11(6)**, 125-130, 1991.

Moore, P. and Rothwell, D.A., A study of gravitational and non-gravitational modelling errors in cross-over differences, manuscripta geodaetica, **15**, 187-206, 1990.

Ponman, T., The analysis of Periodicities in Irregularly Sampled Data, Mon. Not. R. astr. Soc., **196**, 583-596, 1981.

Rapp, R.H., Wang, Y.M. and Pavlis, N.K., The Ohio State 1991 Geopotential and Sea Surface Topography Harmonic Coefficient Models, Report No. 410, Dept. of Geodetic Science and Surveying, The Ohio State University, Columbus, Ohio, U.S.A., 1981.

Rothwell, D.A., Precise orbit determination and analysis from satellite altimetry and laser ranging, PhD thesis, The University of Aston in Birmingham, Birmingham, 1989.

Rowlands, D., The adjustment of SEASAT altimeter data on a global basis for geoid and sea surface height determinations, Reports for the Dept. of Geodetic Science and Surveying, Report No. 325, The Ohio State University, Dept. of Geodetic Science and Surveying, Columbus, Ohio, U.S.A., 1981.

Roy, A.E., Orbital Motion, Hilger, Bristol, 1982.

Sandwell, D.T., Milbert, D.G. and Douglas, B.C., Global Nondynamic Orbit Improvement for Altimetric Satellites, J. Geophys. Res., **91(B9)**, 9447-9451, 1986.

Schrama, E.J.O., The role of orbit errors in processing of satellite altimeter data, Netherlands Geodetic Commission, Publications on Geodesy, New Series Number 33, Thijsseweg 11, Delft, The Netherlands, 1989.

Sinclair, A.T., The determination of orbit corrections by short-arc techniques, with application to ERS-1, manuscripta geodaetica, **14**, 238-246, 1988.

Tapley, B.D. and Rosborough, G.W., Geographically Correlated Orbit Error and Its Effect on Satellite Altimetry Missions, J. Geophys. Res., **90(C6)**, 11817-11831, 1985.

Vass, P. and Handoll, M., U.K. ERS-1 Reference Manual, Doc. No. DC-MA-EOS-ED-0001, Issue 1.0, EODC Documentation and Information Service, Earth Observation Data Centre, Space Dept., Royal Aerospace Establishment, Farnborough, 1991.

Wagner, C.A., and Melchioni, E., On using precise laser ranges to provide vertical control for satellite altimetric surfaces, manuscripta geodaetica, **14**, 305-338, 1989.